

**Fundamental Studies of Stratified Stellar Convection:
Simulations and Theory**

by

Evan H. Anders

B.S., Whitworth University, 2014

M.S., University of Colorado, 2017

A thesis submitted to the
Faculty of the Graduate School of the
University of Colorado in partial fulfillment
of the requirements for the degree of
Doctor of Philosophy
Department of Astrophysical & Planetary Sciences
2020

This thesis entitled:
Fundamental Studies of Stratified Stellar Convection: Simulations and Theory
written by Evan H. Anders
has been approved for the Department of Astrophysical & Planetary Sciences

Prof. Benjamin P. Brown

Prof. Mark P. Rast

Prof. Steven Cranmer

Prof. Ian Grooms

Prof. Keith Julien

Dr. Bradley Hindman

Date _____

The final copy of this thesis has been examined by the signatories, and we find that both the content and the form meet acceptable presentation standards of scholarly work in the above mentioned discipline.

Anders, Evan H. (Ph.D., Astrophysical & Planetary Sciences)

Fundamental Studies of Stratified Stellar Convection: Simulations and Theory

Thesis directed by Prof. Benjamin P. Brown

Convection is a ubiquitous heat transport mechanism in astrophysics and geophysics. In addition to transporting heat, convective motions drive a wide variety of interesting phenomena. In particular, the magnetic dynamos of the Earth and Sun are seated in the turbulent convective motions of their respective core and outer envelope. In addition to driving magnetism, convection is responsible for establishing observable mean flows, such as the Sun's differential rotation. The nonlinear nature of convection in the highly turbulent regime of geophysical and astrophysical settings makes its behavior difficult to predict, understand, and model. In this thesis, I conduct a series of experiments into the fundamental nature of convection.

The first two of these experiments examine numerical simulations of fully compressible convection in the context of stratified atmospheres. From these simulations, we have learned how to study increasingly turbulent, astrophysically-interesting convection while holding the Mach number and the Rossby number (which measures the importance of the Coriolis force) constant. In these studies, we have learned that the fundamental heat transport mechanisms at work in simulations of stratified convection are the same as those at work in more simple, incompressible convection.

The next two studies examine simulations of Boussinesq convection with a specific focus on understanding how simulations of convection relax over time from their initial conditions. In the first of these studies, we develop a simple procedure for coupling simulations with simple boundary value problems to rapidly accelerate the simulation relaxation process. We find very good agreement between accelerated simulations and simulations which traditionally timestep through their thermal relaxation process. In the second of these experiments, we show that the relaxation timescale is linked to the choice of thermal boundary conditions. We further show that thermal relaxation is akin to a walk through parameter space from a turbulent to more laminar regime.

In our final study, we examine the evolution of “thermals” in stratified atmospheres. Thermals are regions of buoyant (or dense) fluid which accelerate due to their buoyancy forces and may be the fundamental unit of convection in the Earth’s atmosphere. We develop a theory describing the evolution of thermals in stratified domains. This theory describes how atmospheric stratification affects buoyant entrainment of atmospheric fluid. We test this theory with laminar 2D and 3D simulations, and discuss implications that this work may have for stellar envelope convection.

Dedication

To Sami. Thanks for dealing with my late-night simulation check-ins, random stress, etc. for (...6?) years now.

...also, to Finn. He's adorable.

Acknowledgements

I'd first and foremost like to thank my family (especially Sami), my cohort (Sam [er, Soaring Eagle], Jhett, Nick, Piyush, Tristan, Jessica), and my other friends and colleagues at CU who supported me, helped me grow as a person/scientist, or just endured horrible meetings alongside me.

I'd like to thank my mentors who have helped me grow as a scientist over the past few years. In this, I'd especially like to thank Ben, who helped teach me to be an open-minded, careful scientist while also teaching me that it's important to balance family life. Beyond Ben, I'm very grateful for the guidance that Jeff Oishi and Daniel Lecoanet have given me as I have navigated the thesis and postdoc process. Outside of my academic mentors, I'd also like to thank my mentors who helped me grow as a teacher: Seth Hornstein, and the ISEE staff, especially Austin Barnes.

I'd like to thank my collaborators and co-authors. The effort and work that Ben Brown, Jeff Oishi, Daniel Lecoanet, Geoff Vasil, Katie Manduca, and Lydia Korre put into our manuscripts vastly improved the quality of the science therein. I'm also broadly grateful to Mark Rast, Nick Featherstone, Brad Hindman, Jon Aurnou, Nadir Jeevanjee, Ian Grooms, and Axel Brandenburg. Discussions with all of these great scientists helped me better understand the problems I was grappling with.

For funding, I'm grateful to the APS department for funding my first year of graduate school as a teaching assistant. I also gratefully acknowledge the support of CU's George Ellery Hale Graduate Student Fellowship, which supported me in years 2-4, and NASA Earth and Space Science Fellowship 80NSSC18K1199, which supported me in years 5-6. I'm also broadly grateful to NASA LWS grant number NNX16AC92G, which has paid for a couple of summer salaries and has enabled travel.

Without the NASA Pleiades supercomputer, none of this work would have been possible. Pleiades is part of the NASA High End Computing (HEC) program through the NASA Advanced Supercomputing (NAS) Division at Ames Research Center. All computations were conducted using allocation GIDs s1647 and g26133.

Contents

Chapter

1	Introduction	1
1.1	Motivation	1
1.1.1	Convection in Astrophysics: Stars, Planets, & Beyond	1
1.1.2	Asteroseismology & Helioseismology	4
1.1.3	The Solar Convective Conundrum	6
1.2	Perspectives on Studies of Convection	8
1.2.1	Rayleigh-Bénard convection	9
1.2.2	More Realistic Geophysical and Astrophysical Experiments	11
1.2.3	Mixing Length Theory & Stellar Structure Models	15
1.2.4	The Impossibility of Astrophysical Parameter Space	17
1.3	Numerical Methods	19
1.3.1	Direct Numerical Simulations vs. Large Eddy Simulations	19
1.3.2	Finite Element vs. Spectral Methods	21
1.3.3	Timestepping: Implicit & Explicit Methods	22
1.3.4	Equation Formulation: From Complexity to Simplicity	23
1.3.5	Dedalus: A Pseudospectral Toolkit	26
2	Convective heat transport in stratified atmospheres at low and high Mach number	30
2.1	Preamble	30

2.2	Published work	31
2.2.1	Introduction	31
2.2.2	Experiment	32
2.2.3	Results & Discussion	35
2.2.4	Discussion & Future Work	40
2.2.5	Appendix A: Table of simulation parameters	42
2.3	Postscript and lessons learned since publication	44
3	Predicting the Rossby Number in Convective Experiments	45
3.1	Preamble	45
3.2	Published work	46
3.2.1	Introduction	46
3.2.2	Experiment	47
3.2.3	Results	51
3.2.4	Discussion	56
3.2.5	Appendix A: Table of Simulations	58
3.3	Postscript and lessons learned since publication	60
4	Accelerated evolution of convective simulations	62
4.1	Preamble	62
4.2	Published work	63
4.2.1	Introduction	63
4.2.2	Experiment	66
4.2.3	The method of Accelerated Evolution	68
4.2.4	Results	72
4.2.5	Computational Time-savings of AE	79
4.2.6	Discussion & Conclusions	81
4.2.7	Appendix A: Table of Runs	82

4.2.8	Appendix B: Accelerated Evolution Recipe	82
4.3	Postscript and lessons learned since publication	86
5	Convective dynamics with mixed temperature boundary conditions: why thermal relaxation matters and how to accelerate it	88
5.1	Preamble	88
5.2	Submitted Mauscript	88
5.2.1	Introduction	88
5.2.2	Simulation Details	90
5.2.3	Results	93
5.2.4	Rotating Rayleigh-Bénard Convection	105
5.2.5	Conclusions & Discussion	108
5.2.6	Appendix A: Table of Simulations	111
6	Entropy Rain: Dilution and Compression of Thermals in Stratified Domains	113
6.1	Preamble	113
6.2	Published work	114
6.2.1	Introduction	114
6.2.2	Model of thermal evolution	117
6.2.3	Simulation setup	123
6.2.4	Model verification	127
6.2.5	Implications for entropy rain hypothesis	130
6.2.6	Summary & Conclusion	136
6.2.7	Appendix A: Thermal Measurements	137
6.2.8	Appendix B: Thermal Tracking Algorithm	137
6.2.9	Appendix C: Table of Simulations	138
6.3	Postscript and lessons learned since publication	140

7 Unpublished Work and Open Mysteries	141
7.1 Flywheel Modes in 2D Convection	141
7.1.1 An argument for the scaling of enstrophy in a Boussinesq, convective system	142
7.1.2 Where does the enstrophy come from?	144
7.1.3 Next steps	145
7.2 The Magnitude of Viscous Terms in Turbulent Convection	145
7.3 Internally Heated, Fully Compressible Convection	147
7.3.1 Preliminaries: convective stability and available flux	147
7.3.2 Disappearance of internal heating term from perturbation equations	149
7.3.3 Two internally heated/cooled basic atmospheric models	149
7.3.4 Density profile construction	151
7.3.5 Next steps	151
7.4 Stratified Accelerated Evolution	151
7.4.1 Modifications to the method of Accelerated Evolution	152
7.4.2 Next steps	154
7.5 A Freefall Nondimensionalization of the Fully Compressible Equations	154
7.5.1 Equation formulation derivation	155
7.6 Convection with Kramer's Opacity	157
7.6.1 Single-layer, polytropic atmospheres	158
7.6.2 A note on implementing a Kramer's Opacity in Dedalus	159
7.7 Turbulent Thermals	160
Bibliography	163

Tables

Table

2.1	Simulation information for Anders & Brown 2017.	43
3.1	Parameter space boundaries explored in Predictive Rossby Number studies	51
3.2	Simulation information for Anders et al 2019	59
4.1	Computational cost of AE and SE	80
4.2	Simulation information for Anders, Brown & Oishi 2018.	83
5.1	PDF moments for FT and TT-to-FT comparisons	102
5.2	Table of simulations for Anders et al. 2020 (submitted)	112
6.1	Measured values of constants in thermal evolution theory.	131
6.2	Simulation information for Anders, Lecoanet, & Brown 2019	139

Figures

Figure

1.1	Images of solar granulation and supergranulation.	2
1.2	Introduction to asteroseismology.	4
1.3	The convective conundrum.	7
1.4	Schematics of hypotheses that solve the convective conundrum.	8
1.5	A description of Rayleigh-Bénard convection studies.	10
1.6	Modification of Nu vs. Ra in rotating RBC and magnetoconvection.	12
1.7	Visualizations of modern simulations of astrophysical convection.	13
1.8	Modern convective laboratory experiments.	14
2.1	Mach number scaling in polytropic solutions.	36
2.2	Flow morphology of 2D, 3D, and low and high Mach number flows.	37
2.3	Scaling of Nusselt and Reynolds number at low and high Mach number.	38
2.4	Stratification: density vs. height at different Mach numbers	41
3.1	Parameter space of rotating convection: critical values and Rossby number dependence on inputs	49
3.2	Depiction of flow morphologies at various values of the Rossby number	52
3.3	Scaling of Nusselt and Reynolds numbers on fixed Predictive Rossby paths.	54
3.4	Boundary layer evolution on fixed Predictive Rossby paths	55
3.5	Initial Ro_p results in spherical simulations	61

4.1	Time evolution traces of an AE and SE convective simulation	71
4.2	Time evolution of the Nusselt number in AE vs. SE	73
4.3	Dynamical description explaining instantaneously negative Nusselt number values . .	75
4.4	Parameter space comparison of AE and SE values	76
4.5	Evolved thermodynamic states of AE and SE simulations.	77
4.6	Probability distribution comparison of AE and SE dynamics	79
4.7	Flux and Temperature Nu vs. Ra.	87
5.1	Snapshots and PDFs comparing temperature fields in FT and TT simulations. . . .	94
5.2	Scalar time traces and parameter space scalings for FT and TT simulations	97
5.3	1D profiles of temperatures and fluxes in TT and FT simulations	98
5.4	Time traces and PDF comparisons of FT and TT-to-FT simulations	100
5.5	PDF and snapshot examination of asymmetries in FT simulations	104
5.6	Time traces, parameter space plot, and snapshots showing evolution of rotating FT simulation	106
6.1	Filling factor evolution of entropy raindrops according to limiting theories and simulations.	116
6.2	Pictoral description of the evolution of thermals as density stratification increases . .	118
6.3	Traces showing simulation values of quantities assumed to be constant in thermal evolution theory	121
6.4	Depth and radius evolution of thermals at varying stratifications.	128
6.5	Comparison of low Mach number Fully Compressible and Anelastic thermal results. .	129
6.6	Implications of thermal experiment results for solar convection and the entropy rain hypothesis	134
7.1	Evolved enstrophy in RBC simulations.	143
7.2	Shearing convection states in low Mach number, stratified convection.	146

7.3 Timeseries of kinetic energy in stratified AE vs. SE.	152
7.4 Evolved turbulent thermals	161

Chapter 1

Introduction

1.1 Motivation

1.1.1 Convection in Astrophysics: Stars, Planets, & Beyond

In nature, thermal buoyancy forces primarily drive two types of flows: gravity waves and convection. Gravity waves are driven when the fluid stratification (e.g., the atmosphere) is convectively **stable**. Convection is the manifestation of buoyancy forces in the presence of an **unstable** or **superadiabatic** stratification. Convection occurs in the Earth’s atmosphere, and cumulus clouds are evidence of that convection (and there is a rich literature investigating atmospheric convection, see Yano (2014) for a recent review). Within the Earth, both the mantle (Schubert et al., 2001) and liquid outer core convect, respectively driving plate tectonics (Bercovici, 2003) and the Earth’s magnetic dynamo (Christensen, 2011). Convection also occurs in more exotic astrophysical systems, including in the planes of accretion disks (Held & Latter, 2018) and in the magnetospheres of giant planets (Thomsen et al., 2012). In short, convection is a ubiquitous process in astrophysics and geophysics. A detailed understanding of the fundamental nature of convection is therefore crucial to understanding emergent convectively-driven phenomena in these fields.

Convection in the interiors and envelopes of stars is likely the most well-studied form of convection in astrophysics. The surface of the Sun is covered in large (~ 1 Mm) convective “granules” (see the left panel of Fig. 1.1) which overturn on roughly a five minute timescale. These granules lay above larger (~ 30 Mm) “supergranules,” pictured in the right panel of Fig. 1.1, which overturn on

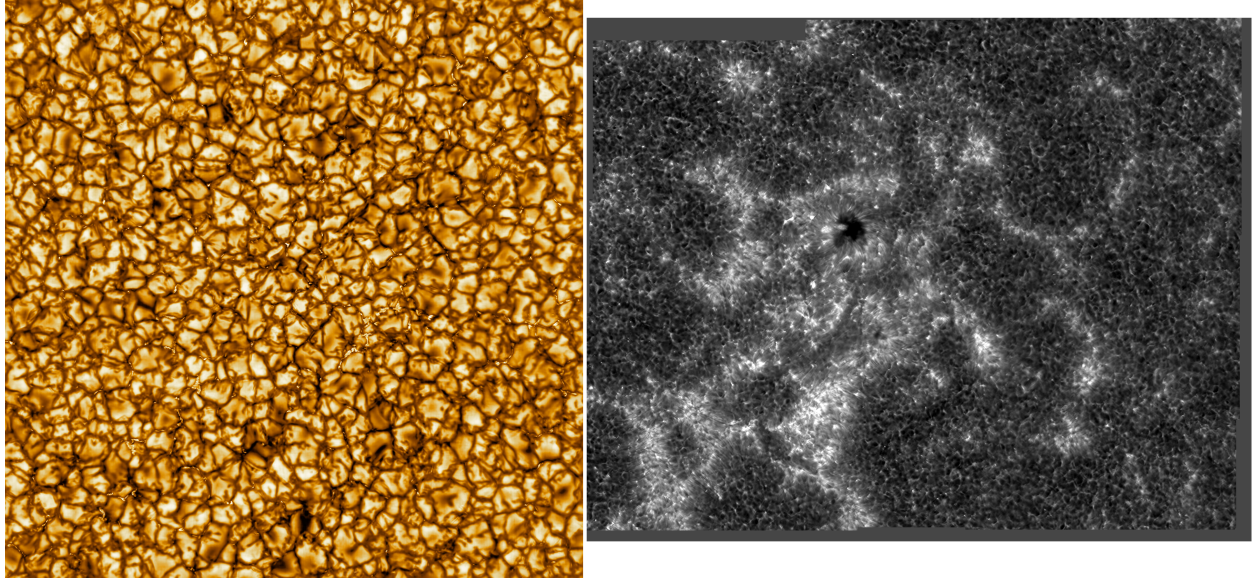


Figure 1.1: (left) first-light image of the solar surface from DKIST (visible light [789 nm], covering 36.5 km^2). Bright, hot granules and relatively cool, dark intergranular lanes can be observed. Magnetically-dominated “bright points” occupying the center of intergranular lanes can also be seen (Van Kooten & Cranmer, 2017). (right) Image of the solar surface from the Dutch Open Telescope (Ca II H line [396.8 nm]). For a sense of scale, the small-scale speckles or “web” of lights in this image trace out intergranular lanes (the dark regions in the left image). The large-scale web of lights roughly traces out the outlines of supergranules, the largest obvious scale of convection that is observed at the solar surface.

timescales of roughly a day. These classical convective features are visible evidence of a convection zone that occupies the outer 30% of the Sun’s radial profile (Miesch, 2005; Nordlund et al., 2009). Most Main Sequence (MS) stars, including the Sun, rely on convective heat transport at one more locations within their interiors. “Early-type” or “Upper-MS” high-mass stars ($M \gtrsim 1.5M_{\odot}$, where M_{\odot} is the solar mass) have convectively unstable cores. In these massive stars, core conditions are sufficiently hot and dense that the CNO cycle (Carbon-Nitrogen-Oxygen) is the dominant source of core hydrogen fusion. The opacity of the stellar material, dominated by free-free interactions (c.f. Ch. 16 of Weiss et al., 2004), is sufficiently high that the extreme CNO-fed luminosities cannot be efficiently carried by radiative processes. Convection must therefore assist radiative conductivity to transport the stellar luminosity outward, resulting in a well-mixed convective core region in these massive stars. The luminosity of less massive stars ($M \leq 1.5M_{\odot}$) is provided by the PP-

chain (proton-proton), allowing many such stars to have stable cores. However, the cooler surface temperatures of these stars allow for phase changes of hydrogen and helium (e.g., from fully ionized to neutral) within their stellar envelopes. These elements are the primary constituents of the stellar material, and neutral atoms greatly increase the stellar opacity through bound-free (photo effect) interactions (and these effects were studied by Rast & Toomre, 1993a,b). In solar-type stars ($1.5M_{\odot} \lesssim M \lesssim 0.3M_{\odot}$), the increased opacity near the stellar surface results in a convectively unstable envelope which overlies a stable, radiative interior. In “Late-type”, “Lower-MS” stars, such as M-dwarf stars, these opacity effects are sufficiently important that the star is convectively unstable throughout its full radial extent. While stars spend the majority of their lifetimes on the MS, convection is also an important process during other evolutionary phases (and I refer the reader to chapter 2 of Hansen et al., 2004, for a broad but brief overview of stellar evolutionary phases).

Convection’s prevalence within stars suggests that it is a crucial process in establishing the stratification and structure of stellar interiors. However, until recently, the insides of stars have been an unobservable region, and there has been a dearth of observations against which to test stellar convection theory. The relatively new fields of helioseismology and asteroseismology (briefly explored in Sec. 1.1.2) have enabled scientists to literally look inside of the Sun and stars. These measurements allow us to put constraints upon and test the validity of stellar structure models, our assumptions about processes in stellar interiors, and our theories of convection. Helioseismology has revealed a major discrepancy between models and observations, commonly referred to as the “Solar Convective Conundrum,” which I explore in detail in Sec. 1.1.3. This conundrum has shown that our fundamental understanding of stellar convection is flawed. The collection of experiments presented in this thesis were motivated by the Solar Convective Conundrum and a desire to rebuild some understanding of stellar convection from fundamental principles.

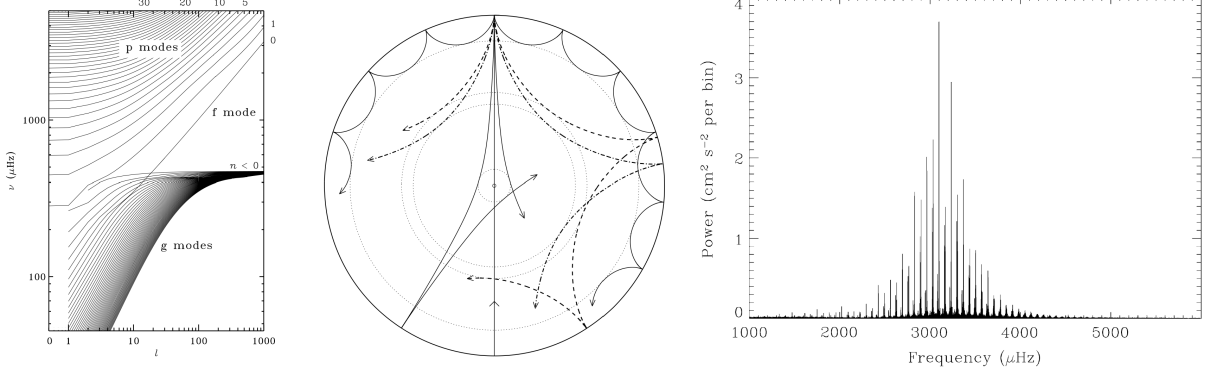


Figure 1.2: Select images describing asteroseismology, taken from Ch. 1 of Aerts et al. (2010). (left, Fig. 1.6) Allowed frequency modes in a standard solar model. The upper part of the diagram is filled with p modes; frequency increases with overtone n and spherical harmonic degree ℓ . The lower part of the diagram is filled with g modes, whose frequency decreases with overtone n . (middle, Fig. 1.7a) Propagation of rays of sound waves in a cross-section of a Sun-like star. Shown are rays (in increasing order of penetration depth) of spherical harmonic degree of $\ell = \{75, 25, 20, 2\}$. (right, Fig. 1.9) A power spectrum of radial velocity variations for 9.5 years of data of the Sun-seen-as-a-star. Distinct peaks corresponding to p-modes (as in the left panel) can be seen.

1.1.2 Asteroseismology & Helioseismology

Stars are seismically active. This seismic activity is the manifestation of complex, 3D oscillations within the star which come in two primary forms: pressure-driven “p”-modes, and buoyancy-driven “g”-modes. The simplest of these modes are radial modes, in which the star experiences spherically symmetric oscillations along its radial coordinate (and the simplest of these modes is the fundamental “breathing” mode, whose spherical harmonic degree is $\ell = 0$, in which the star’s radius expands and contracts as a whole). Theoretically, an infinite number of (radial and nonradial) modes can be excited in a star at a given time. The left image of Fig. 1.2 shows an example of the modes which can be excited within a standard model of the Sun’s stratification. Temporal frequency on the y-axis is plotted against spherical harmonic degree ℓ , and each of the ridges in the plots is an individual mode at a specific overtone n . The bottom of the diagram is filled with low-frequency, buoyancy-driven g-modes while the upper part of the diagram is filled with higher frequency, pressure-driven p-modes.

As these waves propagate into the stellar interior, the stratification of the star (e.g., the

changing sound speed with depth for the p-modes) causes the waves to refract and return to the surface (see the middle panel of Fig. 1.2). These waves therefore directly sample the interior stratification of the star, and the spherical harmonic degree of a given mode determines how deep it propagates before reflecting (with higher ℓ propagating less deeply). Asteroseismology and helioseismology refer to the observation of complex wavefields at the stellar surface which are the summation of these waves which sample various stellar depths. Due to the fact that stars are not spatially resolved, asteroseismology can only detect a limited number of modes. An asteroseismic power spectrum of the Sun-seen-as-a-star is shown in the right panel of Fig. 1.2. Each of the peaks in this power spectrum correspond to one of the ridges in the leftmost panel, and the frequencies at which these peaks occur help constrain the interior structure of a given star. Helioseismology, which is the name for the field that applies asteroseismic techniques to the Sun specifically, has access to high-resolution spatial data and can therefore probe the solar interior in more detail, including revealing the nature of mean flows like differential rotation within the Sun. Helioseismic and asteroseismic theory, observations, and applications have respectively been covered extensively by Christensen-Dalsgaard (2002) and Aerts et al. (2010).

The advent of asteroseismic science has closely paralleled that of exoplanetary science. Early ground-based observations of stellar pulsations (e.g., Kjeldsen & Frandsen, 1991; Bouchy & Carrier, 2001; Bedding et al., 2001) have given way to datasets larger than 10^4 stars (e.g., Yu et al., 2018; Santos et al., 2019) in the age of CoRoT, Kepler, and K2 data. Another 20,000 asteroseismically-interesting targets are being observed in the TESS satellite’s two-year mission (Schofield et al., 2019). By 2030 we expect to have observed 10^7 pulsating red giants and 10^5 dwarfs and subgiants (Huber et al., 2019). This plethora of data will teach us a great deal about the nature of stellar interiors, and will enable the accurate measurement of the ages, masses, and radii of many of these stars. These measurements in turn facilitates studies in numerous astrophysical disciplines, including galactic archaeology and exoplanetary science.

However, inferring information about a star’s structure from asteroseismic data is difficult. Forward modeling using one-dimensional (1D) stellar structure models requires the computation

of many slightly different models to produce a model which lines up well with a given set of observations, and backwards modeling is in and of itself a difficult proposition. For a more complete discussion of the difficulties inherent in asteroseismic techniques, I refer the reader to Chs. 1.4 & 4.1 of Bellinger (2018). Regardless, 1D stellar structure models consistently fail to reproduce some aspects of asteroseismic observations; one such example is that models and observations frequently do not align in the highly supercritical surface layers of solar-like stars (as discussed in Jørgensen & Weiss, 2019). Some of the known deficiencies of stellar structure models are described by Buldgen (2019), and of particular interest in the context of this thesis are their handling of three-dimensional (3D) dynamical phenomena like convection. In order to improve these models, we must improve how stellar structure codes handle convection. By improving convective models and stellar structure models, we can better take advantage of the exponential rise in asteroseismic targets that has occurred—and continues to occur—in recent years.

1.1.3 The Solar Convective Conundrum

Recent observations have revealed that we lack a fundamental understanding of the convective dynamics in the Sun’s convective envelope. Helioseismic observations (Hanasoge et al., 2012; Greer et al., 2015) have reported detections of convective velocity magnitudes which are different by a factor of 100. Despite these disagreements, one way in which these observations broadly agree with one another and broadly agree with measurements of solar surface velocities (Hathaway et al., 2015) is that solar convection has an unexpected absence of velocity at large spatial scales. In short, we do not observe large-scale “giant cells” driven by buoyant motions deep in the solar convection zone in helioseismic (left panel of Fig. 1.3) or surface velocity (right panel of Fig. 1.3) measurements. These measurements, and the absence of giant cells, constitute the Solar Convective Conundrum. Two primary hypotheses currently aim to explain the absence of giant cells:

- (1) The “entropy rain” hypothesis, and
- (2) The rotationally constrained solar interior hypothesis.

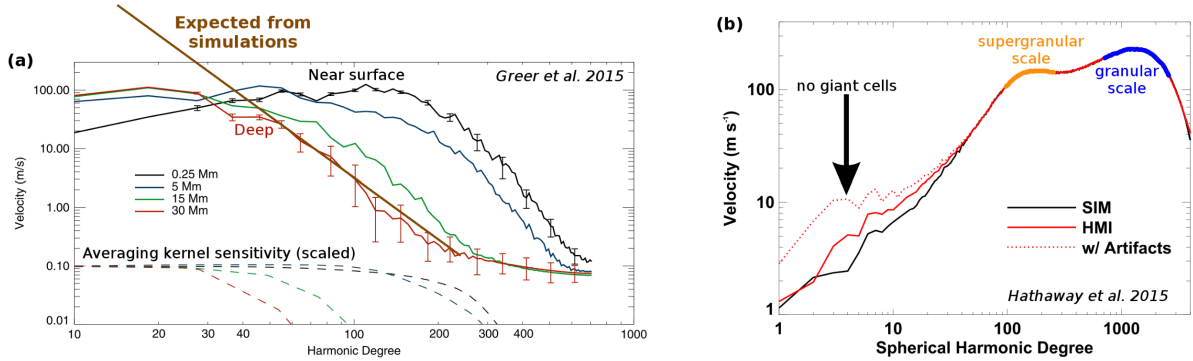


Figure 1.3: (a, annotated Fig. 3 from Greer et al., 2015) Ring-diagram helioseismic observations of the solar velocity power spectrum at various depths. Here, velocity power decreases toward larger scales, unlike what is expected from simulations. (b, annotated Fig. 8 from Hathaway et al., 2015) A spectrum of horizontal velocities at the solar surface, obtained using line-of-sight Doppler velocities. The length scales of surface granules and deeper supergranules appear as distinct features, but the hypothesized giant cells are not observed at low wavenumber.

I will briefly describe each of these hypotheses below.

First suggested by Spruit (1997), the entropy rain hypothesis suggests that many theories over-predict the importance of upflows in solar convection. Instead, perhaps **downflows** are the predominant mechanism responsible for carrying the solar luminosity across the solar convection zone. Recent theory and simulations (Brandenburg, 2016; Käpylä et al., 2017), including some of my own work (Ch. 6), suggest that small, intense downflows can indeed traverse the entire convection zone intact and may be more important than upflows in solar-like convection. A slice of the traditional view of the solar interior is shown in the left panel of Fig. 1.4, and the solar interior under the entropy rain hypothesis is shown in the middle panel.

Meanwhile, the rotationally constrained interior hypothesis suggests that Coriolis forces dominate force balances in the deep solar convection zone, and that these prevent giant cells from being generated. Simulations by Featherstone & Hindman (2016a,b) show that as convective flows become more rotationally constrained, the peak of convective velocity power shifts to smaller length scales. A model of the solar convection zone under this hypothesis is shown in the right panel of Fig. 1.4. However, rotational effects on simulations can be hard to quantify; some simulations which nominally rotate at the solar rate show **anti-solar** differential rotation (Gastine et al., 2014), and other

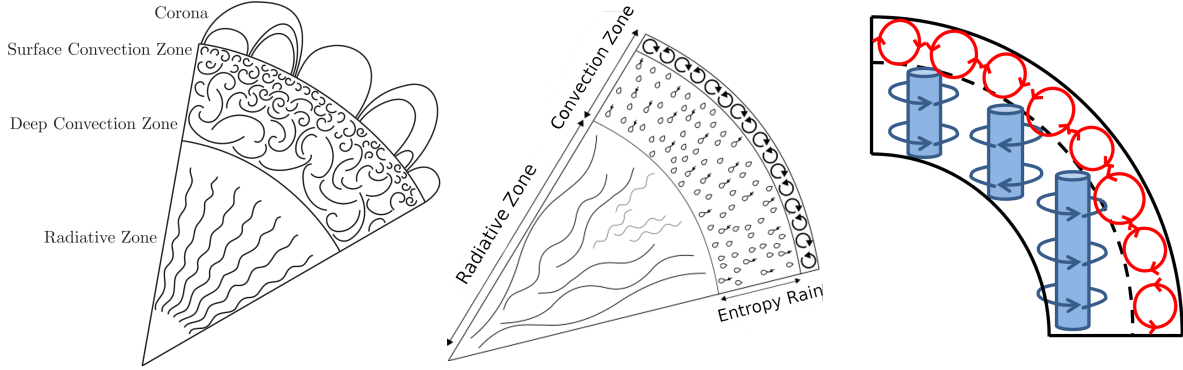


Figure 1.4: (left, image courtesy of Daniel Lecoanet) The classic model of the solar interior. A deep radiative zone lies beneath a convective envelope; within the convective envelope, large convective cells are driven at the base, small cells are driven near the surface, and there is a gradient of cell sizes with increasing radius. (middle) The entropy rain picture of the solar interior. Beneath a thin surface convection zone, downflows or “raindrops” carry the solar luminosity from the solar surface to the base of the convection zone. (right, Fig. 3c of Featherstone & Hindman, 2016b) The picture of the solar convection zone with a low-Rossby number, rotationally constrained interior. Rotational constraint increases with depth; below a certain depth, rotation dominates and convective cells give way to columns aligned with the global solar rotation.

rotationally constrained simulations exhibit Jupiter-like bands (Brun et al., 2017). Regardless, current results and hypotheses suggest that the interplay between downflows and rotational effects must be better understood in stellar convection. In Ch. 3, I make an effort to better understand how to control the degree of rotational constraint in simulations.

1.2 Perspectives on Studies of Convection

Historically, experiments into the nature of convection have come from two distinct lines of motivation. As is the case of the studies presented in this thesis, many studies into convection are motivated by the prevalence of convection in the natural world and a desire to understand convectively-driven processes. The second line of motivation stems from turbulence research, because convective experiments are ideal systems in which to study buoyantly driven turbulent flows. These two motivations have led to a large variety of studies into the nature of convection, which I will attempt to briefly summarize in the following sections. Generally, studies of turbulent flows have focused on simple convective laboratory experiments or simulations in the Boussinesq regime,

whereas astrophysically or geophysically motivated studies range from the same simple experimental setups to complex magnetohydrodynamic, global “dynamo” simulations in spherical domains.

1.2.1 Rayleigh-Bénard convection

The first controlled laboratory experiments of convection (or, a fluid layer heated from below and cooled from above) were performed by Bénard in 1900. However, the first theoretical description of such a convective layer was performed by Rayleigh (1916), who first derived the fundamental control parameter of convection: the Rayleigh number,

$$\text{Ra} = \frac{\alpha g L^3 (\Delta T)}{\nu \chi}, \quad (1.1)$$

where α is the coefficient of thermal expansion ($\alpha \equiv \partial \ln \rho / \partial T$, for the density ρ and temperature T), g is the gravitational acceleration, L is the depth of the fluid layer, ΔT is the temperature difference across the fluid layer, and ν and χ are respectively the viscous and thermal diffusivities. Colloquially, Ra can be thought of as the ratio of buoyant convective driving to viscous dissipation, and the pioneering work of these scientists in the field are the reason that Boussinesq thermal convection is widely known as Rayleigh-Bénard convection (RBC). Together with geometric factors (the size and shape of the experimental domain), boundary conditions, and the Prandtl number ($\text{Pr} = \nu / \chi$), Ra fully describes a convective system. Ra is an ideal control parameter for a convective system, because it is a straightforward knob for convective driving: above some “critical value,” $\text{Ra} > \text{Ra}_{\text{crit}}$, a fluid layer should convect, and the more “supercritical” an experiment is (or, the larger $S = \text{Ra}/\text{Ra}_{\text{crit}}$ is), the more turbulent the convection should be. Furthermore, the value of Ra_{crit} is independent of Pr and is therefore independent of the specific fluid used in a convective experiment (e.g., in air $\text{Pr} = 0.7$ and in water $\text{Pr} = 7$).

Historical reviews of the development of studies of RBC can be found throughout the decades in e.g., Busse (1978); Siggia (1994); Ahlers et al. (2009). In the simplest of terms, much of the research into RBC focuses on the behavior of heat transfer across a convective domain, quantified

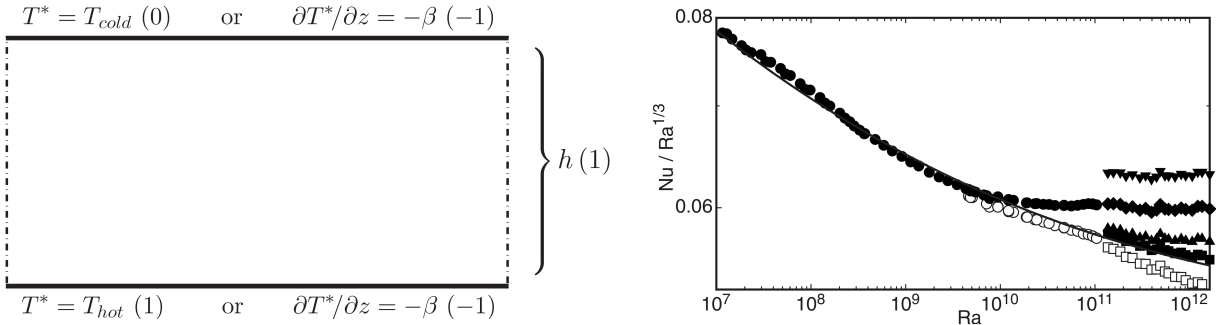


Figure 1.5: (left, Fig. 1 of Johnston & Doering, 2009) A simple schematic of the Rayleigh-Bénard problem. A hot plate sits below a cold plate, and either the flux (temperature gradient) or the temperature is fixed at each plate to maintain the convective instability. (right, Fig. 4 of Ahlers et al., 2009) A compensated scaling plot of Nu vs. Ra . Here, the value of Nu is divided by the expected scaling, $\text{Ra}^{1/3}$. The downward trend at low Ra means that, if you assume $\text{Nu} \propto \text{Ra}^\alpha$, the value of $\alpha < 1/3$ (and $\alpha \approx 2/7$ has been frequently used in the literature). However, at high values of Ra , when the trend flattens, it suggests that a $\text{Ra}^{1/3}$ law is a good description.

by the nondimensional Nusselt number (Nu),

$$\text{Nu} = \frac{\text{Evolved Convective Flux}}{\text{Comparison Hydrostatic Flux}} = \left\langle \frac{wT - \chi \partial_z T}{|\chi \Delta T / L|} \right\rangle, \quad (1.2)$$

where w is the vertical velocity, and T is the temperature field, and $\langle \rangle$ are a volume average over the convective domain. The key historical question that has been asked is: how does Nu scale as Ra and Pr are changed? A schematic of the RBC setup and a sample scaling plot of Nu vs. Ra are shown in Fig. 1.5. The earliest theoretical description developed by Malkus (1954) asserts that the boundary layers of convective domains are always in a marginally stable state, and thus when the Rayleigh number is defined with $L = \delta$, the boundary layer thickness, it should always have a value of Ra_{crit} . This argument suggests that $\delta \propto \text{Ra}^{-1/3}$. Assuming that the convection develops an isothermal interior and that the full temperature jump across the domain occurs in the boundary layers, we can substitute $L = \delta$ in the definition of Nu , and we retrieve a classical scaling law of $\text{Nu} \propto \text{Ra}^{1/3}$. This scaling, or similar scalings have been seen in experiments for decades.

More recently, in Grossmann & Lohse (2000) and following papers, a unifying theory of scaling behavior has been developed that is based around the dissipation of kinetic and thermal energy in convective experiments. The dissipation for each of these energies is split into a bulk and

boundary layer component, as it is assumed that different force balances dominate the equation of motion in the bulk or boundary layers. It is next assumed that, for each type of energy, **either** the bulk **or** boundary layer is predominantly responsible for dissipation of that type of energy. Scaling laws are then determined by where in the domain each type of energy is primarily dissipated, and this results in four regimes in parameter space (e.g., where kinetic energy is dissipated in the boundaries but thermal is dissipated in the bulk, and other permutations). A great number of studies have historically sought out the so-called “ultimate regime” of convection, which is the regime in which boundary layer dissipation is unimportant compared to the bulk. Some authors have recently claimed to have achieved this ultimate regime (see e.g., Zhu et al., 2018), but this is still a point of contention in the community. This theory, and a comparison to experimental and numerical results, are described in detail in the review of Ahlers et al. (2009).

1.2.2 More Realistic Geophysical and Astrophysical Experiments

While modern and historical studies of RBC have allowed the community of convective modelers to understand convective experiments to a much greater degree, they do not contain all of the “ingredients” which are important to astrophysical or geophysical convection. Numerous studies exist which aim to understand these additional complexities, ranging from studies which essentially study RBC with one extra component to studies with realistic radiative transfer, magnetism, etc.

The effects of rotation, and to a lesser extent magnetism, have been studied in the RBC context in great detail. Plumley & Julien (2019) provide an excellent overview of these fields. In general, the presence of global rotation or a strong background magnetic field suppress convection, and thus increase the value of Ra_{crit} . At low supercriticalities above Ra_{crit} , rotational (e.g., Coriolis) or magnetic forces dominate the convective flow balances. As S is increased, these forces become less important until eventually convection behaves almost indistinguishably from its nonrotating or nonmagnetic forms. Theoretical descriptions of these models often focus on understanding scaling laws in the rotationally- (e.g., Julien et al., 2012) or magnetically- (e.g., Cioni et al., 2000) dominated regime. A sample of the manner in which scaling laws change in the rotationally- and

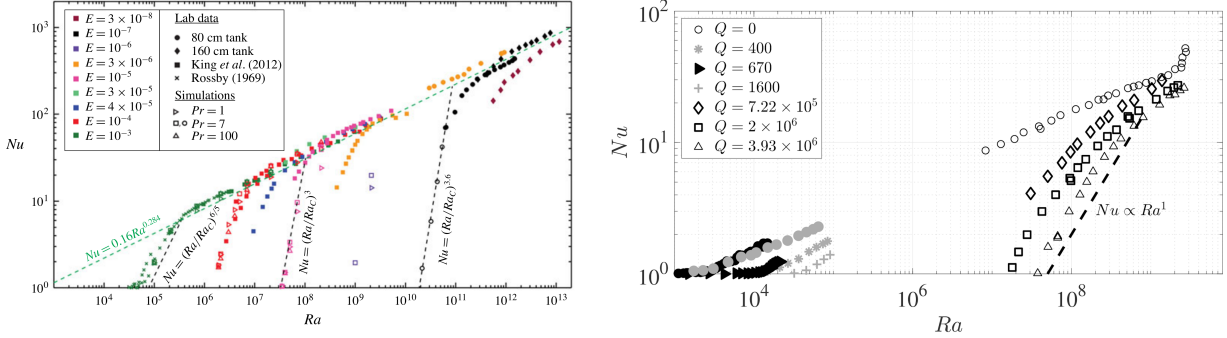


Figure 1.6: (left, Fig. 1 of Julien et al., 2016) Nu vs. Ra scalings of rotating Rayleigh-Bénard convection. The green line shows the rough scaling of Nu vs. Ra in the nonrotating regime. Below that line, rotationally constrained experiments can be seen. Due to rotational stabilization of convection, these experiments have a higher value of Ra_{crit} (and therefore convection “turns on” further to the right). As rotational constraint becomes less important, these simulations rapidly scale upwards towards the nonrotating values, and then follow those values once rotational constraint is not important. (right, Fig. 4 of Plumley & Julien, 2019) The same, but for magnetoconvection. This parameter space is significantly less well-explored.

magnetically-constrained regimes can be seen in Fig. 1.6. In this thesis (Ch. 3), we focus on the effects of rotationally-influenced convection in stratified atmospheres.

Outside of the realm of RBC, the field of convective research is less systematic and focused. Atmospheric density stratification is one key ingredient of convection in geophysical and astrophysical applications. The simplest stratified convection studies utilize a polytropic stratification, which has a linear temperature profile and is therefore at least somewhat comparable to RBC. The first study which determined how to find Ra_{crit} in a polytropic atmosphere was Unno et al. (1960), but the first dynamical simulations of polytropic convections could not be performed until those of Graham (1975). These early works focused on similar questions to those studied in the RBC community (how does Nu behave as Ra increases?) but were limited to a very small range of supercriticalities. Subsequent studies into polytropic convection (e.g., Hurlburt et al., 1984; Cattaneo et al., 1991) have often focused on the morphology of overall convective flows, forces responsible for those morphologies, and the emergent nonlinear phenomena. This trend has continued as complicating physics were added in addition to stratification (e.g., rotation in Brummell et al. (1996, 1998), stably stratified layers in Hurlburt et al. (1986); Singh et al. (1995); Brummell et al. (2002),

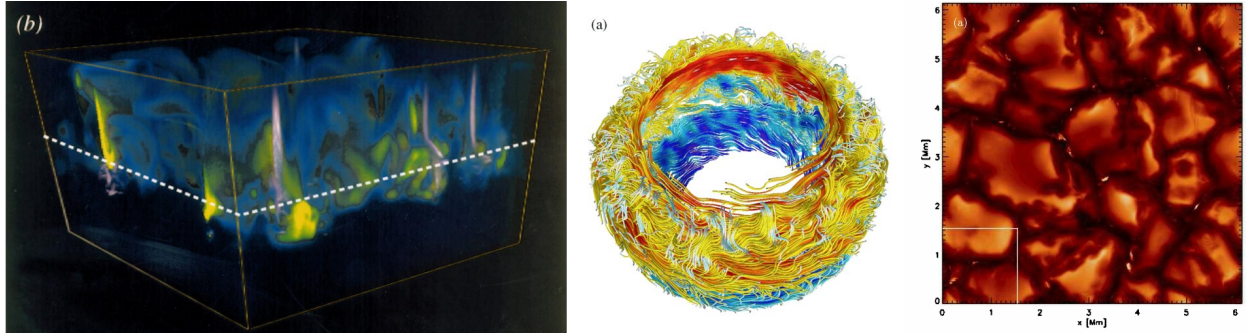


Figure 1.7: (left, Fig. 2b of Tobias et al., 1998) A visualization of enstrophy (purple) and magnetic field (blue, yellow) in a stratified simulation where a convecting region lies above a stable region. (middle, Fig. 2a of Brown et al., 2011) A visualization the azimuthal magnetic field in a spherical dynamo simulation (red is positive, blue is negative). (right, Fig. 6a of Rempel, 2014) Intensity of light near the surface of a realistic, solar surface simulation.

or magnetism/dynamo action in Nordlund et al. (1992); Brandenburg et al. (1996); Tobias et al. (1998)). A visualization of one of dynamics in one of these simulations is shown in the left panel of Fig. 1.7.

As the capabilities of supercomputers have expanded, so too have the complexity of convective simulations. Modern “dynamo simulations” examine the evolution of rotating magnetohydrodynamic convection in spherical domains and have produced fascinating phenomenon. These dynamo simulations regularly produce self-consistent differential rotation (Strugarek et al., 2018), “wreaths” of magnetism (Brown et al., 2010, 2011, and visualized in the middle panel of Fig. 1.7), magnetic cycles (Brown et al., 2011), and more phenomenon. These emergent phenomena parallel observed phenomena on the Sun and suggest that our fundamental understanding of the Sun’s dynamo (that it is driven by turbulent motions in the convective zone) is correct. Unfortunately, these simulations are difficult to run and are extremely complex. As a result, these simulations serve a role similar to observations: it is easy to see what phenomena they produce, but it is hard to understand and predict how those phenomena occurred.

While dynamo simulations are complex due to their geometry and scale, they often do not contain the most “realistic” physics. Small scale “local” simulations with realistic radiative transfer strikingly visually resemble solar surface convection and sunspots (Stein & Nordlund, 1998; Rempel

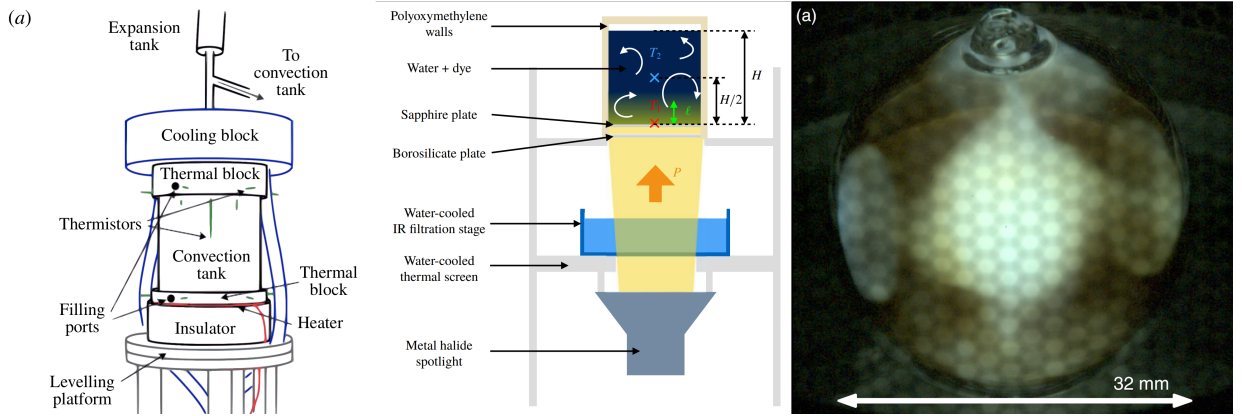


Figure 1.8: (left, Fig. 1a of Aurnou et al., 2018) A cylindrical experiment filled with liquid gallium in which rotating magnetoconvection can be studied. (middle, Fig. 1a of Bouillaut et al., 2019) An experiment in which internally heated convection can be studied. The dye in the water absorbs the light, heating the water throughout the tank, and driving convection. (right, Fig. 3a of Koulakis et al., 2018) An experiment in which pycnoclinic acoustic forces contain a hot plasma sphere at the center of a bulb.

et al., 2009; Stein & Nordlund, 2012; Rempel, 2014). These simulations visually resemble solar surface convection so convincingly (see the right panel of Fig. 1.7) that the raw data of e.g., Rempel (2014)'s simulations are being used directly as high-resolution observations of solar convection (see e.g., Van Kooten & Cranmer, 2017; Shchukina & Trujillo Bueno, 2019, and others). Whether or not such a practice is wise is beyond the editorial domain of this thesis, but as a numericist I generally advise caution in directly viewing the outputs of simulations as comparable to observations.

Outside of simulations, convective experiments have become increasingly complex in recent years. Rotating magnetoconvection experiments have been performed in cylindrical cases using liquid gallium (Aurnou et al., 2018). Distributed dye and light have been used to model driving of convection by internal heating, as in the interior of stars (Bouillaut et al., 2019). Small-scale spherical convecting plasma domains have even been produced (Koulakis et al., 2018). All of these experiments provide excellent opportunities to better understand convection and give us excellent models against which to compare and benchmark simulations. These experiments are shown briefly in Fig. 1.8

The ultimate goal of convective models in the context of solar or stellar convection is to

understand how the solar dynamo operates so that we can eventually predict its behavior. Modern studies have proven that we have the computational resources to create impressive simulations which strongly resemble the Sun. It is now crucial to simplify our simulations to conduct **experiments** in which we study how specific pieces of convection behave (such as in the studies of tachocline interactions of Wood & Brummell, 2018). Through the knowledge gained in more focused studies, we can better predict the results of global simulations. This in turn will help us build better dynamo models to help predict dynamo action in geo- or astrophysical convection.

1.2.3 Mixing Length Theory & Stellar Structure Models

While the first analytical description of convection was performed by Rayleigh (1916), the earliest formulation of a simple mixing length theory was derived by Prandtl (1925). These were later expanded by Vitense (1953) and Böhm-Vitense (1958) into the predecessor to most formulations of stellar mixing length theory (MLT) used today. Modern MLT has many branches, but the one described in Chapter 14 of Weiss et al. (2004) and earlier versions of Cox & Giuli's book provide an excellent and fundamental description of MLT.

MLT serves as a one-dimensional (1D) description of complex three-dimensional convective motions. MLT assumes that, at a given stellar radius, the complex distribution of convective elements present can be modeled as an average convective element whose properties depend on the star's local structure. Each of these elements is assumed to travel the “mixing length” before depositing its thermodynamic signature into the surrounding matter and losing its identity. As a result, hot elements transport warm material upward some mixing length, cold elements transport cold material downward some mixing length, so on average heat is transported outward and a 1D convective flux can be constructed. While MLT is obviously an over-simplification of convective processes, it works qualitatively, and until recently it showed few noticeable disagreements with the observations available. More importantly, there is no other 1D description of convection that is widely accepted by the community, so MLT is all that 1D modelers have available to work with.

State-of-the-art stellar structure models are produced by 1D codes like MESA (Paxton et al.,

2011), which depend on convective parameterizations like MLT. Stellar structure models produced with MLT have aligned well with helioseismic observations for quite some time (Christensen-Dalsgaard et al., 1996), and disagreements between models and observations are generally less than a few percent (Serenelli et al., 2009). One particular area of weakness for these models has been problems due to “near-surface effects” (Kjeldsen et al., 2008). In short, MLT assumes that all convective flows are in perfect pressure equilibrium with their surroundings. This assumption breaks down in the high-Mach number, highly superadiabatic surface layers of solar-like stars. Recent efforts (Jørgensen & Weiss, 2019; Mosumgaard et al., 2020) have successfully coupled 1D stellar evolution models with thin, near-surface, 3D convective shells. These studies have found that their realistic treatment of the highly adiabatic surface layers (via 3D convective simulations) do indeed reduce errors in asteroseismic frequencies between models and observations. However, “patching” together 1D and 3D simulations in this manner is not a thorough solution to this problem. 3D simulations are expensive, and it is infeasible to recompute 3D simulations at each timestep in a 1D stellar structure model over the course of a star’s lifetime. Regardless, these results suggest that MLT fails to describe stellar convection, so our community must either improve models or learn how to cleverly and generally couple 1D models and 3D simulations.

One additional weakness of 1D stellar structure models is that they often neglect complicating effects like magnetism and rotation. MESA has incorporated diffusion of angular momentum to enable at least some basic models of rotating stars (Paxton et al., 2013). Furthermore, recent theoretical and numerical studies have sought to understand how well mixing length theory describes rotating convection (Barker et al., 2014; Currie et al., 2020), and have shown good agreement between modified rotational MLTs and the results of 3D convective simulations. The effects of stellar magnetism on convection are less well-understood than rotation. Recent theoretical work suggests that the topology of a star’s magnetic field can induce variations in pulsational frequencies (Santos et al., 2018), suggesting that magnetism should not be neglected. A deep exploration of dynamo action or magnetoconvection in the stellar context is beyond the scope of this thesis, and I refer the reader to the reviews of Brandenburg & Subramanian (2005); Charbonneau (2010, 2014);

Brun & Browning (2017).

1.2.4 The Impossibility of Astrophysical Parameter Space

One of the reasons that our understanding of stellar convection is so incomplete is that it is impossible for us to model “true” stellar convection. That is – convection in stars occurs in regions of parameter space that are inaccessible to simulations. The Rayleigh number (Ra) is the most important nondimensional parameter used in describing experiments of convection. Ra is roughly a measure of the ratio of the strength of buoyant convective driving to viscous dissipation. In Rayleigh-Bénard convection, Ra is defined as in Eqn. 1.1. However, it is difficult to approximate the value of Ra from its Boussinesq form in the context of stellar convection. In acknowledging that the Boussinesq freefall velocity is $u_{\text{ff}} = \sqrt{\alpha g L \Delta T}$, one can see that the Rayleigh number is simply a product of the freefall Reynolds and Péclet numbers,

$$\text{Pe}_{\text{ff}} = \frac{u_{\text{ff}} L_z}{\chi}, \quad \text{Re}_{\text{ff}} = \frac{u_{\text{ff}} L_z}{\nu}, \quad \text{Ra} = \text{Pe}_{\text{ff}} \text{Re}_{\text{ff}} = \frac{u_{\text{ff}}^2 L_z^2}{\nu \chi}. \quad (1.3)$$

Under this formulation, given an estimate of the diffusivities and MLT convective velocities, one can calculate an approximate value of Ra . Also, in this formulation it is clear to see that Ra is in some ways a direct measure of how turbulent the convective motions are.

Perhaps the best form of Ra for use in astrophysical calculations is that of a “flux Rayleigh number,” (Ra_F), which many authors use (e.g., Featherstone & Hindman, 2016a). Ra_F can be simply derived from Eqn. 1.1. First, assume that the temperature scale is defined based on the temperature gradient $\Delta T = |L \nabla T|$. Second, Assume that the flux is carried entirely by radiative conductivity, $F = -\kappa \nabla T$, where the conductivity relates to the diffusivity by $\kappa = \rho c_P \chi$. Third, assume that the fluid is an ideal gas (pressure, $P = R\rho T$ for a constant R), and thus the coefficient of thermal expansion is $\alpha = -\partial_T \ln \rho = T^{-1}$. Substituting in ΔT and α , and then multiplying the numerator and denominator by κ , we retrieve the definition of Ra_F ,

$$\text{Ra}_F = \frac{gL^4 F}{\rho T c_P \nu \chi^2}, \quad (1.4)$$

where g is the gravity, L is the length scale, F is the flux, ρ is the density, T is the temperature, c_P is the specific heat at constant pressure, ν is the kinematic viscosity, and χ is the thermal diffusivity.

In order to understand the magnitude of Ra_F , I will now estimate its value for the mid solar convection zone. The length scale of the solar convection zone is about $L = 200 \text{ Mm}$, or about 30% of the Sun's 700 Mm radius. At the mid-CZ ($r \approx 600 \text{ Mm}$), most (or at least about half) of the solar luminosity ($L_\odot \approx 3.85 \times 10^{33} \text{ erg/s}$) is carried by the convection. Thus, $F = L_\odot / (4\pi r^2) \approx 8.5 \times 10^{10} \text{ erg/s/cm}^2$. From a simple solar MESA model (a $1 M_\odot$ star evolved to 4.5 Gyr), at the mid-CZ, $T \approx 10^6 \text{ K}$, $\rho \approx 0.05 \text{ g/cm}^3$, $g \approx 3.78 \times 10^4 \text{ cm/s}^2$, and $c_P \approx 3.43 \times 10^7 \text{ erg/K}$.

The diffusivities are a bit harder to estimate. While this is not a perfect approximation, we can model the solar convection zone as a fully-ionized, 100% Hydrogen fluid. In this case, the Spitzer viscosity for a fully ionized gas applies (Eqn. 5-54 of Spitzer, 1962),

$$\nu = (2.21 \times 10^{-15}) \frac{T^{5/2}}{\rho \ln \Lambda} \text{ cm}^2/\text{s}, \quad (1.5)$$

for T and ρ in cgs units. Here, $\ln \Lambda$ is the Coulomb logarithm, defined on page 34 of the 2019 edition of the NRL plasma formulary for a fully ionized hydrogen gas as

$$\ln \Lambda = 23 - \ln \left(\frac{\sqrt{2\rho}}{\sqrt{m_P T^{3/2}}} \right), \quad (1.6)$$

where $m_P = 1.67 \times 10^{-24} \text{ g}$ is the mass of a proton. Under the diffusion approximation (e.g., ch. 14.A-6 of Weiss et al., 2004), the thermal conductivity is

$$\kappa = \frac{16\sigma_{\text{SB}}T^3}{3\rho k}, \quad (1.7)$$

where k is the opacity and $\sigma_{\text{SB}} = 5.67 \times 10^{-5} \text{ erg}/(\text{cm}^2 \text{ K}^4 \text{ s})$. A chi-by-eye estimate of the opacity in this region of the Sun (from OPAL opacities and Fig. 3 of Paxton et al., 2011) is $k \sim 10^3 \text{ cm}^2/\text{g}$.

Rearranging, we can solve for

$$\chi = \frac{16\sigma_{\text{SB}}T^3}{3\rho^2 c_P k}.$$

Plugging in the temperature, density, opacity, etc. of the mid-convection zone, we get roughly

$$\nu \approx 2.5 \text{ cm}^2/\text{s}, \quad \chi \approx 3.5 \times 10^6 \text{ cm}^2/\text{s}. \quad (1.8)$$

Note also that this means that the Prandtl number, $\text{Pr} = \nu/\chi \approx 10^{-6}$, and is generally very small in stellar interiors. With these estimates of the diffusivity, we calculate an approximate solar Ra,

$$\text{Ra}_F \Big|_{r=0.85R_\odot} = \frac{gL^4 F}{\rho T c_P \nu \chi^2} \approx 10^{31}. \quad (1.9)$$

Which is frankly enormous.

The largest values of Ra currently accessible to experiments is $\text{Ra} \approx 10^{15}$ (Zhu et al., 2018), and those experiments are 2D, unstratified, Boussinesq, and possibly not properly numerically resolved. The regime of very-high-Ra stellar convection is inaccessible using modern computational and laboratory tools.

1.3 Numerical Methods

Numerical simulations are the cornerstone of the work presented in this thesis. The following section is by no means meant to be an exhaustive description of numerical methods, but is meant to be a broad overview of terminology and jargon. Furthermore, in Sec. 1.3.4, I review different formulations of the Navier-Stokes equations used in astrophysical convection simulations, and in Sec. 1.3.5, I describe the numerical tool, Dedalus, used in this work.

1.3.1 Direct Numerical Simulations vs. Large Eddy Simulations

Direct Numerical Simulations (DNS) are simulations in which the Navier-Stokes equations are evolved in their entirety without any model for the turbulence, and the term was first coined by Orszag (1970). Due to the fact that they resolve all spatial scales (from the largest contained in the domain down to the turbulent viscous cutoff scale), DNS were until recently limited to studies of relatively laminar flows. As computational resources have expanded over the past decades, so too have the regions of turbulent parameter space available for probing through DNS.

Large Eddy Simulations (LES) were first proposed by Smagorinsky (1963), and first explored numerically by Deardorff (1970). An excellent argument in favor of the use of LES is laid forth by Miesch et al. (2015), and I refer the reader there for a more thorough exploration of this topic than

will be undertaken here. In short, the central premise of LES is that large scale motions dominate both the turbulent transport and energy budget of a fluid system such as the solar convection zone, so a numerical simulation that captures those scales should realistically describe the real system. However, this premise hinges on the fact that the unresolved small scales are realistically taken into account, and these small scale motions are generally either included explicitly as subgrid-scale (SGS) models or handled implicitly through numerical dissipation.

A given simulation can capture length scales which vary between L , the large-scale size of the simulation domain, and ℓ , a small-scale set by e.g., the grid resolution. If $\ell \leq \ell_{\text{diss}}$, the dissipation length scale, then the simulation is a DNS – it explicitly captures scales down to (and possibly below) the dissipation scales. In an LES, the goal is to set L to the largest scales present in the system of interest, and to set $\ell_{\text{diss}} \ll \ell \ll \ell_{\text{max}}$, where $\ell_{\text{max}} < L$ is the dominant length scale of e.g., convective velocities being modeled in the system and $\ell_{\text{max}} < L$. The choices of ℓ and L for an LES in theory achieve a realistic description of the system while using many fewer computational resources than would be required to resolve L and ℓ_{diss} in a DNS.

DNS and LES are two different tools to be used for different problems. In the physics community where Rayleigh-Bénard convection is studied, DNS are the tool of choice. There, simulations are often compared either directly or indirectly with experimental data. A great deal of interest is taken in ensuring that the boundary layers are resolved (Shishkina et al., 2010) due to the dominance of boundary layers in suppressing heat transport throughout the parameter space available to DNS and experiments (Ahlers et al., 2009). When applied to astrophysics, DNS generally aim to understand how flow properties behave as turbulence is increased (as in Ch. 2). These scaling laws can then be extrapolated out to astrophysical quantities (which are often many decades away from the most turbulent values achievable in DNS). In short, in studies of astrophysics, it is acknowledged that DNS cannot achieve a model of the true astrophysical system of interest, but can instead provide insight into the behavior of similar systems at less extreme parameters. The goal of LES is to study dynamics in a system which is as close to a realistic model of the astrophysical system of interest as can be achieved. However, LES are sensitive to choices of how

to model SGS effects. Some recent studies suggest that these two approaches should not be seen as an “either or” choice but a “both and” (Mellado et al., 2018). In other words, DNS studies can be used to accurately model small scales, and those results can better inform SGS choices of LES.

Regardless, both DNS and LES have benefits and limitations, and it is important that the simulator be aware of the limitations of their tool of choice. All of the simulations conducted in this work are DNS.

1.3.2 Finite Element vs. Spectral Methods

The simplest and most straightforward way of modeling a physical system numerically is through the use of finite element, finite volume, and finite difference methods. In these systems, physical space is discretized into a series of coordinates, and the values of relevant quantities (velocity, density, etc.) are tracked at each of those locations, and derivatives are computed based on the values of quantities in neighboring grid cells. Finite volume codes can be used to model problems in complex geometries, but can be difficult to implement for complex equations and converge slowly as the simulation resolution is increased (Burns et al., 2019). Some modern examples of finite volume codes used in astrophysical fluid modeling are the Stagger¹ (Galsgaard, 2011), PLUTO² (Mignone et al., 2012), Athena/Athena++³ (Stone et al., 2008, 2019), the Pencil Code⁴ (Brandenburg & Dobler, 2010), and MUSIC⁵ (Goffrey et al., 2017) (although, the Pencil code acts like a blend of finite element and spectral methods, as described below).

Spectral methods, on the other hand, discretize important quantities by expanding them over a set of bases functions. Common basis choices include Fourier series and Chebyshev polynomials. Such methods can highly accurately follow the value of evolving fields at all spatial locations within a domain, but are generally restricted to simple geometries (Cartesian, cylindrical, and spherical domains). The code used to perform all simulations in this thesis, Dedalus⁶ (described below in

¹ <https://starformation.hpc.ku.dk/?q=node/18>

² <http://plutocode.ph.unito.it/>

³ <https://princetonuniversity.github.io/athena/>

⁴ <http://pencil-code.nordita.org/>

⁵ <https://empslocal.ex.ac.uk/tofu/>

⁶ <http://dedalus-project.org/>

Sec. 1.3.5), is a **pseudospectral** code. This means that, while solving equations, all linear equation terms are handled in a fully spectral sense. Nonlinear terms are dealiased, projected onto a finite volume domain, and analyzed. Pseudospectral methods can be much more efficient than spectral methods in the analysis of certain terms. Some other modern codes which employ spectral methods are Rayleigh⁷, MagIC⁸ (Wicht et al., 2017), SNOOPY⁹ (Lesur, 2015), and ASH (closed source).

A benchmark comparing Dedalus' pseudospectral methods to Athena's finite volume methods for a turbulent, nonlinear Kelvin-Helmholtz instability is explored by Lecoanet et al. (2016).

1.3.3 Timestepping: Implicit & Explicit Methods

The most common class of timestepping methods used are explicit timestepping methods. In these methods, the future state of the system is solved for as a function of the current state of the system and some timestep size, Δt . While these methods are the simplest to implement, they are inefficient at solving stiff problems in which there are two different flows which act on very different timescales. Specifically, in order to ensure that timestepping errors remain small, it is important that timesteps which are “too large” are not taken. Mathematically, the size of the largest possible timestep which can be taken is specified by the Courant-Friedrichs-Lowy (CFL) condition,

$$C = \frac{u\Delta t}{\Delta x} \leq C_{\max}, \quad (1.10)$$

where C is the Courant number, C_{\max} is typically $O(1)$ for explicit methods, \mathbf{u} is the fluid velocity magnitude, and Δx is the grid spacing of a simulation (Courant et al., 1967).

Implicit timestepping methods, on the other hand, solve a linear algebraic system that involves both the current and the future timestep. These methods are as a general rule more memory intensive than explicit methods. The MUSIC code is one of the first astrophysical codes to offer the capability of studying stellar convection which utilizes a fully implicit timestepper. Since implicit methods are not bound as strongly by the CFL condition, there has been great optimism that

⁷ <https://geodynamics.org/cig/software/rayleigh/>

⁸ <https://magic-sph.github.io/>

⁹ <http://geoffroy-lesur.org/snoopy.html>

the implementation of implicit methods could allow numericists to simulate convection over many dynamical timescales using a modest number of timesteps. Unfortunately, as discovered by Viallet et al. (2011, 2013, 2016), implicit methods do not achieve an accurate solution if they superstep the CFL of all simulation flows. Specifically, it was found that implicit methods must take short enough timesteps in order to resolve nonlinear advective flows.

Mixed implicit-explicit (IMEX) methods have been growing in popularity in recent years. These methods utilize the best parts of both implicit and explicit methods. Generally, these methods handle linear terms implicitly, thereby superstepping CFL conditions on linear waves or other linear system solutions. These methods then handle their nonlinear terms explicitly, using significantly less memory than nonlinear implicit methods. All of the simulations presented in this thesis utilize IMEX methods.

1.3.4 Equation Formulation: From Complexity to Simplicity

The equations which are the cornerstone of any fluid dynamical study are at some point an approximation. Even the fully compressible Navier-Stokes equations,

$$\frac{\partial \rho}{\partial t} + \nabla \cdot (\rho \mathbf{u}) = 0 \quad (1.11)$$

$$\frac{\partial \mathbf{u}}{\partial t} + \mathbf{u} \cdot \nabla \mathbf{u} = -\frac{1}{\rho} \nabla P + \mathbf{g} + \frac{1}{\rho} \nabla \cdot (\bar{\bar{\Pi}}), \quad (1.12)$$

are an approximation upon kinetic theory for how an ensemble of particles behaves. Here, ρ is the fluid density, \mathbf{u} is the bulk fluid velocity, P is the pressure, \mathbf{g} the gravity, and $\bar{\bar{\Pi}}$ the viscous stress tensor. It is likely crucial that a simulation studying the near-surface layers of the Sun—where the Mach number is high and compressibility effects are important—use a fully compressible equation set, as formulated above. However, in certain limits, it is often useful to approximate these equations even further.

1.3.4.1 The Lantz-Braginsky-Roberts (LBR) Anelastic Equations

One of the most commonly used approximations of the fully compressible equations in astrophysics is the Anelastic approximation. Under this approximation, density fluctuations are assumed to be small such that Eqn. 1.11 becomes

$$\nabla \cdot (\rho_0 \mathbf{u}) = 0, \quad (1.13)$$

where here ρ_0 is the background atmospheric stratification. This approximation essentially says that density fluctuations away from ρ_0 are so small that they can be neglected. While many formulations of the Anelastic equations have been used, perhaps one of the “best” is the Lantz-Braginsky-Roberts (LBR) formulation attributed to Lantz (1992) and Braginsky & Roberts (1995). This formulation both conserves energy (Brown et al., 2012) and can be derived from Lagrangian constraints (Vasil et al., 2013). In this formulation, the momentum equation (Eqn. 1.12) becomes

$$\frac{\partial \mathbf{u}}{\partial t} + \mathbf{u} \cdot \nabla \mathbf{u} = -\nabla \varpi - \frac{S_1}{c_P} \mathbf{g} + \frac{1}{\rho_0} \nabla \cdot (\bar{\bar{\Pi}}), \quad (1.14)$$

where $\varpi \equiv P_1/\rho_0$ is the reduced pressure (here P_1 are pressure fluctuations away from the background pressure profile P_0 , which is assumed to be in hydrostatic equilibrium) and the specific entropy is given by the linearized ideal gas equation of state,

$$\frac{S_1}{c_P} = \frac{1-\gamma}{\gamma} \frac{P_1}{P_0} + \frac{T_1}{T_0},$$

where T is the temperature.

One benefit of anelastic approximations such as the one here is that they are “soundproof.” In other words, these equations are not stiff: acoustic waves are explicitly filtered out of the linear solution of these equations, so simulations of low Mach number flows can be performed using explicit timestepping techniques without having to take prohibitively small timesteps that follow the sound waves. Anelastic equation formulations have historically been used in many global simulation models (ASH and Rayleigh both use an anelastic equation formulation). More recently, IMEX timestepping methods have enabled low Mach number simulations under the fully compressible

equations which are not bound by the CFL. If these methods become more prevalent, it is possible that Anelastic approximations may become a thing of the past. Regardless, some comparisons of fully compressible low Mach number dynamics and Anelastic dynamics have shown remarkable agreement between the two equation sets (see e.g., Lecoanet et al., 2014; Anders et al., 2019, and chapter 6). As such, due to their simplicity, anelastic models will likely continue to find use in theoretical descriptions of low Mach number flows.

1.3.4.2 The Boussinesq approximation

The simplest possible approximation in which buoyantly driven flows are frequently studied is the Boussinesq approximation. The limits of this approximation were famously explored by Spiegel & Veronis (1960). The Boussinesq approximation applies when thermodynamic and density fluctuations are small compared to the background (as in the Anelastic approximation), **and** when the vertical dimension of the fluid being studied is significantly smaller than the atmospheric scale height. In other words, the Boussinesq approximation applies when the fluid is nearly incompressible, but where buoyant forces are still important. Under these conditions, the continuity equation (Eqn. 1.11) becomes the incompressibility constraint,

$$\nabla \cdot \mathbf{u} = 0, \quad (1.15)$$

and the density is assumed to be a constant (ρ_0) everywhere except on the gravitational term in the momentum equation, where it is $\rho = \rho_0 + \rho_1$. We assume that the background atmospheric profile is in hydrostatic equilibrium $-\nabla P_0 + \rho_0 \mathbf{g} = 0$, and adopt the Boussinesq approximation for density fluctuations on the gravitational term,

$$\rho_1 = \rho_0 \alpha T_1, \quad (1.16)$$

where α is the coefficient of thermal expansion and T_1 is temperature fluctuations away from background temperature profile. The Boussinesq momentum equation is

$$\frac{\partial \mathbf{u}}{\partial t} + \mathbf{u} \cdot \nabla \mathbf{u} = -\nabla \varpi - \alpha T_1 \mathbf{g} + \nu \nabla^2 \mathbf{u}, \quad (1.17)$$

where ϖ is a reduced pressure as in the anelastic case, ν is the viscous diffusivity (in units of cm^2/s), and the viscous term simplifies into a Laplacian due to the incompressible constraint.

Mathematically, the similarity between Eqns. 1.14 and 1.17 is striking. Both have a straightforward buoyant term which makes warm perturbations rise and cool perturbations fall. Both have a reduced pressure gradient which acts as a Lagrangian multiplier to enforce a constraint on the flow (Eqns. 1.13 and 1.15, see Vasil et al. (2013) for a more thorough discussion). The simplicity of these equations allows for more complete analytical manipulation of the equation, which in turn allows for the development of simple, testable hypotheses for application in DNS.

Throughout this thesis, all three of these levels of approximation will be used. In Chs. 2 and 3, fully compressible convection will be studied. In Chs. 4 and 5, convection under the Boussinesq approximation will be examined. In Ch. 6, the evolution of low Mach number fluid parcels will be analyzed using both fully compressible and anelastic simulations.

1.3.5 Dedalus: A Pseudospectral Toolkit

Dedalus is an open source Python package which allows the user to apply pseudospectral and spectral methods to solve arbitrary partial differential equation sets. These equation sets are generally solved in Cartesian domains, although select cylindrical domains are available, and an alpha version of Dedalus in spherical domains has been tested and is available (Vasil et al., 2019; Lecoanet et al., 2019). While the full functionality of Dedalus is covered in detail in its recently released methods paper (Burns et al., 2019), I will briefly cover some of its functionality which enabled the work in this thesis.

1.3.5.1 Arbitrary Equation Sets

Dedalus users input sets of partial differential equations into Dedalus in a plain text format. This means that using any of the three equation sets covered in Section 1.3.4 is straightforward, and going from initial implementation of a new set of equations, to debugging those equations, to getting science results from those equations is a fast process. As an illustrative example, take the

Boussinesq equations (nondimensionalized on a freefall timescale as in Ch. 4):

$$\nabla \cdot \mathbf{u} = 0, \quad (1.18)$$

$$\frac{\partial \mathbf{u}}{\partial t} + \mathbf{u} \cdot \nabla \mathbf{u} = -\nabla \varpi + T_1 \hat{z} + \mathcal{R} \nabla^2 \mathbf{u}, \quad (1.19)$$

$$\frac{\partial T_1}{\partial t} + \mathbf{u} \cdot \nabla T_1 + w \frac{\partial T_0}{\partial z} = \mathcal{P} \nabla^2 T_1. \quad (1.20)$$

In Dedalus, it is common to use a Chebyshev basis in the vertical direction, allowing for arbitrary boundary condition specification at the top and bottom of the domain. The horizontal directions are usually taken to be periodic. In the Chebyshev direction, it is crucial that the equations are entered in a first-order formalism. For a two-dimensional problem with velocity $\mathbf{u} = u\hat{x} + w\hat{z}$, the full equation set is

$$u_z = \frac{\partial u}{\partial z}, \quad (1.21)$$

$$w_z = \frac{\partial w}{\partial z}, \quad (1.22)$$

$$T_{1,z} = \frac{\partial T_1}{\partial z}, \quad (1.23)$$

$$\frac{\partial u}{\partial x} + w_z = 0, \quad (1.24)$$

$$\frac{\partial u}{\partial t} + u \frac{\partial u}{\partial x} + w u_z = -\frac{\partial \varpi}{\partial x} + \mathcal{R} \left(\frac{\partial^2 u}{\partial x^2} + \frac{\partial u_z}{\partial z} \right), \quad (1.25)$$

$$\frac{\partial w}{\partial t} + u \frac{\partial w}{\partial x} + w w_z = -\frac{\partial \varpi}{\partial z} + T_1 + \mathcal{R} \left(\frac{\partial^2 w}{\partial x^2} + \frac{\partial w_z}{\partial z} \right), \quad (1.26)$$

$$\frac{\partial T_1}{\partial t} + u \frac{\partial T_1}{\partial x} + w T_{1,z} + w \frac{\partial T_0}{\partial z} = \mathcal{P} \left(\frac{\partial^2 T_1}{\partial x^2} + \frac{\partial T_{1,z}}{\partial z} \right). \quad (1.27)$$

Given a Dedalus `problem` object, these equations can straightforwardly specified through text strings as follows:

```
problem.add_equation("uz - dz(u) = 0")
problem.add_equation("wz - dz(w) = 0")
problem.add_equation("T1z - dz(T1) = 0")
problem.add_equation("dx(u) + wz = 0")
problem.add_equation("dt(u) + dx(p) - R*(dx(dx(u)) + dz(uz)) = -u*dx(u) - w*uz")
problem.add_equation("dt(w) + dz(p) + T1 - R*(dx(dx(w)) + dz(wz)) = -u*dx(w) - w*wz")
problem.add_equation("dt(T1) + w*T0z - P*(dx(dx(T1)) + dz(T1z)) = -u*dx(T1) - w*T1z")
```

In the above equations, terms are organized such that all linear terms are located on the lefthand side of the equations. The righthand side of the equations is reserved for nonlinear terms.

It is clear to see that, from a user perspective, equation entry in Dedalus is straightforward. However, the most powerful aspect of this simple equation entry is that it is trivial to add additional pieces of physics to these systems. For example, if I wanted to expand this system to study doubly-diffusive convection, I would only have to modify the above equation set by adding a solute evolution equation and by changing the buoyancy term in the vertical momentum equation appropriately. Such a modification could be performed in a number of minutes. This extreme flexibility has in large part enabled the broad and somewhat disparate scientific applications explored in this thesis.

1.3.5.2 Three types of solvers

One of the benefits of the Dedalus framework is that a block of code that solves a given set of equations, such as those specified in Eqns. 1.21-1.27, can be used with multiple types of solvers. Dedalus can solve Initial Value Problems (IVPs), Eigenvalue Problems (EVPs), and Boundary Value Problems (BVPs). All of these solving capabilities were taken advantage of during this thesis, and I will briefly describe them below.

Initial Value Problems are the most common type of solver taken advantage of in this thesis. When we solve an IVP in Dedalus, we are solving a DNS. These problems take an equation set, and, given a set of initial conditions and boundary values, take steps forward in time. The simulation then stops timestepping after reaching a condition specified by the user (typically after a given amount of simulation time has passed).

Eigenvalue Problems have also been utilized in this thesis. We have primarily used EVPs to find the critical value of the Rayleigh number, R_{crit} , for our convective systems. Dedalus performs an EVP on a system of equations like the above Boussinesq equations in the following steps:

- (1) It first ensures that the system is a linear system. It does this by setting all variables (u , uz , w , wz , T_1 , T_{1z} , and p) equal to zero and evaluating the RHS of each equation. If all of the RHS values evaluate to zero under the assumption that all variables are zero, then the system is assumed to be linear.

- (2) The user assumes that each of the variables grows proportionally to $e^{i\omega t}$, and sets a substitution so that $\text{dt}(A) \rightarrow i\omega A$ for each variable A . The user also generally wants to solve the EVP for a specific horizontal wavenumber, and assumes that all fields can be expressed as a constant times $e^{ik_x x}$, and sets $\text{dx}(A) \rightarrow ik_x A$ for each variable A .
- (3) Under these approximations, the above equation system can be expressed as the linear algebraic system,

$$\bar{\bar{A}}\mathbf{x} = \begin{bmatrix} -\partial_z & 0 & 0 & 1 & 0 & 0 & 0 \\ 0 & -\partial_z & 0 & 0 & 1 & 0 & 0 \\ 0 & 0 & -\partial_z & 0 & 0 & 1 & 0 \\ ik_x & 0 & 0 & 0 & 1 & 0 & 0 \\ i\omega + \mathcal{R}k_x^2 & 0 & 0 & \mathcal{R}\partial_z & 0 & 0 & ik_x \\ 0 & i\omega + \mathcal{R}k_x^2 & -1 & 0 & \mathcal{R}\partial_z & 0 & \partial_z \\ 0 & \partial_z T_0 & i\omega + \mathcal{P}k_x^2 & 0 & 0 & \mathcal{P}\partial_z & 0 \end{bmatrix} \begin{bmatrix} u \\ w \\ T_1 \\ u_z \\ w_z \\ T_{1,z} \\ p \end{bmatrix} = \mathbf{0}, \quad (1.28)$$

In this work, the eigenvalue we have always been interested in is ω , whose imaginary component describes whether the solution experiences exponential growth (convection) or exponential decay (not convection). In solving for this eigenvalue, Dedalus takes the determinant of the 7x7 matrix displayed above, sets $\text{Det}(\bar{\bar{A}}) = 0$, and solves for ω given a set of physical values (e.g., k_x , \mathcal{P} , \mathcal{R}). Dedalus internally deals with ∂_z 's by substituting in appropriate derivative expressions for the Chebyshev polynomials that it is resolving.

Boundary Value Problems have found some use in this thesis (see Ch. 4). Usually we solve one-dimensional boundary value problems in the z direction, and therefore use a simpler set of equations than the aforementioned equation set. In Dedalus, BVPs are solved using a Newton solver (using a Newton-Raphson root-finding method). Given an initial guess for the answer as a function of height, Dedalus iteratively attempts to shoot the solution closer to one which satisfies both the equations and boundary conditions.

Chapter 2

Convective heat transport in stratified atmospheres at low and high Mach number

2.1 Preamble

The following work is the culmination of my comprehensive exam II research and was published in Physical Review Fluids (Anders & Brown, 2017). The text in section 2.2 is the text of the paper as it was accepted for publication. Following the published work, in section 2.3, I comment on a few lessons that have been learned since we published these results.

This work was motivated in large part by the study of Brandenburg et al. (2005) and conversations with Axel Brandenburg and Ben Brown. In Axel's 2005 work, he argues that the superadiabatic excess, ϵ , defined below near Eqn. 2.1, should be large if one aims to study astrophysical convection. He finds in his experiments that, as ϵ grows, the fraction of the system flux carried by the evolved convection approaches unity. However, we knew that as ϵ grows, so too does the Mach number of the convection. We were convinced that low ϵ polytropes were an ideal experimental setup in which to study low Mach number, stratified convection. Furthermore, the radiative background flux carried by the background adiabat in polytropes **does not interact with the nonlinear flows**. It is to first order in hydrostatic and thermal equilibrium, and so it should “fall out” of the equations of motion.

Despite our conviction that low ϵ and high ϵ convection were both valid convective experiments, we had no way to **prove** that was the case. In this work, we came to a more full understanding of how to define the Nusselt number in compressible flows, and we found that—indeed—a

properly defined measure of the convective flux (Nu) scales similarly at low and high ϵ . This suggests that, regardless of ϵ , properly measured convection in a polytrope can sample the nature of turbulent convective flows as the convective driving (Rayleigh number) is increased.

2.2 Published work

2.2.1 Introduction

Convection transports energy in stellar and planetary atmospheres where flows are compressible and feel the atmospheric stratification. This stratification is significant in regions such as the convective envelope of the Sun, which spans 14 density scale heights. In the bulk of these systems, particularly in the deep interior, flows are at very low Mach number (Ma). Unfortunately, numerical constraints have restricted most studies of compressible convection to high Ma. These prior studies (Graham, 1975; Chan et al., 1982; Hurlburt et al., 1984; Cattaneo et al., 1990; Brummell et al., 1996; Brandenburg et al., 2005) have provided insight into the nature of convection in the low temperature, high Ma region near the Sun’s surface. Few fundamental properties of low Ma compressible convection, such as the scaling of convective heat transport, are known.

In the widely-studied Rayleigh-Bénard problem of incompressible Boussinesq convection (RBC), a sufficiently negative temperature gradient causes convective instability. In the evolved solution, upflows and downflows are symmetrical, the temperature in the interior becomes isothermal, and the conductive flux ($\propto \nabla T$) approaches zero there. For compressible convection in a stratified atmosphere, a negative entropy gradient causes convective instability. Early numerical experiments of moderate-to-high Ma compressible convection in two (Graham, 1975; Chan et al., 1982; Hurlburt et al., 1984; Cattaneo et al., 1990) and three (Cattaneo et al., 1991; Brandenburg et al., 2005; Brummell et al., 1996) dimensions revealed a different evolved state from RBC. Downflow lanes become fast and narrow, and upflow lanes turn into broad, slow upwellings. Furthermore, the **entropy** gradient is negated by convection in the interior, so a significant temperature gradient and conductive flux can persist despite efficient convection.

In RBC, there exist two primary dynamical control parameters: the Rayleigh number (Ra , the ratio of buoyant driving to diffusive damping) and the Prandtl number (Pr , the ratio of viscous to thermal diffusivity). These numbers control two useful measures of turbulence in the evolved solution: the Reynolds number (Re , the strength of advection to viscous diffusion) and the Peclet number (Pe , advection vs. thermal diffusion). In stratified atmospheres, the magnitude of the unstable entropy gradient joins Ra and Pr as a third important and independent control parameter. This **superadiabatic excess**, ϵ , sets the scale of the atmospheric entropy gradient (Graham, 1975). We find here that ϵ primarily controls the Ma of the evolved solution.

Here we study the behavior of convective heat transport, quantified by the Nusselt number (Nu), in plane-parallel, two- and three-dimensional, polytropically stratified atmospheres. We vary ϵ and Ra while holding Pr , aspect ratio, boundary conditions, and initial atmospheric stratification constant. We also examine the behavior of flow properties, as quantified by Ma and Re . We find here that the scaling of Nu in stratified, compressible convection is similar to that in Rayleigh-Bénard convection, and that this scaling is not appreciably changed by the magnitude of the superadiabaticity.

2.2.2 Experiment

We examine a monatomic ideal gas with an adiabatic index of $\gamma = 5/3$ whose equation of state is $P = R\rho T$. This is consistent with the approach used in earlier work (Graham, 1975; Chan et al., 1982; Brandenburg et al., 2005; Hurlburt et al., 1984; Cattaneo et al., 1990, 1991; Brummell et al., 1996) and is the simplest stratified extension of RBC. The atmospheres studied here are initially polytropically stratified,

$$\begin{aligned}\rho_0(z) &= \rho_t(1 + L_z - z)^m, \\ T_0(z) &= T_t(1 + L_z - z),\end{aligned}\tag{2.1}$$

where m is the polytropic index and L_z is the depth of the atmosphere. The polytropic index is set by the superadiabatic excess, $\epsilon = m_{ad} - m$, where $m_{ad} = (\gamma - 1)^{-1}$ is the adiabatic value of m . The height coordinate, z , increases upwards in the range $[0, L_z]$. Subscript 0 indicates initial conditions

and subscript t indicates values at $z = L_z$. Stratified atmospheres have a fourth non-dimensional parameter, the number of density scale heights, $n_\rho = \ln [\rho_0(z=0)/\rho_t]$. We specify the depth of the atmosphere, $L_z = e^{n_\rho/m} - 1$, by choosing the initial value of n_ρ . Throughout this work we set $n_\rho = 3$. Satisfying hydrostatic equilibrium sets the value of gravity, $g = RT_t(m+1)$, which is constant with depth. We study atmospheres with aspect ratios of 4 where both the x and y coordinates have the range $[0, 4L_z]$. In our 2D cases, we only consider x and z .

These domains are nondimensionalized by setting $R = T_t = \rho_t = 1$ at $z = L_z$. By this choice, the non-dimensional length scale is the inverse temperature gradient scale and the timescale is the isothermal sound crossing time, τ_I , of this unit length. Meaningful convective dynamics occur on timescales of the atmospheric buoyancy time, $t_b = \tau_I \sqrt{L_z m c_P / g \epsilon n_\rho}$, where $c_P = R\gamma/(\gamma-1) = 2.5$ is the specific heat at constant pressure.

At fixed n_ρ , convective dynamics are controlled by ϵ as well as the atmospheric diffusivities. At a fixed value of ϵ , the diffusivities are set by the Rayleigh number (Ra) and the Prandtl number (Pr),

$$\text{Ra}_t = \frac{gL_z^3(\Delta S_0/c_P)}{\nu_t \chi_t}, \quad \text{Pr} = \frac{\nu}{\chi}, \quad (2.2)$$

where $\Delta S_0 = \epsilon \ln(1 + L_z) = \epsilon n_\rho/m$ is the initial specific entropy difference across the domain, χ is the thermal diffusivity, and ν is the kinematic viscosity. Throughout this work we specify that $\text{Pr} = 1$ and is depth invariant. The initial thermal conductivity, $\kappa_0 = \chi \rho_0$, is constant with depth, such that (2.1) is in thermal equilibrium ($\nabla \cdot [\kappa_0 \nabla T_0] = 0$). By these choices, $\nu(z) \equiv \chi(z) \equiv \chi_t/\rho_0$. This formulation sets Ra at the bottom of the domain greater than Ra_t by a factor of e^{2n_ρ} . Henceforth when we specify Ra we are referring to Ra_t . The full values of $\kappa = \rho \chi$ and $\mu = \rho \nu$ (the dynamic viscosity) change as the density profile evolves. The diffusivities scale as $\chi_t, \nu_t \propto \sqrt{gL_z^3(\Delta S_0/c_P)/\text{Ra}_t}$. Defining the thermal diffusion timescale as $t_\chi \equiv \tau_I L_z^2 / \chi$, the ratio of t_χ to the buoyancy time is

$$\frac{t_\chi}{t_b} = \text{Ra}_t^{1/2}. \quad (2.3)$$

We carry out two experiments in this study. In the first, we fix ϵ and increase Ra, thus increasing

the ratio in (2.3). In the second, we fix Ra and vary ϵ , scaling the dynamical timescales (t_b, t_χ) as $\epsilon^{-1/2}$ relative to the speed of sound; we see this reflected in the evolved Mach number scaling (Fig. 2.1).

We use $\ln \rho$ and T as our thermodynamic variables and solve the Fully Compressible Navier-Stokes equations,

$$\frac{\partial \ln \rho}{\partial t} + \nabla \cdot \mathbf{u} = -\mathbf{u} \cdot \nabla \ln \rho, \quad (2.4)$$

$$\frac{\partial \mathbf{u}}{\partial t} + \nabla T - \nu \nabla \cdot \bar{\boldsymbol{\sigma}} - \bar{\boldsymbol{\sigma}} \cdot \nabla \nu = -\mathbf{u} \cdot \nabla \mathbf{u} - T \nabla \ln \rho + \mathbf{g} + \nu \bar{\boldsymbol{\sigma}} \cdot \nabla \ln \rho, \quad (2.5)$$

$$\frac{\partial T}{\partial t} - \frac{1}{c_V} (\chi \nabla^2 T + \nabla T \cdot \nabla \chi) = -\mathbf{u} \cdot \nabla T - (\gamma - 1) T \nabla \cdot \mathbf{u} + \frac{1}{c_V} (\chi \nabla T \cdot \nabla \ln \rho + \nu [\bar{\boldsymbol{\sigma}} \cdot \nabla] \cdot \mathbf{u}), \quad (2.6)$$

with the viscous stress tensor given by

$$\sigma_{ij} \equiv \left(\frac{\partial u_i}{\partial x_j} + \frac{\partial u_j}{\partial x_i} - \frac{2}{3} \delta_{ij} \nabla \cdot \mathbf{u} \right), \quad (2.7)$$

where δ_{ij} is the Kronecker delta. Taking an inner product of (2.5) with $\rho \mathbf{u}$ and adding it to $\rho c_V \times (2.6)$ reveals the full energy equation,

$$\frac{\partial}{\partial t} \left(\rho \left[\frac{|\mathbf{u}|^2}{2} + c_V T + \phi \right] \right) + \nabla \cdot (\mathbf{F}_{\text{conv}} + \mathbf{F}_{\text{cond}}) = 0, \quad (2.8)$$

where $\mathbf{F}_{\text{conv}} \equiv \mathbf{F}_{\text{enth}} + \mathbf{F}_{\text{KE}} + \mathbf{F}_{\text{PE}} + \mathbf{F}_{\text{visc}}$ is the convective flux and $\mathbf{F}_{\text{cond}} = -\kappa \nabla T$ is the conductive flux. The individual contributions to \mathbf{F}_{conv} are the enthalpy flux, $\mathbf{F}_{\text{enth}} \equiv \rho \mathbf{u} (c_V T + P/\rho)$; the kinetic energy flux, $\mathbf{F}_{\text{KE}} \equiv \rho |\mathbf{u}|^2 \mathbf{u}/2$; the potential energy flux, $\mathbf{F}_{\text{PE}} \equiv \rho \mathbf{u} \phi$ (with $\phi \equiv -gz$); and the viscous flux, $\mathbf{F}_{\text{visc}} \equiv -\rho \nu \mathbf{u} \cdot \bar{\boldsymbol{\sigma}}$. Understanding how each of these fluxes interact is crucial in characterizing convective heat transport.

We utilize the Dedalus¹ pseudospectral framework (Burns et al., 2016) to time-evolve (2.4)-(2.6) using an implicit-explicit (IMEX), third-order, four-step Runge-Kutta timestepping scheme RK443 (Ascher et al., 1997). Thermodynamic variables are decomposed such that $T = T_0 + T_1$ and $\ln \rho = (\ln \rho)_0 + (\ln \rho)_1$, and the velocity is $\mathbf{u} = w \hat{\mathbf{z}} + u \hat{\mathbf{x}} + v \hat{\mathbf{y}}$. In our 2D runs, $v = 0$. Subscript 0

¹ <http://dedalus-project.org/>

variables, set by (2.1), have no time derivative and vary only in z . Variables are time-evolved on a dealiased Chebyshev (vertical) and Fourier (horizontal, periodic) domain in which the physical grid dimensions are 3/2 the size of the coefficient grid. Domain sizes range from 64x256 coefficients at the lowest values of Ra to 1024x4096 coefficients at $\text{Ra} > 10^7$ in 2D, and from 64x128² to 256x512² in 3D. By using IMEX timestepping, we implicitly step the stiff linear acoustic wave contribution and are able to efficiently study flows at high (~ 1) and low ($\sim 10^{-4}$) Ma. Our equations take the form of the FC equations in Lecoanet et al. (2014), extended to include ν and χ which vary with depth, and we follow the approach there. This IMEX approach has been successfully tested against a nonlinear benchmark of the compressible Kelvin-Helmholtz instability (Lecoanet et al., 2016).

We impose impenetrable, stress free, fixed temperature boundary conditions at the top and bottom of the domain, with $w = \partial_z u = T_1 = 0$ at $z = \{0, L_z\}$. T_1 is initially filled with random white noise whose magnitude is infinitesimal compared to ϵT_0 . We filter this noise spectrum in coefficient space, such that only the lower 25% of the coefficients have power. All reported results are taken from time averages over many t_b beginning $\{100, 40\}t_b$ after the start of our {2D, 3D} simulations to ensure our results are not biased by the convective transient.

2.2.3 Results & Discussion

Solutions were time-evolved until a long time average of the fluxes showed little variance with depth. A linear stability analysis determined that convective onset occurs at $\text{Ra}_{\text{crit}} = \{11.15, 10.06, 10.97, 10.97\}$ for $\epsilon = \{1.0, 0.5, 10^{-4}, 10^{-7}\}$, respectively.

2.2.3.1 Evolved fluid numbers & flow morphology

We measure the adiabatic Mach number ($\text{Ma} = |\mathbf{u}|/\sqrt{\gamma T}$), and find that it is a strong function of ϵ and a weak function of Ra. In our 2D runs, when $\text{Ma} < 1$, we observe a scaling law of $\text{Ma}(\text{Ra}, \epsilon) \propto \epsilon^{1/2} \text{Ra}^{1/4}$. This relation breaks down as the mean Ma approaches 1 (Fig. 2.1). This transition occurs near $\text{Ra}/\text{Ra}_{\text{crit}} \approx \{10^2, 10^3\}$ for $\epsilon = \{1, 0.5\}$. In our limited 3D runs, Ma appears to be a function of ϵ alone, with $\text{Ma} \propto \epsilon^{1/2}$, so at high Ra, $\text{Ma}_{3D} < \text{Ma}_{2D}$. We conjecture

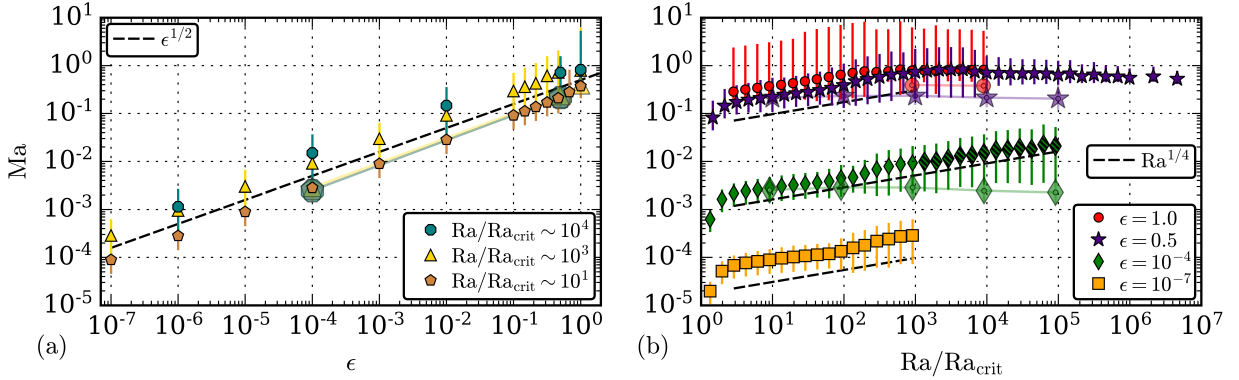


Figure 2.1: The mean adiabatic Mach number of long-time-averaged profiles is shown. Error bars show the full range of Ma over the depth of the atmosphere. (a) Ma, at various values of Ra, is plotted as a function of ϵ . (b) Ma, at various values of ϵ , is plotted as a function of $\text{Ra}/\text{Ra}_{\text{crit}}$. Larger symbols with inlaid circles designate 3D runs.

that the scaling of Ma with Ra in the 2D runs is due to the formation of coherent high-velocity “spinners,” which form between upflow and downflow lanes. These structures, which are reminiscent of flywheel modes in RBC, do not appear in our 3D runs at these parameters (Jones et al., 1976; Brummell et al., 2002). Simulations in the range of $\text{Ra}/\text{Ra}_{\text{crit}} > 10^3$ at $\epsilon = 10^{-4}$ exhibited “windy” states of convection, in which a large-scale horizontal shearing flow replaced the more standard upflow/downflow morphology of convection. Similar states have been studied in RBC (Goluskin et al., 2014). These runs are represented in Figs. 2.1, 2.3, & 2.4 as hatched points, and while this phenomenon does not appear to greatly modify the scaling of fluid properties measured in this work, these states warrant further investigation.

In 2D, low Ma flows (e.g., $\epsilon = 10^{-4}$) display the classic narrow downflow and broad upflow lanes of stratified convection (Fig. 2.2a). At high Ma (e.g., $\epsilon = 0.5$, $\text{Ra}/\text{Ra}_{\text{crit}} \gtrsim 10^3$), bulk thermodynamic structures are similar but shock systems form in the upper atmosphere near downflow lanes (Fig. 2.2b&c), as reported previously (Cattaneo et al., 1990; Malagoli et al., 1990). At large Ra, the diffusion timescale becomes long (2.3), and thermodynamic structures form small eddies which traverse the domain repeatedly before diffusing (Fig. 2.2c). As evidenced by the colorbar scalings, the amplitudes of thermodynamic fluctuations scale with ϵ .

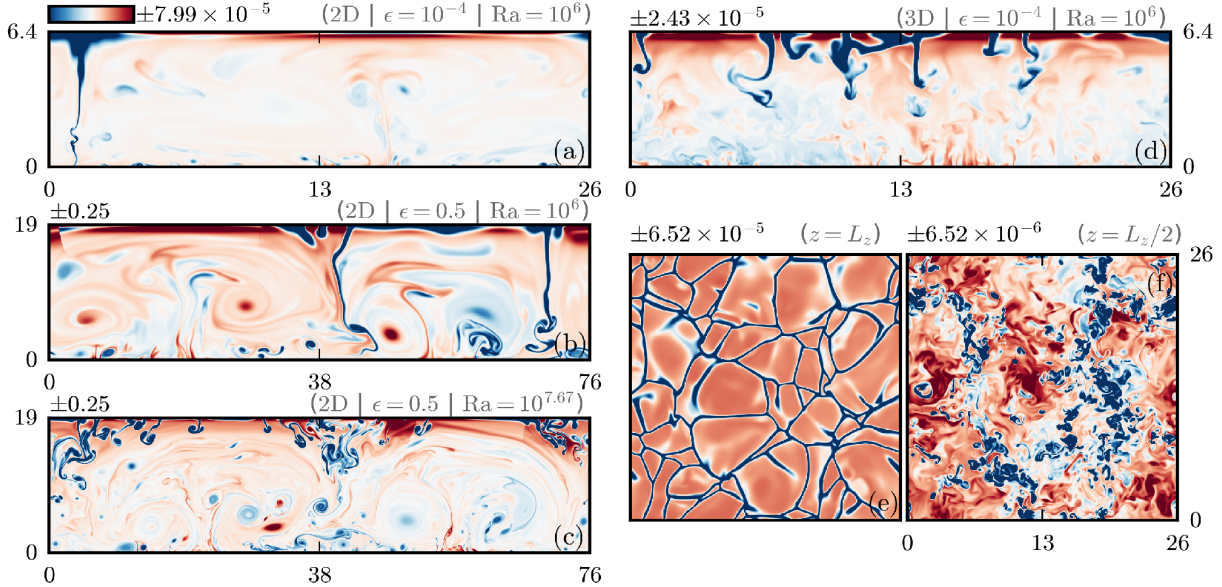


Figure 2.2: Characteristic entropy fluctuations in evolved flows roughly $\{140, 60\} t_b$ after the start of simulations for $\{2D, 3D\}$ runs. The time- and horizontally-averaged profile is removed in vertical slices (a)-(d). The time- averaged mean value is removed in horizontal slices (e) and (f). (a) A low Ma flow at moderate Ra. (b) A high Ma flow at the same Ra as in (a). (c) A high Ma flow at high Ra. Shock systems can be seen in the upper atmosphere of the high Ma flows, for example at $(x, z) \sim (5, 15 - 19)$ in (b) and $(x, z) \sim (50, 15 - 19)$ in (c). (d)-(f) A low Ma 3D run at the same parameters as in (a), where (d) is a vertical (x, z) slice at $y = L_y/2$, (e) is a horizontal slice at $z = L_z$, and (f) is a horizontal slice at $z = L_z/2$.

In 3D, the same upflow/downflow asymmetry is seen, but other aspects of the flow are distinctly different. Fig. 2.2d-f show select snapshots of a 3D simulation with the same input parameters as the 2D case in Fig. 2.2a. In 2D, large-scale, coherent spinners dominate the flow, leading to a single upflow and downflow. New downflowing plumes at the upper boundary are efficiently swept into the large coherent structure (near $x \sim 1$ and spanning the vertical domain). The behavior of downflows in 3D is strikingly different (Fig. 2.2d). In 3D, many individual plumes detach from the upper boundary, but do not organize into a single dominant downflow in the same fashion. Horizontal cuts near the top of the domain (Fig. 2.2e) reveal a network of narrow downflow lanes surrounding broad upflows. Stronger clusters of downflows near the surface are linked to sheets of low entropy at the midplane of the domain (Fig. 2.2f). As the flows evolve in time, new downflows appear at the top of the domain in the middle of upflows and join the surrounding

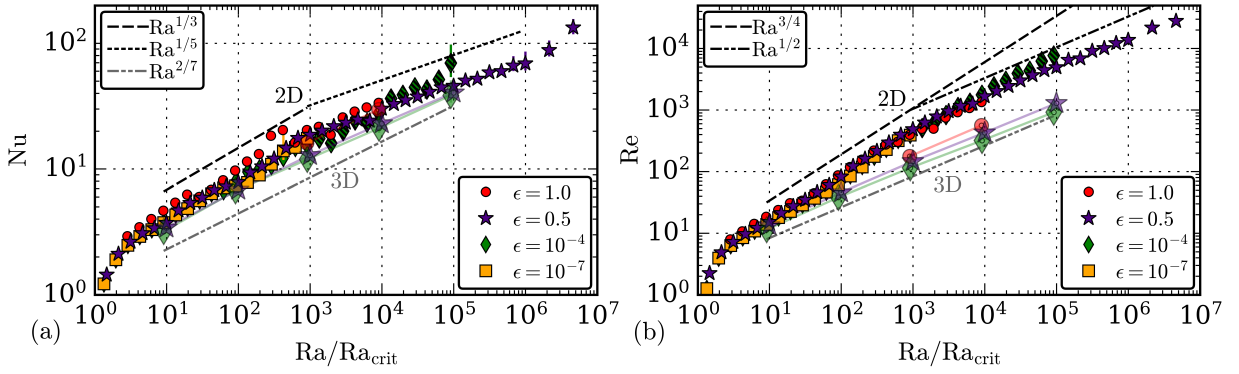


Figure 2.3: Flow properties at high and low ϵ . (a) Nu vs. $\text{Ra}/\text{Ra}_{\text{crit}}$. Errors bars indicate the variance of Nu with depth; large error bars indicate a poorly converged solution. (b) Re vs. $\text{Ra}/\text{Ra}_{\text{crit}}$. Re is measured at the midplane of the atmosphere. Larger symbols with inlaid circles designate 3D runs.

downflow network, causing the convective structures to fragment. There is no preferred orientation in the newly forming downflows, and the convective flow field constantly evolves, which appears to prevent the occurrence of either spinners or windy states.

The efficiency of convection is quantified by the Nusselt number (Nu). Nu is well-defined in RBC as the total flux normalized by the steady-state conductive flux (Johnston & Doering, 2009; Otero et al., 2002). In stratified convection Nu is more difficult to define, and we use a modified version of a traditional stratified Nusselt number (Graham, 1975; Hurlburt et al., 1984),

$$\text{Nu} \equiv \frac{\langle F_{\text{conv},z} + F_{\text{cond},z} - F_A \rangle}{\langle F_{\text{cond},z} - F_A \rangle} = 1 + \frac{\langle F_{\text{conv},z} \rangle}{\langle F_{\text{cond},z} - F_A \rangle} \quad (2.9)$$

where $F_{\text{conv},z}$ and $F_{\text{cond},z}$ are the z-components of \mathbf{F}_{conv} and \mathbf{F}_{cond} , and $\langle \rangle$ are volume averages. $F_A \equiv -\langle \kappa \rangle \partial_z T_{\text{ad}}$ is the conductive flux of the proper corresponding adiabatic atmosphere. For a compressible, ideal gas in hydrostatic equilibrium, $\partial_z T_{\text{ad}} \equiv -g/c_P$ (Spiegel & Veronis, 1960). It is important to measure the evolved value of $\langle \kappa \rangle = \langle \rho \chi \rangle$, which is nearly κ_0 for small ϵ but changes appreciably for large values of ϵ . In incompressible Boussinesq convection, where $\nabla S = 0$ only when $\nabla T = 0$, and where κ is constant with depth and time, this definition reduces to the traditionally defined Nusselt number (Otero et al., 2002; Johnston & Doering, 2009).

The variation of Nu with Ra is shown in Fig. 2.3a. We find that the Nu depends primarily

on Ra , not on ϵ , except where dynamical regimes change. In 2D and at low to moderate Ra , $\text{Nu} \propto \text{Ra}^{1/3}$ regardless of ϵ , reminiscent of scaling laws in Rayleigh-Bénard boundary layer theory (Grossmann & Lohse, 2000; Ahlers et al., 2009; King et al., 2012). As the flow becomes supersonic, $\text{Nu} \propto \text{Ra}^{1/5}$. It is also important to note that, in 2D, the value of Nu is heavily dependent upon the specific thermodynamic structures of the solution, and slight changes in Ra can result in a simulation converging to one solution or another. Select simulations were run at higher aspect ratios (8 and 16), and similar flow morphologies were obtained, suggesting that these states are not highly sensitive to aspect ratio. In our limited 3D runs, it appears that $\text{Nu} \propto \text{Ra}^{2/7}$, a classic scaling law seen in RBC (Johnston & Doering, 2009).

The rms Reynolds number ($\text{Re} = |\mathbf{u}|L_z/\nu$) and Peclet number ($\text{Pe} = \text{Pr Re}$) compare the importance of advection to diffusion in the evolved convective state. For $\text{Pr} = 1$, $\text{Pe} = \text{Re}$. Our choice of $\{\nu, \chi\} \propto \rho_0^{-1}$ drastically changes the value of Re between the top and bottom of the atmosphere. We report values of Re at the midplane ($z = L_z/2$) of the atmosphere in Fig. 2.3b. We find that Re depends largely on Ra , but not ϵ , except when the flow regime changes. In 2D $\text{Re} \propto \text{Ra}^{3/4}$ at low Ra . When the 2D flows become supersonic, $\text{Re} \propto \text{Ra}^{1/2}$, as expected from (2.3). In our limited 3D runs, $\text{Re} \propto \text{Ra}^{1/2}$, consistent with the supersonic results. The heightened scaling of Re in 2D follows the scaling of velocity (Ma) with Ra , as seen in Fig. 2.1, and reflects the presence of coherent spinners, which do not exist in 3D.

2.2.3.2 Evolved stratification

In the evolved state, the flows can change the density stratification. In Fig. 2.4a, we measure the time- and horizontally-averaged density profile in two ways. Empty symbols show the number of density scale heights between the maximum and minimum of the atmospheric density profile. Solid symbols show the number of density scale heights between the top and bottom of the atmosphere. We find that near-sonic and supersonic flows support significant, persistent density inversions in the boundary layers, as was reported previously Brandenburg et al. (2005). This is visible when solid symbols lie below empty symbols. We find this in 2D and 3D, even at very large ϵ .

Sample evolved density profiles are displayed in Fig. 2.4b. The natural log of the temporally and horizontally averaged density profile, $\ln \rho = \ln \rho_0 + \ln \rho_1$, is displayed for four cases. At low ϵ (dotted green line), the density stratification is, to first order, unchanged from the initial density stratification. At high ϵ , in both 2D (solid purple line) and 3D (dashed purple line and dash-dot-dot red line), the evolved stratification differs significantly from the initial state and does not increase monotonically with depth. To measure the number of density scale heights between two points in the atmosphere, z_1 & z_2 , we calculate $n_\rho(z_1, z_2) = \ln \rho(z_2) - \ln \rho(z_1)$. Thus, the values plotted in Fig. 2.4a for the cases in Fig. 2.4b can be directly read off. For example, at $\epsilon = 1$ and $\text{Ra}/\text{Ra}_{\text{crit}} \sim 10^4$ (dash-dot-dot red line), measuring the stratification between the boundaries retrieves $n_\rho(L_z, 0) \approx -0.3$, but measuring between the maximum and minimum value of the profile retrieves $n_\rho(\min, \max) \approx 1.6$.

Surprisingly, the evolved n_ρ is always less than the initial $n_\rho = 3$, and turbulent pressure support plays a larger role than atmospheric slumping. This appears to arise as a result of convection making the interior isentropic in the presence of fixed-temperature boundary conditions; we expect the behavior of the stratification to be dependent on the choice of thermal boundary conditions. The agreement of Nu & Re across ϵ (Fig. 2.3), particularly at low Ra in which all four of our cases collapse onto a single power law, is striking in light of the vastly different evolved stratifications felt by the flows.

2.2.4 Discussion & Future Work

We have found that the evolved flow properties of stratified, compressible convection scale in a manner reminiscent of incompressible, Boussinesq Rayleigh-Bénard convection. We argue that polytropically stratified atmospheres are the natural extension of the RBC problem with an additional control parameter, ϵ , whose primary role is to set the Ma of the flows. We show that other properties of the evolved solutions (Nu, Re) are nearly identical at vastly different values of ϵ , except for where there is a transition between the subsonic and supersonic regimes. We also see that Nu scales similarly in 2D and 3D, and that Ma in 3D solutions appears to be a

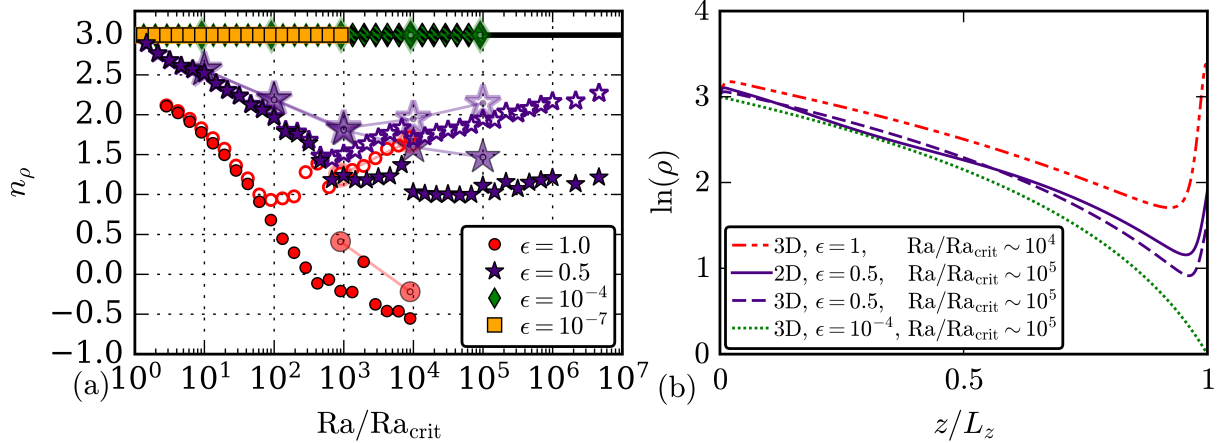


Figure 2.4: (a) Solid symbols show the density contrast measured in density scale heights between the upper and lower boundary, $n_\rho = \ln[\rho(z=0)/\rho(z=L_z)]$. Empty symbols show $n_\rho = \ln[\max(\rho)/\min(\rho)]$. At low ϵ the evolved n_ρ is close to the initial conditions of $n_\rho = 3$. At high ϵ , the density stratification decreases. Once the mean Ma approaches 1 (at $\text{Ra}/\text{Ra}_{\text{crit}} \approx \{10^2, 10^3\}$ for $\epsilon = \{1, 0.5\}$ as in Fig. 2.1b), density inversions form within the thermal boundary layers. Larger symbols represent 3D runs. (b) The natural log of time- and horizontally-averaged density profiles are shown for select simulations, to illustrate the inversions which appear in the boundary layers.

function of ϵ alone, allowing for simple specification of the evolved Ma using input parameters. The stratification of these polytropic atmospheres evolves in a complex manner, and future work should aim to understand the importance of stratification on convective heat transport and other flow properties.

Our studies here will serve as a foundation for comparing heat transport in stratified convection to that in RBC (Johnston & Doering, 2009) and for better quantifying transport in stratified convection. These results can be used to determine if fluid properties scale appropriately in simplified equation sets, such as the anelastic equations. This work will also be useful in coming to understand more realistic systems, such as rapidly rotating atmospheres (Julien et al., 2012), atmospheres bounded by stable regions (Hurlburt et al., 1986), and regions with realistic profiles of κ .

2.2.5 Appendix A: Table of simulation parameters

In table 2.1, we report both the input parameters (ϵ , Ra_t , resolution) and output values (evolved Nu , Re , Ma , n_ρ) of select simulations. All 3D simulations are listed, and the corresponding 2D simulations at the same parameters are included. A full table of all information is included as a CSV file in the supplemental materials.

Table 2.1: Input simulation parameters of ϵ , Ra, and resolution are given for select simulations. Output values of Nu, Ma, Re, and n_ρ , as plotted throughout the paper, are provided for the corresponding run. The mean of Nu and Ma is reported, as well as the distance from the mean to the atmospheric maximum and minimum. Re is reported at the midplane. The evolved n_ρ is reported using the two metrics described in Fig. 2.4.

ϵ	Rat	3D	n_z	n_x	n_y	Nu	Re	Ma	$n_{\rho,\text{max}}$	$n_{\rho,\text{bounds}}$
1	10^4	No	256	1024	—	$20.43^{+0.24}_{-0.21}$	397.69	$0.79^{+5.49}_{-0.35}$	1.26	-0.21
	10^5	No	512	2048	—	$33.60^{+1.03}_{-0.41}$	1356.44	$0.82^{+4.51}_{-0.33}$	1.72	-0.55
0.5	100	No	64	256	—	$3.72^{+0.01}_{-0.01}$	15.22	$0.22^{+0.33}_{-0.11}$	2.52	2.52
	1000	No	128	512	—	$7.87^{+0.09}_{-0.04}$	83.02	$0.39^{+0.71}_{-0.26}$	1.98	1.96
0.5	10^4	No	128	512	—	$18.69^{+0.63}_{-0.38}$	487.35	$0.74^{+1.50}_{-0.54}$	1.51	1.24
	10^5	No	256	1024	—	$30.14^{+0.39}_{-0.15}$	1677.07	$0.71^{+0.87}_{-0.34}$	1.70	1.03
0.5	10^6	No	512	2048	—	$45.86^{+3.76}_{-1.90}$	4943.73	$0.64^{+0.62}_{-0.24}$	1.95	1.11
	100	No	64	256	—	$3.75^{+0.01}_{-0.01}$	13.93	$2.82^{+1.91}_{-1.39} \cdot 10^{-3}$	3.00	3.00
10^{-4}	1000	No	128	512	—	$7.97^{+0.28}_{-0.07}$	65.85	$4.51^{+3.95}_{-2.66} \cdot 10^{-3}$	3.00	3.00
	1000	No	128	512	—	$15.21^{+0.32}_{-0.14}$	391.38	$9.30^{+11.7}_{-7.11} \cdot 10^{-3}$	3.00	3.00
10^{-4}	10^4	No	256	1024	—	$27.83^{+0.42}_{-0.47}$	1766.70	$1.50^{+2.19}_{-1.17} \cdot 10^{-2}$	3.00	3.00
	10^5	No	512	2048	—	$69.68^{+28.24}_{-15.80}$	7684.29	$2.10^{+3.15}_{-1.74} \cdot 10^{-2}$	3.00	3.00
10 ⁻⁴	10^4	Yes	128	256	256	$16.10^{+0.15}_{-0.99}$	176.84	$0.39^{+3.78}_{-0.13}$	1.24	0.41
	10^5	Yes	256	512	512	$29.67^{+0.44}_{-1.90}$	562.40	$0.38^{+3.71}_{-0.14}$	1.67	-0.22
0.5	100	Yes	64	128	128	$3.42^{+0.06}_{-0.11}$	13.42	$0.21^{+0.33}_{-0.08}$	2.56	2.57
	1000	Yes	128	256	256	$6.83^{+0.18}_{-0.25}$	46.03	$0.23^{+0.38}_{-0.08}$	2.19	2.19
0.5	10^4	Yes	128	256	256	$12.89^{+0.30}_{-0.62}$	146.92	$0.23^{+0.45}_{-0.08}$	1.83	1.81
	10^5	Yes	256	512	512	$23.05^{+1.41}_{-1.04}$	429.63	$0.21^{+0.43}_{-0.08}$	1.95	1.59
0.5	10^6	Yes	256	512	512	$40.53^{+0.66}_{-0.72}$	1291.61	$0.20^{+0.46}_{-0.08}$	2.15	1.47
	100	Yes	64	128	128	$3.19^{+0.06}_{-0.10}$	11.48	$2.53^{+1.93}_{-9.97} \cdot 10^{-3}$	3.00	3.00
10^{-4}	1000	Yes	128	256	256	$6.72^{+0.57}_{-0.19}$	38.32	$2.88^{+2.55}_{-1.09} \cdot 10^{-3}$	3.00	3.00
	1000	Yes	128	256	256	$11.92^{+1.34}_{-0.40}$	115.06	$2.85^{+3.11}_{-1.13} \cdot 10^{-3}$	3.00	3.00
10^{-4}	10^4	Yes	256	512	512	$21.11^{+4.74}_{-1.69}$	319.84	$2.46^{+2.90}_{-1.07} \cdot 10^{-3}$	3.00	3.00
	10^5	Yes	256	512	512	$38.50^{+12.54}_{-4.71}$	920.21	$2.26^{+2.84}_{-1.02} \cdot 10^{-3}$	3.00	3.00
10^{-4}	10^6	Yes	256	512	512	$38.50^{+12.54}_{-4.71}$	920.21	$2.26^{+2.84}_{-1.02} \cdot 10^{-3}$	3.00	3.00

2.3 Postscript and lessons learned since publication

Our choice to study convection in the presence of stress-free boundary conditions likely made our efforts to understand these convective systems significantly more difficult. In addition to permitting shearing states (as in e.g., Goluskin et al., 2014) at high Ra, our choice of stress-free boundaries allowed for the development of large-scale “flywheel” modes. From subsequent work over the past three years, we have learned that, for a given aspect ratio, 2D convection exhibits flywheel modes at low supercriticalities and shearing states at high supercriticalities. In both cases, these phenomena are driven by baroclinic driving of vortical convective rolls, and the choice of stress-free boundary conditions prevents vorticity from exiting the domain at the boundaries. At low supercriticalities, the energy in the flywheel builds up to the point where baroclinic driving comes into balance with viscous dissipation, and a long-lived flywheel mode is observed. At large supercriticalities, before this source and corresponding sink of vorticity can come into balance, the flywheel becomes sufficiently energetic that it becomes unstable, rips itself apart, and exhibits domain-wide shearing states. Viewed in this light, our high-Mach number results presented here suggest that flywheels in compressible flows can be stable even in highly turbulent flows due to the extra dissipation shocks are capable of achieving. At the end of this thesis, I examine the nature of Boussinesq flywheel modes in more detail (see sec. 7.1).

The scaling laws that we observed in this work suggest that, in studies of polytropic convection, the convective heat flux is controlled by dissipation in the boundary layers. However, unlike in Rayleigh-Bénard convection, the boundary layers in our work are **not** symmetrical – instead, the boundary layer at the bottom of the atmosphere is physically smaller than the one at the top of the atmosphere. It is unclear at this time whether it is the bottom boundary layer, the top boundary layer, or **both** boundary layers in which dissipation is maximized. Some initial theoretical work on this topic is being performed by Chris Jones (as presented in Jones et al., 2019), but to date little or no careful work on this theory has been published.

Chapter 3

Predicting the Rossby Number in Convective Experiments

3.1 Preamble

The following work was published in the Astrophysical Journal (Anders et al., 2019b). The text in section 3.2 is the text of the paper as it was accepted for publication. Following the published work, in section 3.3, I comment on a few lessons that have been learned since we published these results.

This work was motivated by a fundamental lack of understanding of how to conduct a “proper” experiment in rotating convection. In Ch. 2, we established that if you hold the Mach number constant in polytropic convection (via ϵ) and increase the value of Ra, you naturally step into a more turbulent region of parameter space in a manner similar to standard Rayleigh-Bénard convection. We supposed that analogous paths could be walked in rotating convection: that is, if you hold the **Rossby number** constant (the degree of rotational constant on the convective flows), and increase the Rayleigh number, you should be able to walk into a more turbulent region of parameter space analogous to **nonrotational** Rayleigh-Bénard convection.

This work started in the summer of 2018 and was performed in close collaboration with Katie Manduca, who was a post-baccalaureate researcher in our group. Her initial explorations of parameter space got us close enough to discovering Rop that she deserves a huge chunk of the credit for this paper ever existing in a published state.

3.2 Published work

3.2.1 Introduction

Rotation influences the dynamics of convective flows in stellar and planetary atmospheres. Many studies on the fundamental nature of rotating convection in both laboratory and numerical settings have provided great insight into the properties of convection in both the rapidly rotating regime and the transition to the rotationally unconstrained regime (King et al., 2009; Zhong et al., 2009; Schmitz & Tilgner, 2009; King et al., 2012; Julien et al., 2012; King et al., 2013; Ecke & Niemela, 2014; Stellmach et al., 2014; Cheng et al., 2015; Gastine et al., 2016) The scaling behavior of heat transport, the nature of convective flow structures, and the importance of boundary layer-bulk interactions in driving dynamics are well known. Yet, we do not know of any simple procedure for predicting the magnitude of vortical flow gradients purely from experimental control parameters, such as bulk rotation rate and thermal input.

In the astrophysical context, many studies of rotating convection have investigated questions inspired by the solar dynamo (Glatzmaier & Gilman, 1982; Busse, 2002; Brown et al., 2008, 2010, 2011; Augustson et al., 2012; Guerrero et al., 2013; Käpylä et al., 2014). Even when these simulations nominally rotate at the solar rate, they frequently produce distinctly different behaviors than the true Sun, such as anti-solar differential rotation profiles (Gastine et al., 2014; Brun et al., 2017). It seems that these differences occur because the simulations produce less rotationally constrained states than the Sun. The influence of rotation results from the local shear gradients, and these are not direct input parameters. Recent simulations predict significant rotational influence in the deep solar interior, which can drastically affect flows throughout the solar convection zone (Featherstone & Hindman, 2016a; Greer et al., 2016). In the planetary context, the balance between magnetic and rotational forces likely leads to the observed differences between ice giant and gas giant dynamos in our solar system (Soderlund et al., 2015). The work of Aurnou & King (2017) demonstrates the importance of studying a dynamical regime with the proper balance between Lorentz, Coriolis, and inertial forces when modeling astrophysical objects such as planetary dynamos.

In short, simulations must achieve the proper rotational balance if they are to explain the behavior of astrophysical objects. In Boussinesq studies, rotational constraint is often measured by comparing dynamical and thermal boundary layers or deviation in heat transport from the non-rotating state (King et al., 2012; Julien et al., 2012; King et al., 2013). Such measurements are not available for astrophysical objects, where the degree of rotational influence is best assessed by the ratio between nonlinear advection magnitude and the linear Coriolis accelerations. The *Rossby number* is the standard measure of this ratio,

$$\text{Ro} \equiv \frac{|\nabla \times \mathbf{u}|}{2|\boldsymbol{\Omega}|} \sim \frac{|(\nabla \times \mathbf{u}) \times \mathbf{u}|}{|2\boldsymbol{\Omega} \times \mathbf{u}|}, \quad (3.1)$$

where $\boldsymbol{\Omega}$ denotes the bulk rotation vector. Many proxies for the dynamical Rossby number exist that are based solely on input parameters, most notably the *convective* Rossby number. However, all proxies produce imperfect predictions for the true dynamically relevant quantity.

In this letter, we demonstrate an emperical method of predicting the output Rossby number of convection in a simple stratified system.

In Anders & Brown (2017) (hereafter AB17), we studied non-rotating compressible convection without magnetic fields in polytropic atmospheres. In this work, we extend AB17 to rotationally-influenced, *f*-plane atmospheres (e.g., Brummell et al., 1996, 1998; Calkins et al., 2015). We determine how the input parameters we studied previously, which controlled the Mach and Reynolds numbers of the evolved flows, couple with the Taylor number (Ta, Julien et al., 1996), which sets the magnitude of the rotational vector.

In subsection 3.2.2, we describe our experiment and paths through parameter space. In subsection 3.2.3, we present the results of our experiments and in subsection 3.2.4 we offer concluding remarks.

3.2.2 Experiment

We study fully compressible, stratified convection under precisely the same atmospheric model as in AB17, but here we have included rotation. We study polytropic atmospheres with $n_p = 3$

density scale heights and a superadiabatic excess of $\epsilon = 10^{-4}$ such that flows are at low Mach number. We study a domain in which the gravity, $\mathbf{g} = -g\hat{z}$, and rotational vector, $\boldsymbol{\Omega} = \Omega\hat{z}$, are antiparallel (as in e.g., Julien et al., 1996; Brummell et al., 1996).

We evolve the velocity (\mathbf{u}), temperature (T), and log density ($\ln \rho$) according to the Fully Compressible Navier-Stokes equations in the same form presented in AB17, with the addition of the Coriolis term, $2\boldsymbol{\Omega} \times \mathbf{u}$, to the left-hand side of the momentum equation. We impose impenetrable, stress-free, fixed-temperature boundary conditions at the top and bottom of the domain.

We specify the kinematic viscosity (ν), thermal diffusivity (χ), and strength of rotation (Ω) at the top of the domain by choosing the Rayleigh number (Ra), Prandtl number (Pr), and Taylor number (Ta),

$$\text{Ra} = \frac{gL_z^3 \Delta S / c_P}{\nu \chi}, \quad \text{Pr} = \frac{\nu}{\chi}, \quad \text{Ta} = \left(\frac{2\Omega L_z^2}{\nu} \right)^2, \quad (3.2)$$

where L_z is the depth of the domain as defined in AB17, $\Delta S \propto \epsilon n_\rho$ is the specific entropy difference between the top and bottom of the atmosphere, and the specific heat at constant pressure is $c_P = \gamma/(\gamma - 1)$ with $\gamma = 5/3$. Throughout this work we set $\text{Pr} = 1$. The Taylor number relates to the often-quoted Ekman number by the equality $\text{Ek} \equiv \text{Ta}^{-1/2}$.

Due to stratification, Ra and Ta both grow with depth as $(\text{Ra}, \text{Ta}) \propto \rho^2$ (see AB17). We nondimensionalize our atmospheres at the top of the domain, and so all values of Ra and Ta quoted in this work are the minimal value of Ra and Ta in the domain at $z = L_z$. For direct comparison to Boussinesq studies, past work has found that the value of Ra at the atmospheric midplane ($z = L_z/2$) varies minimally with increasing stratification (Unno et al., 1960). For the atmospheres presented in this work, midplane Ra and Ta values are larger than reported top-of-atmosphere values by a factor of ~ 70 , and values at the bottom of the atmosphere are larger by ~ 400 .

When Ta is large, the wavenumber of convective onset increases according to $k_{\text{crit}} \propto \text{Ta}^{1/6}$ (Chandrasekhar, 1961; Calkins et al., 2015). We study horizontally-periodic, 3D Cartesian domains with extents of $x, y = [0, 4(2\pi/k_{\text{crit}})]$ and $z = [0, L_z]$. At large values of Ta, these domains are

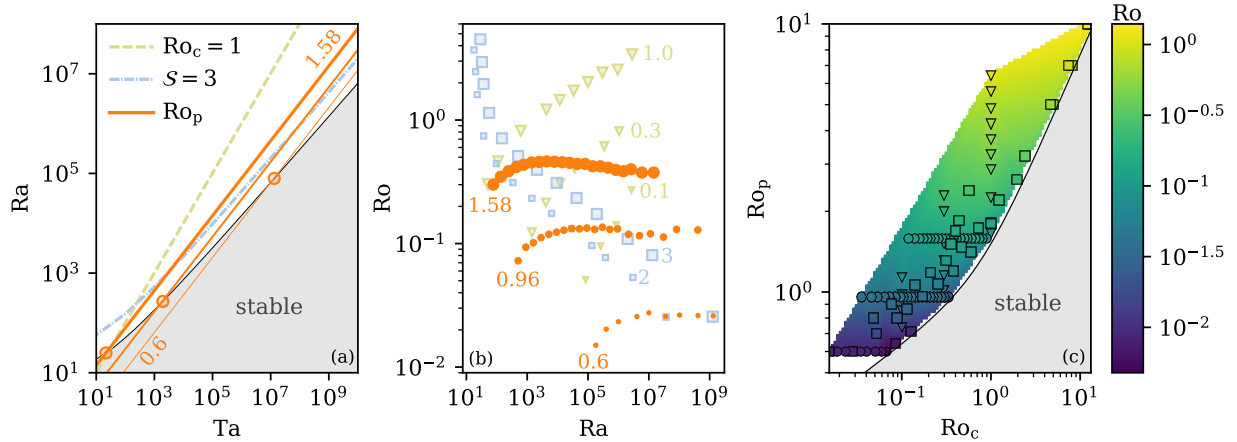


Figure 3.1: (a) The critical Rayleigh number, as a function of the Taylor number, is plotted as a solid black line. The grey shaded region is subcritical, and rotation suppresses convection there. Paths of constant Convective Rossby number (Ro_c , green dashed line), constant supercriticality (S , blue dash-dot line), and constant Predictive Rossby number (Ro_p , orange solid lines) are shown. From thickest to thinnest, paths with $Ro_p = [1.58, 0.96, 0.6]$ are plotted, and the value of $(Ta_{\text{crit}}, Ra_{\text{crit}})$ for each path is denoted by a circular marker (see Table 3.1). (b) Evolved Ro is plotted vs. Ra along paths of $Ro_p = [1.58, 0.96, 0.6]$ for [big, medium, small] orange circles. For comparison, paths of constant S (blue squares, $S = [3, 2]$ for [big, small] squares) and constant Ro_c (green triangles, $Ro_c = [1, 0.3, 0.1]$ for [big, medium, small] triangles) are shown. (c) The evolved value of Ro is shown as a function of Ro_p and Ro_c . Each of the experiments in (b) is outlined by a black (circle, triangle, square) for points along constant (Ro_p, Ro_c, S) paths. The color inside of the marker represents the exact measured Ro of that experiment, while the colormap outside of markers is a linear interpolation of the data set.

tall and skinny, as in Stellmach et al. (2014). We evolve our simulations using the Dedalus¹ pseudospectral framework, and our numerical methods are identical to those presented in AB17. The supplemental materials of this paper include a `.tar` file which contains the code used to perform the simulations in this work, and this tarball is also published online in a Zenodo repository (Anders et al., 2019c).

The critical value of Ra at which rapidly rotating convection onsets also depends on Ta (see the black line in figure 3.1a), roughly according to $Ra_{\text{crit}} \sim Ta^{2/3}$ (Chandrasekhar, 1961; Calkins et al., 2015). Even taking account of linear theory, the dependence of the evolved nonlinear fluid flows on the input parameters makes predicting the rotational constraint very challenging. We will

¹ <http://dedalus-project.org/>

explore three paths through Ra-Ta space:

$$\text{Ra} = \begin{cases} \mathcal{S} \text{Ra}_{\text{crit}}(\text{Ta}), & (\text{I}) \\ (\text{Ro}_c)^2 \text{Pr} \text{Ta}, & (\text{II}) \\ (\text{Ro}_p)^2 \text{Pr}^{1/2} \text{Ta}^{3/4} & (\text{III}). \end{cases} \quad (3.3)$$

Paths on constraint I are at constant supercriticality, $\mathcal{S} \equiv \text{Ra}/\text{Ra}_{\text{crit}}(\text{Ta})$ (blue dash-dot line in figure 3.1a). Paths on constraint II (green dashed line in figure 3.1a) are at a constant value of the classic *convective* Rossby number,

$$\text{Ro}_c = \sqrt{\frac{\text{Ra}}{\text{Pr} \text{Ta}}} = \frac{1}{2\Omega} \sqrt{\frac{g \Delta S}{c_p L_z}}, \quad (3.4)$$

which has provided (e.g., Julien et al., 1996; Brummell et al., 1996) a common proxy for the degree of rotational constraint. This parameter measures the importance of buoyancy relative to rotation without involving dissipation. Paths on constraint III (e.g., orange solid lines in figure 3.1a) set constant a ratio which we call the “Predictive Rossby number,”

$$\text{Ro}_p = \sqrt{\frac{\text{Ra}}{\text{Pr}^{1/2} \text{Ta}^{3/4}}} = \frac{1}{(2\Omega)^{3/4}} \sqrt{\frac{g \Delta S}{c_p \chi^{1/2}}} \quad (3.5)$$

Unlike paths through parameter space which hold Ro_c constant, paths with constant Ro_p feel changes in diffusivities but not the depth of the domain. To our knowledge, these paths have not been reported in the literature, although the importance of $\text{Ra}/\text{Ta}^{3/4} = \text{Ra} \text{Ek}^{3/2}$ has been independently found by King et al. (2012) using a boundary layer analysis. We compare our results to their theory in Section 3.2.4.

In this work, we primarily study three values of Ro_p . These values are shown in Fig. 3.1a and Table 3.1. Table 3.1 lists the values of $(\text{Ra}_{\text{crit}}, \text{Ta}_{\text{crit}})$ for each value of Ro_p , and also the maximum value of (Ra, Ta) studied in this work for each path. We additionally walked two pathways at constant supercriticality (constraint I, $\mathcal{S} = \{2, 3\}$) and three pathways at constant convective Rossby number (constraint II, $\text{Ro}_c = \{1, 0.3, 0.1\}$). Full details on all cases are provided in Appendix 3.2.5 and the supplemental materials.

Table 3.1: Parameter space: Values of the critical Ra and Ta for each Ro_p track are reported, as well as the maximal values of Ra and Ta studied on each track. All values reported are for the top of the atmosphere. A fuller set of simulations are reported in Table 3.2 with midplane Ra and Ta values as well.

Ro_p	$(\text{Ra}_{\text{crit}}, \text{Ta}_{\text{crit}})$	$(\text{Ra}_{\text{max}}, \text{Ta}_{\text{max}})$
0.60	$(10^{4.88}, 10^{7.10})$	$(10^{9.09}, 10^{12.72})$
0.96	$(10^{2.44}, 10^{3.30})$	$(10^{8.58}, 10^{11.49})$
1.58	$(10^{1.39}, 10^{1.33})$	$(10^{7.14}, 10^{8.99})$

3.2.3 Results

In our stratified domains, for $\text{Ta} \geq 10^5$, a best-fit to results from a linear stability analysis provides $\text{Ra}_{\text{crit}}(\text{Ta}) = 1.459\text{Ta}^{2/3}$ and $k_{\text{crit}}(\text{Ta}) = 0.414\text{Ta}^{1/6}$ for direct onset of convection. In figure 3.1a, the value of $\text{Ra}_{\text{crit}}(\text{Ta})$ is shown. Sample paths for each criterion in equation 3.3 through this parameter space are also shown. In this work, we often find it instructive to use one critical Ra for an entire Ro_p path. This Ra_{crit} is determined by the intersubsection of the onset curve and Ro_p path (indicated by the orange circles in figure 3.1a, and quoted in Table 3.1). In the high Ta regime, we find that $\text{Ra}_{\text{crit}} = 18.5\text{Ro}_p^{-16}$.

In figure 3.1b, we display the evolution of Ro with increasing Ra along various paths through parameter space. We find that Ro increases on constant Ro_c paths, decreases on constant \mathcal{S} paths, and remains roughly constant along constant Ro_p paths. In figure 3.1c, the value of Ro is shown simultaneously as a function of Ro_p and Ro_c for all experiments conducted in this study. We find a general power-law of the form $\text{Ro} = CRo_c^\alpha Ro_p^\beta$. In the rotationally-dominated regime where $\text{Ro} < 0.2$ and $\text{Re}_\perp > 5$ (see Eqn. 3.6), we find $\alpha = -0.02$, and Ro can be said to be a function of Ro_p alone. Under this assumption, we report a scaling of $\text{Ro} = (0.148 \pm 0.003)\text{Ro}_p^{3.34 \pm 0.07}$. In the less rotationally dominated regime of $\text{Ro} > 0.2$ and $\text{Re}_\perp > 5$, we find $\{C, \alpha, \beta\} = \{0.2, -0.19, 1.5\}$.

In figure 3.2, sample snapshots of the evolved entropy field in the x - y plane near the top and at the middle of the domain are shown. In the left column, flows are at $\text{Ro} \sim 1$ and resemble the classic granular structure of nonrotating convection (see e.g., figure 2 in AB17), where strong narrow downflow lanes punctuate broad upwellings. The narrow downflows at the top organize

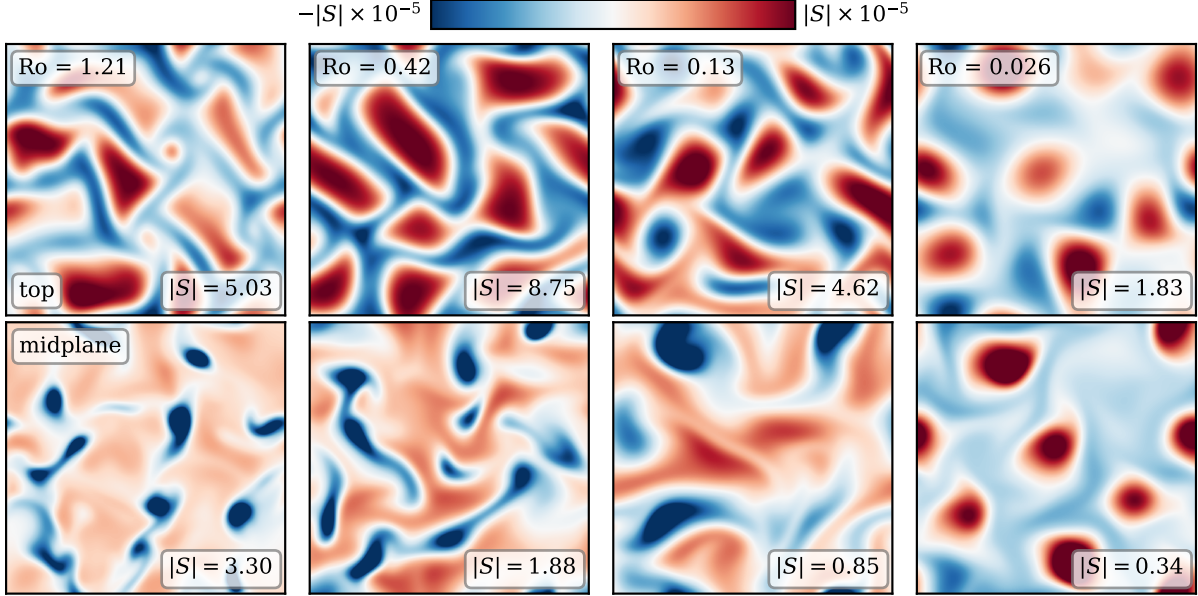


Figure 3.2: Horizontal slices of the evolved entropy deviation from the mean at $z = 0.95L_z$ (top row) and $z = 0.5L_z$ (bottom row) are shown for select simulations. All runs displayed here have an evolved volume-averaged $\text{Re}_\perp \approx 32$. As Ro decreases from $O(1)$ on the left to $O(0.03)$ on the right, and thus the rotational constraint on the flow increases, significant changes in flow morphology are observed. As Ro decreases, Coriolis forces more effectively deflect the convective flows, and the classic granular convective pattern gives way to vortical columns that are quasi-two-dimensional.

themselves into intense coherent structures at the midplane, and at the midplane the downflows have much stronger entropy fluctuations than the broad and slower upflows.

Ro decreases from left to right into the rotationally constrained regime. As Ro decreases, the narrow downflow lanes begin to disappear and the flows at midplane become more symmetric. In the rotationally constrained regime ($\text{Ro} \sim 0.03$), the convective structures are distinctly different. Here we observe dynamically persistent, warm upflow columns surrounded by bulk weak downflow regions. At the midplane, the upflow columns have substantially higher entropy perturbations than the surrounding weak downflows which sheathe them, and the locations of the columns are tightly correlated with their positions at the top of the domain. These quasi-two-dimensional dynamics are similar to those seen in rapidly rotating Rayleigh-Bénard convection (e.g., Stellmach et al., 2014). The select cases displayed in figure 3.2 each have an evolved volume-averaged $\text{Re}_\perp \approx 32$ (defined

below in equation 3.6).

We measure the Nusselt number (Nu), which quantifies heat transport in a convective solution, as defined in AB17. In figure 3.3a, we plot Nu as a function of $\text{Ra}/\text{Ra}_{\text{crit}}$ at fixed Ro_p . We find that $\text{Nu} \propto \{\text{Ra}^{0.29 \pm 0.01}, \text{Ra}^{0.29 \pm 0.01}, \text{Ra}^{0.24}\}$ for $\text{Ro}_p = \{0.6, 0.957, 1.58\}$. In the regime of $\text{Ro} \lesssim 0.1$, these scaling laws are indistinguishable from a classic $\text{Ra}^{2/7}$ power law scaling, which is observed in nonrotating Rayleigh-Bénard and stratified convection (Ahlers et al., 2009, AB17). Our results seem consistent with the stress-free, rotating Rayleigh-Bénard convection results of Schmitz & Tilgner (2009), whose re-arranged Eqn. 7 returns a best-fit of $\text{Nu} \propto \text{Ra}^{0.26}$ at fixed Ro_p . Their work primarily spans the transition regime between rotationally constrained and unconstrained convection, and so it is perhaps not surprising that their power law is a blend of our rotationally-constrained $\text{Ra}^{2/7}$ power law and the fairly rotationally unconstrained $\text{Ra}^{0.24}$ at $\text{Ro}_p = 1.58$.

Flows are distinctly different parallel to and perpendicular from the rotation vector, which aligns with gravity and stratification. We measure two forms of the RMS Reynolds number,

$$\text{Re}_{\parallel} = \frac{|\mathbf{u}|L_z}{\nu}, \quad \text{Re}_{\perp} = \frac{|\mathbf{u}|}{\nu} \frac{2\pi}{k_{\text{crit}}}, \quad (3.6)$$

where the length scale in Re_{\perp} is the wavelength of convective onset, and is related to the horizontal extent of our domain (see subsection 3.2.2). From our work in AB17, we expect the RMS velocity to scale as $|\mathbf{u}| \propto \sqrt{\Delta S}$. By definition, $\nu \propto \sqrt{\text{Ra}/(\text{Pr } \Delta S)}$, and L_z is a constant set by the stratification while $k_{\text{crit}} \propto \text{Ta}^{1/6}$. Along paths of constant Ro_p , we thus expect $\text{Re}_{\parallel} \propto \text{Ra}^{1/2}$ and $\text{Re}_{\perp} \propto \text{Ra}^{5/18}$ when Pr is held constant.

In figure 3.3b, we plot Re_{\parallel} and Re_{\perp} as a function of $\text{Ra}/\text{Ra}_{\text{crit}}$ at fixed Ro_p . We find that $\text{Re}_{\parallel} \propto \{\text{Ra}^{0.44 \pm 0.01}, \text{Ra}^{0.45 \pm 0.01}, \text{Ra}^{0.44}\}$ and $\text{Re}_{\perp} \propto \{\text{Ra}^{0.22 \pm 0.01}, \text{Ra}^{0.23 \pm 0.01}, \text{Ra}^{0.21}\}$ for $\text{Ro}_p = \{0.6, 0.957, 1.58\}$. These scalings are similar to but slightly weaker than our predictions in all cases. However, the scaling of $\text{Re}_{\parallel} \propto \text{Ra}^{0.45}$, is once again a power law observed frequently in nonrotating convection (Ahlers et al., 2009, AB17). We also observe that Re_{\perp} collapses for each Ro_p track, while Re_{\parallel} experiences an offset to larger values as Ro_p shrinks. The offset in Re_{\parallel} is unsurprising, because more rotationally constrained flows result in smaller

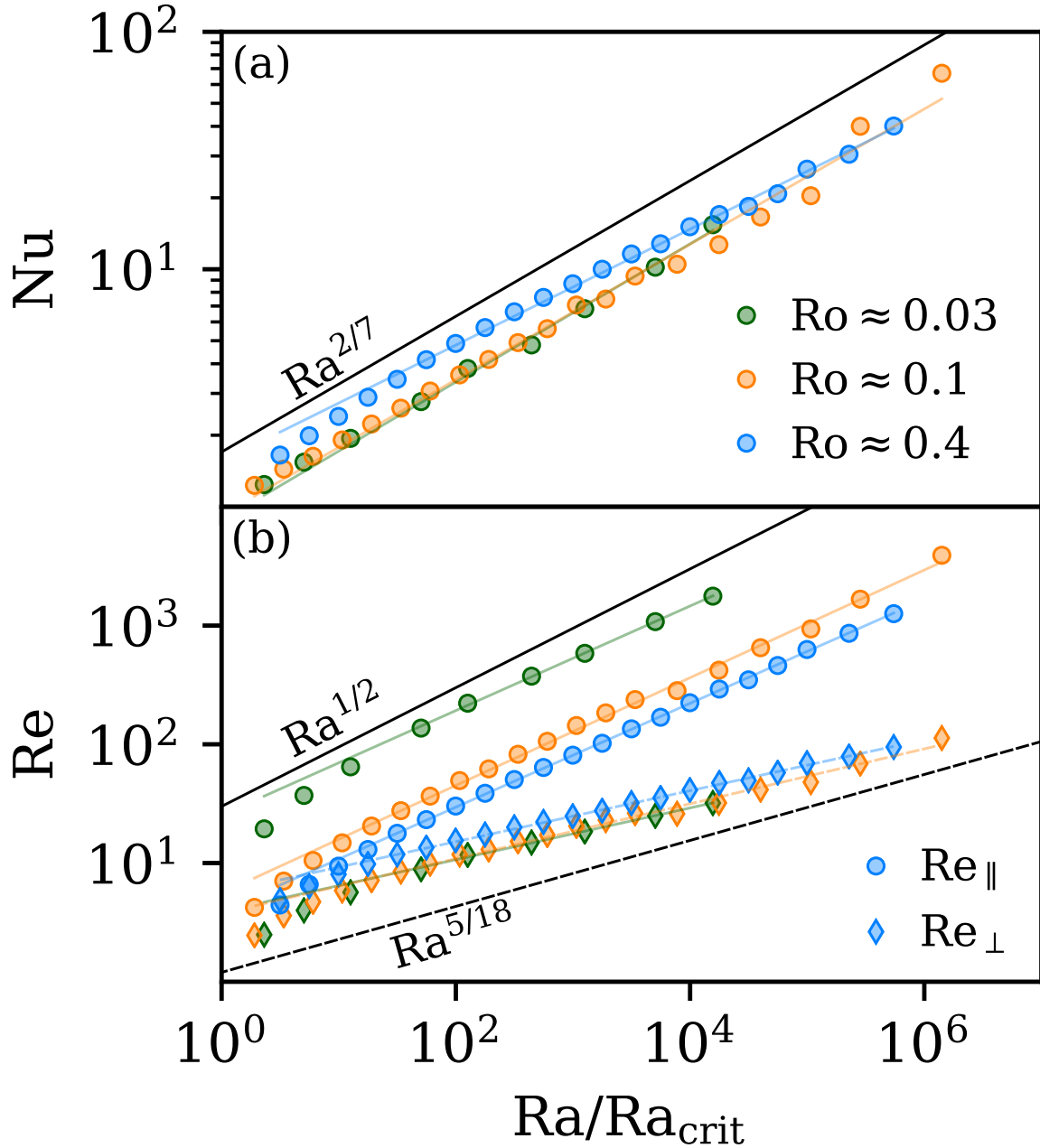


Figure 3.3: Scaling laws for paths at $\text{Ro}_p = 1.58$ ($\text{Ro} \approx 0.4$), $\text{Ro}_p = 0.96$ ($\text{Ro} \approx 0.1$), and $\text{Ro}_p = 0.6$ ($\text{Ro} \approx 0.03$) are shown. Numbers are plotted vs. $\text{Ra}/\text{Ra}_{\text{crit}}$, where Ra_{crit} is given in Table 3.1. (a) Nu , as defined in AB17, is shown. (b) Re_{\parallel} and Re_{\perp} , as defined in equation 3.6, are shown. All values of Ro_p trace out similar Nu and Re_{\perp} tracks, whereas Re_{\parallel} tracks shift upwards as Ro decreases.

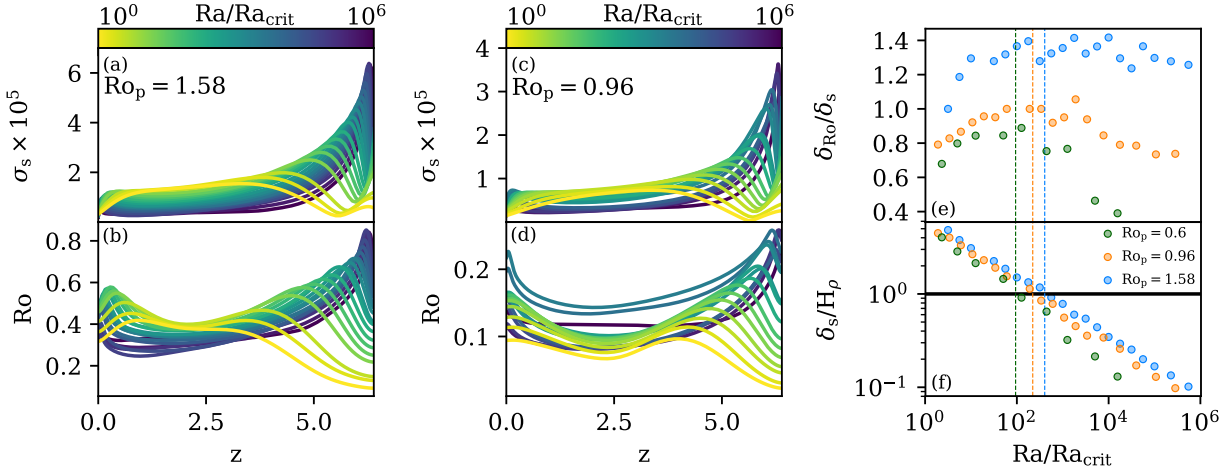


Figure 3.4: Horizontally-averaged profiles of the standard deviation of entropy (σ_s , a) and Rossby number (Ro , b) are shown vs. height for $\text{Ro}_p = 1.58$ ($\text{Ro} \approx 0.4$). Similar profiles are shown in (c) and (d) for $\text{Ro}_p = 0.96$ ($\text{Ro} \approx 0.1$). The color of the profiles denotes the value of $\text{Ra}/\text{Ra}_{\text{crit}}$, where Ra_{crit} is given in Table 3.1. (e) The ratio of the thicknesses of the dynamical boundary layers (δ_{Ro}) and thermal boundary layers (δ_s) is shown vs. $\text{Ra}/\text{Ra}_{\text{crit}}$ for fixed Ro_p . (f) δ_s is plotted vs. $\text{Ra}/\text{Ra}_{\text{crit}}$ in units of the density scale height at the top of the atmosphere (H_ρ). Vertical lines denote when $\delta_s/H_\rho = 1$ for each value of Ro_p .

boundary layers relative to the vertical extent of our stratified domain. The horizontal extent of our domain scales with the strength of rotation, and so regardless of Ro_p , flows perpendicular to the rotational and buoyant direction are comparably turbulent at the same $\text{Ra}/\text{Ra}_{\text{crit}}$. We find Re_\perp and Re_\parallel are, respectively, good proxies for the horizontal and perpendicular resolution required to resolve an experiment.

Figure 3.4 shows time- and horizontally-averaged profiles of Ro and the standard deviation of the entropy, σ_s . Figures 3.4a&b show these profiles for $\text{Ro}_p = 1.58$ ($\text{Ro} \approx 0.4$), while Figures 3.4c&d show these profiles for $\text{Ro}_p = 0.96$ ($\text{Ro} \approx 0.1$). The transition in profile behavior from low Ra (yellow) to high Ra (purple) is denoted by the color of the profile. As Ra increases at a constant value of Ro_p , both the thermal (σ_s) and dynamical (Ro) boundary layers become thinner. We measure the thickness of the thermal boundary layer (δ_s) at the top of the domain by finding the location of the first maxima of σ_s away from the boundary. We measure the thickness of the Ro boundary layer (δ_{Ro}) in the same manner. In figure 3.4e, we plot $\delta_{\text{Ro}}/\delta_s$, the ratio of the sizes of

these two boundary layers. As anticipated, the dynamical boundary layer (δ_{Ro}) becomes relatively thinner with respect to the thermal boundary layer (δ_s) as Ro and Ro_p decrease. However, the precise scaling of this boundary layer ratio with Ro_p and Ra is unclear, and we cannot immediately compare these ratios to similar measures from the Rayleigh-Bénard convection literature, such as Fig. 5 of King et al. (2013). They measure the dynamical boundary layer thickness as the peak location of the horizontal velocities, but our horizontal velocities are subject to stress-free boundary conditions, and we find that the maxima of horizontal velocities occur precisely at the boundaries. In figure 3.4f, we plot δ_s in units of the density scale height at the top of the atmosphere, and we plot vertical lines when this crosses 1. We find no systematic change in behavior when δ_s is smaller than the local density scale height.

3.2.4 Discussion

In this letter, we studied low-Mach-number, stratified, compressible convection under the influence of rotation. We examined three paths through Ra-Ta space, and showed that the newly-defined Predictive Rossby number, $Ro_p = Ra/(Pr^{1/2}Ta^{3/4})$, determines the value of the evolved Rossby number.

Shockingly, along these constant Ro_p pathways, particularly when $Ro \lesssim 0.1$, we find $Nu \propto Ra^{2/7}$ and $Re_{\parallel} \propto Ra^{0.45}$. These scalings are indistinguishable from the scalings of Re and Nu with Ra in non-rotating Boussinesq convection (Ahlers et al., 2009). Julien et al. (2012) theorized that in the rapidly rotating asymptotic limit, $(Nu - 1) \propto (Ra^{3/2}/Ta) = (Ra/Ra_{crit}(Ta))^{3/2}$. Thus, at fixed Ta , a very sharp $Ra^{3/2}$ scaling law is expected. At a fixed $Ta = 10^{14}$, Stellmach et al. (2014) found that the $Ra^{3/2}$ scaling described the results of stress-free DNS in Boussinesq cylinders very well. Gastine et al. (2016) studied Boussinesq convection in spherical shells with no-slip boundaries, and also found good agreement with the theory of Julien et al. (2012) for various Ra at $Ta \geq 10^{10}$.

Here, when we run simulations at fixed Ro_p , the value of Ta is coupled to the value of Ra , and both increase simultaneously. Recasting the scaling of Julien et al. (2012) into this perspective, we find $(Nu - 1) \propto Ra^{3/2}/Ta = Ro_p^{8/3}Ra^{1/6} \propto (Ra/Ra_{crit})^{1/6}$, where in this final result we use the

Ra_{crit} value of the whole Ro_p path, such as those specified in Table 3.1. This $\text{Ra}^{1/6}$ scaling is much weaker than the $\text{Ra}^{2/7}$ law we find here. We leave it to future work to explain this discrepancy between Boussinesq theory and our observed Nu vs. Ra scaling.

In this work, we experimentally arrived at the $\text{Ra}/\text{Ta}^{3/4} = \text{Ra}\text{Ek}^{3/2}$ scaling in Ro_p , but this relationship was independently discovered by King et al. (2012). Arguing that the thermal boundary layers should scale as $\delta_S \propto \text{Ra}^{-1/3}$ and rotational Ekman boundary layers should scale as $\delta_{\text{Ro}} \propto \text{Ta}^{-1/4} = \text{Ek}^{1/2}$, they expect these boundary layers to be equal in size when $\text{Ra}/\text{Ta}^{3/4} \sim 1$. They demonstrate that when $2 \lesssim \text{Ra}/\text{Ta}^{3/4} \lesssim 20$ flows are in the transitional regime, and for $\text{Ra}/\text{Ta}^{3/4} \lesssim 2$, flows are rotationally constrained. We remind the reader that Boussinesq values of Ra and Ta are not the same as their values in our stratified domains here, as diffusivities change with depth (see subsection 3.2.2). Taking into account this change with depth, our simulations fall in King et al. (2012)'s rotationally constrained ($\text{Ro}_p = 0.6$) and near-constrained transitional regime ($\text{Ro}_p = \{0.957, 1.58\}$). The measured values of Ro in Fig. 3.1b and the observed dynamics in Fig. 3.2 agree with this interpretation.

We note briefly that the scaling $\text{Ra} \propto \text{Ta}^{3/4}$ is very similar to another theorized boundary between fully rotationally constrained convection and partially constrained convection predicted in Boussinesq theory, of $\text{Ra} \propto \text{Ta}^{4/5}$ (Julien et al., 2012; Gastine et al., 2016). This $\text{Ta}^{4/5}$ scaling also arises through arguments of geostrophic balance in the boundary layers, and is a steeper scaling than the $\text{Ta}^{3/4}$ scaling present in Ro_p . This suggests that at sufficiently low Ro_p , a suite of simulations across many orders of magnitude of Ra will not only have the same volume-averaged value of Ro (as in Fig. 3.1b), but will also maintain proper force balances within the boundary layers.

Our results suggest that by choosing the desired value of Ro_p , experimenters can select the degree of rotational constraint present in their simulations. We find that $\text{Ro} \propto \text{Ro}_p^{3.34 \pm 0.07}$, which is within 2σ of the estimate in King et al. (2013), who although defining Ro very differently from our vorticity-based definition here, find $\text{Ro} \propto \text{Ro}_p^{3.84 \pm 0.28}$. We note briefly that they claim that the value of Ro is strongly dependent upon the Prandtl number studied, and that low Ro can be achieved at high Pr without achieving a rotationally constrained flow. We studied only $\text{Pr} = 1$

here, and leave it to future work to determine if the scaling of $\text{Ro}_p \propto \text{Pr}^{-1/4}$ is the correct scaling to predict the evolved Rossby number.

Despite the added complexity of stratification and despite our using stress-free rather than no-slip boundaries, the boundary layer scaling arguments put forth in King et al. (2012) seem to hold up in our systems. This is reminiscent of what we found in AB17, in which convection in stratified domains, regardless of Mach number, produced boundary-layer dominated scaling laws of Nu that were nearly identical to the scaling laws found in Boussinesq Rayleigh-Bénard convection.

We close by noting that once Ro_p is chosen such that a convective system has the same Rossby number as an astrophysical object of choice, it is straightforward to increase the turbulent nature of simulations by increasing Ra , just as in the non-rotating case. Although all the results reported here are for a Cartesian geometry with antiparallel gravity and rotation, preliminary 3D spherical simulations suggest that Ro_p also specifies Ro in more complex geometries (Brown et al. 2019 in prep).

3.2.5 Appendix A: Table of Simulations

Information for select simulations in this work are shown in Table 3.2. The simulation at minimum (Ra , Ta) and maximum (Ra , Ta) for each of the Ro_p , Ro_c , and \mathcal{S} paths in Fig. 3.1b are shown. This information for the displayed simulations and all other simulations in this work is included as a .csv file in the supplemental materials and is published online in a Zenodo repository (Anders et al., 2019c).

Table 3.2: Table of simulation information: Input parameters and output parameters for select simulations are shown. For each of the eight paths in Fig. 3.1b, we show information for the lowest and highest (Ra , Ta) point on that path. The first six rows show information for constant Ro_p paths, the next six for constant Ro_c paths, and the last four for constant \mathcal{S} paths. We show the input Ra , Ta , and Ro_p at the top of the atmosphere, as well as their stratification-weighted values at the midplane of the atmosphere, which provide a more direct comparison to Boussinesq values (Unno et al., 1960). We also provide the input Ro_c at the top of the atmosphere, \mathcal{S} , aspect ratio (L_x/L_z), and coefficient resolution (nz, nx, ny). Each dimension of the physical grid is 3/2 the size of the coefficient grid for adequate dealiasing of quadratic nonlinear terms. Output values of Ro, Re_{\parallel} , Re_{\perp} , and Nu are also provided. This table in its entirety is published as a supplemental .csv file with this manuscript and also online in a Zenodo repository (Anders et al., 2019c).

Ra_{top}	Ta_{top}	$\text{Ro}_{p, \text{top}}$	Ra_{mid}	Ta_{mid}	$\text{Ro}_{p, \text{mid}}$	Ro_c	\mathcal{S}	L_x/L_z	(nz, nx, ny)	Ro	Re_{\parallel}	Re_{\perp}	Nu
Constant Ro_p, path III													
1.8×10^5	4.1×10^7	0.60	1.4×10^7	3.0×10^9	1.03	0.067	1.1	0.51	(256, 32, 32)	0.015	19.4	2.5	1.2
1.2×10^9	5.2×10^{12}	0.60	9.2×10^{10}	3.8×10^{14}	1.03	0.015	3.0	0.07	(2048, 64, 64)	0.026	1771	32.0	15.4
5.2×10^2	4.6×10^3	0.96	3.8×10^4	3.4×10^5	1.64	0.333	1.13	2.28	(64, 64, 64)	0.074	4.2	2.5	1.2
3.8×10^8	3.1×10^{11}	0.96	2.8×10^{10}	2.3×10^{13}	1.64	0.035	6.0	0.12	(2048, 64, 64)	0.129	3906	113	66.9
7.9×10^1	1.0×10^2	1.58	5.8×10^3	7.4×10^3	2.70	0.888	1.56	4.44	(64, 64, 64)	0.303	4.4	4.9	1.7
1.4×10^7	9.7×10^8	1.58	1.0×10^9	7.2×10^{10}	2.70	0.119	10.0	0.30	(512, 128, 128)	0.376	1257	94.9	40.1
Constant Ro_c, path II													
8.6×10^4	8.6×10^6	0.74	6.3×10^6	6.3×10^8	1.26	0.1	1.47	0.68	(128, 128, 128)	0.051	40.2	6.7	2.2
2.6×10^6	2.6×10^8	1.13	1.9×10^8	1.9×10^{10}	1.93	0.1	4.64	0.39	(256, 512, 512)	0.27	565	53.2	33.3
1.4×10^3	1.6×10^4	1.01	1.1×10^5	1.2×10^6	1.72	0.3	1.47	1.90	(64, 128, 128)	0.124	11.3	5.4	1.8
1.1×10^6	1.2×10^7	2.29	7.8×10^7	8.6×10^8	3.93	0.3	14.7	0.65	(192, 384, 384)	0.808	529	83.5	27.3
5.5×10^1	5.5×10^4	1.65	4.0×10^3	4.0×10^3	2.82	1.0	1.47	4.84	(64, 128, 128)	0.303	3.6	4.4	1.5
2.8×10^6	2.8×10^6	6.39	2.0×10^8	2.0×10^8	10.93	1.0	100	0.82	(256, 512, 512)	3.357	1099	220	46.6
Constant \mathcal{S}, path I													
1.9×10^1	1.1×10^{-1}	10.00	1.4×10^3	7.9×10	17.12	13.2	2.0	9.91	(64, 64, 64)	3.668	3.0	10.2	1.7
3.0×10^6	1.1×10^9	0.70	2.2×10^8	8.1×10^{10}	1.20	0.052	2.0	0.30	(512, 128, 128)	0.053	242	17.9	6.0
3.0×10^1	2.0×10^{-1}	10.00	2.2×10^3	1.5×10^1	17.12	12.2	3.0	9.48	(64, 64, 64)	4.418	5.0	15.5	2.1
1.3×10^7	5.6×10^9	0.80	9.7×10^8	4.2×10^{11}	1.37	0.048	3.0	0.23	(512, 128, 128)	0.08	592	33.4	13.6

3.3 Postscript and lessons learned since publication

The most unfortunate detail of this work is that it was conducted in stratified, fully compressible domains rather than in Boussinesq domains. There are so few comparison data points available in the stratified literature that it's really hard to understand where the simulations that we conducted here sit among the hundreds of simulations and experiments that have been reported in the Rayleigh-Bénard literature. However, it is interesting to note that this study has revealed an interesting quirk of convective experiments (and studies). The desire to understand the Nusselt number and how it scales has essentially led scientists who study convection to rarely consider the importance of other measures of their flows. Essentially every paper about convective parameter space reports a value for Nu, fewer papers report a value for the Reynolds number, and even fewer report a true measurement of the Rossby number. Put simply – Nu has become the measurement that we, as a community, use to tell us **everything** about convection, and it's very possible that what we really need to do is study Nu, Re, Ro, and other quantities in light of each other. Time will tell, as will follow-up work.

The results presented here have spawned many interesting follow-up conversations and studies. Preliminary results (See Fig. 3.5) from simulations by Ben Brown shows that Ro_p does a decent job of predicting the Rossby number in 3D, spherical, anelastic dynamo simulations (Brown 2020, private communication). In these simulations, the Rossby number seems to be a weak function of Ek along constant Ro_p paths, suggesting that Ro_p is **close** to the “right” parameter for conducting suites of simulations along constant Rossby number paths. However, Ro_p is not perfect, and future work should aim to determine what the “right” parameter is that would achieve a constant Ro as Ek or Ra are varied.

The results in our published work have led to some fruitful discussions with Keith Julien & Ian Grooms. We are interested in understanding how Ro varies with Ra and Ek from a theoretical perspective. Or, put differently, we are interested in understanding how Ro scales by applying the logic that the Rayleigh-Bénard convection community has put towards understanding how e.g., the

Nusselt number scales with Ra and Ek. I look forward to continuing discussions with them over the spring and summer.

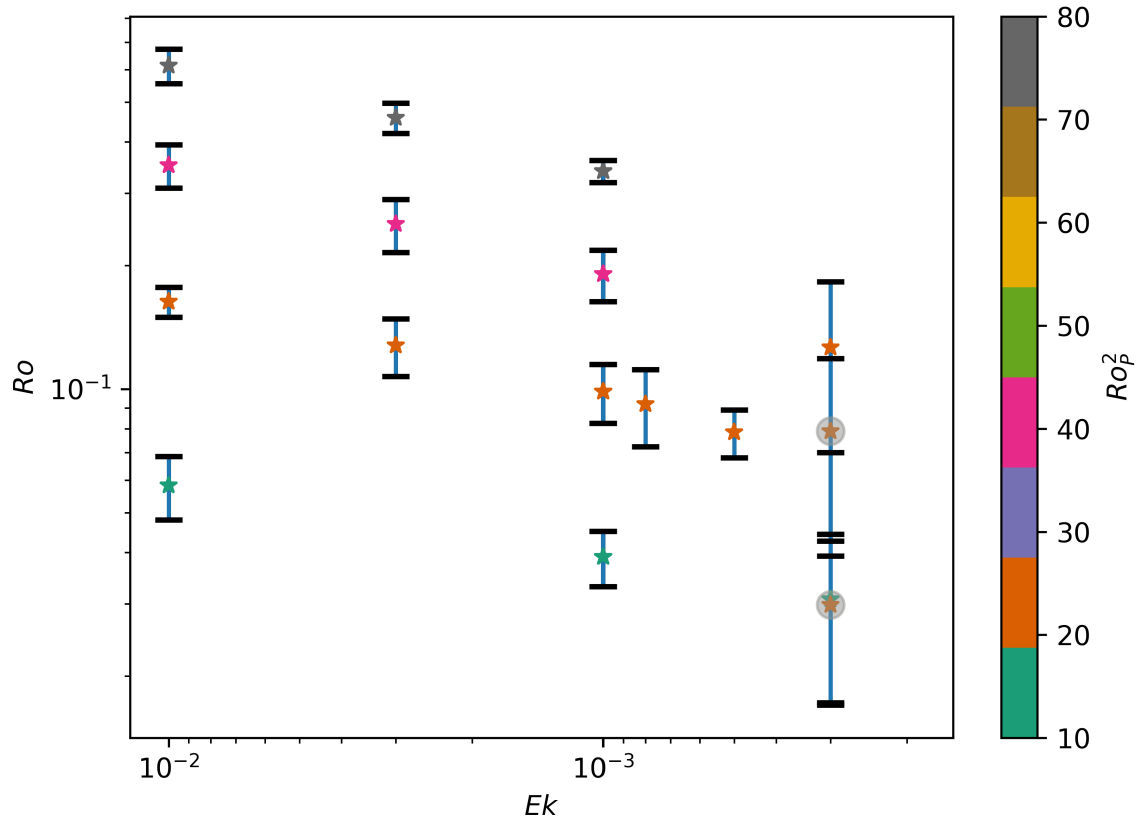


Figure 3.5: Experimental measurements of the evolved simulation Rossby number as a function of decreasing Ekman number (increasing rotational forcing). Points are grouped according to their Ro_p value according to the colorbar. Simulations show a weak trend toward smaller Ro values as Ek is decreased. Simulations marked with grey circles have not yet timestepped through a full thermal diffusion time, and their results may not be accurate.

Chapter 4

Accelerated evolution of convective simulations

4.1 Preamble

The following work was published in Physical Review Fluids (Anders et al., 2018). The text in section 4.2 is the text of the paper as it was accepted for publication. Following the published work, in section 4.3, I comment on a few lessons that have been learned since we published these results.

This work was motivated by some preliminary simulation work that was being performed in internally heated, compressible atmospheres (see 7.3). In these domains, the convecting region sits above a stable layer. The evolutionary timescale of the stratification of these atmospheres was so long that it was computationally infeasible to relax them in the regime of turbulent, astrophysical convection. Initial “Accelerated Evolution” (AE) procedures were created and tested (to seemingly a great deal of success) in those internally heated simulations. Those atmospheres were, unfortunately, completely new and unstudied in the literature, and so we decided that they were not the best testing ground of these AE techniques. We decided that AE should be tested in the simplest possible simulation setup: Boussinesq, Rayleigh-Bénard convection. In this work, we develop a basic AE procedure and verify that it produces the “correct” convective state.

4.2 Published work

4.2.1 Introduction

Astrophysical convection occurs in the presence of disparate timescales. Studying realistic models of natural systems through direct numerical simulations is infeasible because of the large separation between various flow timescales and relaxation times. Stiffness in astrophysical systems can manifest in multiple ways, some of which can be handled by clever choices of numerical algorithms, and some which cannot. For example, flows in the convection zones of stars like the Sun are characteristically low Mach number (Ma) in the deep interior. Initial value problems solved using explicit timestepping methods are bound by the Courant-Friedrich-Lowy (CFL) timestep limit corresponding to the fastest motions (sound waves), resulting in timesteps which are prohibitively small for studies of the deep, low- Ma motions. These systems are numerically stiff, and the difference between the sound crossing time and the convective overturn time has made studies of low- Ma stellar convection difficult. This stiffness can be avoided using approximations such as the anelastic approximation, in which sound waves are explicitly filtered out (Brown et al., 2010; Featherstone & Hindman, 2016a). Recently, advanced numerical techniques which use fully implicit (Viallet et al., 2011, 2013, 2016) or mixed implicit-explicit (Lecoanet et al., 2014; Anders & Brown, 2017; Bordwell et al., 2018) timestepping mechanisms have made it possible to study convection in the fully compressible equations at low Mach numbers, and careful studies of deep convection which would have been impossible a decade ago are now widely accessible.

Unfortunately, astrophysical convective systems are stiff in more than one timescale. Specifically, the Peclet number (Pe), the ratio of the thermal diffusion timescale to the convective velocity timescale, is large. In a high Pe system, many convective timescales must pass before the domain thermally relaxes into a steady state in which evolution of the thermal structure of the convective region has ceased. As the timestep size of implicit methods is bound to the fastest nonlinear flows (convection), fully implicit methods cannot be used to address this form of stiffness (Viallet et al., 2011, 2013, 2016).

Resolving dynamics in atmospheres which are sufficiently thermally relaxed therefore remains a challenging problem. Solar convection is a prime example of this phenomenon, as dynamical timescales in the solar convective zone are relatively short (convection overturns every ~ 5 min at the solar surface) compared to the Sun’s thermal relaxation timescale, which is $O(10^7)$ years (Stix, 2003). In such a system, it is impossible to resolve the convective dynamics while also meaningfully evolving the thermal structure of the system using traditional timestepping techniques alone. As modern simulations aim to model natural, high-Pe convection in the high-Rayleigh-number (Ra) regime, the thermal diffusion timescale (t_κ , defined in Sec. 4.2.3) becomes intractably large compared to dynamical timescales such as the freefall time (t_{ff} , defined in Sec. 4.2.2) (Anders & Brown, 2017),

$$\frac{t_\kappa}{t_{\text{ff}}} \propto (\text{Ra})^{1/2}. \quad (4.1)$$

Furthermore, as dynamical and thermal timescales separate, simulations become more turbulent. Capturing appropriately resolved turbulent motions requires finer grid meshes and smaller timesteps. Thus, the progression of simulations into the high- Ra regime of natural convection is slowed by two simultaneous effects: timestepping through a single convective overturn time becomes more computationally expensive and the number of overturn times required for systems to thermally relax grows.

The vast difference between convective and thermal timescales has long plagued numericists studying convection, and an abundance of approaches has been employed to study thermally relaxed solutions. One popular method for accelerating the convergence of high- Ra solutions is by “bootstrapping” – the process of using the relaxed flow fields and thermal structure of a low Ra solution as initial conditions for a simulation at high Ra . This method has been used with great success (Johnston & Doering, 2009; Verzicco & Camussi, 1997), but it is not without its faults. In systems in which there are multiple stable solutions, such as a roll state and a shearing state of convection, the large-scale convective structures present in the low Ra solution imprint onto the dynamics of the new, high Ra solution. It is possible that this puts the high Ra solution

into a different stable state than it would naturally reach from an initial, hydrostatically stable configuration. Another commonly-used tactic in moderate-Ra simulations is to first solve a simple model of the system in question, and then use the solution of that model as initial conditions for full nonlinear direct numerical simulations. For example, past studies have used initial conditions from a linear eigenvalue solve (Hurlburt et al., 1984) in plane-parallel studies, or axisymmetric solutions in studies of convection in three-dimensional (3D) cylinders (Verzicco & Camussi, 1997). In other systems, particularly when convective zones are adjacent to stable regions, authors often choose initial conditions which are not in a classic, hydrostatic, conductive state. Rather, either through knowledge of low-Ra solutions (Couston et al., 2017) or broader convective theories such as Mixing Length Theory (Brandenburg et al., 2005), initial conditions can be adjusted such that the stratification within the convective domain is closer to a relaxed state than the largely unstable hydrostatic state.

Despite the numerous methods that have been used, the most straightforward way to achieve a thermally relaxed solution is to evolve a convective simulation through a thermal timescale. Some modern studies do just that (Featherstone & Hindman, 2016a). Such evolution is computationally **expensive**, and state-of-the-art simulations at the highest values of Ra can only reasonably be run for hundreds of freefall timescales (Stevens et al., 2011), much less the thousands or millions of freefall times required for thermal relaxation.

In this work, we study a method of achieving accelerated evolution of convective simulations. Our technique is similar in essence to the approach used in asymptotically reduced models of rapidly rotating convection, in which the mean temperature profile evolves separately from the fast convective dynamics (Julien et al., 1998; Sprague et al., 2006). We couple measurements of the dynamics of unstable, evolving convective simulations with knowledge about energy balances in the relaxed solution to instantaneously and self-consistently adjust the mean vertical thermodynamic profile toward its relaxed state. While a technique of this kind has been used by many studies previously (e.g., (Hurlburt et al., 1986)), the details of implementation, the convergence properties, and whether or not the thermally relaxed state achieved from accelerated evolution corresponds

to the relaxed state in standard evolution are not documented. In Sec. 4.2.2, we describe our convective simulations and numerical methods. In Sec. 4.2.3, we describe the procedure for achieving accelerated evolution. In Sec. 4.2.4, we compare accelerated evolution solutions to solutions obtained from standard evolution through a full thermal diffusion timescale. In Sec. 4.2.5, we compare the numerical cost of accelerated solutions to standard solutions. Finally, in Sec. 4.2.6, we offer concluding remarks and discuss extensions of the methods presented here.

4.2.2 Experiment

In this work we study a simple form of thermal convection: incompressible Rayleigh-Bénard convection under the Oberbeck-Boussinesq approximation, such that the fluid has a constant kinematic viscosity (ν), thermal diffusivity (κ), and coefficient of thermal expansion (α). The density of the fluid is a constant, ρ_0 , except in the buoyancy term, where it is $\rho = \rho_0(1 - \alpha T_1)$. The gravitational acceleration, $\mathbf{g} = -g\hat{\mathbf{z}}$, is constant. The equations of motion are (Spiegel & Veronis, 1960):

$$\nabla \cdot \mathbf{u} = 0, \quad (4.2)$$

$$\frac{\partial \mathbf{u}}{\partial t} + \mathbf{u} \cdot \nabla \mathbf{u} = -\frac{1}{\rho_0} \nabla P - g(1 - \alpha T_1) \hat{\mathbf{z}} + \nu \nabla^2 \mathbf{u}, \quad (4.3)$$

$$\frac{\partial T_1}{\partial t} + \mathbf{u} \cdot \nabla (T_0 + T_1) = \kappa \nabla^2 (T_0 + T_1), \quad (4.4)$$

where $\mathbf{u} = u\hat{\mathbf{x}} + v\hat{\mathbf{y}} + w\hat{\mathbf{z}}$ is the velocity, $T = T_0(z) + T_1(x, y, z, t)$ are the initial and fluctuating components of temperature, and P is the kinematic pressure. The initial temperature profile, T_0 , decreases linearly with height. We non-dimensionalize these equations such that length is in units of the layer height (L_z), temperature is in units of the initial temperature jump across the layer ($\Delta T_0 = L_z \partial_z T_0$), and velocity is in units of the freefall velocity ($v_{\text{ff}} = \sqrt{\alpha g L_z^2 \partial_z T_0}$). By these choices, one time unit is a freefall time ($t_{\text{ff}} = L_z/v_{\text{ff}}$). We introduce a reduced kinematic pressure, $\varpi \equiv (P/\rho_0 + \phi + |\mathbf{u}|^2/2)/v_{\text{ff}}^2$, where the gravitational potential, ϕ , is defined such that $\mathbf{g} = -\nabla \phi$. In non-dimensional form, and substituting $\mathbf{u} \cdot \nabla \mathbf{u} = \nabla(|\mathbf{u}|^2/2) - \mathbf{u} \times (\nabla \times \mathbf{u})$ and $\nabla^2 \mathbf{u} = -\nabla \times (\nabla \times \mathbf{u})$,

Eqs. (4.3) and (4.4) become

$$\frac{\partial \mathbf{u}}{\partial t} + \nabla \varpi - T_1 \hat{z} + \mathcal{R} \nabla \times \boldsymbol{\omega} = \mathbf{u} \times \boldsymbol{\omega}, \quad (4.5)$$

$$\frac{\partial T_1}{\partial t} - \mathcal{P} \nabla^2 T_1 + w \frac{\partial T_0}{\partial z} = -\mathbf{u} \cdot \nabla T_1, \quad (4.6)$$

where $\boldsymbol{\omega} = \nabla \times \mathbf{u}$ is the vorticity. The dimensionless control parameters \mathcal{R} and \mathcal{P} are set by the Rayleigh (Ra) and Prandtl (Pr) numbers,

$$\mathcal{R} \equiv \sqrt{\frac{\text{Pr}}{\text{Ra}}}, \quad \mathcal{P} \equiv \frac{1}{\sqrt{\text{Pr Ra}}}, \quad \text{Ra} = \frac{g\alpha L_z^4 \partial_z T_0}{\nu \kappa} = \frac{(L_z v_{\text{ff}})^2}{\nu \kappa}, \quad \text{Pr} = \frac{\nu}{\kappa}. \quad (4.7)$$

We hold $\text{Pr} = 1$ constant throughout this work, such that $\mathcal{P} = \mathcal{R}$. \mathcal{P} and \mathcal{R} are related to the inverse Reynolds and Peclet numbers of the evolved flows.

In Eqs. (4.2), (4.5), and (4.6), linear terms are grouped on the left-hand side of the equations, while nonlinear terms are found on the right-hand side. We timestep linear terms implicitly, and nonlinear terms explicitly. We utilize the Dedalus¹ pseudospectral framework (Burns et al., 2016) to evolve Eqs. (4.2), (4.5), and (4.6) forward in time using an implicit-explicit (IMEX), third-order, four-stage Runge-Kutta timestepping scheme RK443 (Ascher et al., 1997). The code used to run the simulations in this work is included in the supplemental materials as a zip file².

Variables are time-evolved on a dealiased Chebyshev (vertical) and Fourier (horizontal, periodic) domain in which the physical grid dimensions are 3/2 the size of the coefficient grid. We study two- (2D) and three-dimensional (3D) convection in which the domain is a cartesian box, whose dimensionless vertical extent is $z \in [0, 1]$, and which is horizontally periodic with an extent of $x, y \in [0, \Gamma]$, where $\Gamma = 2$ is the aspect ratio, as has been previously studied (Goluskin et al., 2014; Johnston & Doering, 2009). In 2D simulations, we set $v = \partial_y = 0$. We specify no-slip, impenetrable boundary conditions at both the top and bottom boundaries,

$$u = v = w = 0 \text{ at } z = 0, 1. \quad (4.8)$$

¹ <http://dedalus-project.org/>

² See Supplemental Material published with paper for a .zip file of the python run scripts used to perform all simulations in this work. This code was run using the Dedalus mercurial repository (<https://bitbucket.org/dedalus-project/dedalus/src/default/>) at commit node ID dab6af2abaab03c059a4e9513f6a4d98320c2f02.

The temperature is fixed at the top boundary, and the flux is fixed at the bottom boundary, such that

$$T_1 = 0 \text{ at } z = 1, \quad \frac{\partial T_1}{\partial z} = 0 \text{ at } z = 0. \quad (4.9)$$

For this choice of boundary conditions, the critical value of Ra at which the onset of convection occurs is $\text{Ra}_{\text{crit}} = 1295.78$ (Goluskin, 2016), and the supercriticality of a run is defined as $S \equiv \text{Ra}/\text{Ra}_{\text{crit}}$. Studies of convection which aim to model astrophysical systems such as stars often employ mixed thermal boundary conditions, as we do here (Hurlburt et al., 1984; Cattaneo et al., 1991; Korre et al., 2017). Our choice of the thermal boundary conditions in Eqn. (4.9) was motivated by the fact that accelerated evolution is simpler when both the thermal profile and the flux through the domain are fixed at a boundary (see Sec. 4.2.3).

The initial temperature profile is linearly unstable, $T_0(z) = 0.5 - z$. On top of this profile, we fill T_1 with random white noise whose magnitude is $10^{-6}\mathcal{P}$, and which is vertically tapered so as to match the thermal boundary conditions. This ensures that the initial perturbations are much smaller than the evolved convective temperature perturbations, even at large Ra. We filter this noise spectrum in coefficient space, such that only the lower 25% of the coefficients have power; this low-pass filter is used to avoid populating the highest wavenumbers with noise in order to improve the stability of our spectral timestepping methods.

4.2.3 The method of Accelerated Evolution

Here we describe a method of Accelerated Evolution (AE), which we use to rapidly relax the thermodynamic state of convective simulations. We compare this AE method to Standard Evolution (SE), in which we evolve the atmosphere from noise initial conditions for one thermal diffusion time, $t_\kappa = \mathcal{P}^{-1}$. Both AE and SE simulations begin with identical initial conditions, as described in Sec. 4.2.2. As Ra increases, and \mathcal{P} decreases, SE solutions become intractable, while the timeframe of convergence for an AE solution remains nearly constant in simulation freefall time units (see table 4.2 in appendix 4.2.7).

We study in depth a 2D simulation at $S = 10^5$ to demonstrate the power of AE. We compare

kinetic energy (KE, black line) and mean temperature (blue line) traces from a SE run in Fig. 4.1(a) to an AE run in Fig. 4.1(c). In Fig. 4.1(a), the time evolution of the SE simulation is shown. The KE grows exponentially from white noise during the first $\sim 25 t_{\text{ff}}$. The solution then saturates and begins to slowly relax toward the saturated isothermal profile in the interior of the domain. This slow relaxation is evident in the behavior of the blue line, which measures $\langle T \rangle - T_{\text{top}}$, where $\langle T \rangle$ is the volume-average of T , and $T_{\text{top}} = -0.5$ is the temperature at the upper boundary. The mean atmospheric temperature and kinetic energies are fully converged when $t = 4000t_{\text{ff}} = 0.35t_{\kappa}$. We show roughly the first thousand freefall time units of evolution, as well as the evolved thermodynamic state reached after a full thermal time of evolution. In Fig. 4.1(c), similar traces are shown for the corresponding AE solution at the same parameters. The same linear growth phase occurs, but shortly after the peak of convective transient we accelerate the convergence of the atmosphere through the process which we describe below. We adjust the 1D vertical profile of the atmosphere three times, as denoted by the three labeled arrows in the graph numbered 1-3. The third profile adjustment associated with arrow 3 is small enough (see appendix 4.2.8) that we assume the atmosphere is sufficiently converged, and we begin to sample the evolved convective dynamics.

The horizontally averaged profiles of the vertical conductive flux, $F_{\kappa} = \langle -\kappa \partial_z T \rangle_{x,y}$, and the vertical convective enthalpy flux, $F_E = \langle wT \rangle_{x,y}$, are the basis of the AE method. Here we use $\langle \cdot \rangle_{x,y}$ to represent a horizontal average. We measure both of these fluxes early in a simulation, retrieving profiles such as those shown in Fig. 4.1(b). As the atmosphere relaxes towards the isothermal profile specified by the upper (cold) boundary condition, excess temperature throughout the atmosphere must leave the domain. This excess thermal energy leaves through the upper boundary, as seen in Fig. 4.1(b), where the amount of flux exiting at the top of the domain is nearly 20 times larger than the flux entering the bottom of the domain. Once the atmospheric temperature profile reaches its evolved state, the flux entering the bottom boundary is equal to the flux exiting through the upper boundary. In general, this evolution is slow in SE [Fig. 4.1(a)], but AE [Fig. 4.1(c)] can rapidly advance a system whose fluxes are in a strongly disequilibrium state [Fig. 4.1(b)], into a

near-equilibrium state, as shown in Fig. 4.1(d). In this final state both boundaries conduct the same amount of flux. The converged fluxes achieved through AE are at most 5% different from the SE solution, as shown in Fig. 4.1(e). This is a very small difference considering the short timescales on which convergence is reached and the strongly disequilibrium state used to inform the AE process.

In order to adjust the temperature profile to achieve AE, we calculate the total flux, $F_{\text{tot}} = F_E + F_\kappa$, and then derive the profiles

$$f_E(z) = \frac{F_E}{F_{\text{tot}}}, \quad f_\kappa(z) = \frac{F_\kappa}{F_{\text{tot}}}, \quad (4.10)$$

which have the systematic asymmetries [Fig. 4.1(b)] removed. These profiles describe which parts of the atmosphere depend on convection to carry flux (where $f_E(z) = 1$ and $f_\kappa(z) = 0$). We presume that the early convection occupies roughly the same volume as the evolved convection, and thus that the extent of the early thermal boundary layers (where $f_\kappa(z) = 1$ and $f_E(z) = 0$) will not change significantly over the course of the atmosphere's evolution. Under this assumption, in order to reach the converged state, the flux through the atmosphere must be decreased by some amount,

$$\xi(z, t) \equiv \frac{F_B}{F_{\text{tot}}}, \quad (4.11)$$

where $F_B = \mathcal{P}$ is the amount of flux that enters the atmosphere at the bottom, fixed-flux boundary. For example, in Fig. 4.1b, $F_{\text{tot}} \approx 19\mathcal{P}$ at the upper boundary, but in the relaxed state it should just be \mathcal{P} , so $\xi \approx 1/19$ at that depth.

To reduce the conductive flux by ξ , we examine the horizontally- and time-averaged Eqs. (4.5) and (4.6) in the time-stationary state; after neglecting terms which vanish due to symmetry, these equations become

$$\frac{\partial}{\partial z} \langle \varpi \rangle_{x,y} - \langle T_1 \rangle_{x,y} \hat{z} = \langle \mathbf{u} \times \boldsymbol{\omega} \rangle_{x,y, \text{ ev}}, \quad (4.12)$$

$$\frac{\partial}{\partial z} F_{E, \text{ ev}} - \mathcal{P} \frac{\partial^2}{\partial z^2} \langle T_1 \rangle_{x,y} = 0. \quad (4.13)$$

Here, we construct $F_{E, \text{ ev}} = \xi F_E$ and $\langle \mathbf{u} \times \boldsymbol{\omega} \rangle_{x,y, \text{ ev}} = \xi \langle \mathbf{u} \times \boldsymbol{\omega} \rangle_{x,y}$. Using these profiles and Eqs. (4.12) and (4.13), we solve for $\langle \varpi \rangle_{x,y}$ and $\langle T_1 \rangle_{x,y}$. Our choice of fixing the temperature

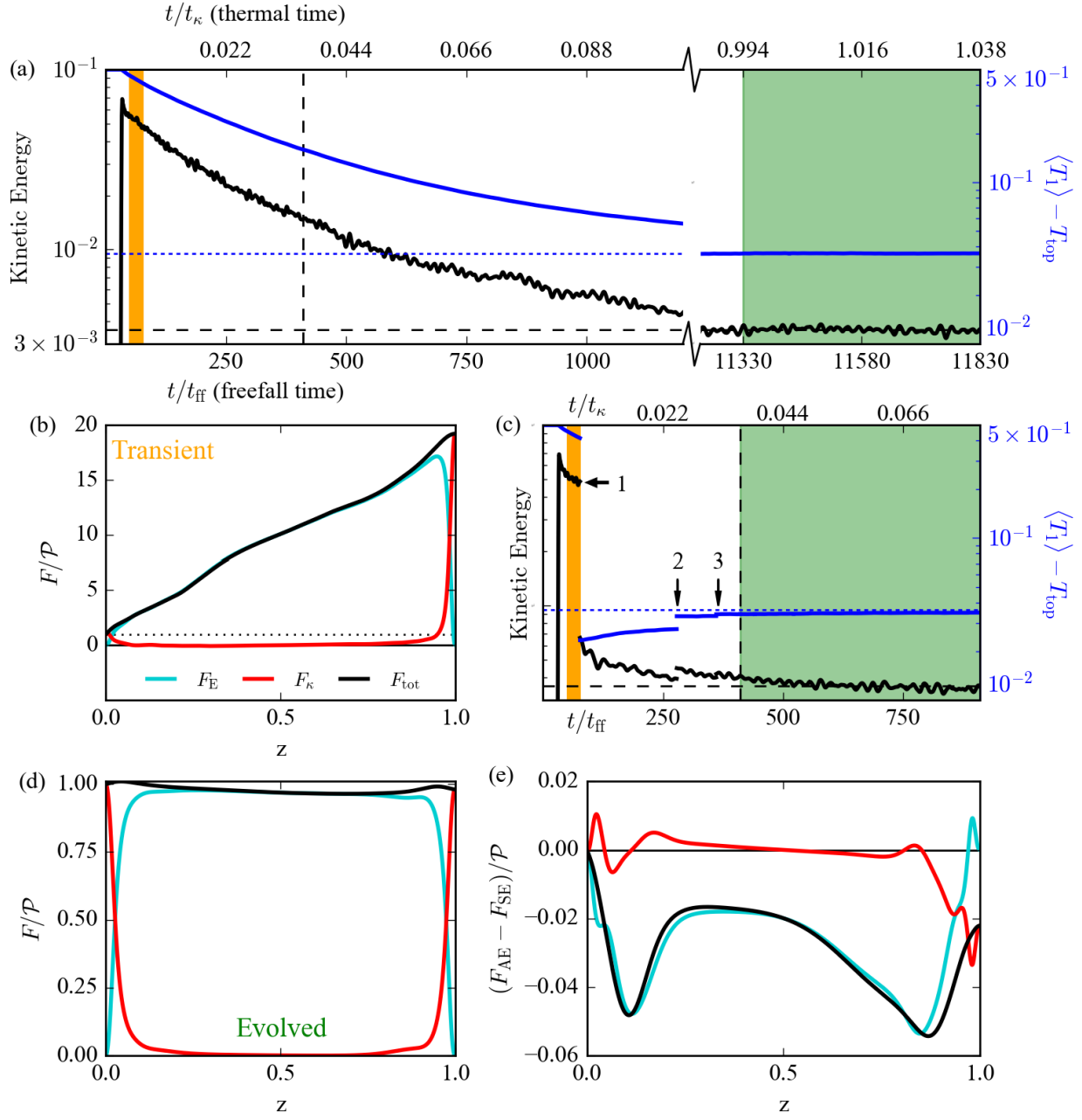


Figure 4.1: (a) Kinetic energy (black) and $\langle T \rangle - T_{\text{top}}$ (blue) vs. time are shown for a SE run at $S = 10^5$. The mean evolved values of kinetic energy and mean temperature, averaged over the time shaded in green, are denoted by the horizontal dashed lines. (b) The time- and horizontally-averaged flux profiles are shown for the times highlighted in orange in (a). (c) The same quantities as in (a) are shown, but for AE at the same parameters. The axes are scaled identically in (a) and (c), and the AE method is used three times, marked by the numbered arrows. The fluxes averaged over the green shaded region of (c) are shown in (d). The difference between the fluxes in the AE and SE solutions is shown in (e).

at the top boundary and the flux at the bottom boundary ensures that there is a unique solution for $\langle T_1 \rangle_{x,y}$ given the evolved fluxes. If flux were fixed at both boundaries, there would be infinitely many temperature solutions. If temperature were fixed at both boundaries, F_B would not be precisely known **a priori**.

Solving the above equations adjusts the mean thermal state and F_κ of the atmosphere while leaving F_E unchanged. In the bulk of the domain, convective enthalpy flux dominates transport, and so there we assume that $F_{\text{tot}} \approx F_E$. Upon removing terms which vanish due to symmetry, we note that the convective enthalpy flux is carried solely by the velocity field and perturbations in temperature away from the mean state, $F_E = \langle w(T_1 - \langle T_1 \rangle) \rangle$. In order to instantaneously decrease the convective enthalpy flux in a manner which is consistent with the conductive flux, we multiply both the velocity, \mathbf{u} , and temperature perturbations about the mean state, $T_1 - \langle T_1 \rangle_{x,y}$, by $\sqrt{\xi}$. This scaling of the velocity field is the reason that we multiply $\langle \mathbf{u} \times \boldsymbol{\omega} \rangle_{x,y}$, which is nondimensionally of order u^2/L , by ξ while constructing $\langle \mathbf{u} \times \boldsymbol{\omega} \rangle_{x,y, \text{ev}}$.

In general, the AE method occurs in the following steps. First, we pause a convective simulation and construct $\xi(z,t)$ from measured flux profiles in the convective domain. We solve a 1D boundary value problem (BVP) consisting of Eqs. (4.12) and (4.13) to obtain an evolved thermodynamic profile, and its corresponding conductive flux. We multiply both the temperature perturbations around the mean and the convective velocity flows by $\sqrt{\xi}$. After adjusting the fields of a simulation in this manner, we continue timestepping forward. For specifics on the precise implementation of the AE method, we refer the reader to appendix 4.2.8.

4.2.4 Results

We study evolved standard evolution (SE) solutions whose supercriticalities (S) are $S \in (1, 10^5]$ in 2D and $S \in (1, 10^4]$ in 3D. We compare their properties to accelerated evolution (AE) runs at $S \in (1, 10^7]$ in 2D and $S \in (1, 10^4]$ in 3D. We refer the reader to appendix 4.2.7 for a full list of simulations.

The Nusselt number (Nu) quantifies the efficiency of convective heat transport and is defined

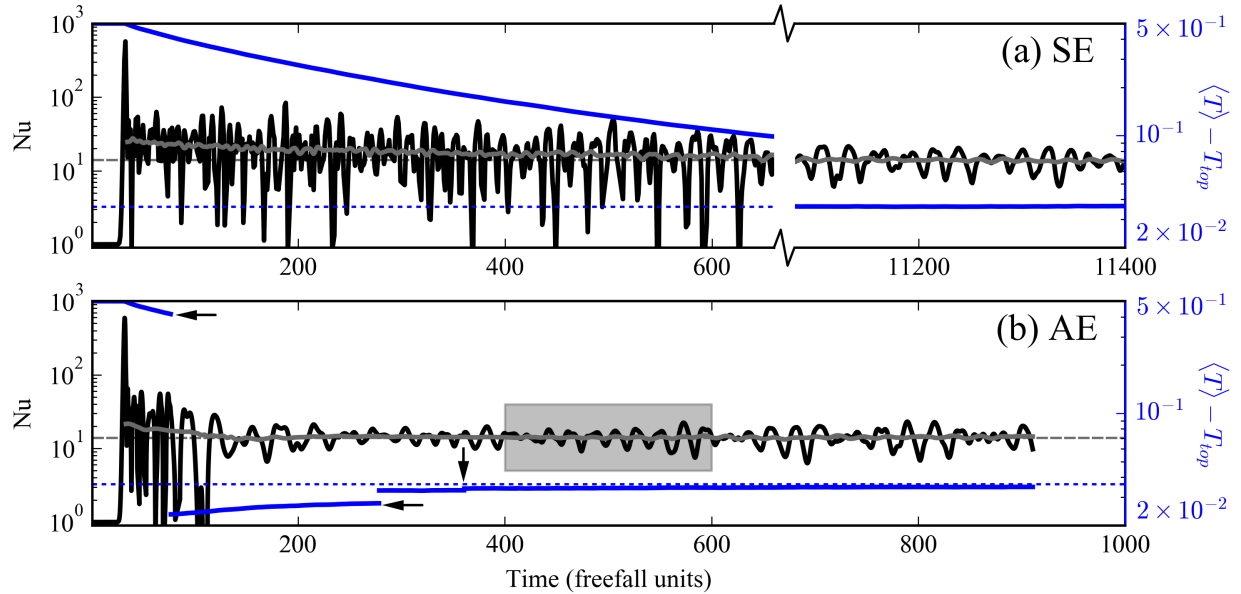


Figure 4.2: The time evolution of Nu (black) and $\langle T \rangle - T_{\text{top}}$ (blue) are shown for simulations at $S = 10^5$ in SE (a) and AE (b). A moving average of Nu , using a centered boxcar with a span of 50 freefall time units, is overplotted as a gray line. We see that the mean value of Nu reaches its relaxed value quickly compared to $\langle T \rangle$. Regardless, fluctuations of Nu about the mean value are much smaller in the thermally relaxed state. The times at which AE solves occur are denoted by arrows in (b), and the gray boxed region is examined in more detail in Fig. 4.3.

as

$$\text{Nu} = \frac{\langle F_{\text{conv}} + F_{\text{cond}} \rangle}{\langle F_{\text{cond, ref}} \rangle} = \frac{\langle wT - \mathcal{P}\partial_z T \rangle}{\langle -\mathcal{P}\partial_z T \rangle}, \quad (4.14)$$

where the volume average of a quantity, η , is shown as $\langle \eta \rangle$. The time evolution of Nu in AE and SE is compared to the mean temperature evolution in Fig. 4.2. In Fig. 4.2(a), we show the evolution of the SE run at $S = 10^5$. The black trace shows the instantaneous value of Nu , and the overplotted gray line shows a moving time average of Nu . The time average is taken using a centered boxcar window whose width is 50 t_{ff} . The mean value of Nu evolves towards its relaxed value (dashed horizontal gray line) rapidly compared to $\langle T \rangle - T_{\text{top}}$ (blue), which approaches its evolved state (dashed horizontal blue line) slowly. As such, it is possible to measure the statistically stationary mean value of Nu after only a few hundred simulated freefall times, as has been done previously (Stevens et al., 2010). However, fluctuations in Nu around the mean value at early times have both a larger magnitude and higher frequency than the fluctuations in the relaxed state. In Fig. 4.2(b),

we show the AE traces of Nu and $\langle T \rangle - T_{\text{top}}$ at $S = 10^5$. The times at which AE solves occur are marked by arrows. Nu reaches its evolved mean value slightly more rapidly than in the SE case, and the frequency and magnitude of fluctuations in Nu away from the mean resemble the final relaxed state of SE.

When $S < 10^{3.67}$ in 2D and for all runs in 3D, the evolved system is characterized by a time-stationary value of Nu , and is thus in a state of constant convective heat transport. At larger S in 2D, the value of Nu varies significantly over time even in the relaxed state (as seen in Fig. 4.2). We examine the shaded region of Fig. 4.2(b) in more detail in the top left panel of Fig. 4.3, as well as a comparable time trace at $S = 10^7$ (bottom, left panel). We find that these systems exhibit large Nu during states in which temperature fluctuations travel in their natural buoyant direction (Fig. 4.3, Ia and IIa, where cold elements fall and hot elements rise). However, when wrongly-signed temperature perturbations are entrained in an upflow or downflow with oppositely signed fluid, Nu is suppressed (Fig. 4.3, Ib and IIb, where warm fluid is pulled down by the downflow lane, and cool fluid is drawn up by the upflow lane). The plumes in these systems naturally oscillate horizontally over time, switching between transport being dominated by a counterclockwise cell, as pictured in Fig. 4.3, and a clockwise cell. Our choice of no-slip boundary conditions prevents the fluid from entering a full domain shearing state (Goluskin et al., 2014), and the oscillatory motions of the plumes are a long-lived, stable phenomenon. However, thanks to our choice of periodic boundary conditions and despite the no-slip conditions, the full system of the upflow and downflow plumes is free to slowly migrate to the left or right over time, and we observe this phenomenon in our solutions. The 2D SE simulations exhibit the same horizontally oscillatory behavior as the AE solutions for the same initial conditions. This time-dependent behavior of Nu is not seen strongly in our 3D solutions, however most 3D simulations we conducted were at low S compared to the runs in which this behavior was observed in 2D.

The time- and volume-averaged values of Nu , the RMS Peclet number (Pe), and the mean temperature are shown for AE solutions in Figs. 4.4(a)-4.4(c). Mean values are shown by the symbols (purple circles and red stars), and the vertical lines represent the standard deviation of the

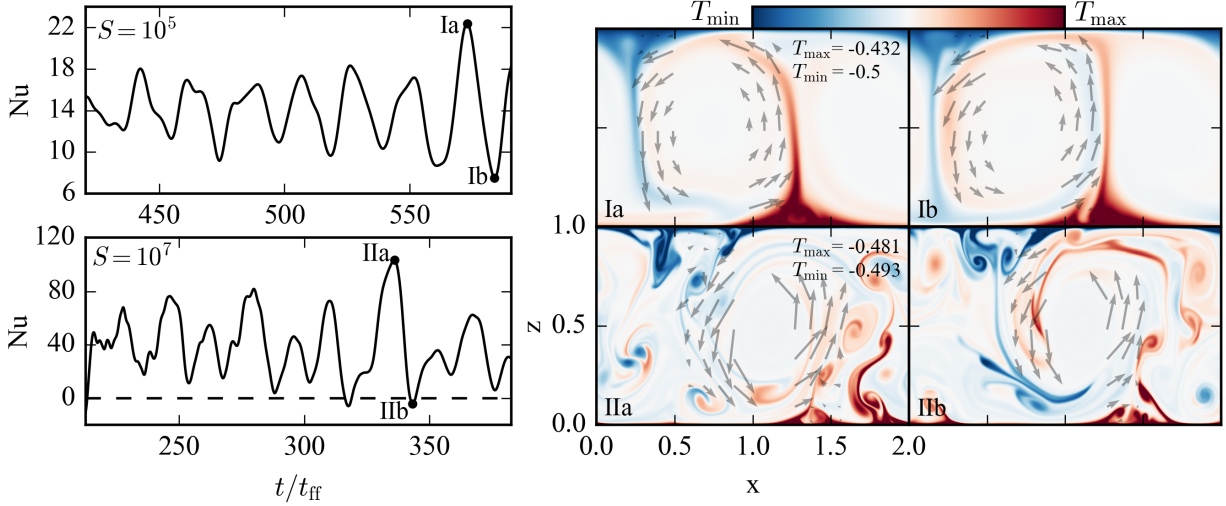


Figure 4.3: The time variation of the Nusselt number is shown for two AE cases at $S = 10^5$ (top) and $S = 10^7$ (bottom). On the left, the instantaneous value of \bar{N} is shown as a function of time. On the right, temperature snapshots are shown for \bar{N} maxima (Ia and IIa) and minima (Ib and IIb). The suppressed value of \bar{N} at the minima arises from entrainment of fluid elements whose temperature perturbations are wrongly signed (e.g., hot material going downwards and cold material going upwards in Ib and IIb). The colorbar scaling of panels Ia&b are the same, as are the scalings of panels IIa&b. The minimum temperature is chosen by the fixed-temperature boundary condition at the top, $T_{\text{top}} = -0.5$. The decreased range of the colorbar scaling for IIa&b was chosen to better display the convective dynamics.

measurement over time. \bar{N} is shown as a function of Ra and S in Fig. 4.4a, while $\text{Pe} = \langle |\mathbf{u}| \rangle / \mathcal{P}$ is shown in Fig. 4.4(b), and $\langle T \rangle - T_{\text{top}}$ (the mean temperature value minus its value at the upper, fixed temperature boundary) is shown in Fig. 4.4(c). We report $\bar{N} \propto \text{Ra}^{1/5}$, $\text{Pe} \propto \text{Ra}^{0.45}$, and $(\langle T \rangle - T_{\text{top}}) \propto \text{Ra}^{-1/5}$. The average temperature, $\langle T \rangle$, is dominated by its value in the isothermal interior, so this measurement serves as a probe of the temperature jump across the boundary layers. Thus, the inverse scaling of average temperature and \bar{N} that we find here is expected for thermally equilibrated solutions (Otero et al., 2002).

In Figs. 4.4(d)-4.4(f), we report the fractional difference between measurements in the AE and SE solutions. The mean values of \bar{N} and $\langle T \rangle - T_{\text{top}}$ measured in AE are accurate to SE values to within $\sim 1\%$. Pe measurements show marginally greater error, with AE measurements being $\leq 2\%$ different from SE measurements.

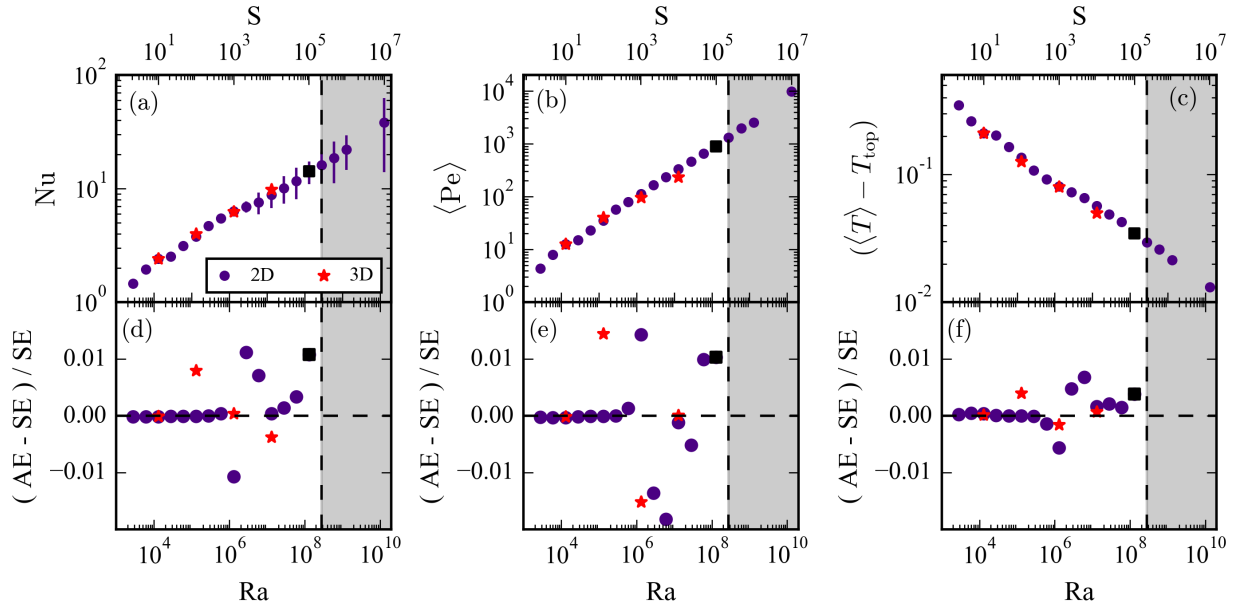


Figure 4.4: Volume- and time-averaged measurements of the Nusselt number (Nu), the RMS Peclet number ($\langle \text{Pe} \rangle$), and the mean temperature ($\langle \langle T \rangle \rangle$) for AE runs are shown in (a)-(c). Symbols are located at the mean value of each measurement and denote 2D (purple circles) and 3D (red stars). The run at $S = 10^5$ marked as a black square is examined in more detail in Figs. 4.1-4.3, 4.5, and 4.6. Vertical lines represent the standard deviation of the measurement, and quantify natural variation over the averaging window. (a) Nu scales as $\text{Ra}^{1/5}$; at high S in 2D the value of Nu fluctuates over time (see Fig. 4.3). (b) Pe , which measures turbulence in the solution, scales as $\text{Ra}^{0.45}$. (c) The difference between $\langle \langle T \rangle \rangle$ and the value of T at the fixed-temperature top boundary is shown; this quantity scales as $\text{Ra}^{-1/5}$, the inverse of Nu . Relative error for measurements of (d) Nu , (e) Pe , and (f) $\langle \langle T \rangle \rangle - T_{\text{top}}$ between AE solutions and SE solutions are shown. The greyed area of the plots indicates the region in which only AE runs were carried out due to computational expense.

For the select 3D runs conducted in this study, the scaling of Nu , Pe , and $\langle \langle T \rangle \rangle - T_{\text{top}}$ reported in Figs. 4.4(a)-4.4(c) is nearly identical to the 2D simulations. Errors between AE and SE solutions in 3D fall within the same range as errors in 2D in Figs. 4.4(d)-4.4(f). AE is therefore equally effective in both 2D and 3D, and we restrict much of our study to 2D here in order to more thoroughly sample parameter space.

The measurements presented in Fig. 4.4 demonstrate that AE can be powerfully employed in parameter space studies in which large numbers of simulations are compared in a volume-averaged sense. We now turn our examination to a more direct comparison of AE and SE for 2D convection at $S = 10^5$, the time, flux, and Nu evolution of which are shown in Figs. 4.1, 4.2, and 4.3. All comparisons that follow for these two runs occur over the times shaded in green in Figs. 4.1(a) and

4.1(c). Measurements are sampled every 0.1 freefall time units for 500 total freefall time units.

As AE is fundamentally a 1D adjustment to the thermodynamic structure of the solution, we compare the horizontally- and time-averaged temperature profiles attained by AE and SE in Fig. 4.5(a). The boundary layer width and structure are nearly identical between the two solutions, but the the mean temperature in the isothermal interior differs by roughly 0.5% [Fig. 4.5(c)].

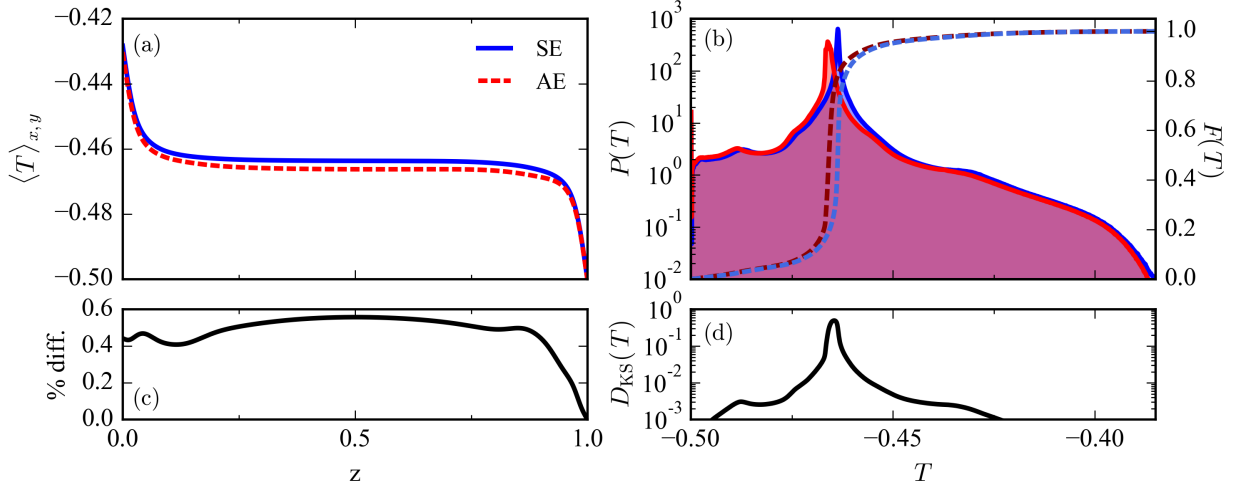


Figure 4.5: Comparisons of the evolved thermodynamic states of an AE and SE run at $S = 10^5$ are shown. (a) Evolved horizontally- and time-averaged temperature profiles, as a function of height. (b) Probability Distribution Functions (PDFs, $P(T)$) and their integrated Cumulative Distribution Functions (CDFs, $F(T)$) of point-by-point measurements of the temperature field. (c) The percentage difference between the mean temperature profiles as a function of height. The difference between the mean profiles is very small, $O(0.5\%)$. (d) $D_{KS}(T)$, as defined in Eqn. 4.15, is shown. The small difference in the mean interior temperature between AE and SE results in a large difference between the two temperature distributions near the values of the temperature maxima. The spread of temperature around the maxima, which includes the fluctuations that drive convection, are nearly identical between the two runs.

The probability distribution functions (PDFs) of point-by-point temperature measurements are compared for the two runs in Fig. 4.5(b). To construct these PDFs, we interpolate the full temperature field at each measurement time onto an evenly spaced grid, determine the frequency distribution of all T values over the duration of the 500 t_{ff} measurement window, and then normalize the distribution such that its integral is unity. The two PDFs have noticeably different maxima, as is expected from Fig. 4.5(a). Over long timescales, the 0.5% difference between the two profiles

would disappear, as the AE solution evolves to be exactly the SE solution; this is evident in the asymmetry of the AE PDF near the maxima in Fig. 4.5(b) and also the trend of the mean temperature over time in Fig. 4.1(c).

One method of comparing two PDFs to determine if they are drawn from the same underlying sample distribution is through the use of a Kolmogorov-Smirnov (D_{KS}) test (Wall & Jenkins, 2012). We calculate the D_{KS} statistic for a PDF of some value, q , as

$$D_{KS}(q) = F_{AE}(q) - F_{SE}(q), \quad (4.15)$$

where F stands for cumulative distribution function (CDF), the integral of the PDF. A traditional Kolmogorov-Smirnov statistic is just a single value, $\overline{D_{KS}(q)} = |D_{KS}(q)|_\infty = \max|D_{KS}(q)|$, and we use both the profile $KS(q)$ and $\overline{D_{KS}(q)}$ to gain insight into the likeness of two PDFs. We show $D_{KS}(T)$ in Fig. 4.5(d), and the CDFs used to construct it overlay the PDFs in Fig. 4.5(b). Near the maxima of the temperature PDFs, $\overline{D_{KS}(T)} = 0.495$, which is very large and implies that roughly half of all measurements in the AE case are at a lower T than those in the SE case. While this difference is significant, it is also expected from Fig. 4.5(a). Fortunately, $D_{KS}(T)$ is very small away from the maxima, indicating that the temperature fluctuations off of the maxima, which are the primary drivers of convective transport, are nearly identical.

In addition to adjusting the 1D thermal profile, the AE method also scales the simulation velocities and temperature fluctuations by $\sqrt{\xi}$. In Fig. 4.6 we examine the velocities and heat transport found in the evolved states. Shown are the PDFs of vertical velocity [w , Fig. 4.6(a)], horizontal velocity [u , Fig. 4.6(b)], and the nonlinear vertical convective flux [$w(T_1 - \langle T_1 \rangle_{x,y})$, Fig. 4.6(c)]. Each PDF here shows a strong peak near zero due to the no-slip, impenetrable velocity boundary conditions (Eq. (4.8)). The CDFs of each profile are overplotted, and corresponding KS profiles are shown in Figs. 4.6(d)-4.6(f). We report $\overline{D_{KS}(w)} = 0.00615$, $\overline{D_{KS}(u)} = 0.0349$, and $\overline{D_{KS}(w(T_1 - \langle T_1 \rangle_{x,y}))} = 0.0263$. The difference in vertical velocity and heat transport between AE and SE is negligible, which is unsurprising in light of the Nu measurements of Figs. 4.4(a) and 4.4(d). This also confirms that the large $\overline{D_{KS}(T)}$ in Fig. 4.5(d) is not of concern, and that the AE

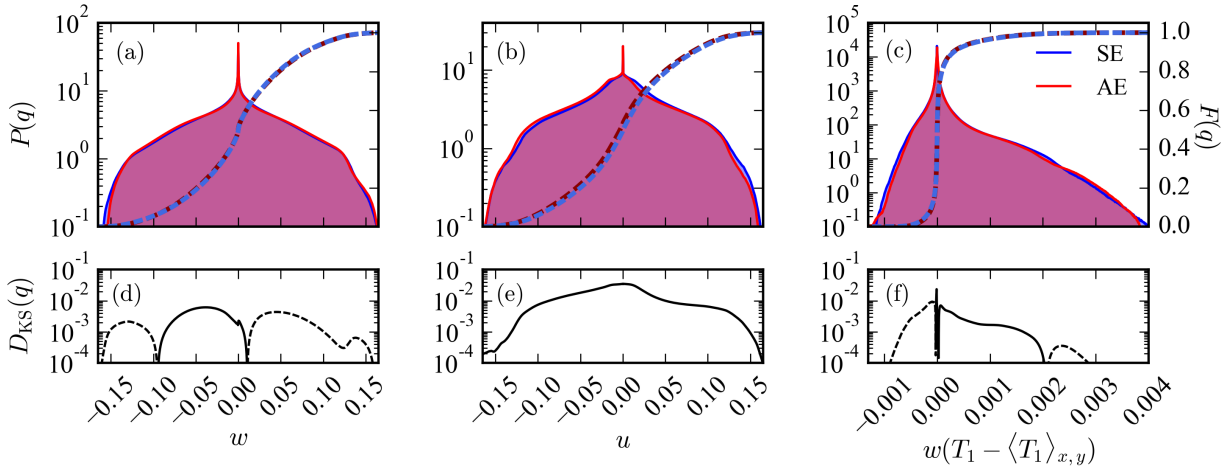


Figure 4.6: Probability distribution functions (PDFs, $P(q)$) of (a) the vertical velocity ($q = w$), (b) the horizontal velocity ($q = u$), and (c) nonlinear convective transport [$q = w(T_1 - \langle T_1 \rangle_{x,y})$] are shown for 2D runs achieved through SE (blue) and AE (red) at $S = 10^5$. The cumulative distribution function (CDF) is overplotted for each PDF. (d-f) The D_{KS} profiles, as defined in Eq. (4.15), are shown for the related distributions; solid lines indicate positive values while dashed lines are negative values. Unlike the temperature distributions in Fig. 4.5, these distributions show very good agreement and small values of the D_{KS} statistic.

run achieves the same relaxed convective solution as the SE run. We find that the difference in $D_{\text{KS}}(u)$, which consistently has more probability of flows moving left (in the $-x$ direction), appears to be caused by a more prominent migration of the full roll system in the $-x$ direction in the AE run than in the SE run. This migration does not appear to affect the vertical transport appreciably.

4.2.5 Computational Time-savings of AE

Computational time-saving is the primary reason to use AE rather than evolving all solutions through SE. In table 4.1, we compare cpu-hour cost for select 2D and 3D runs in which both AE and SE solutions were computed. Times reported for AE and SE runs only include the time required to reach a relaxed state, and do not include the time over which measurements were taken in that state (e.g., the green shaded regions of Figs. 4.1(a) and 4.1(c) are not included in the $S = 10^5$ times). All simulations were performed on Broadwell nodes on NASA’s Pleiades supercomputer (Intel Xeon E5-2680v4 processors). The key metric which highlights the usefulness of AE is the number of

cpu-hours used for the AE run divided by cpu-hours used for the SE run ($t_{\text{CPU,AE}}/t_{\text{CPU,SE}}$). We see that at low resolution and low supercriticality, $t_{\text{CPU,AE}}/t_{\text{CPU,SE}} > 1$, and AE is not useful. However, as S grows, $t_{\text{CPU,AE}}/t_{\text{CPU,SE}}$ shrinks. At the highest supercriticalities for which AE and SE were compared in this work, AE runs cost roughly an order of magnitude less computing time than SE runs.

Integrating information about the mean state in time (fluxes, etc.) decreases the rate at which our solver timesteps early in the AE cases. However, the first application of AE in a given simulation [e.g., Fig. 4.1(c), at the arrow labeled “1”] drastically increases the average timestep by fastforwarding the simulation into a more stable state with lower convective velocities. For the $S = 10^5$ case we examined in detail, the average time step grew by a factor of 2-3. At $S = 10^7$, the AE solve immediately improved the timestep size by nearly a factor of 4.

Table 4.1: Shown are details regarding the computational cost of select AE and SE runs in 2D and 3D. The supercriticality (S), coefficient resolution (nz, nx, ny), number of CPUs used to perform the calculation (N_{CPU}), number of CPU-hours used to perform the run ($t_{\text{CPU,AE/SE}}$), and ratio of CPU-hours used in the AE run compared to the SE run are provided.

S	nz \times nx \times ny	N_{CPU}	$t_{\text{CPU, SE}}$	$t_{\text{CPU, AE}}$	$t_{\text{CPU,AE}}/t_{\text{CPU,SE}}$
2D Runs					
10^2	64×128	32	2.2	4.4	2.0
10^3	128×256	64	53	21	0.39
10^4	256×512	128	1.2×10^3	1.8×10^2	0.15
10^5	512×1024	256	2.4×10^4	2.8×10^3	0.12
3D Runs					
10^1	$32 \times 64 \times 64$	512	62	1.1×10^2	1.7
10^2	$64 \times 128 \times 128$	512	1.9×10^2	1.1×10^2	0.60
10^3	$128 \times 256 \times 256$	2048	7.0×10^3	1.4×10^3	0.20
10^4	$256 \times 512 \times 512$	8192	3.3×10^5	2.3×10^4	0.070

4.2.6 Discussion & Conclusions

In this work we have studied a method of Accelerated Evolution (AE) which can be employed to achieve rapid thermal relaxation of convective simulations. We compared this technique to the Standard Evolution (SE) of convection through a full thermal diffusion timescale, and we showed that AE rapidly obtains solutions whose dynamics are statistically similar to SE solutions. The AE method is valid at low values of S , where SE solutions converge quickly due to the short thermal timescale, and AE remains applicable at high values of S , where SE solutions are intractable. As discussed, AE is equally applicable in 2D and 3D; here we have restricted most of our study to 2D to extend our parameter space coverage. At the largest values of S in which AE and SE are compared in this work, we find time savings of nearly an order of magnitude.

Here we studied the simplest possible case for the application of AE: Rayleigh-Bénard convection at low aspect ratio with mixed thermal boundary conditions. We anticipate that this technique will be powerful in its extensions to more complicated studies. To achieve AE in more complicated systems, one need only derive the steady-state, horizontally-averaged equations governing the convective dynamics [e.g., the analogs to Eqs. (4.12) and (4.13)] and couple those equations with knowledge of the boundary conditions and current dynamics as described in Sec. 4.2.3 and appendix 4.2.8. In general, AE should be useful in studies where there are two disparate timescales which must both be resolved and which cannot be overcome through clever timestepping techniques. Some avenues in which extensions of AE could be beneficial for expanding the available parameter space of exploration include studies of internally heated convection (Goluskin, 2016), convection with height-dependent conductivities (Käpylä et al., 2017), penetrative convection (Hurlburt et al., 1986; Brandenburg et al., 2005; Couston et al., 2017), or fully compressible, stratified convection (Anders & Brown, 2017). As AE is fundamentally a horizontally uniform adjustment to the thermodynamic structure of the convective domain, it is unlikely that these techniques should be applied straightforwardly to nonperiodic convective domains.

We conclude by noting that AE should be extended to these more complicated studies with

caution. While AE was extremely effective in this simple case studied here (where the aspect ratio was low, the bounds of the convective domain were pre-defined, and the solutions were simple rolls), this may not be the case for more complicated systems. For example, at higher aspect ratios, multiple stable solution branches may exist, and there is no guarantee that AE and SE will arrive at the same solution. Some assumptions which inform the AE solution, such as the assumption that the convection initially occupies the same space as the evolved convection, may not hold in studies of penetrative convection, despite the fact that similar methods have long been used in those studies (Hurlburt et al., 1986). Extensions to fully compressible convection in which there are two true thermodynamic variables (Anders & Brown, 2017) must contain a very careful treatment of AE pressure adjustments, so as to avoid wave-launching pressure mismatches. Our work here serves as a basis for determining if AE techniques are effective in more complex studies of convection.

4.2.7 Appendix A: Table of Runs

In Table 4.2 we list key properties of all simulations conducted in this work.

4.2.8 Appendix B: Accelerated Evolution Recipe

In order to achieve Accelerated Evolution (AE), we pause the Direct Numerical Simulation (DNS) which is evolving the dynamics of convection and solve a 1D Boundary Value Problem (BVP) consisting of Eqns. (4.12) & (4.13). After solving this BVP, we appropriately adjust the fields being evolved in the DNS towards their evolved state, and then we continue running the now-evolved DNS. The specific steps taken in completing the AE method are as follows:

- (1) Wait some time, $t_{\text{transient}}$, before beginning the AE process.
- (2) During the DNS, calculate time averages of the 1D vertical profiles of F_E , F_{tot} , and $\langle \mathbf{u} \times \boldsymbol{\omega} \rangle_{x,y}$, updating them every timestep. To calculate these averages, we use a trapezoidal-rule integration in time, and then divide by the total time elapsed over which the average is taken.

Table 4.2: Simulation parameters. We report the supercriticality (S), Rayleigh number (Ra), and coefficient resolution (nz, nx, and ny are the number of coefficients in the z, x, and y directions respectively). Simulation run times required to reach convergence are reported for the SE solutions (t_{SE}) and the AE solutions (t_{AE}). The amount of time over which simulations measurements were taken in the evolved state is listed (t_{avg}). All times are in freefall time units. The volume-averaged Nusselt number (Nu) of the AE and SE solutions are shown. In the upper part of the table, information pertaining to 2D runs is reported, while information pertaining to 3D runs is in the lower part of the table.

S	Ra	nz \times nx \times ny	t_{SE}	t_{AE}	t_{avg}	Nu _{SE}	Nu _{AE}
2D Runs							
$10^{1/3}$	2.79×10^3	32 \times 64	52.8	340	100	1.46	1.46
$10^{2/3}$	6.01×10^3	32 \times 64	77.6	282	100	1.95	1.95
10^1	1.30×10^4	32 \times 64	114	265	100	2.43	2.42
$10^{1+1/3}$	2.79×10^4	32 \times 64	167	251	100	2.54	2.54
$10^{1+2/3}$	6.01×10^4	32 \times 64	245	245	100	3.14	3.14
10^2	1.30×10^5	64 \times 128	360	326	100	3.8	3.8
$10^{2+1/3}$	2.79×10^5	64 \times 128	528	248	100	4.71	4.71
$10^{2+2/3}$	6.01×10^5	64 \times 128	776	251	100	5.5	5.5
10^3	1.30×10^6	128 \times 256	1.14×10^3	268	200	6.4	6.33
$10^{3+1/3}$	2.79×10^6	128 \times 256	1.67×10^3	247	500	6.87	6.95
$10^{3+2/3}$	6.01×10^6	256 \times 512	2.45×10^3	275	500	7.54	7.59
10^4	1.30×10^7	256 \times 512	3.60×10^3	301	500	8.83	8.83
$10^{4+1/3}$	2.79×10^7	256 \times 512	5.28×10^3	317	500	10.13	10.14
$10^{4+2/3}$	6.01×10^7	256 \times 512	7.76×10^3	326	500	11.65	11.69
10^5	1.30×10^8	512 \times 1024	1.14×10^4	411	500	14.02	14.18
$10^{5+1/3}$	2.79×10^8	512 \times 1024	1.67×10^4	391	500	—	16.21
$10^{5+2/3}$	6.01×10^8	512 \times 1024	2.45×10^4	453	500	—	18.58
10^6	1.30×10^9	1024 \times 2048	3.60×10^4	436	500	—	22.13
10^7	1.30×10^{10}	2048 \times 4096	1.14×10^5	183	170	—	38.29
3D Runs							
10^1	1.30×10^4	32 \times 64 \times 64	114	261	100	2.42	2.42
10^2	1.30×10^5	64 \times 128 \times 128	360	249	100	3.97	4
10^3	1.30×10^6	128 \times 256 \times 256	1.14×10^3	243	500	6.27	6.27
10^4	1.30×10^7	256 \times 512 \times 512	3.60×10^3	244	500	9.92	9.88

- (3) Pause the DNS once the averages are sufficiently converged. To ensure that an average is converged, at least some time t_{\min} must have passed since the average was started to ensure that the full range of convective dynamics are probed, and the profiles must change by no more than $P\%$ on a given timestep.
- (4) Construct ξ , $F_{E, \text{ev}}$, and $\langle \mathbf{u} \times \boldsymbol{\omega} \rangle_{x,y, \text{ev}}$, as specified in Sec. 4.2.3 from the averaged profiles.
- (5) Solve the BVP for $\langle T_1 \rangle_{x,y}$ and $\langle \varpi \rangle_{x,y}$ of the evolved state. Set the horizontal average of the current DNS thermodynamic fields equal to the results of the BVP.
- (6) Multiply the velocity field, $\mathbf{u} = u\hat{x} + v\hat{y} + w\hat{z}$, and the temperature fluctuations, $T - \langle T \rangle_{x,y}$, by $\sqrt{\xi}$ in the DNS to properly reduce the convective flux.
- (7) Continue running the DNS.

We refer to this process as an “AE BVP solve.”

While the use of a single AE BVP solve rapidly advances the convecting state to one that is closer to the relaxed state, we find that repeating this method multiple times is the best way to ensure that the AE solution is truly converged. For all runs in 2D at $S < 10^5$, we set $t_{\text{transient}} = 50$, completed an AE BVP solve with $t_{\min} = 30$ and $P = 0.1$, and then repeated the procedure. For all 3D runs and 2D runs with $S \in [10^5, 10^6]$, we did a first AE BVP solve with $t_{\text{transient}} = 20$, $t_{\min} = 20$, and $P = 1$ in order to quickly reach a near-converged state and vastly increase our timestep size. After this first solve, we completed two AE BVP solves, with $t_{\text{transient}} = 30$, $t_{\min} = 30$, and $P = 0.1$ to get very close to the solution (as in Fig. 4.1c). At very high $S = 10^7$, we ran two AE BVP solves with $t_{\min} = 20$ and $P = 1$. For the first solve, we set $t_{\text{transient}} = 20$, and for the second we set $t_{\text{transient}} = 30$. We used fewer solves at this high value of S in part to reduce the computational expense of the run, and in part because a third BVP generally did not greatly alter the solution (as in Fig. 4.1c, arrow 3). We wait 50 freefall times after the final AE BVP solve of each run before beginning to take measurements.

In general, to use AE, a threshold, f , should be chosen. When the fractional change of

the mean temperature profile from an AE BVP solve becomes less than f , the solution can be considered converged on its chosen solution branch. In other words, once

$$\frac{|\langle T \rangle_{\text{DNS}} - \langle T \rangle_{\text{AE}}|}{|\langle T \rangle_{\text{DNS}}|} < f, \quad (4.16)$$

the solution is converged. In this work, we chose our number of AE iterations such that $f \approx 10^{-2}$. In general, the user of AE could set f smaller, and in doing so reduce the separation between the AE and SE solutions, which can be seen in e.g., Fig. 4.5a&b. However, smaller values of f require additional AE BVP solves, and likely require smaller values of P , resulting in longer wait times while the horizontal averages are computed.

4.3 Postscript and lessons learned since publication

This work was initially motivated by studies of stratified convection which included stable regions, but we have not yet had the chance to robustly test a similar method in those more complex atmospheres. We have performed some initial work to expand AE to convection in polytropes, and the changes to the procedure that we described here can be found in Sec. 7.4.

In the years since we have published this work, we have learned a great deal more about our choice of thermal boundary conditions that we used in this work (“FT” boundaries, where we fix the flux at the bottom and the temperature at the top). This knowledge is largely synthesized in work that has been submitted for publication in Ch. 5. I would like to note two specific lessons learned that perhaps conflict with the results presented here:

- (1) The value of Nu **does not** necessarily converge quickly in simulations with FT boundary conditions. The rapid convergence in Fig. 2 actually suggests that the case we studied in this AE paper has a fairly short evolutionary timescale compared to our estimate for the timescale of thermal relaxation ($\tau_{\text{th}} \sim \sqrt{\text{Ra}}$). It is probably more accurate to say roughly $\tau_{\text{th}} \sim \sqrt{\text{Ra}/\text{Ra}_{\text{crit}}}$. We show time traces of more supercritical (e.g., flux $\text{Ra} = 10^{10.5}$) simulations in our subsequent work, and show that Nu (and most quantities) converge slowly.
- (2) The somewhat bizarre scaling laws for Nu in Fig. 4.4 arise as a result of the fact that we report the **flux** Ra ($\text{Ra}_{\partial_z T}$) rather than the **temperature** Ra ($\text{Ra}_{\Delta T}$) on the x-axis. As we will see in our future work, $\text{Ra}_{\partial_z T} \approx \text{Ra}_{\Delta T} \text{Nu}$. Here we roughly found that $\text{Nu} \propto \text{Ra}_{\partial_z T}^{1/5}$. Substituting to find a scaling law in terms of $\text{Ra}_{\Delta T}$, we find $\text{Nu} \propto \text{Ra}_{\Delta T}^{1/4}$. These scalings are plotted in Fig. 4.7, and while 1/4 is not quite the classical 2/7 law, it may be because we are in a small-Ra range of parameter space (Johnston & Doering, 2009). So: lesson learned, there can be multiple values of the Rayleigh number for a given system, and it’s important to know how the choice of Ra that you’re using changes your results.

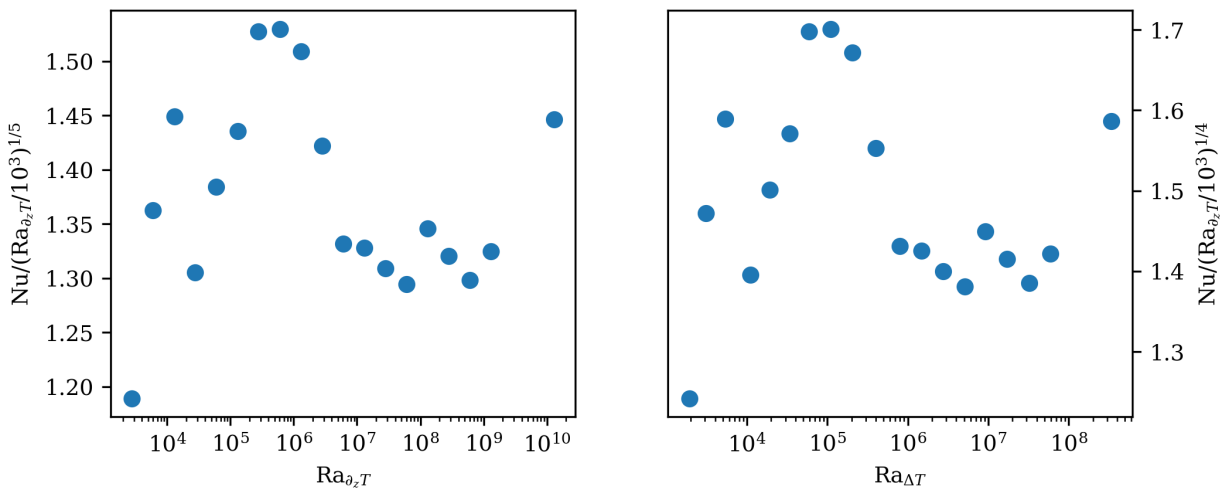


Figure 4.7: (left) Compensated scaling plot of Nu vs. the flux Ra reported in this paper, where a $\text{Ra}^{1/5}$ law is a good fit. (right) Compensated scaling plot of Nu vs. the temperature Ra, where $\text{Ra}_{\Delta T} = \text{Ra}_{\partial_z T}/\text{Nu}$, where a $\text{Ra}^{1/4}$ law is a good fit. While this is not a classical $2/7$ law, the region of parameter space here is at a fairly low supercriticality compared to most modern studies.

Chapter 5

Convective dynamics with mixed temperature boundary conditions: why thermal relaxation matters and how to accelerate it

5.1 Preamble

This manuscript in Sec. 5.2 appears as it was submitted to Physical Review Fluids on Feb. 28, 2020. It was posted to arXiv the same day, and should be available online on my arXiv page at https://arxiv.org/a/anders_e_1.html starting Tuesday, March. 3. As of the submission of this thesis to the committee, its arXiv identifier has not yet been generated.

This work was motivated tangentially by our work in Ch. 4. Over the summer of 2019, we started asking the question, “what do you get wrong if you do not allow a simulation to thermally converge?” The answer is: based on your boundary conditions, either nothing or a lot.

5.2 Submitted Manuscript

5.2.1 Introduction

Convection is a crucial heat transport mechanism in the atmospheres and interiors of stars and planets. Numerical simulations are a commonly-used tool in studies of geophysical or astrophysical convection. These studies range from examinations of convection in the simplified Boussinesq approximation Spiegel & Veronis (1960); Ahlers et al. (2009); Plumley & Julien (2019) to highly complex “dynamo simulations” which include magnetism and atmospheric density stratification Charbonneau (2014); Toomre (2019). Regardless of complexity, numerically simulated convection

is fundamentally driven by some combination of imposed boundary conditions and internal heating profiles Goluskin (2016). In studies of Boussinesq convection, the standard choice is to hold constant the temperature difference across the domain by fixing the temperature at the upper and lower boundaries. However, a common choice of thermal boundary conditions in astrophysical convection Glatzmaier & Gilman (1982); Hurlburt et al. (1986); Cattaneo et al. (1990); Featherstone & Hindman (2016a); Korre et al. (2019); Wood & Brummell (2018); Käpylä et al. (2019) is to fix the flux entering the domain through the bottom boundary and to fix the value of a thermodynamic quantity (e.g., temperature or entropy) at the top boundary. We are unaware of any study which has examined the consequences of imposing the “mixed” boundaries that are frequently favored in astrophysical convection studies.

In this work, we examine how the choice of using “mixed” boundaries affects the evolved nonlinear convective state in the simplest possible model: Rayleigh-Bénard convection (RBC) under the Boussinesq approximation. In RBC, temperature is the only thermodynamic quantity and throughout this work we will refer to the choice of fixing the flux at the bottom and temperature at the top as “FT” boundary conditions. We will refer to the common choice of fixing temperature at both boundaries as “TT” boundaries, and fixing the flux at both boundaries as “FF” boundaries¹. It is generally assumed that FT and FF boundaries should fundamentally behave similarly Goluskin (2016), and the behavior of FF boundaries is well-known Otero et al. (2002); Johnston & Doering (2009). FF and TT boundaries exhibit the same scaling of convective heat transport (quantified by the Nusselt number, Nu) as a function of increased convective driving (quantified by the Rayleigh number, Ra) Johnston & Doering (2009). It is natural to assume that FT simulations should follow the same Nu vs. Ra scaling laws as FF and TT boundary conditions. However, FT boundaries introduce complexities into the convective solution which neither FF nor TT boundaries are exposed to. First, the evolved mean temperature of a simulation with FT boundaries differs from the initial mean temperature, and therefore the thermal reservoir of the convective system must evolve (“relax”) over time Anders et al. (2018). Second, FT boundary conditions are fundamentally

¹ Note, in ref. Goluskin (2016), our TT, FF, and FT are respectively called RB1, RB2, and RB3.

asymmetric, and it is unclear if these asymmetries affect the evolved convective solution.

In this paper, we investigate the thermal relaxation of and the asymmetries in RBC with FT boundary conditions. We also compare relaxed FT solutions to TT solutions. Our results suggest that the thermal relaxation of FT systems is very long compared to TT systems, in which it is nearly instantaneous. The thermal relaxation of FT simulations is analogous to a sweep through parameter space in which dynamics are sampled over a range of values of Ra. We find that this long thermal relaxation can be bypassed by using the results of TT simulations as initial conditions for FT simulations. Finally, FT boundaries create some asymmetries in the convective flows, but these asymmetries do not meaningfully change the mean convective state compared to TT simulations.

We present these findings as follows. In subsection 5.2.2, we describe our simulation setup and numerical methods. In subsection 5.2.3, we first describe our findings with respect to the time evolution of FT systems, and then describe the asymmetries in these systems. In subsection 5.2.4, we show that these findings carry over to a more complex system (rotating Rayleigh-Bénard convection) with some interesting implications. Finally, in subsection 5.2.5, we summarize our findings and briefly describe the implications of this work for the field of astrophysical convection.

5.2.2 Simulation Details

We study incompressible RBC under a freefall nondimensionalization; for details of this nondimensionalization, we refer readers to our previous work Anders et al. (2018). In subsection 5.2.4, we study convection in the presence of vertical global rotation Julien et al. (1996), and include the Coriolis term in the momentum equation for generality. The Boussinesq equations of motion are

$$\nabla \cdot \mathbf{u} = 0 \quad (5.1)$$

$$\frac{\partial \mathbf{u}}{\partial t} + \left(\boldsymbol{\omega} + \frac{1}{\text{Ek Reff}} \hat{z} \right) \times \mathbf{u} = -\nabla \varpi + T_1 \hat{z} - \frac{1}{\text{Reff}} \nabla \times \boldsymbol{\omega}, \quad (5.2)$$

$$\frac{\partial T_1}{\partial t} + \mathbf{u} \cdot \nabla T_1 + w \frac{\partial T_0}{\partial z} = \frac{1}{\text{Peff}} \nabla^2 T_1, \quad (5.3)$$

where $\mathbf{u} = (u, v, w)$ is the velocity, $T = T_0(z) + T_1(x, y, z, t)$ is the temperature (where T_0 is the initial profile and T_1 are the fluctuations around that profile), ϖ is the reduced kinematic pressure Anders et al. (2018) which enforces the incompressibility constraint, and $\boldsymbol{\omega} = \nabla \times \mathbf{u}$ is the vorticity. The dimensionless control parameters are the Rayleigh (Ra), Prandtl (Pr), and Ekman (Ek) numbers, defined respectively as

$$\text{Ra} = \frac{g\alpha L_z^3 \Delta}{\nu\kappa} = \frac{(L_z u_{\text{ff}})^2}{\nu\kappa}, \quad \text{Pr} = \frac{\nu}{\kappa}, \quad \text{Ek} = \frac{\nu}{2\Omega L_z^2}, \quad (5.4)$$

where u_{ff} is the freefall velocity, g is the gravity, α is the coefficient of thermal expansion, L_z is the domain depth, ν and κ are respectively the viscous and thermal diffusivity, Ω is the global rotation frequency, and Δ is the nondimensional temperature scale (defined below). These parameters set the freefall Reynolds (Re_{ff}) and Péclet (Pe_{ff}) numbers,

$$\text{Re}_{\text{ff}} = \sqrt{\frac{\text{Ra}}{\text{Pr}}}, \quad \text{Pe}_{\text{ff}} = \text{Pr} \text{Re}_{\text{ff}}, \quad (5.5)$$

and throughout this work we hold $\text{Pr} = 1$ so that $\text{Re}_{\text{ff}} = \text{Pe}_{\text{ff}}$. In non rotating RBC (subsection 5.2.3), we set $\text{Ek} = \infty$.

The extent of our numerical domain vertically is $z = [-0.5, 0.5]$ and horizontally is $x, y = [-\Gamma/2, \Gamma/2]$, where Γ is the aspect ratio. The initial temperature profile, $T_0(z) = 0.5 - z$, is unstable and linearly decreases from a value of 1 to 0 across the domain. The temperature scale, Δ , is set by the temperature jump across the domain ($\Delta = \Delta T_0 = T_0(z = 0.5) - T_0(z = -0.5)$) for TT boundaries or by the temperature gradient length scale ($\Delta = L_z \partial_z T_0$) for FT boundaries. We respectively define a temperature ($\text{Ra}_{\Delta T}$) and a flux ($\text{Ra}_{\partial_z T}$) Rayleigh number for these cases,

$$\text{Ra}_{\Delta T} = \frac{g\alpha L_z^3 \Delta T_0}{\nu\kappa}, \quad \text{Ra}_{\partial_z T} = \frac{g\alpha L_z^4 \partial_z T_0}{\nu\kappa}. \quad (5.6)$$

We impose FT and TT boundary conditions respectively as

$$(\text{FT}) : \partial_z T_1 = 0 \text{ at } z = -0.5 \text{ & } T_1 = 0 \text{ at } z = 0.5; \quad (\text{TT}) : T_1 = 0 \text{ at } z = \{-0.5, 0.5\}. \quad (5.7)$$

In subsection 5.2.3, we study two-dimensional (2D) convection where $\partial_y = v = 0$. For comparison with the literature, we specify $\Gamma = 2$ and these simulations employ no-slip, impenetrable

boundaries,

$$u = w = 0 \text{ at } z = \{-0.5, 0.5\}. \quad (5.8)$$

For this choice of boundary conditions, the critical value of the Rayleigh number is $\text{Ra}_{\partial_z T} = 1296$ for FT boundaries and $\text{Ra}_{\Delta T} = 1708$ for TT boundaries Goluskin (2016). Due to this difference in onset, it is reasonable to expect important differences between FT and TT solutions at low supercriticalities. However, for the supercriticalities of $O(10^{5+})$ studied in Sec. 5.2.3, we do not expect this difference in linear stability to be very important.

The rotating cases in subsection 5.2.4 employ stress-free, impenetrable boundaries,

$$\partial_z u = \partial_z v = w = 0 \text{ at } z = \{-0.5, 0.5\}. \quad (5.9)$$

We follow previous work Stellmach et al. (2014) and study three-dimensional (3D) tall, skinny boxes with $\Gamma = 10\lambda_c(\text{Ek})$, where $\lambda_c(\text{Ek})$ is the wavelength of convective onset at the specified value of Ek . For the cases studied here at $\text{Ek} = 10^{-6}$, and for TT boundaries, $\lambda_c(10^{-6}) \approx 4.81 \times 10^{-2}$ and the critical Rayleigh number is $\text{Ra}_{\Delta T} \approx 9.2 \times 10^8$.

We utilize the Dedalus² pseudospectral framework Burns et al. (2016, 2019) to evolve Eqs. (5.1-5.3) forward in time. Our 2D simulations use an implicit-explicit (IMEX), third-order, four-stage Runge-Kutta timestepping scheme RK443; our 3D rotating simulations use the second-order, two-stage Runge-Kutta scheme RK222 Ascher et al. (1997). The code used to run simulations and to create the figures in this work are available publicly online in a repository of supplemental materials Anders et al. (2020)³. Variables are time-evolved on a dealiased Chebyshev (vertical) and Fourier (horizontal, periodic) domain in which the physical grid dimensions are 3/2 the size of the coefficient grid. We fill T_1 with random white noise whose magnitude is $10^{-6}/\text{Pe}_{\text{eff}}$, and which is vertically tapered to zero at the boundaries. We filter this noise spectrum in coefficient space, such that only the lower 25% of the coefficients have power; this low-pass filter is used to avoid populating the highest wavenumbers with noise in order to improve the stability of our spectral timestepping methods.

² <http://dedalus-project.org/>

³ Simulations were conducted using v1.0.0 of our `boussinesq_convection` github repository Anders (2020).

5.2.2.1 Nondimensional Output Quantities

Throughout this work we will measure and report the evolved value of the Nusselt number (Nu). We define and measure Nu instantaneously as

$$\text{Nu} \equiv \left\langle \frac{wT - \text{Pe}_{\text{eff}}^{-1} \partial_z T}{-\text{Pe}_{\text{eff}}^{-1} \langle \partial_z T \rangle} \right\rangle = 1 + \text{Pe}_{\text{eff}} \frac{\langle wT \rangle}{-\Delta T}, \quad (5.10)$$

where $\langle \cdot \rangle$ represent a volume average ($\langle A \rangle \equiv \iint A dx dz / \Gamma$ in 2D and $\langle A \rangle \equiv \iiint A dx dy dz / \Gamma^2$ in 3D for some quantity A), and $\Delta T = \langle \partial_z T \rangle$ is the (negative) temperature difference between the top and bottom plate. In an evolved, statistically stationary state, $\text{Nu} = 1 + \text{Pe}_{\text{eff}} \langle wT \rangle = \partial_z T|_{z=\{-0.5,0.5\}}$ when TT boundaries are employed, and $\text{Nu} = (-\Delta T)^{-1}$ when FT boundaries and a flux nondimensionalization are employed. This implies that Nu is the conversion between a temperature and flux nondimensionalization such that the equilibrated state of any convective solution is characterized by $\text{Ra}_{\Delta T}$ and $\text{Ra}_{\partial_z T}$ according to

$$\text{Ra}_{\partial_z T} = \text{Ra}_{\Delta T} \text{Nu}. \quad (5.11)$$

Throughout this work, we will also measure the evolved Péclet number (Pe) and in subsection 5.2.4 we will measure the Rossby number (Ro). These nondimensional quantities are defined as

$$\text{Pe} = \langle |\mathbf{u}| \rangle \text{Pe}_{\text{eff}}, \quad \text{Ro} = \langle |\boldsymbol{\omega}| \rangle \text{Ek} \text{Re}_{\text{eff}}, \quad (5.12)$$

where $|\mathbf{A}|$ represents the magnitude of the vector \mathbf{A} .

5.2.3 Results

5.2.3.1 Time Evolution

In Fig. 5.1, we compare the time evolution of the temperature field of an FT simulation with $\text{Ra}_{\partial_z T} = 4.83 \times 10^{10}$ to two TT simulations (with $\text{Ra}_{\Delta T} = 10^{10}$ and $\text{Ra}_{\Delta T} = 10^9$, respectively). As shown in the top four panels, we see the expected convective roll solution in both TT simulations (top row) and at early and late times in the FT simulation (bottom row). Interestingly, we find highly asymmetrical dynamics at early times in the FT simulation (bottom left), in which the

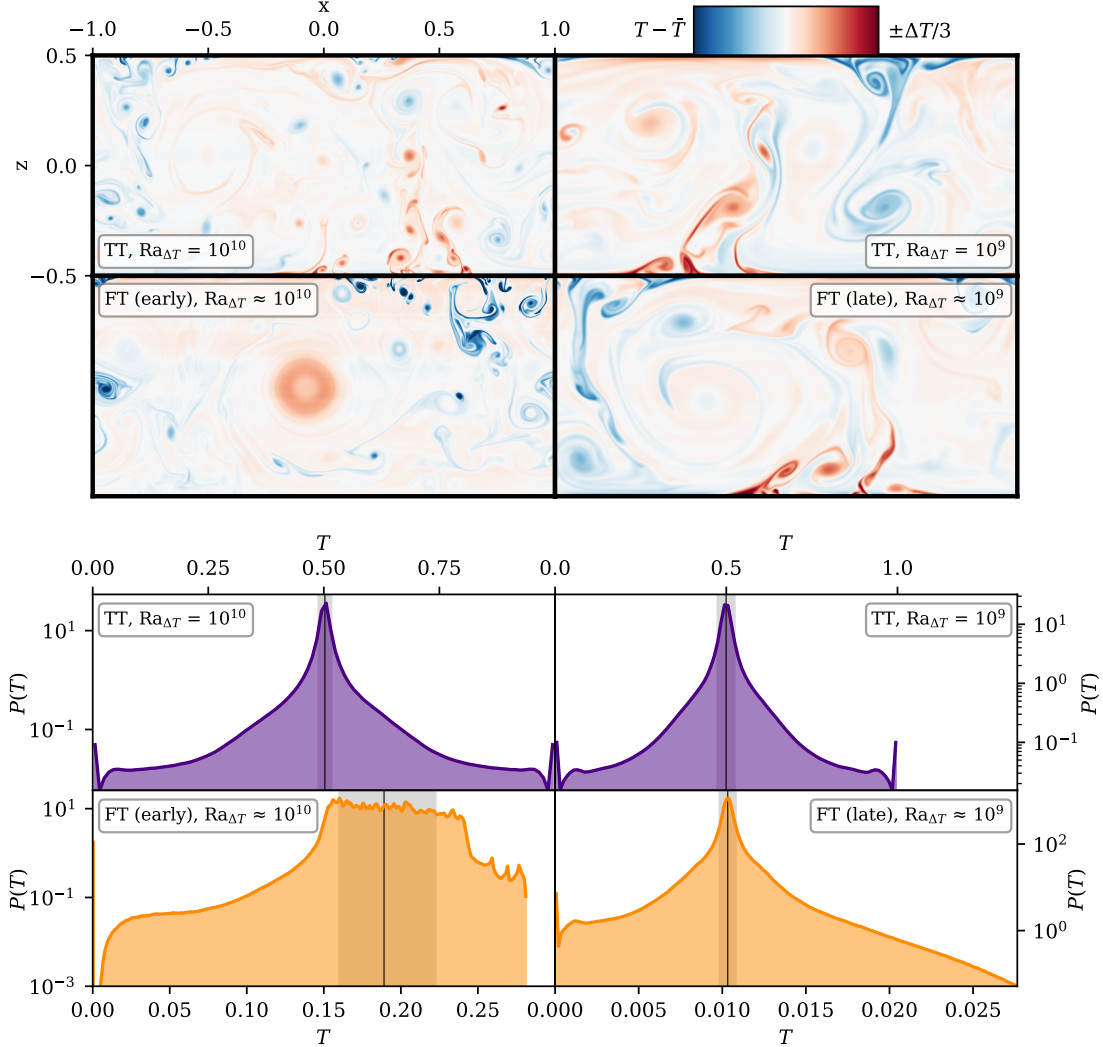


Figure 5.1: (Upper four panels) Snapshots of the temperature anomaly in two TT simulations (top row) and in an FT simulation at early and late times (bottom row). (Left two panels) Dynamics in a TT case at $\text{Ra}_{\Delta T} = 10^{10}$ and early in an FT simulation when $\text{Ra}_{\Delta T} \approx 10^{10}$. To first order, both cases have similar flow structures: a large convective cell and plumes which break apart into small turbulent eddies. However, in the FT case, the temperature anomaly of the cold plume is much larger than the hot plume, which does not appear on this color scale. (Right two panels) Dynamics in a TT case at $\text{Ra}_{\Delta T} = 10^9$ and in the relaxed state of the previously pictured FT simulation with $\text{Ra}_{\Delta T} \approx 10^9$. The relaxed FT simulation is visually indistinguishable from its comparable TT simulation.

(Bottom four panels) Probability distribution functions (PDFs) of the full temperature field in each of the four dynamical panels pictured above. PDFs sample the dynamics in each simulation once every simulation freefall time unit over the course of 500 freefall time units. The black vertical line shows the median value, and the grey outline shows the 68% confidence interval, or where the cumulative distribution function (CDF)'s value ranges from 0.16 to 0.84. (Top row) In both TT simulations, the temperature field has a mean value at $T = 0.5$ and a symmetric distribution around that peak with maxima at the fixed values of the boundaries. (Bottom left) At early times in the FT simulation, the modal value of the PDF constantly moves left (towards the cold fixed-temperature boundary). (Bottom right) At late times, the temperature PDF from the cold fixed-temperature value (on the left) to the mode is indistinguishable from the TT PDF, but from the mode to the fixed-flux boundary there is a large tail characterized by low-probability, hot elements.

temperature anomaly in the cold plume is much greater than in the warm plume. This excess cold material slowly fills the domain and mixes, reducing the temperature difference between the top and bottom plates from $\Delta T = -1$ to $\Delta T = -\text{Nu}^{-1}$ in the relaxed state. In this relaxed state, the supply of warm fluid from the bottom plume and cold fluid from the top plume come into balance, and the FT dynamics (bottom right) are indistinguishable from TT dynamics (top right).

In the bottom four panels, we examine these temperature fields statistically by displaying their probability distribution functions (PDFs). To create these PDFs, we sample the full simulation temperature field once every simulation freefall time unit over the span of 500 time units. We interpolate the (unevenly spaced) vertical Chebyshev grid points onto an evenly spaced grid before histogramming the flow values into 200 bins and creating the PDFs.

We find that this statistical analysis of the simulations tells the same story as the dynamical images shown above. The temperature field in both of the TT simulations (top row) is dominated by the modal temperature of 0.5 in the bulk; a smaller fraction of the domain is filled with equal portions of hotter/colder material (mostly contained in the plumes), and the temperature field is rigidly bounded by the fixed-temperature boundary values. The story is more complex for the FT simulation. At early times (lower left), the FT simulation is characterized by two features: an extreme tail (to the left) that characterizes the cold plume at the upper boundary, and a migrating modal temperature that shifts from the right (hotter) to the left (cooler) as cold material mixes in the interior. At late times (lower right), the FT simulation's PDF is indistinguishable from the TT PDF between the cold (left), fixed-temperature boundary and the modal value. From the modal value towards warmer temperatures, we find that the fixed-flux (lower boundary) is capable of producing more extreme temperature events and results in a more extended PDF tail. This long tail is explored further in subsection 5.2.3.4.

In the left panels of Fig. 5.2, we examine the time evolution of scalar quantities from the FT simulation shown in Fig. 5.1 (orange lines) and compare it to the TT simulation with $\text{Ra}_{\Delta T} = 10^9$ (purples lines). Simulation time is shown in nondimensional freefall units on the x-axis; the latest time displayed for each simulation, t_{final} , is subtracted for direct comparison of the relaxed states.

Traces of $\text{Ra}_{\Delta T}$ and $\text{Ra}_{\partial_z T}$ are shown in the top-left panel. In the FT simulation, $\text{Ra}_{\Delta T}$ relaxes to its final value over thousands of simulation time units, and this final value is the input value of the equivalent TT case. In comparison, $\text{Ra}_{\partial_z T}$ for the TT case instantaneously reaches its final value, which is the input value for the FT simulation. This discrepancy in evolution timescales, where TT simulations evolve quickly and FT simulations evolve slowly, is also seen in the equilibration of Nu (middle panel) and Pe (bottom panel).

The right panels of Fig. 5.2 show that the relaxation of $\text{Ra}_{\Delta T}$ in FT simulations is akin to a sweep through $\text{Ra}_{\Delta T}$ parameter space. The orange ($\text{Ra}_{\partial_z T} = 4.83 \times 10^{10}$, as on the left) and yellow ($\text{Ra}_{\partial_z T} = 2.61 \times 10^9$) lines show the evolution of FT simulations, and the arrows give the sense of time in the simulations. For comparison, we plot results from TT simulations (purple circles) and the reported results of ref. Zhu et al. (2018) (black crosses). The purple circles filled with orange and yellow circles are comparison TT simulations for the relaxed states of the FT simulations. The top-right panel is a scaling plot for Nu vs. $\text{Ra}_{\Delta T}$ compensated by the best fit reported in ref. Johnston & Doering (2009). The bottom-right panel is a scaling plot of Pe vs $\text{Ra}_{\Delta T}$ compensated by the expected scaling Ahlers et al. (2009). We find that FT simulations carry marginally more flux (higher Nu) and are more turbulent (higher Pe) than comparable TT simulations as they relax through this parameter space. These heightened values of Nu and Pe suggest that the dynamics do not immediately “forget” the higher- $\text{Ra}_{\Delta T}$ state that they recently timestepped through on their way to achieving thermal relaxation.

FT simulation dynamics evolve slowly during thermal relaxation, and these images, PDFs, and traces demonstrate the importance of waiting for thermal relaxation to be achieved when conducting an FT simulation.

5.2.3.2 Evolved Structure

In Fig. 5.3, we compare the time- and horizontally-averaged profiles of the temperature and fluxes in the evolved FT and TT cases presented in Fig. 5.2. Time averages are taken over 500 nondimensional freefall time units for the TT case and over 2000 nondimensional freefall time units for the FT case, sampled once every 0.1 time units (the difference in averaging window is explained

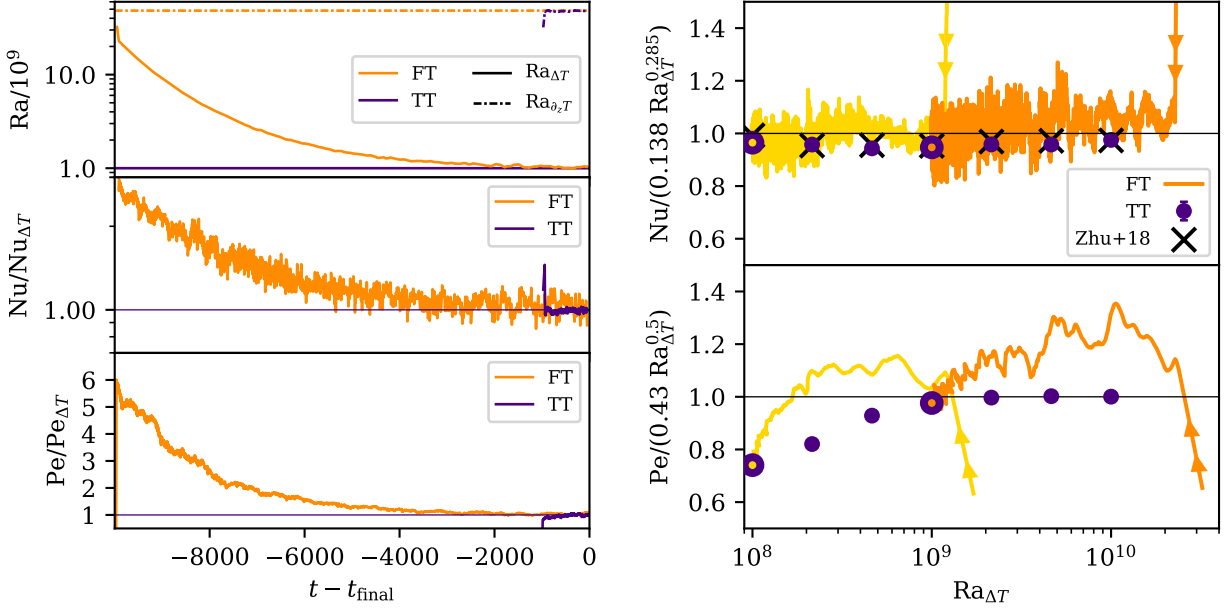


Figure 5.2: (Left three panels) Time traces of scalar quantities in an FT (orange) and TT (purple) simulation are shown. All traces have been averaged over a rolling window of 100 freefall time units to increase the clarity of the evolutionary trend. We display evolutionary traces of Ra (top, normalized by the input $\text{Ra}_{\Delta T} = 10^9$ value of the TT simulation) as well as Nu (middle) and Pe (bottom), both of which are normalized by their mean values measured over the last 500 freefall times of the TT simulation (reported in appendix 5.2.6). (Right two panels) Compensated scaling plots of Nu (upper) and Pe (lower) vs. $\text{Ra}_{\Delta T}$. Nu vs. Ra is compensated by $(0.138 \text{Ra}_{\Delta T}^{0.285})$, the best-fit reported by ref. Johnston & Doering (2009). Re vs. Ra is compensated by a $\text{Ra}_{\Delta T}^{1/2}$ law, the anticipated scaling of Pe Ahlers et al. (2009). The orange trace is the time evolution of the FT case from the left panels with the arrows showing the sense of time. The yellow trace shows the evolution of an FT case with $\text{Ra}_{\Delta T} = 10^8$. Purple circles are the measured values of Nu and Pe in our TT simulations (reported in appendix 5.2.6); error bars show the standard deviation of the sample mean and are smaller than the marker in all cases. The purple circles filled in with yellow and orange are the TT comparisons for the evolved states of the two FT cases. Black crosses show comparison TT simulations as reported by ref. Zhu et al. (2018).

in Sec. 5.2.3.3). In the three left panels, we display profiles of (top) the mean temperature, (middle) the mean temperature in upflows (solid) and downflows (dashed), and (bottom) the convective enthalpy flux ($F_{\text{enth}} = wT$, solid) and the conductive flux ($F_{\text{cond}} = -\text{Pe}_{\text{ff}}^{-1} \nabla T$, dashed). Most of the interesting structure is in the boundary layers, located between the sides of the plots and the thin vertical black lines. Zoomed in plots of the bottom and top boundary layers are respectively shown in the middle and right columns. Inset panels show the percentage difference between the

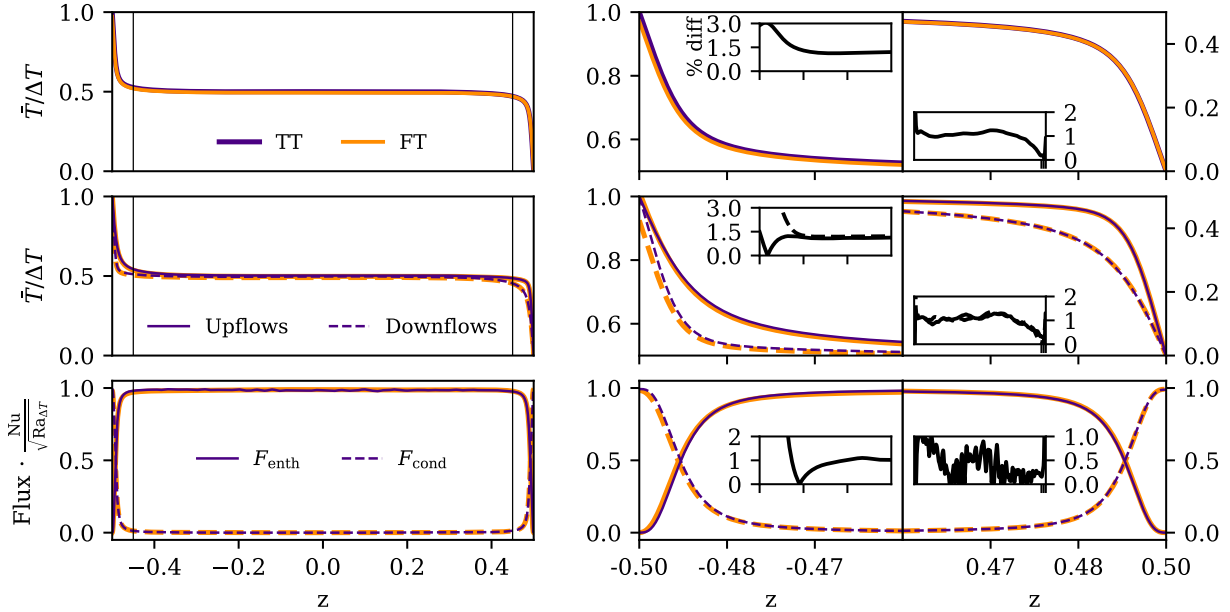


Figure 5.3: (Left three panels) We compare time- and horizontally-averaged profiles from an FT (orange) and TT (purple) simulation at $\text{Ra}_{\Delta T} = 10^9$. Shown are the (top) temperature, (middle) temperature in upflows (solid) and downflows (dashed), and (bottom) enthalpy (solid) and conductive (dashed) fluxes. The boundary layer regions are separated from the bulk by thin vertical lines and are examined in more detail in the right six panels. (Right six panels) The three panels on the left examine the bottom boundary layers and the right panels examines the top boundary layers. The insets show the % difference between the FT and TT solutions. There are slight (a few %) differences between the two cases near the bottom boundary, but otherwise the two cases are nearly the same to within $\sim 1\%$.

FT and TT solutions. In the flux panels (bottom row), we do not plot the percentage difference in the conductive flux, as this quantity is undefined in the bulk of the interior where that flux is zero. The conductive flux of the two cases agrees to within a few % in the boundary layers, and the largest deviations away from zero in the interior are $O(0.01)$ in the plotted units.

We find good ($\sim 1\%$) agreement between the FT and TT temperature profiles and enthalpy fluxes throughout the full depth of the domain, with slightly larger differences near the bottom boundary where the boundary conditions differ. When we split the temperature profile into upflows and downflows, we find that FT upflows/downflows are slightly warmer/cooler than their TT counterparts at the hot, bottom boundary. These differences are interesting, and are explored further in subsection 5.2.3.4 and Fig. 5.5, but vanish in the interior and do not likely affect the convective dynamics appreciably.

5.2.3.3 TT-to-FT: Rapidly equilibrated FT simulations

Achieving thermal relaxation in pure FT simulations is computationally costly for two reasons: (1) the turbulent dynamics at the large initial $Ra_{\Delta T}$ require more spectral modes to resolve than the equilibrated state (compare the left and right dynamics in Fig. 5.1), and (2) thousands of freefall times must pass during relaxation (see Fig. 5.2). For example, for the cases displayed in the left panels of Fig. 5.2 with a modest $Ra_{\Delta T} = 10^9$, the shown evolution of 10^4 time units of the FT simulation cost $\sim 4.5 \times 10^5$ cpu-hours, while the TT equivalent case cost only 5.6×10^4 cpu-hours – nearly an order of magnitude difference. In the previous subsections, we have shown that relaxed FT and TT simulations are very similar. It should therefore be possible to use results from a TT simulation to quickly reach the relaxed state of a comparable FT simulation, saving up to an order of magnitude in computational cost.

We now briefly describe a procedure which takes advantage of the fast evolution of TT simulations to achieve equilibrated FT simulations. In short, the evolved flow fields in the TT simulation are properly re-nondimensionalized and used as initial conditions for an FT simulation. Throughout this work, we will refer to simulations conducted this way as “TT-to-FT” simulations.

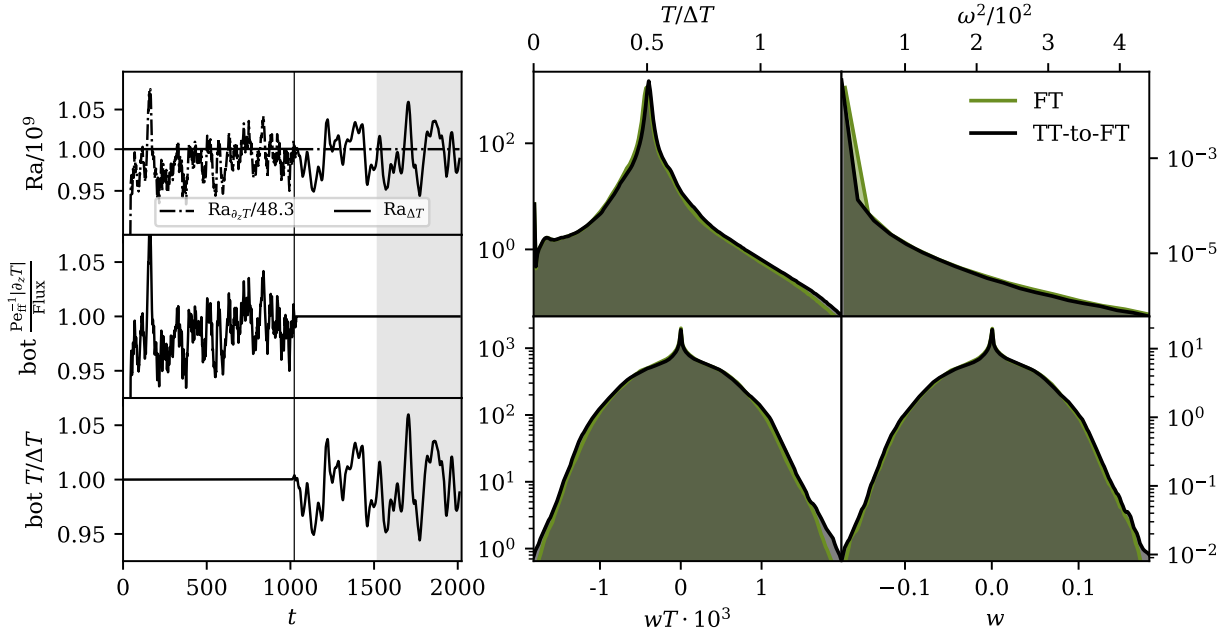


Figure 5.4: (Left three panels) Time traces of scalar quantities, which have been averaged over a rolling time window of 25 simulation time units, are shown for a simulation with $\text{Ra}_{\Delta T} = 10^9$ which starts with TT boundary conditions and then is switched to FT boundary conditions. The time of the change of boundary conditions is denoted by the vertical black line. (Top panel) The evolution of Ra is shown; $\text{Ra}_{\partial_z T}/(4.83 \times 10^{10})$ is shown as a dashed-dot line, while $\text{Ra}_{\Delta T}/10^9$ is shown as a solid line. The mean value of temperature gradient (middle panel) and temperature (bottom panel) at the bottom boundary are also shown. In the TT initial state, the temperature is held constant at a value of 1 and the temperature derivative fluctuates around a value of Nu . In the FT final state, the temperature derivative is held constant at a value of -1 and the temperature value fluctuates around a value of Nu^{-1} . (right four panels) PDFs are shown which compare the dynamics during the grey time window in the left panels (black PDFs, TT-to-FT) to dynamics from a comparable time window in the FT case from Fig. 5.2. We display the temperature field (upper left), enstrophy (upper right), nonlinear convective enthalpy flux (bottom left), and vertical velocity (bottom right).

To achieve this, we perform these steps:

- (1) Run a TT simulation to its statistically stationary state ($\sim 100+$ freefall time units). Measure Nu in that state.
- (2) Re-nondimensionalize from $\Delta = \Delta T \rightarrow \partial_z T$, and from $\text{Ra}_{\Delta T} \rightarrow \text{Ra}_{\partial_z T}$, as in Eqn. 5.11. In our freefall nondimensionalization, this means setting the velocities in the FT simulation to $\mathbf{u}_{\text{FT}} = \mathbf{u}_{\text{TT}}/\sqrt{\text{Nu}}$, and setting the temperature field to $T_{\text{FT}} = T_{\text{TT}}/\text{Nu}$.
- (3) Restart the simulation with FT boundaries and continue timestepping.

We show this procedure in practice in Fig. 5.4. In the left three panels, we display the temporal behavior of (top) Ra, (middle) the flux at the bottom boundary, and (bottom) the temperature difference between the top and bottom boundaries. We take the full evolution of the $\text{Ra}_{\Delta T} = 10^9$ TT simulation shown in Fig. 5.2, then change its boundary conditions to FT at $\text{Ra}_{\partial_z T} = 4.83 \times 10^{10}$ and restart the simulation using the above procedure. The change from TT to FT boundaries occurs at the time denoted by the thin vertical line. Unlike in the FT case displayed in Fig. 5.2, there is no thermal rundown in the FT state, due to the rapid relaxation achieved during the TT portion of the simulation.

In the right four panels of Fig. 5.4, we compare PDFs of flow fields in this TT-to-FT simulation and the comparable FT simulation which we timestepped through thermal relaxation. Shown are PDFs of the temperature field (upper left), enstrophy (upper right), convective flux (lower left), and vertical velocity (lower right). In Table 5.1, we display the first four moments of each of these distributions,

$$\begin{aligned} \mu(A) &\equiv \sum_i A_i P(A_i) \Delta A, & \sigma(A) &\equiv \sqrt{\sum_i [A_i - \mu(A)]^2 P(A_i) \Delta A}, \\ \text{Skewness}(A) &\equiv \frac{1}{\sigma(A)^3} \sum_i [A_i - \mu(A)]^3 P(A_i) \Delta A, & \text{Kurtosis}(A) &\equiv \frac{1}{\sigma(A)^4} \sum_i [A_i - \mu(A)]^4 P(A_i) \Delta A, \end{aligned} \tag{5.13}$$

where A is a flow quantity, $P(A)$ is the PDF of A , μ is the mean, σ is the standard deviation, ΔA is the spacing between the discrete PDF bins, and i is the index of the bin. The PDFs are

qualitatively similar, and there is generally good agreement between the moments of the PDFs. The remaining discrepancies between the PDFs are small and seem to primarily be due to the randomness of the flows in the time windows over which we sampled the simulations.

We note briefly that this TT-to-FT mechanism is only one of many ways of accelerating the thermal relaxation of an FT simulation. We discuss other mechanisms, and explore one in detail, in our previous work Anders et al. (2018). We note however that the TT-to-FT setup described here is likely the least complicated mechanism for achieving rapid relaxation in a simplified RBC setup that we are aware of. The successful degree with which this mechanism reproduces the evolved dynamics suggests that thermal relaxation occurs in two parts:

- (1) Changes to the simulation energy reservoir, and
- (2) Restratiﬁcation of the experiment.

The thermal energy reservoir of TT simulations does not change between the initial and final state. The rapid relaxation of TT simulations therefore suggests that experimental restratiﬁcation occurs rapidly in RBC. The long rundown of FT experiments on display in Fig. 5.2 is entirely due to the energy reservoir (the mean temperature) drifting over time. Put differently, the classic RBC setup for $T_0(z)$ is a bad choice of initial conditions for FT boundaries, and TT-to-FT simulations use TT dynamics to choose a more ideal set of initial conditions.

Changing Timescales One surprising result of our FT simulations is that the nondimen-

Table 5.1: The first four moments, as deﬁned in Eqn. 5.13, of each of the PDFs shown in Fig. 5.4 are displayed below.

Quantity	Case	μ	σ	Skewness	Kurtosis
T	FT	1.03×10^{-2}	1.49×10^{-3}	0.656	27.0
	TT-to-FT	1.05×10^{-2}	1.53×10^{-3}	0.729	26.8
ω^2	FT	16.7	10.3	96.2	2.72×10^4
	TT-to-FT	11.7	10.6	86.0	1.63×10^4
wT	FT	4.50×10^{-6}	4.87×10^{-4}	0.0133	3.06
	TT-to-FT	4.47×10^{-6}	5.08×10^{-4}	0.0110	3.06
w	FT	3.62×10^{-6}	4.70×10^{-2}	-0.0211	3.00
	TT-to-FT	4.22×10^{-6}	4.82×10^{-2}	-0.0187	3.02

sional dynamical freefall timescale is a poor description of the **evolved** freefall timescale. As noted above in our TT-to-FT procedure, the velocities in an FT simulation are smaller than the velocities in a TT simulation by a factor of $\sqrt{\text{Nu}}$. As a result, every simulation freefall time unit in a TT simulation samples a factor of $\sqrt{\text{Nu}}$ more dynamics than a nondimensional freefall time in an FT simulation. This is on display in the left panels of Fig 5.4, where the flow variations occur at a higher temporal frequency in the TT portion of the simulation than in the FT portion.

These results imply that the true nondimensional freefall time of an FT simulation is $\tau_{\text{ff}} = \sqrt{\text{Nu}}$ in simulation freefall time units. However, we note that $\text{Ra}_{\partial_z T}$ is the input value of Ra for an FT simulations, and that $\text{Ra}_{\partial_z T}/\text{Ra}_{\Delta T} = \text{Nu}$. The thermal diffusion timescale, τ_{th} , which scales like $\tau_{\text{th}} \propto \sqrt{\text{Ra}_{\text{input}}}$, is also larger in an FT simulation than in a comparable TT simulation by a factor of $\sqrt{\text{Nu}}$. One convective freefall timescale therefore occurs over the same fraction of a diffusion timescale regardless of boundary conditions or temperature nondimensionalization, $\tau_{\text{ff}}/\tau_{\text{th}} \neq f(\text{Nu})$. These findings suggest that comparing FT and TT dynamics may be more straightforward under a thermal diffusion nondimensionalization Goluskin (2016) than the freefall nondimensionalization we have used throughout this work.

5.2.3.4 Asymmetries induced by mixed boundaries

We now study in more detail the asymmetries introduced into a solution by FT boundaries. We run a TT and TT-to-FT simulation at $\text{Ra}_{\Delta T} = 10^{10}$ and $\text{Ra}_{\partial_z T} = 9.51 \times 10^{11}$, respectively. In Fig. 5.5, we examine the dynamical nature of the asymmetries which FT boundaries introduce into the simulation near the fixed-flux boundary. In the left panel, we plot PDFs of the temperature fields in comparable TT and FT simulations. These PDFs agree remarkably well near the mean and for cold temperatures (near the fixed temperature boundary), but diverge in the tail of the PDF for hot temperatures where $T/\Delta T \gtrsim 0.8$, where the boundary conditions differ. Interestingly, there are no temperature fluctuations which exceed the specified boundary values in the convective domain for TT simulations. However, the FT PDF has a much longer tail and the FT solution achieves fluid parcels which are hotter than the average bottom boundary value by more than 50%. In order to

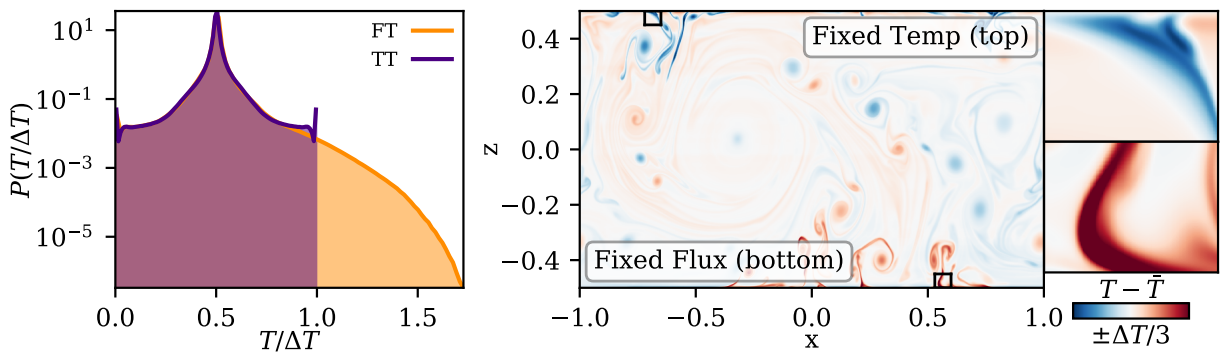


Figure 5.5: (Left panel) PDFs of temperature measurements of a TT-to-FT (orange) and TT (purple) case with $\text{Ra}_{\Delta T} = 10^{10}$ are displayed. The right tail of the distribution (near the hot fixed-flux boundary for the FT case) shows that fixed flux boundaries achieve more extreme temperature events than fixed temperature boundaries. (Middle panel) A snapshot of the temperature anomaly in the FT simulation. Zoomed in views of the regions outlined in black boxes are shown in the right two panels. Near the top (fixed temperature) boundary, the temperature anomaly at the root of the plume vanishes, but this does not happen near the bottom (fixed flux) boundary, allowing for more extreme instantaneous values.

understand how this is possible, we examine a snapshot of the FT simulation's temperature anomaly in the middle panel. We have outlined a portion of a cold plume near the upper (fixed-temperature) boundary and a portion of a hot plume near the lower (fixed-flux) boundary, and these regions are magnified in the rightmost panels. The TT upper boundary suppresses temperature anomaly at the upper boundary and regulates the temperature minima which can be achieved. The fixed-flux lower boundary does no such suppression and allows for extreme temperature values to be achieved in the plume-launching area, thus allowing for the asymmetry in the tails of the temperature PDF.

We note briefly that these asymmetries do not seem to affect mean or volume-averaged quantities in these simulations appreciably (see the agreement between FT and TT in Figs. 5.2&5.3). However, the fact that fixed-flux boundaries produce a wider temperature distribution with more extreme values may be important in some astrophysical studies. We explore this further in the discussion in subsection 5.2.5.

5.2.4 Rotating Rayleigh-Bénard Convection

We now extend our study to a more complicated experiment: 3D rotating RBC with an Ekman number of 10^{-6} . We study a TT case at $\text{Ra}_{\Delta T} = 2.75 \times 10^9$, and an FT case at $\text{Ra}_{\partial_z T} = 2.1 \times 10^{10}$ (the supercriticality of the TT case is ~ 3). These simulations employ stress free boundary conditions which allow for the generation of mean flows such as large scale vortices (LSV) Couston et al. (2019).

In the left three panels of Fig. 5.6, we compare the time evolution of the FT and TT cases. The top left panel shows the evolution of $\text{Ra}_{\partial_z T}$ and $\text{Ra}_{\Delta T}$. Even in the presence of strong rotation, the TT immediately equilibrates, but the FT case takes thousands of freefall times to achieve thermal relaxation. In the middle panel, we show the evolution of Ro; the evolved flows in both simulations exhibit rotationally constrained dynamics with $\text{Ro} \approx 0.1$, but the flows in the FT simulation relax to this state from an initially unconstrained state ($\text{Ro} \approx 1$). This implies that the thermal relaxation process can walk through the parameter space of flow balances (e.g., the balance between Inertial and Coriolis forces) in addition to the $\text{Ra}_{\Delta T}$ parameter space. In the bottom panel, we display the

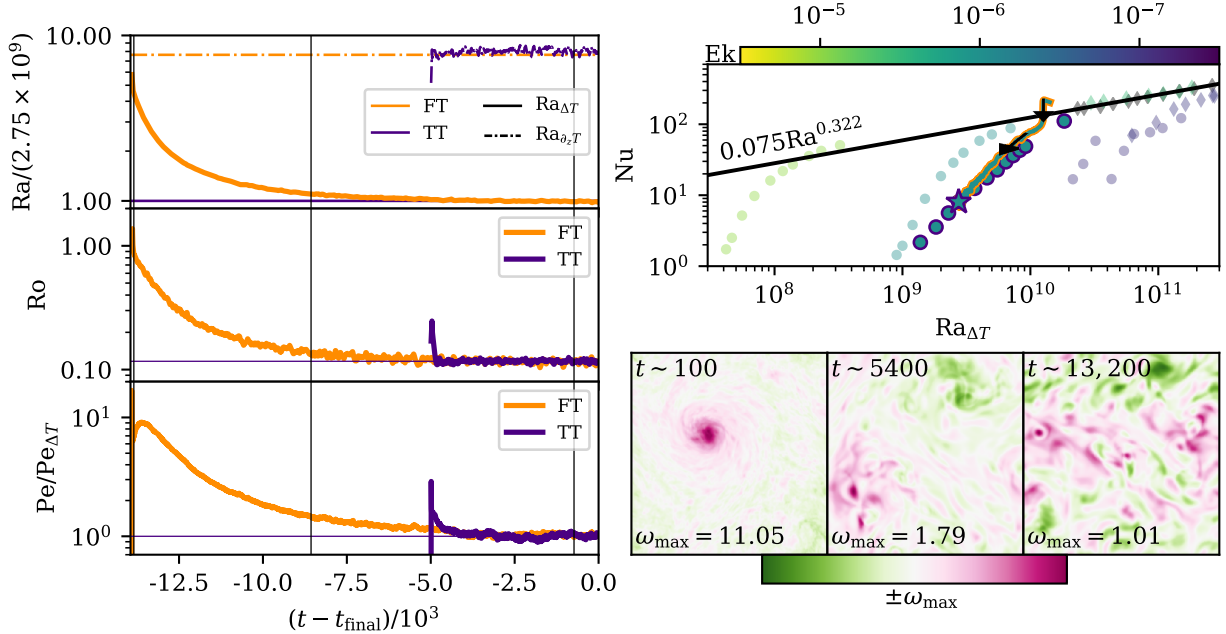


Figure 5.6: (Left three panels) Time traces of scalar quantities in an FT (orange) and TT (purple) simulation are shown. All traces have been averaged over a rolling window of 50 freefall time units to increase the clarity of the evolutionary trend. (Top panel) Ra, normalized by the input $\text{Ra}_{\Delta T} = 2.75 \times 10^9$ of the TT simulation. (Middle panel) Ro evolution of both simulation; the bulk flow of the FT simulation transitions from a marginally rotationally unconstrained state to a constrained state, while the TT simulation is always rotationally constrained. (Bottom panel) Pe evolution of the simulations is shown, normalized by the mean value measured over the last 500 freefall times of the TT simulation. (Upper right panel) Parameter space of Nu vs. $\text{Ra}_{\Delta T}$ in rotating convection. Circular and diamond data points are respectively simulations and experimental data points from Cheng et al. (2015). The color of the data points signifies the Ekman number of the points, and black points are non rotating. Data from our $\text{Ek} = 10^{-6}$ FT experiment are shown as a thick orange line with a cyan interior, where the black arrows give the direction of time. Some TT simulations are shown as purple circles with a cyan interior, and the TT case which corresponds to the relaxed state of the FT simulation is shown as a star. (Bottom right panels) Snapshots of the vertically integrated z-component of the vorticity from the FT simulation. At early times (left panel), a powerful large scale vortex with positive vorticity develops. This vortex slowly decays and becomes a vortex pair (middle panel), as seen in ref. Stellmach et al. (2014). In the converged state, we see oscillatory behavior between this vortex pair behavior and jets (right panel). The TT case exhibits the oscillatory behavior between vortex pairs and jets throughout its whole evolution. The three vertical black lines in the left panels signify the times at which these snapshots are taken.

evolution of Pe over time. Strangely, the peak value of Pe occurs a few hundred freefall times after the convective transient. After achieving this peak value, Pe monotonically decreases toward its relaxed state.

In the upper right panel of Fig. 5.6, we plot Nu vs. Ra for rotating simulations. Select TT cases are plotted as cyan circles with purple outlines (where the cyan color denotes the value of $E_k = 10^{-6}$ according to the color bar). The evolution of the FT case in the left panels is shown as a thick orange line with a cyan interior and the black arrows show the direction of time. The TT case that corresponds to the FT case is a purple star with a cyan interior. We have additionally included some literature data from numerical simulations (circles) and experiments (diamonds) as reported in the appendix tables of ref. Cheng et al. (2015). These experiments were conducted in a cylindrical geometry at a different Pr, and are not meant to be one-to-one-comparable, but are meant to guide the eye to the nature of the parameter space of rotating convection. The solid black line is the best-fit line for rotationally unconstrained simulations with $Ra \geq 10^{10}$ from ref. Cheng et al. (2015). As expected, the scaling of Nu vs. Ra is steep in the rotationally constrained regime Julien et al. (2012); Plumley & Julien (2019), which these simulations trace through. As in Fig. 5.2, the FT values of Nu are once again somewhat elevated above the comparable TT simulations.

In the bottom right three panels of Fig. 5.6, we plot the vertically integrated vertical vorticity in the simulation at three different times. In the left panel, a dominant LSV which is aligned with the global rotation dominates the simulation at early times. Over thousands of freefall times, this LSV evolves into a long-lived vortex pair, displayed in the middle panel. Finally, in the evolved state, this vortex pair solution begins to oscillate with domain-wide jets, such as those displayed in the right panel. We find that the TT solution shows this oscillatory behavior between vortex pairs and jets immediately and throughout the full 5000 freefall timescales of evolution that we simulated.

We suspect that the strange behavior of Pe in the bottom left panel can be explained by the evolution of the dominant flow structures over time. At early times, the initially large value of $Ra_{\Delta T}$ in the FT case drives the displayed dominant LSV. This powerful driving injects energy

into the LSV, causing Pe to grow. As $\text{Ra}_{\Delta T}$ and convective driving decrease over time, the LSV saturates and then starts to wind down, leading to the “bump” in the Pe trace.

We once again find it important to briefly note the difference in computational cost between the FT and TT simulations conducted here. The TT simulation shown in the left panels of Fig. 5.6 only cost 2.6×10^4 cpu-hours. By comparison, the cost of the FT simulation shown in the same panels was **two orders of magnitude larger**— 2.3×10^6 cpu-hours. The TT simulation’s coefficient resolution was 128^3 . The FT simulation’s initial resolution required to resolve the convective transient was 512×384^2 coefficients. We reduced the resolution to 256×384^2 after 100 freefall times, and then later to 128×384^2 after $\sim 3.3 \times 10^3$ freefall times. At each of these times, we found that lowering the **horizontal** coefficient resolution of the simulation did not reproduce the simulation solution with fidelity. This suggests that small scale turbulent velocity structures—which are injected by the vigorous transient and perhaps associated with the LSV—are long lived throughout the thermal evolution of the simulation.

5.2.5 Conclusions & Discussion

In short, we find that FT simulations experience a long thermal relaxation which is not experienced by TT simulations and, to first order, FT boundaries do not introduce important asymmetries into the solution.

In this paper, we have studied the time evolution of Rayleigh-Bénard convection (RBC) under two different formulations of the thermal boundary conditions: “FT” boundaries, where the flux is fixed at the bottom and temperature is fixed at the top, and “TT” boundaries, where temperature is fixed at the top and bottom. Through studying this relaxation and the relaxed states of both simulations, we come to the following conclusions:

- (1) Thermal relaxation in RBC has two components: (a) changes in the energy reservoir and (b) changes in the stratification. We find that the long relaxation of FT simulations is due to changes in the energy reservoir; this reservoir is roughly constant in TT simulations due to the lack of evolution of the average domain temperature. The rapid evolution of our TT

simulations suggests that RBC restratifies itself instantaneously.

- (2) Dynamical measurements taken during the thermal relaxation of an FT simulation may be misleading. Dynamics during the relaxation are more turbulent than in the evolved state, and exhibit evolving flow balances in the equation of motion (as quantified by e.g., the Rossby number).
- (3) The thermal relaxation process of an FT simulation performs a sweep through $\text{Ra}_{\Delta T}$ parameter space. We find that convective heat transport (the Nusselt number) and turbulent velocities (the Péclet number) are elevated above classical scaling laws along these parameter space sweeps.
- (4) Great computational expense achieving thermal relaxation in an FT simulation can be avoided by using the evolved state of a TT simulation as a “better” set of initial conditions for an FT simulation.
- (5) Despite minor asymmetries near the fixed-flux boundary, we find no meaningful difference between the mean state of FT and TT simulations.

We now describe some lessons that should be applied from this work to astrophysical convection, and comment on some open areas of research.

Throughout this work, we have made the assumption that convection is only “interesting” in its final, fully equilibrated state. In nature, convection is not always in an equilibrium state. For example, in the late stages of the lifetimes of stars, some core burning regions have sufficiently short lifetimes that they likely do not come into thermal relaxation (Clarkson et al., 2018; Andrassy et al., 2020). The use of FT boundaries or initial conditions that we have here considered to be “bad” choices may help in understanding these transient lifetime stages. However, for most convective studies where the lifetime of the natural convective system is much larger than its Kelvin-Helmholtz timescale, it is essential to study relaxed convection, and our results point towards the importance of either choosing good initial conditions (TT or TT-to-FT simulations) or running simulations to

thermal relaxation.

One question which our study of RBC is not able to address is: how long does it take for a complex convective system to restratify? Our fully convective domains restratified instantaneously, but it is likely that mixed convective-and-stably-stratified domains (Brummell et al., 2002; Käpylä et al., 2019; Pratt et al., 2017; Korre et al., 2019) should have regions that are not turbulently mixed by convection which could also have long relaxation timescales. It would be extremely helpful for future studies to examine relaxational timescales in systems where the energy reservoir is fixed, but where convection does not effectively mix the whole domain. Fortunately, clever techniques (e.g., as we explored in ref. Anders et al. (2018)) can likely be used to rapidly restratify atmospheres in such simulations.

RBC is fundamentally symmetrical, but many natural convective processes occur in density-stratified domains in which the symmetries of the problem are fundamentally broken. In the present study, we observed that flux boundaries produce more extreme thermodynamic events than temperature boundaries. In studies of overshooting convection, it is possible that plumes produced by a flux boundary layer could launch further into a stable layer than plumes produced by a temperature boundary. Some authors have aimed to quantify the nature of overshooting plumes from a convective region into a stable region Pratt et al. (2017); Korre et al. (2019), and it is unclear if different choices of boundary conditions could change the observed distribution of overshooting plumes observed there.

Some of the most complex astrophysical convection experiments aim to understand self-consistently evolving magnetic dynamos in rotating, spherical, magnetohydrodynamical domains Brown et al. (2010); Yadav et al. (2016); Strugarek et al. (2017, 2018). These dynamo simulations involve large numbers of timesteps through many freefall timescales in order to study the generation and evolution of magnetic fields and mean flows. We found in our FT rotating simulation that the unrelaxed state generated a mean flow (a LSV, Fig. 5.6) that was much more intense and large-scale than the eventual flows that developed in the relaxed state. If we had terminated our FT rotating simulation too early, we would not have seen the eventual destruction of this LSV or the

later oscillatory behavior between jets and vortex pairs. Many dynamo simulations are performed in highly turbulent regimes at the cutting-edge of what is achievable using modern computational resources. As a result, timestepping through thousands of freefall timescales is not possible in these simulations. It is therefore crucial that dynamo simulations be set up in such a manner as to avoid large changes to the system's energy reservoir such as those that we observed and studied here. Some authors who study astrophysical convection (Featherstone & Hindman, 2016a; Strugarek et al., 2018; Bordwell et al., 2018; Matilsky et al., 2019) employ FF boundary conditions, and our results here suggest that such a choice may be ideal in those complex simulations.

In conclusion, we note that our results here should provide astrophysical convection simulations with reason for optimism. Some problems that we encounter (e.g., long thermal rundown in FT simulations) can be completely avoided through a careful understanding of the numerical system being solved.

5.2.6 Appendix A: Table of Simulations

Input and output information for the simulations in this work are shown in Table 5.2. The code used to run these simulations can be found online in the repository of supplemental materials Anders et al. (2020).

Table 5.2: Input and output values from the simulations in this work are shown; all simulations have a Prandtl number of 1. Input quantities are the boundary conditions (BCs), Rayleigh number (Ra), coefficient resolution ($\text{nz} \times \text{nx} \times \text{ny}$), and the total simulation run time in freefall units $t_{\text{simulation}}$ and in cpu-hours. Output quantities are the Nusselt (Nu), Péclet (Pe), and Rossby (Ro) numbers. Reported values of Nu, Re, and Ro are the sample mean over the last 500 freefall time units. Reported uncertainties are the standard deviation of the sample mean; when the uncertainty is not reported, it is smaller than the number of reported digits. The “Nu comp” values are comparison Nu values reported in ref. Zhu et al. (2018). Resolutions marked by a * show the initial, highest resolution utilized in the simulation. The 2D FT $\text{Ra} = 4.83 \times 10^{10}$ simulation’s resolution was changed to 1024×2048 about 500 freefall time units after transient. The rotating FT case’s resolution was reduced to 256×384^2 about one hundred freefall time units after transient, and was further reduced to 128×384^2 about 3.3×10^3 freefall times after transient.

BCs	Ra	$\text{nz} \times \text{nx} \times \text{ny}$	$t_{\text{simulation}}$	cpu-hours	Nu	Nu comp	Pe	Ro
2D Runs ($\Gamma = 2$, no-slip)								
TT	1.00×10^8	512x1024	1023	5.57×10^3	25.4 ± 0.1	26.1	3.18×10^3	—
FT	2.61×10^9	1024x2048	9410	1.21×10^5	25.3 ± 0.2	26.1	3.31×10^3	—
TT-to-FT	2.61×10^9	512x1024	1000	1.88×10^3	26.1 ± 0.1	26.1	3.22×10^3	—
TT	2.15×10^8	512x1024	1023	5.73×10^3	31.3 ± 0.2	31.2	5.17×10^3	—
TT	4.64×10^8	1024x2048	1024	4.66×10^4	38.4 ± 0.3	38.9	8.60×10^3	—
TT	1.00×10^9	1024x2048	1023	5.58×10^4	48.0 ± 0.4	48.3	1.33×10^4	—
FT	4.83×10^{10}	2048x4096*	16230	5.36×10^5	48.7 ± 0.4	48.3	1.41×10^4	—
TT-to-FT	4.83×10^{10}	1024x2048	1000	1.11×10^4	48.7 ± 0.3	48.3	1.36×10^4	—
TT	2.15×10^9	1024x2048	1029	6.38×10^4	60.4 ± 0.5	61.1	1.99×10^4	—
TT	4.64×10^9	1536x3072	1024	3.29×10^5	75.2 ± 0.6	76.3	2.94×10^4	—
TT	1.00×10^{10}	2048x4096	1039	7.79×10^5	95.3 ± 0.7	95.1	4.30×10^4	—
TT-to-FT	9.51×10^{11}	2048x4096	1000	7.91×10^4	93.2 ± 0.8	95.1	4.11×10^4	—
3D Rotating Runs ($\text{Ek} = 10^{-6}$, $\Gamma = 0.481$, stress-free)								
TT	1.38×10^9	128x64 ²	2565	2.98×10^3	2.17	—	2.84×10^2	$(3.38 \pm 0.17) \times 10^{-2}$
TT	1.83×10^9	128x64 ²	2545	3.54×10^3	3.56	—	5.28×10^2	$(5.67 \pm 0.33) \times 10^{-2}$
TT	2.29×10^9	128 ³	2537	1.08×10^4	5.61	—	8.91×10^2	$(8.56 \pm 0.44) \times 10^{-2}$
TT	2.75×10^9	128 ³	5035	2.6×10^4	8.04 ± 0.01	—	1.71×10^3	$(1.17 \pm 0.06) \times 10^{-1}$
FT	2.1×10^{10}	512x384 ² *	13950	2.3×10^6	7.86 ± 0.01	—	1.76×10^3	$(1.14 \pm 0.06) \times 10^{-1}$
TT	3.67×10^9	128 ³	2532	1.55×10^4	12.5	—	3.39×10^3	$(1.74 \pm 0.08) \times 10^{-1}$
TT	4.58×10^9	128 ³	2530	1.69×10^4	17.6	—	4.77×10^3	$(2.35 \pm 0.08) \times 10^{-1}$
TT	5.50×10^9	192 ³	2402	7.35×10^4	22.8	—	6.38×10^3	$(2.96 \pm 0.11) \times 10^{-1}$
TT	6.42×10^9	192 ³	2226	7.35×10^4	29.5	—	7.86×10^3	$(3.65 \pm 0.16) \times 10^{-1}$
TT	7.33×10^9	256 ³	1147	1.47×10^5	36.2	—	9.52×10^3	$(4.33 \pm 0.17) \times 10^{-1}$
TT	8.25×10^9	256 ³	1079	1.47×10^5	43.0	—	1.10×10^4	$(5.01 \pm 0.20) \times 10^{-1}$
TT	9.17×10^9	256 ³	1030	1.47×10^5	48.9	—	1.24×10^4	$(5.63 \pm 0.26) \times 10^{-1}$
TT	1.834×10^{10}	256 ³	971.9	1.84×10^5	111	—	2.21×10^4	1.18 ± 0.09

Chapter 6

Entropy Rain: Dilution and Compression of Thermals in Stratified Domains

6.1 Preamble

The following work was published in the *Astrophysical Journal* (Anders et al., 2019). The text in section 6.2 is the text of the paper as it was accepted for publication. Following the published work, in section 6.3, I comment on a few lessons that have been learned since we published these results.

This work was initially motivated by discussions with Axel Brandenburg from around 2015–2016, in which he was interested in using the propagation of Hill vortices as a model for entropy rain. He conducted a couple of initial simulations of these vortices and reported briefly on them in the appendices of Brandenburg (2016). The results of those initial simulations looked unfortunate for the “Entropy Rain” hypothesis – that is, they compressed with increasing atmospheric density, as expected. I had completely forgotten about these discussions until reading the more recent results of Lecoanet & Jeevanjee (2019), which showed that “thermals” in **unstratified** atmospheres produce propagating **buoyant** vortex rings which expand as they propagate. Buoyant vortex rings as a model for entropy rain should therefore exhibit a blend of these phenomena: atmospheric compression and buoyant expansion. This published work below sought to understand how these effects interact with one another from a theoretical perspective, and to test out that theory with some simple simulations.

This work was initially intended to be a direct follow-up to Lecoanet & Jeevanjee (2019). That is, we had intended to run an ensemble of laminar and turbulent simulations of thermals in

atmospheres that were increasingly stratified. However, as we ran initial simulations and developed the theory in sec. 6.2.2, we realized that the development and verification of a theory for laminar thermals was a sufficiently difficult (and complex) contribution to warrant publication alone. Sometime in the next year I hope to revisit this work and understand if this theory describes the evolution of turbulent thermals.

6.2 Published work

6.2.1 Introduction

Recent observations of solar convection have revealed a convective conundrum. Power spectra of horizontal velocities show weaker flows than anticipated at large length scales Hanasoge et al. (2012); Greer et al. (2015). These observations cast doubt on the existence of giant cells driven by deep convection which should manifest as powerful, large-scale motions at the solar surface. This discrepancy between theory and observations has called into question our fundamental understanding of convection, sparking numerous targeted investigations into the nature of solar convection Featherstone & Hindman (2016a); O’Mara et al. (2016); Cossette & Rast (2016); Käpylä et al. (2017); Hotta (2017).

Rather than appealing to giant cells, Spruit (1997) hypothesized that convective motions in the Sun may be primarily driven by cooling in narrow downflow lanes at the solar surface. Brandenburg (2016) incorporated this “entropy rain” concept into a non-local mixing length theory, and suggested the entropy rain could take the form of propagating vortex rings. The entropy rain hypothesis assumes these small vortex rings can maintain their entropy perturbation as they traverse the entire solar convection zone. This allows them to transport the solar luminosity via enthalpy fluxes. However, the vortex rings described by Brandenburg (2016) do not include a fundamental aspect of entropy rain: entropy perturbations relative to the background atmosphere. Entropy rain is dense, and buoyancy forces will modify its dynamics.

It is important to understand how the propagation of these basic convective elements is

affected by their negative buoyancy. In the context of Earth’s atmosphere, “thermals,” or buoyant fluid regions which evolve into rising vortex rings, are thought to be the basic unit of convection (e.g., Romps & Charn, 2015). Atmospheric thermals are buoyant and rise, but the term is also used for dense, falling fluid. We thus study the entropy rain hypothesis by investigating the evolution of individual dense thermals.

Thermals in the Boussinesq limit have been well studied in the laboratory for decades (see e.g. Morton et al., 1956; Scorer, 1957), and more recently through Direct Numerical Simulation (DNS, Lecoanet & Jeevanjee, 2018). These studies find that thermals expand radially and decelerate as they propagate. Such a deceleration may cause the thermals to move so slowly they would diffuse away their entropy perturbation before reaching the bottom of the solar convection zone. Brandenburg & Hazlehurst (2001) found that hot, buoyant thermals in stratified domains behave qualitatively similar to Boussinesq thermals. However, we are not aware of past work which carefully examines the effects of stratification on **negatively** buoyant thermals.

Ignoring entropy variations, Brandenburg (2016) suggests the filling fraction f of entropy rain should decrease like $f \propto \rho^{-1}$ for horizontal compression and $f \propto \rho^{-2/3}$ for spherical compression, where ρ is the density. On the other hand, the filling fraction of Boussinesq thermals **increases** like $f \propto d^2$, where d is the depth of the thermal. These regimes are shown in Fig. 6.1, and compared to the true propagation of a numerically simulated dense thermal which includes both entropy variations and density stratification.

In this paper, we extend Lecoanet & Jeevanjee (2018) (hereafter LJ19) to study the propagation of low-Mach number, low-entropy thermals in stratified domains. We are specifically interested in how the buoyancy force affects the scaling of the thermal radius, or filling fraction, with depth. If buoyancy dominates, it is possible that entropy rain would simply grow too large and stall before reaching the bottom of the solar convection zone. On the other hand, if the compression effects of Brandenburg (2016) are dominant, then these thermals could propagate to the bottom of the solar convection zone, validating the entropy rain picture.

In subsection 6.2.2, we develop a theoretical description of thermals in a stratified domain.

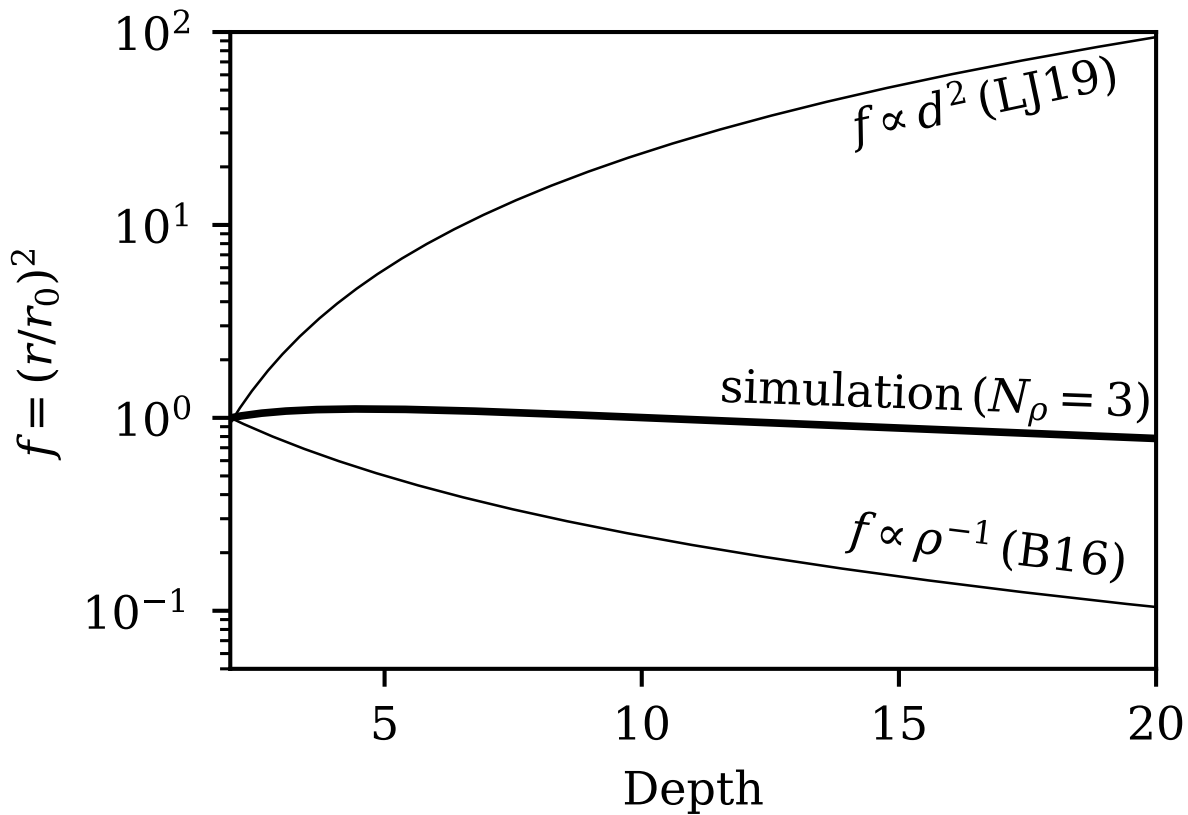


Figure 6.1: Shown is the filling fraction of a dense thermal as a function of depth in an atmosphere which spans three density scale heights (the $N_\rho = 3$ case examined later in this work). Thin solid lines indicate the predictions for filling fraction growth in the Boussinesq case (LJ19) and for pure horizontal compression (B16, Brandenburg, 2016).

In subsection 6.2.3, we describe the numerical experiments conducted in this work. In subsection 6.2.4, we compare our theory and simulation results. In subsection 6.2.5, we discuss what our results imply for the entropy rain hypothesis. Finally, in subsection 6.2.6, we summarize our findings and conclusions.

6.2.2 Model of thermal evolution

6.2.2.1 Phenomenological description of thermal evolution

In Fig. 6.2, we show snapshots of 3D simulation data depicting the descent of cold thermals released from rest in two domains which span a different number of density scale heights, N_ρ . The left panel shows a weakly stratified domain with $N_\rho = 0.5$, whereas the right panel shows a strongly stratified domain with $N_\rho = 3$. In both cases, the thermal is initialized with a spherical negative entropy perturbation whose diameter is 5% of the domain depth. This dense sphere spins up into an axisymmetric vortex ring, and the vertical cross subsection through this vortex ring shows two circular vorticity and entropy extrema. In the $N_\rho = 0.5$ simulation, the thermal grows with depth, similar to thermals in the Boussinesq regime. On the other hand, in the $N_\rho = 3$ simulation, the thermal’s radius decreases marginally with depth.

The goal of this paper is to understand the evolution of the thermal in the vortex ring stage. All of the thermals studied in this work are laminar, similar to the Hill vortices studied by Brandenburg (2016). Crucially, LJ19 showed little difference between the evolution of laminar and turbulent thermals in the Boussinesq limit. As a result, we leave studies of turbulent thermals in stratified domains for future work.

In the following subsections, we will use the impulse of dense vortex rings to derive expressions for the evolution of their depth and radii with time. In this work we study vortex rings generated by discrete cold thermals, but “plumes” driven by time-stationary cooling produce similar vortex ring structures (as in e.g., Rast, 1998). The following description of vortex ring evolution should therefore be broadly applicable.

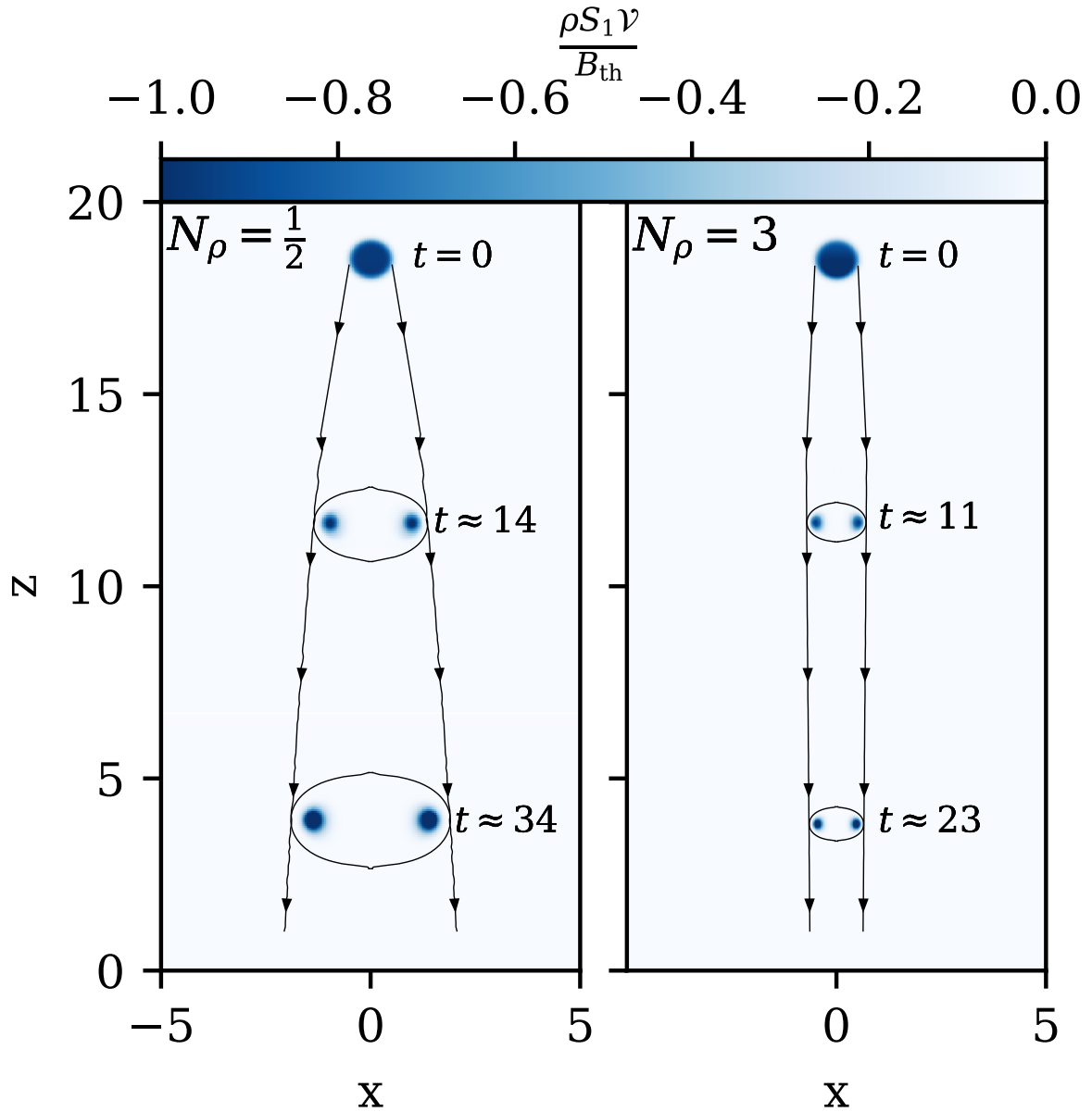


Figure 6.2: Shown is the evolution of entropy perturbations, normalized by the thermal's buoyancy perturbation, from 3D simulations conducted in this work. (left) A thermal in a weakly stratified domain with $N_\rho = 1/2$ density scale heights, and (right) a thermal in a strongly stratified domain with $N_\rho = 3$. While both start with precisely the same initial condition, the thermal in low stratification expands with depth and slows down, whereas the thermal in strong stratification compresses with depth and accelerates.

6.2.2.2 Impulse

The evolution of thermals in the Boussinesq limit has been understood for decades (see e.g., LJ19 for a description and references). While many theoretical descriptions rely on self-similarity arguments, we will show how the impulse of a thermal controls its evolution. This subsection parallels a similar analysis for the Boussinesq case, presented in McKim et al. (2019).

The hydrodynamic impulse is defined as Shivamoggi (2010),

$$\mathbf{I} = \frac{1}{2} \int_{\mathcal{V}} \mathbf{x} \times (\nabla \times (\rho \mathbf{u})) dV, \quad (6.1)$$

where \mathbf{x} is the position vector and \mathbf{u} is the fluid velocity. The impulse is the time-integrated work which has acted on the fluid to result in the current fluid motion. It is thus unaffected by internal forces (e.g., pressure or viscous). Upon integration by parts, it is obvious that the impulse encompasses the momentum of the fluid within the volume \mathcal{V} . However, one can also show that the surface terms correspond to the momentum outside the volume \mathcal{V} (e.g. Akhmetov, 2009). A thermal with volume \mathcal{V} , density ρ , and translating with velocity $\mathbf{u} = w_{\text{th}} \hat{\mathbf{z}}$ thus has an impulse

$$I_z = (1 + k) \rho \mathcal{V} w_{\text{th}}, \quad (6.2)$$

where k encompasses the “virtual mass effect” from the environmental fluid moving together with the thermal Tarshish et al. (2018).

We now restrict our study to an ideal gas in the low Mach-number regime, in an adiabatic background. This is the appropriate regime of deep solar convection. Due to rapid pressure equilibration in low Mach-number flows, we can approximate

$$\frac{\rho_1}{\rho_0} \approx -\frac{S_1}{c_P},$$

where S_1 is the specific entropy perturbation and c_P is the specific heat at constant pressure; thermodynamic variables are decomposed into background (subscript 0) and fluctuating (subscript 1) components.

The rate of change of the impulse is

$$\frac{d\mathbf{I}}{dt} = \int_{\mathcal{V}} \rho_1 \mathbf{g} dV,$$

because the surface terms completely cancel. Assuming a uniform, vertical gravity, $\mathbf{g} = -g\hat{z}$, it is useful to define the buoyancy perturbation,

$$B \equiv \int_{\mathcal{V}} \rho_0 S_1 \frac{g}{c_P} dV. \quad (6.3)$$

such that

$$\frac{dI_z}{dt} = B. \quad (6.4)$$

In the limit of a low Mach-number, thin-core vortex ring, the impulse can be approximated as

$$I_z \approx \pi \rho_0 r^2 \Gamma, \quad (6.5)$$

where r is the radius of the thermal from its axis of symmetry to its vorticity extremum, and $\Gamma = \int_{\mathcal{A}} (\nabla \times \mathbf{u}) dA$ is the circulation in a cross-subsection of the vortex ring. The circulation can change due to baroclinic torques,

$$\frac{d\Gamma}{dt} = \oint_{\mathcal{C}} g \frac{S_1}{c_P} \hat{z} \cdot d\mathbf{x}, \quad (6.6)$$

where $\mathcal{C} = \partial\mathcal{A}$ is the contour around the thermal's vorticity. For the case of a vortex core in which the entropy perturbation is contained tightly in the core, as in Fig. 6.2, a contour can be drawn for which $S_1 \approx 0$. Thus, there are no net baroclinic torques, and we will treat the circulation of a developed vortex ring as a conserved quantity.

6.2.2.3 Model of thermal evolution

The thermals studied here began as initial spherical perturbations and spin up into vortex rings. The spun up vortex ring phase can be modeled as having evolved from a “virtual origin” where the vortex ring had zero radius. We model the thermal as having been located at its virtual origin at a temporal offset $t = -t_{\text{off}}$, where $t = 0$ is the time at which the true thermal was released from rest.

In our simulations, we find the thermal undergoes weak detrainment (loss of buoyant signature to environmental fluid), so the negative buoyancy of the thermal decreases slightly in time (Fig. 6.3,

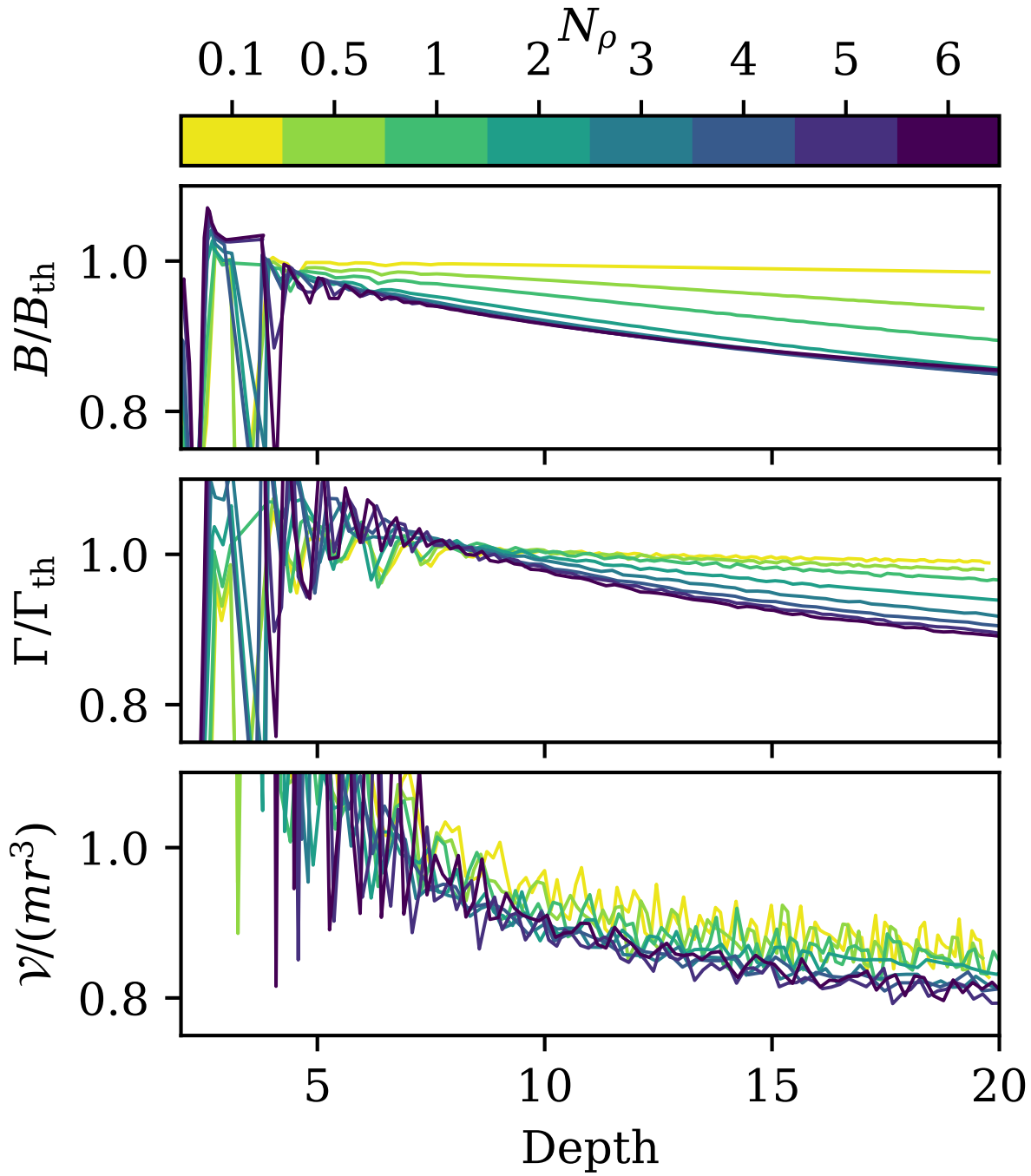


Figure 6.3: Shown is the evolution of buoyancy perturbation (top), circulation (middle), and volume factor (bottom) for each 2D simulation conducted in this work. All three of these quantities remain nearly constant after an initial spin-up phase. With increasing stratification, we see marginally more detrainment (loss of buoyant signature) in the top panel.

top panel). We thus express the buoyancy perturbation as

$$B \approx \eta B_{\text{th}}, \quad (6.7)$$

where η is a constant of $\mathcal{O}(1)$ which represents this detrainment and B_{th} is the thermal's characteristic buoyancy perturbation. We then integrate Eqn. 6.4,

$$I_z = \eta B_{\text{th}}(t + t_{\text{off}}).$$

Combining this with Eqn. 6.5, we retrieve our first main result,

$$r = \sqrt{\frac{\eta B_{\text{th}}(t + t_{\text{off}})}{\pi \rho_0 \Gamma_{\text{th}}}}, \quad (6.8)$$

Here, Γ_{th} is the characteristic circulation of the thermal. As there are no net baroclinic torques, Γ_{th} remains nearly constant in our simulations (Fig. 6.3, middle panel). In the Boussinesq limit where $\rho \rightarrow \text{constant}$, we retrieve the $r \propto \sqrt{t}$ scaling found in LJ19. In the limit of strong stratification, we find $r \propto \rho^{-1/2}$, corresponding to purely horizontal compression, with $r^2 \propto \rho^{-1}$ Brandenburg (2016).

To solve for the vertical evolution of the thermal, we can use Eqn. 6.2. We approximate the volume as $\mathcal{V} \approx mr^3$, where m is a parameter which we take to be constant (which is a decent assumption in our simulations; see Fig. 6.3, bottom panel). Here, m accounts for volumetric constants (e.g., $4\pi/3$), the aspect ratio of the thermal, and the cubed ratio between the full radius of the spheroidal thermal and r . Defining the thermal velocity $w_{\text{th}} \equiv dz_{\text{th}}/dt$, we find

$$\frac{dz_{\text{th}}}{\rho(z_{\text{th}})^{1/2}} = \left(\frac{(\pi \Gamma_{\text{th}})^{3/2}}{m(1+k)(\eta B_{\text{th}})^{1/2}} \right) \frac{dt}{(t + t_{\text{off}})^{1/2}}. \quad (6.9)$$

This can be easily integrated given an atmospheric stratification $\rho(z)$.

To summarize, we model thermals as thin-core vortex rings. The vortex ring is parameterized by its buoyancy perturbation and circulation, which are assumed to be nearly constant after spin-up. The impulse increases in magnitude due to buoyancy forces (Eqn. 6.4), and allows us to relate the size of the vortex ring (Eqn. 6.5) to the momentum of the thermal and its ambient fluid (Eqn. 6.2). Assuming the thermals' volume is spheroidal and that the virtual mass effect and detrainment can be parameterized as constants, we arrive at Eqn. 6.9.

6.2.2.4 Polytropic atmosphere solution

In this work, we study an ideal gas with an adiabatic index of $\gamma = 5/3$. An adiabatic polytrope satisfies

$$T_0 = 1 + (z - L_z) \nabla_{\text{ad}}, \quad (6.10)$$

$$\rho_0 = T_0^{n_{\text{ad}}}, \quad (6.11)$$

where $n_{\text{ad}} = (\gamma - 1)^{-1}$ and ∇_{ad} is the adiabatic temperature gradient. All thermodynamic quantities are nondimensionalized such that $\rho_0 = T_0 = 1$ at $z = L_z$, the top of the domain.

Integrating Eqn. 6.9 under this polytropic density stratification, we find

$$z_{\text{th}} = \nabla_{\text{ad}}^{-1} \left[\left(\frac{2C}{\alpha} \sqrt{t + t_{\text{off}}} + T_{\text{th},0}^{1/\alpha} \right)^{\alpha} - 1 \right] + L_z, \quad (6.12)$$

where

$$C \equiv \frac{\nabla_{\text{ad}}}{m(1+k)} \sqrt{\frac{(\pi \Gamma_{\text{th}})^3}{\eta B_{\text{th}}}}.$$

The thermal is at the virtual origin, $z = z_{\text{th},0}$, at time $t = -t_{\text{off}}$, and the temperature there is $T_{\text{th},0} = 1 + (z_{\text{th},0} - L_z) \nabla_{\text{ad}}$. We define $\alpha^{-1} \equiv 1 - n_{\text{ad}}/2$, and in the limit of large stratification, we find that $z_{\text{th}} \propto t^2$ for our case of $\alpha = 4$.

In our simulations, the thermal is initialized as a uniform sphere of dense fluid but it quickly spins up into a vortex ring. While we do not attempt to model the spin-up phase in this paper, it can be parameterized by the buoyancy B_{th} , circulation Γ_{th} , as well as the virtual origin $z_{\text{th},0}$, and temporal offset t_{off} . Our theory also involves the volumetric aspect ratio of the thermal, m , the detrainment fraction, η , and the effective buoyancy, k . These appear to be only weakly dependent on the stratification for the thermals we have simulated.

6.2.3 Simulation setup

To test our theory, we run a series of thermal simulations using the 3D fully compressible equations in cartesian domains. We additionally compute 2D azimuthally-symmetric simulations using the anelastic equations in cylindrical domains. We verify the 3D and 2D simulations produce

the same results when run with the same parameters. Because 2D simulations are less computationally expensive, we use them to cover a broader parameter regime.

While solar convection is very turbulent, we restrict our study to laminar thermals. In the Boussinesq limit, LJ19 showed the evolution of turbulent vortex rings is well described by laminar theory; we expect this will also hold in the stratified case. In future work, we will apply this laminar theory to turbulent thermals with density stratification, which necessitates 3D simulations.

6.2.3.1 2D Anelastic Simulations

The LBR anelastic equations are Lecoanet et al. (2014),

$$\nabla \cdot \mathbf{u} = -w\partial_z \ln \rho_0, \quad (6.13)$$

$$\begin{aligned} \partial_t \mathbf{u} + \mathbf{u} \cdot \nabla \mathbf{u} = & \\ -\nabla \varpi + S_1 \hat{z} + \frac{1}{\rho_0 \text{Re}} \left[\nabla^2 \mathbf{u} + \frac{1}{3} \nabla (\nabla \cdot \mathbf{u}) \right] & \end{aligned} \quad (6.14)$$

$$\begin{aligned} \partial_t S_1 + \mathbf{u} \cdot \nabla S_1 = & \\ \frac{1}{\text{Re}} \left(\frac{1}{\rho_0 c_P \text{Pr}} [\nabla^2 S_1 + \partial_z \ln T_0 \cdot \partial_z S_1] \right. & \quad (6.15) \\ \left. + \frac{-\nabla_{\text{ad}}}{\rho_0 T_0} \sigma_{ij} \partial_{x_i} u_j \right), & \end{aligned}$$

where $\bar{\sigma}$ is the viscous stress tensor in units of inverse time. We solve these equations in cylindrical geometry, assuming axisymmetry.

Following LJ19, we non-dimensionalize the equations on the initial diameter of the thermal and its freefall velocity. These equations are then fully specified in terms of the Reynolds number and Prandtl number,

$$\text{Re} = \frac{u_{\text{th}} L_{\text{th}}}{\nu}, \quad \text{Pr} = \frac{u_{\text{th}} L_{\text{th}}}{\chi}, \quad u_{\text{th}}^2 = \frac{gL_{\text{th}} \Delta s}{c_P}, \quad (6.16)$$

where u_{th} is the freefall velocity, L_{th} is the thermal length scale, and Δs is the magnitude of the specific entropy signature of the thermal.

The background density and temperature are given by Eqs. 6.10 & 6.11. The adiabatic temperature gradient is $\nabla_{\text{ad}} = g(e^{N_{\rho}/n_{\text{ad}}} - 1)/(L_z c_P)$, where $L_z = 20$ is the height of the domain

and N_ρ is the number of density scale heights spanned by the domain.

We choose an atmospheric model in which the dynamic viscosity, $\mu = \rho_0\nu$, and the thermal conductivity, $\kappa = \rho_0\chi$, are both uniform in space and constant in time. We make this choice because μ and κ appear in the density-weighted momentum and entropy equations, and we find the density-weighted entropy and momentum to be key quantities in our thermal theory. The diffusivities ν and χ therefore scale inversely with the density. As the diffusivities scale with depth, Re is specified at the thermal's initial depth. All simulations conducted in this work use an initial value of $\text{Re} = 600$ and $\text{Pr} = 1$.

6.2.3.2 3D Fully Compressible Simulations

In order to verify our 2D anelastic simulations, we also simulate thermals with the 3D Navier Stokes equations. We use the $(T, \ln \rho)$ formulation of the equations Lecoanet et al. (2014); Anders & Brown (2017),

$$\frac{\partial \ln \rho_1}{\partial t} + \epsilon^{-1} (\mathbf{u} \cdot \nabla \ln \rho_0 + \nabla \cdot \mathbf{u}) = -\mathbf{u} \cdot \nabla \ln \rho_1, \quad (6.17)$$

$$\begin{aligned} \frac{\partial \mathbf{u}}{\partial t} + \frac{1}{-\nabla_{\text{ad}}} [\nabla T_1 + T_1 \nabla \ln \rho_0 + T_0 \nabla \ln \rho_1] = \\ -\frac{\epsilon}{-\nabla_{\text{ad}}} T_1 \nabla \ln \rho_1 + \frac{1}{\rho \text{Re}} \left[\nabla^2 \mathbf{u} + \frac{1}{3} \nabla (\nabla \cdot \mathbf{u}) \right] \end{aligned} \quad (6.18)$$

$$\begin{aligned} \frac{\partial T_1}{\partial t} + \epsilon^{-1} [\mathbf{u} \cdot \nabla T_0 + (\gamma - 1) T_0 \nabla \cdot \mathbf{u}] = \\ -[\mathbf{u} \cdot \nabla T_1 + (\gamma - 1) T_1 \nabla \cdot \mathbf{u}] + \frac{-\nabla_{\text{ad}}}{\rho c_V \text{Re}} \left[\frac{1}{\text{Pr}} \nabla^2 T_1 + \sigma_{ij} \partial_{x_i} u_j \right]. \end{aligned} \quad (6.19)$$

These equations are non-dimensionalized in the same way as the anelastic equations, and use the same background atmosphere. The new parameter $\epsilon = -u_{\text{th}}^2/\nabla_{\text{ad}}$ is the magnitude of entropy perturbations and sets the Mach number of the thermal flows analogously to the adiabatic excess in polytropic convection Anders & Brown (2017); we use $\epsilon = 10^{-4}$ in this work.

6.2.3.3 Initial conditions

The simulations are initialized with a spherical specific entropy perturbation,

$$S_1 = \frac{1}{2} \left[\operatorname{erf} \left(\frac{r' - r_{\text{th}}}{\delta} \right) - 1 \right]. \quad (6.20)$$

Here, $r' = \sqrt{r^2 + (z - z_0)^2}$, where $z_0 = L_z - 3r_{\text{th}}$, with the thermal radius set as $r_{\text{th}} = 0.5$, and a smoothing width, $\delta = 0.1$. As mentioned previously, $\text{Re} = 600$ and $\text{Pr} = 1$ are specified at the thermal's initial depth, $z = z_0$.

For the fully compressible simulations, we must also specify the density perturbation ρ_1 . We pick perturbations that are in pressure equilibrium,

$$\ln \rho_1 = S_1/c_P, \quad T_1 = T_0(e^{-\epsilon \ln \rho_1} - 1)/\epsilon. \quad (6.21)$$

In all cases, we do not add any symmetry breaking perturbations (e.g., noise).

6.2.3.4 Numerics

We simulate the thermals using the Dedalus¹ pseudospectral framework Burns et al. (2016, 2019). The 2D simulations use an implicit-explicit (IMEX), third-order, four-stage Runge-Kutta timestepping scheme RK443 Ascher et al. (1997), and the 3D simulations use the second-order semi-implicit backward differentiation formulation SBDF2 Wang & Ruuth (2008).

The 2D simulation domain is periodic in the z -direction with $z \in [-L_z/4, L_z]$ and the radial direction spans $r \in [0, L_r]$. The boundary conditions are $\partial_r S_1 = w = (\nabla \times \mathbf{u})_\phi = 0$ at $r = L_r$, and the regularity of the equations automatically impose $u = \partial_r(w) = \partial_r(S_1) = 0$ at $r = 0$. The 3D simulation domain is periodic in the horizontal directions ($x, y \in [-L_r, L_r]$) and vertically spans $z \in [0, L_z]$. We impose impenetrable, stress free, fixed-temperature boundary conditions at the upper and lower boundaries. In all of our simulations we specify $L_z = 20$ and $L_r = 5$. We extend our 2D simulation domains to $z = -L_z/4$ because those simulations are vertically periodic. This extension allows us to study the full transit of the thermal above $z = 0$ and terminate the simulation before it begins to wrap through the bottom of the periodic domain.

¹ <http://dedalus-project.org/>

In our 2D simulations, we represent the radial direction with Chebyshev polynomials so that we can include geometric factors in our equations and capture the singularity at $r = 0$. We then assume the z direction is periodic to make the calculations more efficient, and we end the simulations before the thermal can interact with the vertical periodic boundaries. Remarkably, the results of these simulations vary only minimally from our 3D simulations, as we will show in the next subsection, indicating that the vertical periodicity and the different side boundaries (cylinder vs. cube) do not influence the thermal properties.

All of the code used to perform the simulations in this work can be found online in the supplementary materials in a Zenodo repository Anders et al. (2019a) at <https://doi.org/10.5281/zenodo.3311894>.

6.2.4 Model verification

To compare to the model, we must measure the thermal's depth and radius. We define the thermal's depth and radius using the thermal's entropy minimum. For specifics on how these measurements are conducted in our simulations, we refer the reader to appendix 6.2.7.

In the top panel of Fig. 6.4 we show the depth, $d_{\text{th}} = L_z - z_{\text{th}}$, of the thermal as a function of time for simulations with different stratifications. At very low stratification (e.g., $N_\rho = 0.1$), the thermal is small compared to the local density scale height at all depths, and it evolves roughly according to the Boussinesq prediction of $d \propto \sqrt{t}$. As the stratification increases, the thermal transits the domain more quickly and approaches the limit of $d \propto t^2$ predicted in the highly stratified limit of Eqn. 6.12. The theoretical fits for depth from the prediction of Eqn. 6.12 are plotted over the measured data. The theoretical fits are poor at early times when the thermal is spinning up from its initial spherical state into the vortex ring state. Once the thermal is spun up into a vortex ring, the theory shows remarkable agreement with the data.

In the bottom panel of Fig. 6.4 we show the corresponding thermal velocity as a function of depth. Low density ($N_\rho = 0.1$) thermals decelerate with depth. With increasing stratification, this deceleration stops and sufficiently stratified runs ($N_\rho \geq 3$) experience acceleration.

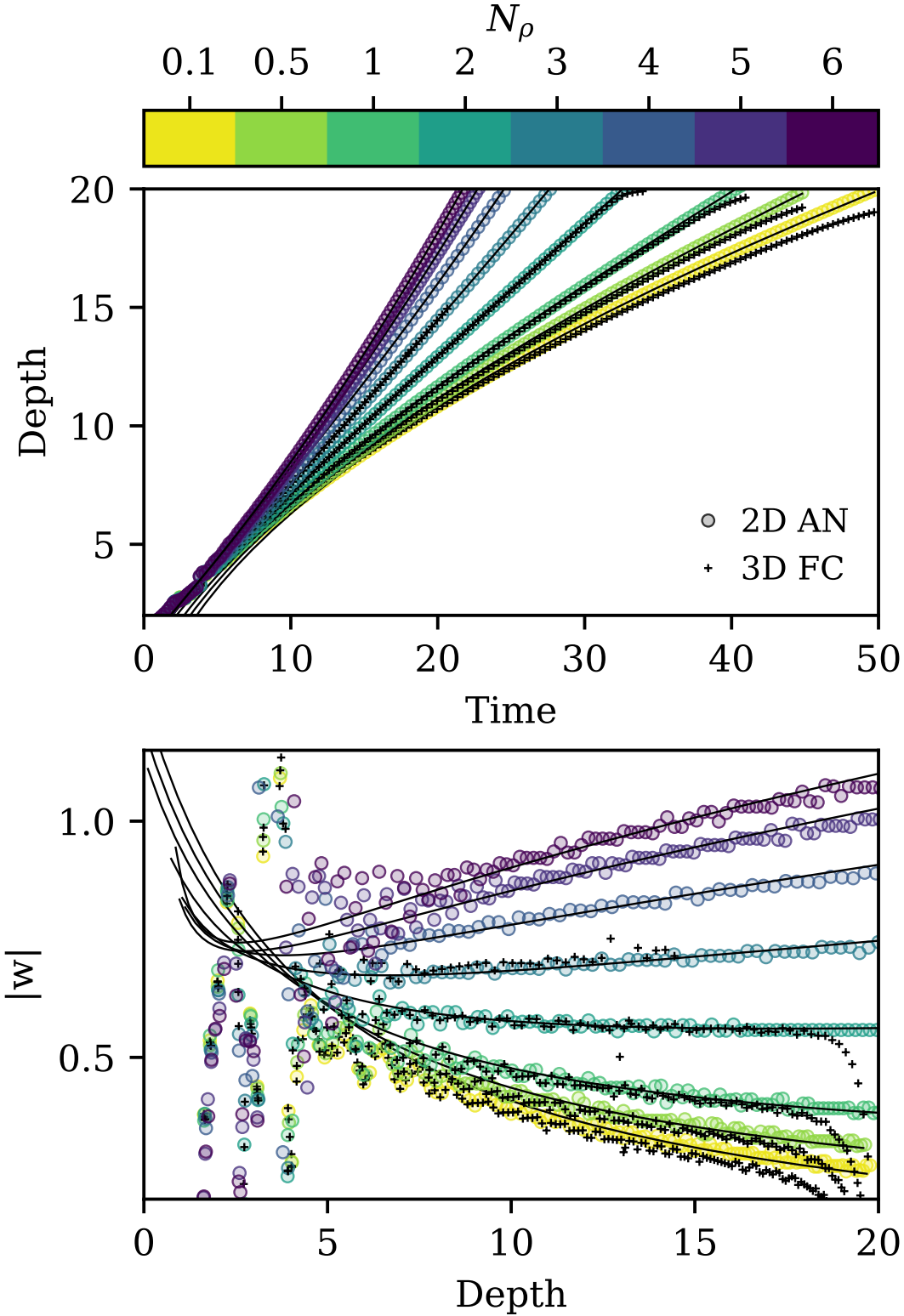


Figure 6.4: (top) The thermal depth as a function of time for the 2D anelastic (AN) and 3D fully compressible (FC) simulations. (bottom) The corresponding thermal velocities as a function of depth. Theoretical predictions from subsection 6.2.2 are plotted in thin solid lines for each case (see parameters in table 6.1).

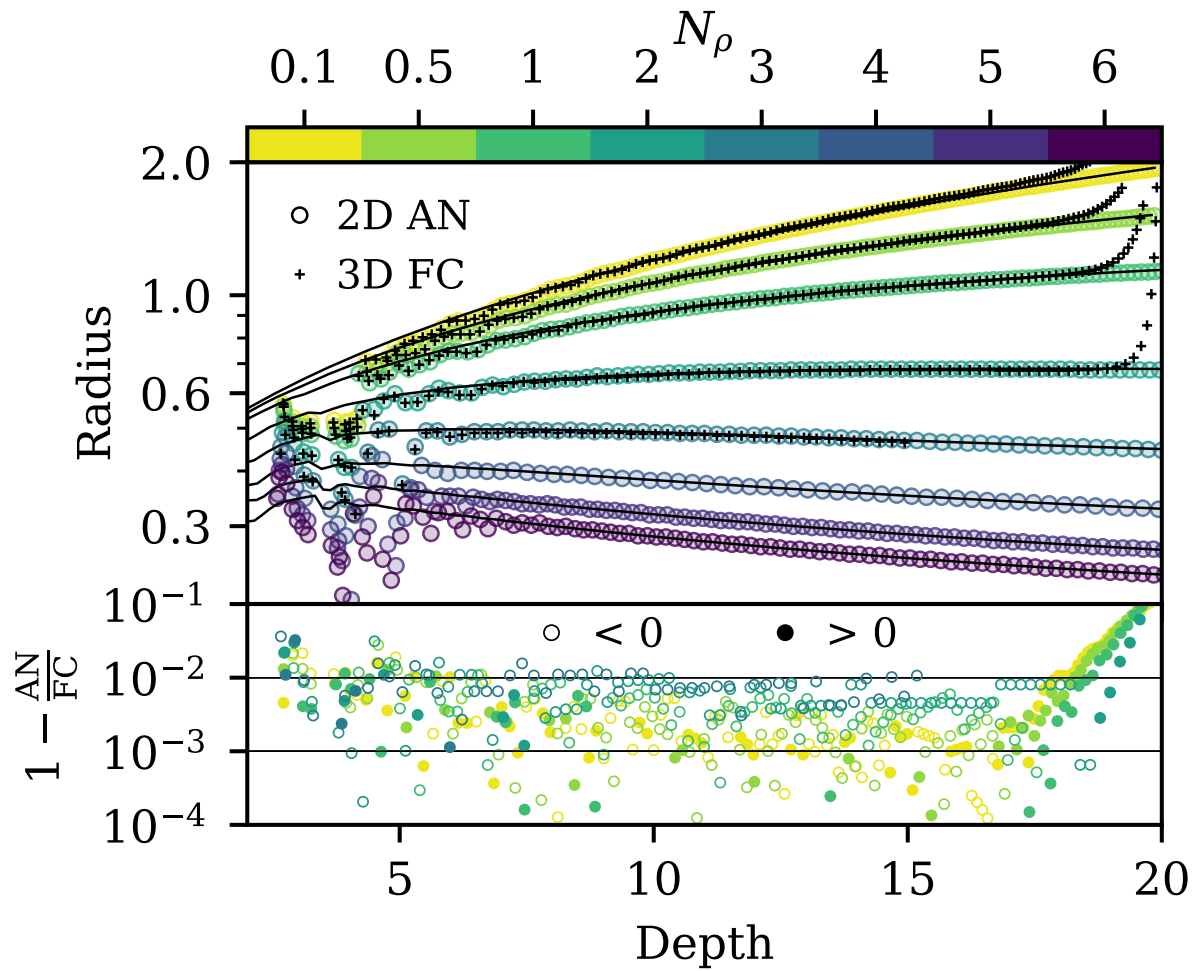


Figure 6.5: (top) Thermal radius as a function of depth for the 2D anelastic (AN) and 3D fully compressible (FC) simulations. Theoretical predictions from subsection 6.2.2 are plotted in thin solid lines. (bottom) The fractional difference between anelastic and fully compressible simulations.

The top panel of Fig. 6.5 plots the thermal radius as a function of depth. In the low stratification limit, the radius of the thermal grows linearly with depth, $r \propto d$, as is the case in the Boussinesq limit (LJ19). The growth of the thermal is due to entrainment of environmental fluid, which causes the thermal to decelerate like $w \propto d^{-1}$, as is shown in the bottom panel of Fig. 6.4. However, as stratification increases, the thermal entrainment of environmental fluid decreases and it experiences less expansion. In the limit of large stratification ($N_\rho \geq 3$), thermals contract with depth, and the thermals accelerate as they fall.

Finally, we quantify the excellent agreement between the 2D anelastic and 3D fully compressible simulations in Fig. 6.5, bottom panel. We ran simulations in both models for $N_\rho = [0.1, 0.5, 1, 2, 3]$. There are slight discrepancies early in the simulation, when the thermal is spinning up, and late in the simulation, when the 3D simulations begin interacting with the bottom of the domain. Outside these times, we find differences in the measured radius of less than 1%. This gives us confidence that our high stratification anelastic simulations are producing reliable results. Lecoanet et al. (2014) also found close agreement between low Mach-number anelastic and fully compressible simulations.

The values of the parameters described in subsection 6.2.2 for each of our simulations are presented in table 6.1. As anticipated, η is $\mathcal{O}(1)$ and decreases slightly in value with increasing stratification, consistent with Fig. 6.3. In all cases, the buoyancy B_{th} is similar to the integrated buoyancy in the initial conditions, with some losses due to detrainment in the spin-up. We also find that the non-dimensional circulation is roughly -2 for each of our cases, and decreases in magnitude with increasing stratification.

6.2.5 Implications for entropy rain hypothesis

Our theory shows that the evolution of dense thermals in stratified domains is complex. Neither the assumption of pure compression (as in e.g., Brandenburg, 2016) nor the evolution of thermals in the Boussinesq regime (LJ19) fully describes thermal behavior. Rather, the results fall somewhere in between, and theory and simulations suggest that there are two regimes of

Table 6.1: Simulation output parameterization Parameters presented in this table are best fits to simulation output data in the range $z = [0.1L_z, 0.65L_z]$. Above this range, the thermal is still spinning up from initial conditions; below this range, 3D cases are heavily interacting with the bottom boundary.

N_ρ	$z_{\text{th},0}$	t_{off}	B_{th}	Γ_{th}	m	η	k
2D Anelastic Simulations (Cylindrical)							
0.1	24.6	0.144	-0.548	-2.17	8.05	1.04	0.732
0.5	24.2	0.695	-0.569	-2.12	8.34	0.977	0.715
1	23.7	1.11	-0.602	-2.05	8.65	0.915	0.703
2	22.3	1.27	-0.713	-1.89	9.23	0.842	0.682
3	21.2	1.01	-0.947	-1.73	9.81	0.807	0.654
4	20.5	0.615	-1.47	-1.59	10.2	0.794	0.642
5	20.0	0.425	-2.70	-1.49	10.7	0.781	0.609
6	19.8	0.041	-5.73	-1.43	10.8	0.787	0.616
3D Fully Compressible Simulations (Cartesian)							
0.1	23.4	-0.337	-0.547	-2.17	8.98	1.06	0.636
0.5	23.8	0.572	-0.568	-2.12	8.79	0.978	0.678
1	23.6	1.15	-0.601	-2.05	8.87	0.907	0.689
2	22.4	1.38	-0.711	-1.89	9.31	0.828	0.680
3	21.1	0.78	-0.949	-1.75	9.99	0.815	0.648

downflowing thermal behavior:

- (1) A low-stratification “stalling” regime, in which the thermal entrains environmental fluid and slows down, acting much like the Boussinesq regime, and
- (2) A high-stratification “falling” regime, in which the thermal falls sufficiently fast that atmospheric compression dominates over entrainment and the thermal accelerates as it falls deeper into the atmosphere.

We note that both of these regimes could have interesting implications for the entropy rain hypothesis.

If the solar downflows are in the stalling regime, convective elements would grow enormously in size and slow down very close to the solar surface. In a perfectly quiescent atmosphere, these slow, large convective elements would eventually propagate to the base of the convection zone over long timescales. In fact, their large length scales would likely help shield them from any dissipative effects despite their low velocities. However, the solar convection zone is highly turbulent, and we expect that a more likely outcome for such large, coherent, and slowly propagating structures is that they would be torn apart by turbulent motions.

On the other hand, if solar convection is comprised of thermals in the falling regime, then it is likely that solar surface elements would reach deep into the Sun. Neglecting buoyancy, we expect that downward propagating vortex rings in the solar convection zone would likely compress to sizes on which conductivity could become important. Our theory of thermals suggests that, instead, buoyancy counteracts some of the compressional effects of stratification, and could help convective elements maintain their entropy perturbation as they cross the solar convection zone.

We now estimate the behavior of thermals in the Sun based on the simulations presented in this work. The thermal evolution depends on a variety of parameters (see table 6.1). However, we find the only parameter which changes appreciably as we increase the stratification is the normalized buoyancy B_{th} . To estimate B_{th} in the sun, we approximate the dimensional buoyancy perturbation of Eqn. 6.3 as $\tilde{B} = \rho \mathcal{V} g (S_1/c_p)$, and calculate this quantity for thermals launched from the solar

photosphere, assuming that solar downflow lanes quickly break up into thermals. Using the VAL atmospheric data of Avrett & Loeser (2008), we estimate the solar surface to have a temperature of $T_0 \approx 6000$ K, a density of $\rho_0 \approx 1.74 \times 10^{-7}$ g/cm³, and a sound speed of $c_s = 9.5 \times 10^5$ cm/s. We estimate that thermal diameters would be roughly the width of downflow lanes ($L_{\text{th}} = 0.1$ Mm), and the average atmospheric density over the first L_{th} of the solar interior is $\bar{\rho} = 1.17\rho_0$. Estimating downflows to have a temperature deviation of $T_1 = -500$ K Borrero & Bellot Rubio (2002), the nondimensional entropy signature of solar downflows is $S_1/c_p \sim \gamma^{-1} \ln(1 + T_1/T_0) = -5.22 \times 10^{-2}$. Using a solar surface gravity value of $g = 2.74 \times 10^4$ cm/s² and assuming thermal formation occurs at the solar photosphere, the buoyancy of a spherical thermal is

$$\tilde{B} \approx \bar{\rho} \left[\frac{4\pi}{3} \left(\frac{L}{2} \right)^3 \right] g \frac{S_1}{c_p} = -1.52 \times 10^{17} \text{ g cm}^4/\text{s}^2.$$

Nondimensionalizing this by $B_0 = (S_1/c_p)L^2 u_{\text{th}}^2 \rho_0$ with $u_{\text{th}} = c_s \sqrt{S_1/c_p}$, we find $B_{\text{th}} = \tilde{B}/B_0 = -3.57$, which lies between the $N_\rho = 5$ and $N_\rho = 6$ simulations we studied here (see table 6.1).

Because solar downflows likely break up into thermals of various sizes, we will examine the fate of thermals with dimensionless buoyancy in the interval $[B_\ell, B_u] = 0.5B_{\text{th}}, 2B_{\text{th}}$. Interpolating and extrapolating the data in Table 6.1, we use Eqns. 6.8 & 6.12 to calculate theoretical predictions for how thermals with these buoyancies would evolve over extended atmospheres like the solar convection zone. Using a simple solar interior model calculated using MESA Paxton et al. (2011) to map the density profiles of our simulation domains onto the density profile of the Sun, we plot the evolution of thermals in our estimated interval in Fig. 6.6. In the first and second panels of Fig. 6.6, we show the evolution of these thermals' radii and velocities inside of the Sun, and compare their radial evolution to pure horizontal compression and their velocity evolution to the speed of sound. We use the solar diffusivity models of Brown (2011) to estimate the timescale over which the thermal would diffuse its entropy signature ($\tau_\kappa = \chi/r_{\text{th}}^2$) and the thermal freefall timescale over its own radial length scale ($\tau_{\text{ff}} = r_{\text{th}}/w_{\text{th}}$). In the third panel of Fig. 6.6, we plot the ratio of these two timescales over the thermal's evolution.

We find that our estimated solar thermal is likely in the falling regime. These thermals

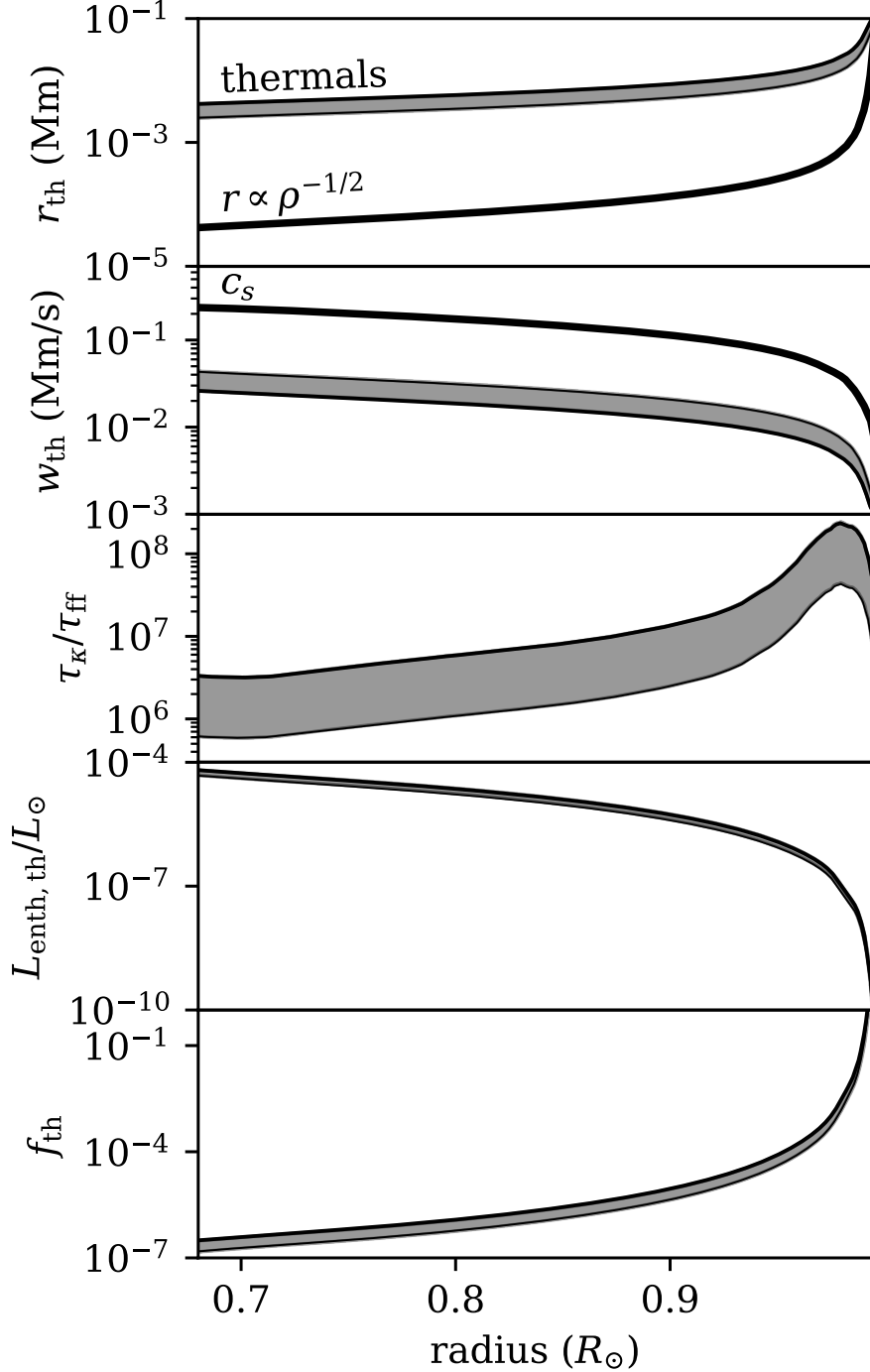


Figure 6.6: (First panel) Bounds on the evolution of the radii of entropy rain in the Sun are shown and compared to what the radii would be under purely horizontal compression. (Second panel) The corresponding range of velocities of solar-like thermals are shown. (Third panel) Shown is the estimated range of the ratio of the thermal diffusion timescale normalized by the freefall timescale over the thermal radial length scale. Diffusivities are calculated using the realistic solar-like diffusion profiles of Brown (2011). (Fourth panel) An estimate of the luminosity of these thermals, normalized by the solar luminosity, is shown. (Fifth panel) An estimate of the filling factor of thermals required to carry the solar luminosity.

experience radial compression with corresponding increases in velocity, but experience much less compression than a naive approximation based on the density stratification alone. Interestingly, the thermal's Mach number is roughly a value of 0.1 throughout the full extent of the solar convection zone. Furthermore, throughout the thermal's fall, we find that $\tau_\kappa \gg \tau_{\text{ff}}$, and thus we do not expect the thermal to diffuse its entropic signature. We find a fractional diffusion rate over the thermal's transit of the solar convection zone of

$$\int_{R_\odot}^{0.7R_\odot} \tau_\kappa^{-1} \frac{dr}{w_{\text{th}}} = [6.55, 1.57] \times 10^{-3} \text{ for } [B_\ell, B_u].$$

Thus, the thermal loses less than 1% of its entropic signature to diffusion.

We now briefly estimate the enthalpy flux carried by a thermal. Following Brandenburg (2016), we estimate the enthalpy flux of the thermal as $F_{\text{enth}} = \rho_0(z_{\text{th}})T_0(z_{\text{th}})w_{\text{th}}S_{1,\text{th}}$. We estimate the thermal's entropic signature as $S_{1,\text{th}} = B_{\text{th}}/(\rho_0(z_{\text{th}})V_{\text{th}}g/c_P)$, where the thermal volume is $V_{\text{th}} = mr_{\text{th}}^3$. We take $\rho_0(z_{\text{th}})$, $T_0(z_{\text{th}})$, and g/c_P from our solar MESA model at the depth of the thermal over its evolution. We take r_{th} and w_{th} to be the thermal radius and velocity shown in the first and second panels of Fig. 6.6. We find m from the data in Table 6.1 in the same manner as we found B_{th} for these solar thermals. To estimate the total luminosity carried by one thermal, we calculate $L_{\text{enth, th}} = \pi r_{\text{th}}^2 F_{\text{enth}}$, and we plot this value as a function of depth, normalized by the solar luminosity, in the fourth panel of Fig. 6.6.

From this estimate of the luminosity carried by one thermal, we now calculate the filling factor of downward propagating thermals required to carry the solar luminosity. We calculate $f_{\text{th}} = [(L_\odot/L_{\text{enth, th}})(\pi r_{\text{th}}^2)]/(4\pi R^2)$, where R is the thermal's radial distance from the center of the Sun. The final panel of Fig. 6.6 displays f_{th} vs. depth. The filling factor of thermals required to carry L_\odot at the solar surface is greater than unity; this is unsurprising, as we know that solar surface convection carries the solar luminosity through the combined effects of upflows and downflows. A few percentage of the solar radius beneath the photosphere, f_{th} drops to a very modest 10^{-4} , and by the base of the solar convection zone approaches 10^{-7} . These estimates suggest that even if a large fraction of the thermals launched from the solar surface break apart due to turbulence,

entropy rain could still efficiently carry the solar luminosity deep in the convection zone.

We briefly note that our handling of the enthalpy flux here ignores the contributions of the kinetic energy flux, potential energy flux, and viscous flux. While we expect the last of these to be inconsequential, the kinetic energy flux (which transports luminosity inwards) and the potential energy flux (which transports luminosity outwards) may be large. We encourage future work to examine these fluxes more thoroughly, but such an examination is outside of the scope of this work.

6.2.6 Summary & Conclusion

In this paper we developed a simple theory of the evolution of negatively buoyant vortex rings in stratified atmospheres. This theory predicts that dense thermals experience less entrainment than Boussinesq thermals due to increasing atmospheric density with depth. Likewise, these thermals experience less compression than would be expected due to pure atmospheric compression of a neutrally buoyant vortex ring. We performed 2D anelastic & 3D fully compressible simulations of thermal evolution in the laminar regime for varying degrees of stratification, and showed that our parameterized theory describes the evolution of thermals in these systems remarkably well. We found excellent agreement between the 2D & 3D simulations. The evolution of dense thermals in stratified domains is complex, but can be classified into a near-Boussinesq “stalling” and a high-stratification “falling” regime. We estimate that solar downflows would fall into this latter regime.

The “entropy rain” hypothesis states that narrow downflows can transport the luminosity of the Sun via enthalpy fluxes. If the rain stalls near the surface or its entropy diffuses away before it hits the bottom, then it cannot transport the flux. We find that with our more accurate model for thermal propagation, solar thermals should maintain their entropy all the way to the base of the convection zone. Hence, entropy rain is a possible mechanism for transporting the solar luminosity.

6.2.7 Appendix A: Thermal Measurements

Throughout this work, we frequently report the thermal's radius or its height. We measure the thermal's radius and height as the radius from the axis of symmetry and the height above $z = 0$ at which the thermal's vortex core is located. We assume that the vortex core is located at the thermal's entropy minima. To find the entropy minima vertically, we integrate $\int \rho S_1 r dr$ in our Dedalus domain, then use the spectral data of that profile to sample it on a 4096-point vertical grid; we take the location of the minima on that grid to be the thermal height. To find the entropy minima horizontally, we integrate $\int \rho S_1 dz$ in our Dedalus domain, then sample the spectral data onto a 2048-point radial grid, and take the minima of that profile to be the radius of the thermal. For our 2D simulations, we use entropy data from the full simulation domain to perform these calculations. For our 3D simulations, we assume that the vortex ring is azimuthally symmetric, and thus use the entropy data in the $y = 0$ plane at radial values of $x \geq 0$. In order to find the thermal's velocity as a function of time, we use a five-point stencil to differentiate the thermal's depth, d_{th} ,

$$w_{\text{th}}(t) = \frac{d}{dt} d_{\text{th}}(t) = \frac{-d_{\text{th}}(x + 2\Delta t) + 8d_{\text{th}}(t + \Delta t) - 8d_{\text{th}}(t - \Delta t) + d_{\text{th}}(t - 2\Delta t)}{12\Delta t}$$

Calculating integral quantities such as the circulation, Γ , the buoyancy, B , and the volume, \mathcal{V} , require knowledge of what fraction of the domain constitutes the thermal. We use the thermal tracking algorithm described in appendix 6.2.8 to determine the radial contour, \mathcal{C} , that outlines the thermal as a function of height. We then use this contour to find our integral quantities,

$$\Gamma = \int_0^{L_z} \int_0^{\mathcal{C}} (\nabla \times \mathbf{u})_\phi dr dz, \quad B = 2\pi \int_0^{L_z} \int_0^{\mathcal{C}} \rho S_1 r dr dz, \quad \mathcal{V} = 2\pi \int_0^{L_z} \int_0^{\mathcal{C}} r dr dz. \quad (6.22)$$

6.2.8 Appendix B: Thermal Tracking Algorithm

We use a thermal tracking algorithm very similar to the one used in Lecoanet & Jeevanjee (2018) and inspired by the work of Romps & Charn (2015) in order to determine the full extent of the thermal, as pictured by the elliptical outlines in Fig. 6.2. We begin by measuring the thermal's

velocity versus time, w_{th} , as described in appendix 6.2.7. We calculate the streamfunction of the velocity field as in Romps & Charn (2015),

$$\frac{\partial \psi}{\partial r} = 2\pi\rho r(w - w_{\text{th}}), \quad (6.23)$$

using vertical velocity data, w , in a 2D domain which radially spans $r = [0, L_r]$ and vertically spans the same depth as the simulation domain. For our 2D simulations, this is simply the output of the simulations. For our 3D simulations, we assume that the vortex ring is azimuthally symmetric, and thus use the vertical velocity data in the $y = 0$ plane at values of $x \geq 0$. We solve Eqn. 6.23 with the boundary condition that $\psi = 0$ at $r = 0$. The contour $\psi = 0$ is taken to be the contour bounding the thermal, \mathcal{C} .

6.2.9 Appendix C: Table of Simulations

Information regarding the simulation resolution, evolution time, and CFL safety factor for each of the simulations presented in this work is contained in table 6.2. The Python scripts used to perform all simulations and analysis in this work are stored online in a Zenodo repository Anders et al. (2019a) at <https://doi.org/10.5281/zenodo.3311894>. The 3D, $N_\rho = 3$ simulation displays spectral instabilities at very late times as the simulation is under-resolved at these times. This affects thermal radial measurements at depths ≥ 17.5 . We therefore truncate the data from that simulation at a depth of 15, which corresponds to multiple freefall times before these instabilities affect the solution.

Table 6.2: Table of simulation information: Our 2D cylindrical sims have spectral mode resolution of nr x nz, and our 3D cartesian sims have spectral mode resolution of nx x ny x nz. We evolve our simulations from initial conditions until $t_{\text{evolution}}$ dimensionless freefall times have passed. We use a CFL to determine the appropriate size of our timestep at each timestep in our simulation, and the CFL safety factor decreases with increasing stratification. Our 2D sims use the RK443 timestepper and our 3D sims use the SBDF2 timestepper, resulting in different safety factor sizes in 2D and 3D.

N_ρ	nr or nx = ny	nz	$t_{\text{evolution}}$	safety
2D Anelastic Simulations				
0.1	128	512	50	0.6
0.5	128	512	45	0.6
1	128	512	41	0.6
2	128	1024	34	0.4
3	192	1024	29	0.4
4	256	1024	26	0.3
5	256	1536	25	0.14
6	256	1536	23	0.08
3D Fully Compressible Simulations				
0.1	256	512	50	0.15
0.5	256	512	45	0.15
1	256	512	41	0.15
2	384	1024	34	0.1
3	384	2048	25	0.15

6.3 Postscript and lessons learned since publication

I haven't had the chance to fully investigate this, but I think thermals are an excellent testing ground in which to understand two fairly mundane topics:

- (1) The nature of viscous heating, and
- (2) how different choices for the simulation diffusivities (e.g., constant kinematic viscosity vs. constant dynamic viscosity) affect the results of the simulation and interpretation of results.

We noted briefly in sec. 6.2.3.1 that we chose constant **dynamic** diffusivities in this work due to the fact that those are the diffusivities that appear in the evolution equations for momentum and full entropy. However, it is unclear how a choice of constant **diffusivities** (units of cm^2/s) would affect the dynamics. I discuss the implications of this further in sec. 7.7.

An interesting implication of this work relates to the manner in which entropy raindrops would interact with the solar radiative zone. From Fig. 6.6, the size of thermals at the base of the convection zone is $r_{\text{th}} = \text{a few } \times 10^{-3} \text{ Mm}$. The solar radius there is $R_{\text{CZ}} \approx 500 \text{ Mm}$. The spherical harmonic degree of these thermals is $\ell \approx R_{\text{CZ}}/r_{\text{th}} \approx 10^5$. This high spherical harmonic degree could have huge implications for the gravity wave spectrum excited within the radiative interior. Unfortunately, I haven't had the chance to pursue in depth the implications of entropy rain interactions with the radiative zone (either with regards to wave excitation or overshoot and mixing).

Chapter 7

Unpublished Work and Open Mysteries

Many promising projects have been abandoned over the course of my thesis work due to limited brain bandwidth, and due to the previous five chapters showing more promising and clear results. In the following sections, I will briefly outline progress that has been made on some of these abandoned projects, in the hope that they can be revisited and completed in the future.

7.1 Flywheel Modes in 2D Convection

This project **almost** became a paper, but we couldn't find an angle in which to make it sufficiently interesting. Our goal was to study Rayleigh-Bénard convection at **high aspect ratio with stress free boundaries**, and show:

- (1) An argument for how the average system enstrophy should scale as a function of Ra (see section 7.1.1).
- (2) A description of the physical mechanism that creates this enstrophy (see section 7.1.2).
- (3) A description of the timescales over which flywheels spin up (or down, depending on thermal boundary condition choice). Presumably this is related to the viscous diffusion timescale, but it's a bit unclear what it is.
- (4) A comparison to no-slip sims, and whether they have a similar spin-up (how do they avoid these modes?).

- (5) A demonstration of what you get wrong if you take your measurements before the spin-up is done at high Ra (I think you probably get flux-related quantities like Nu right but velocity-related quantities like Re wrong).

7.1.1 An argument for the scaling of enstrophy in a Boussinesq, convective system

The Boussinesq momentum equation, nondimensionalized on a freefall timescale, is

$$\frac{\partial \mathbf{u}}{\partial t} = -\nabla \varpi + T_1 \hat{z} - \mathcal{R} \mathbf{u} \cdot \nabla \times (\boldsymbol{\omega}) + \mathbf{u} \times \boldsymbol{\omega}, \quad (7.1)$$

where \mathbf{u} is the velocity vector, ϖ is the reduced pressure (a Lagrange multiplier that enforces incompressibility), T_1 is the temperature deviation from background, $\mathcal{R} = \sqrt{\text{Pr}/\text{Ra}}$, and $\boldsymbol{\omega} = \nabla \times (\mathbf{u})$ is the vorticity. We dot \mathbf{u} into this equation in order to get the kinetic energy equation,

$$\frac{\partial u^2/2}{\partial t} + \nabla \cdot (\varpi \mathbf{u} + \mathcal{R} \boldsymbol{\omega} \times \mathbf{u}) = w T_1 - \mathcal{R} \omega^2. \quad (7.2)$$

Under the assumption of impenetrable boundaries ($w = 0$, so $w\varpi = 0$), coupled with no-slip ($\mathbf{u} = 0$) or stress-free boundaries ($\boldsymbol{\omega} = 0$), the fluxes disappear at the top and bottom plate. So – kinetic energy cannot exit the domain through the boundaries, but must instead be generated and destroyed by the source and sink terms. If we define the volume average as $\langle \rangle = \mathcal{V}^{-1} \int_{\mathcal{V}} dV$, where \mathcal{V} is the volume of our domain, and we take the volume average of this equation, we get

$$\left\langle \frac{\partial u^2/2}{\partial t} \right\rangle = \langle w T_1 \rangle - \mathcal{R} \langle \omega^2 \rangle. \quad (7.3)$$

Assuming that the kinetic energy in the convection reaches a steady state, the LHS of this expression disappears and we find,

$$\langle \omega^2 \rangle = \mathcal{R}^{-1} \langle w T_1 \rangle, \quad (7.4)$$

the evolved value of the **enstrophy**, ω^2 , is determined by the evolved value of the convective heat transport. The heat transport can be expressed in terms of the Nusselt number,

$$\text{Nu} \equiv 1 + \frac{\langle w T_1 \rangle}{-\mathcal{P} \langle \partial_z (T_0 + T_1) \rangle}, \quad (7.5)$$

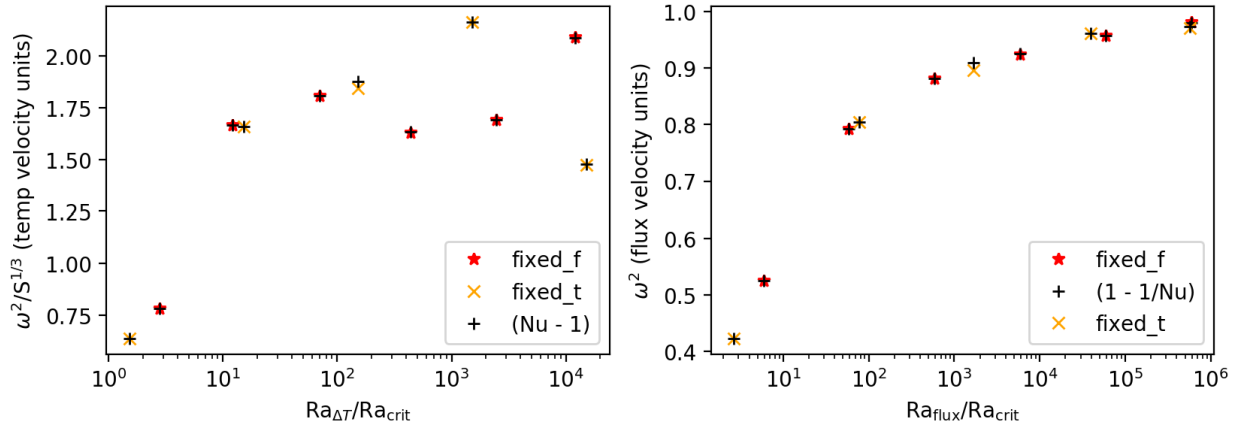


Figure 7.1: (left) Enstrophy in inverse freefall time units nondimensionalized by the evolved temperature jump across the domain, and normalized by the supercriticality to the third power. (right) Enstrophy in inverse freefall time units nondimensionalized by the evolved system flux. Simulation measurements are shown from simulations run with FF boundaries (red stars), TT boundaries (orange crosses), and the expected value of enstrophy as a function of Nu is overplotted.

where $\mathcal{P} = \mathcal{R}/Pr$, and in an equilibrated state

$$\langle wT_1 \rangle = \begin{cases} \mathcal{P}(Nu - 1) & \text{TT boundaries,} \\ \mathcal{P}(1 - Nu^{-1}) & \text{FT or FF boundaries} \end{cases} . \quad (7.6)$$

Or, through a straightforward substitution, we expect

$$\langle \omega^2 \rangle = \begin{cases} Pr^{-1}(Nu - 1) & \text{TT boundaries,} \\ Pr^{-1}(1 - Nu^{-1}) & \text{TT or FT boundaries} \end{cases} . \quad (7.7)$$

We find that this is indeed a good description of the enstrophy contained in the evolved flywheels for stress-free simulations, see Fig. 7.1. Note, these scalings hold up for no-slip boundary conditions, as well. In the case of no-slip boundaries, the enstrophy is localized near the boundary (where the bulk velocities must go to zero over a small length scale of the boundary layer thickness).

7.1.2 Where does the enstrophy come from?

In order to determine where the enstrophy comes from, we first curl Eqn. 7.1 to retrieve the vorticity equation,

$$\frac{\partial \boldsymbol{\omega}}{\partial t} = -(\mathbf{u} \cdot \nabla) \boldsymbol{\omega} + (\boldsymbol{\omega} \cdot \nabla) \mathbf{u} + \nabla \times (T_1 \hat{z}) + \mathcal{R} \nabla^2 \boldsymbol{\omega}. \quad (7.8)$$

We now dot $\boldsymbol{\omega}$ into this equation to retrieve the enstrophy evolution equation,

$$\frac{\partial \omega^2/2}{\partial t} + \nabla \cdot (\boldsymbol{\omega} \times (T_1 \hat{z} - \mathcal{R} \nabla \times (\boldsymbol{\omega}) + \mathbf{u} \times \boldsymbol{\omega})) = (T_1 \hat{z} - \mathcal{R} \nabla \times (\boldsymbol{\omega}) + \mathbf{u} \times \boldsymbol{\omega}) \cdot \nabla \times (\boldsymbol{\omega}). \quad (7.9)$$

We are specifically interested in the 2D case where $\mathbf{u} = u\hat{x} + w\hat{z}$ and $\boldsymbol{\omega} = \omega\hat{y}$. In this limit, the enstrophy equation is

$$\begin{aligned} \frac{\partial \omega^2/2}{\partial t} + \nabla \cdot \left(\boldsymbol{\omega} \left[\left(T_1 + u\omega - \mathcal{R} \frac{\partial \omega}{\partial x} \right) \hat{x} + \left(w\omega - \mathcal{R} \frac{\partial \omega}{\partial z} \right) \hat{z} \right] \right) = \\ T_1 \frac{\partial \omega}{\partial x} + \frac{1}{2} \left(w \frac{\partial \omega^2}{\partial z} + u \frac{\partial \omega^2}{\partial x} \right) - \mathcal{R} \left(\left[\frac{\partial \omega}{\partial z} \right]^2 + \left[\frac{\partial \omega}{\partial x} \right]^2 \right). \end{aligned} \quad (7.10)$$

We can see immediately that all enstrophy fluxes vanish at the boundaries for stress-free boundary conditions (where $\boldsymbol{\omega} = 0$ at the boundaries). For this case, we take a volume average and find:

$$\left\langle \frac{\partial \omega^2}{\partial t} \right\rangle = 2 \left\langle T_1 \frac{\partial \omega}{\partial x} \right\rangle + \left\langle w \frac{\partial \omega^2}{\partial z} + u \frac{\partial \omega^2}{\partial x} \right\rangle - 2\mathcal{R} \left\langle \left[\frac{\partial \omega}{\partial z} \right]^2 + \left[\frac{\partial \omega}{\partial x} \right]^2 \right\rangle. \quad (7.11)$$

On the RHS, there are three source terms for the enstrophy. From left to right, they are the baroclinic term (from buoyancy), a term from advection (vortex stretching), and viscous dissipation. Viscosity acts in a straightforward way: it aims to reduce enstrophy anywhere there is a gradient of the vorticity. Buoyancy also acts in a fairly straightforward way: Downflows ($T_1 < 0$) separate areas of positive vorticity (on the left) and negative vorticity (on the right), meaning $\frac{\partial \omega}{\partial x} < 0$, and produce a net positive enstrophy. Upflows act in the same way, where the signs on both terms are switched and the product remains positive. The advective term is more complicated. The $u \frac{\partial \omega^2}{\partial x}$ term seems to destroy enstrophy at plume generation sites and produce it at plume impacting sites. The $w \frac{\partial \omega^2}{\partial z}$ term seems to both generate and destroy enstrophy at impacting sites (probably canceling out), but it generates enstrophy at plume launching sites.

Initial simulation results suggest that the advective generation terms are unimportant, and average out to about zero across the domain. It seems that the baroclinic term generates enstrophy and the viscous term destroys it. When these two terms come into balance, the flywheel is fully developed.

7.1.3 Next steps

Unfortunately, this was as far as this work progressed. Logical next steps would be to figure out the timescales over which the flywheels develop (from theoretical efforts such as those laid out above, and from simulations). Furthermore, carrying out a similar procedure for the compressible equations to understand if the flywheels are as simple to understand there would be crucial in understanding why our Mach number increases with Ra in 2D polytropic convection sims (in Fig. 2.1). Finally, it would be fascinating to understand how the fully compressible equations dissipate flywheel energy at high Mach number (as in the high-Mach 2D cases in Fig. 2.1).

7.2 The Magnitude of Viscous Terms in Turbulent Convection

Historically, the magnitude of viscous terms (like viscous fluxes, and viscous heating) have been thought to be negligible in turbulent convection when diffusivities are small. However, recent work by Currie & Browning (2017) has shown that the volume-integrated contributions of the viscous heating (viscous dissipation) term can exceed the luminosity of the convection, even at very high Rayleigh number. Some of our unpublished work also suggests that viscous dissipation processes can be generally important in stratified convection. For example, the shearing states that we discovered at low Mach number in Ch. 2 had important contributions from the viscous flux. In Fig. 7.2, a simulation with $\text{Ra} = 10^{5.5}$ and $\epsilon = 10^{-4}$ (and otherwise constructed as described in Ch. 2) which displays shearing states is shown, including the large contributions from the viscous fluxes in those states. An extension of the flywheel work, mentioned in the previous section, into the realm of stratified convection would likely be one of the best routes for understanding the importance and magnitude of viscous dissipation and viscous fluxes.

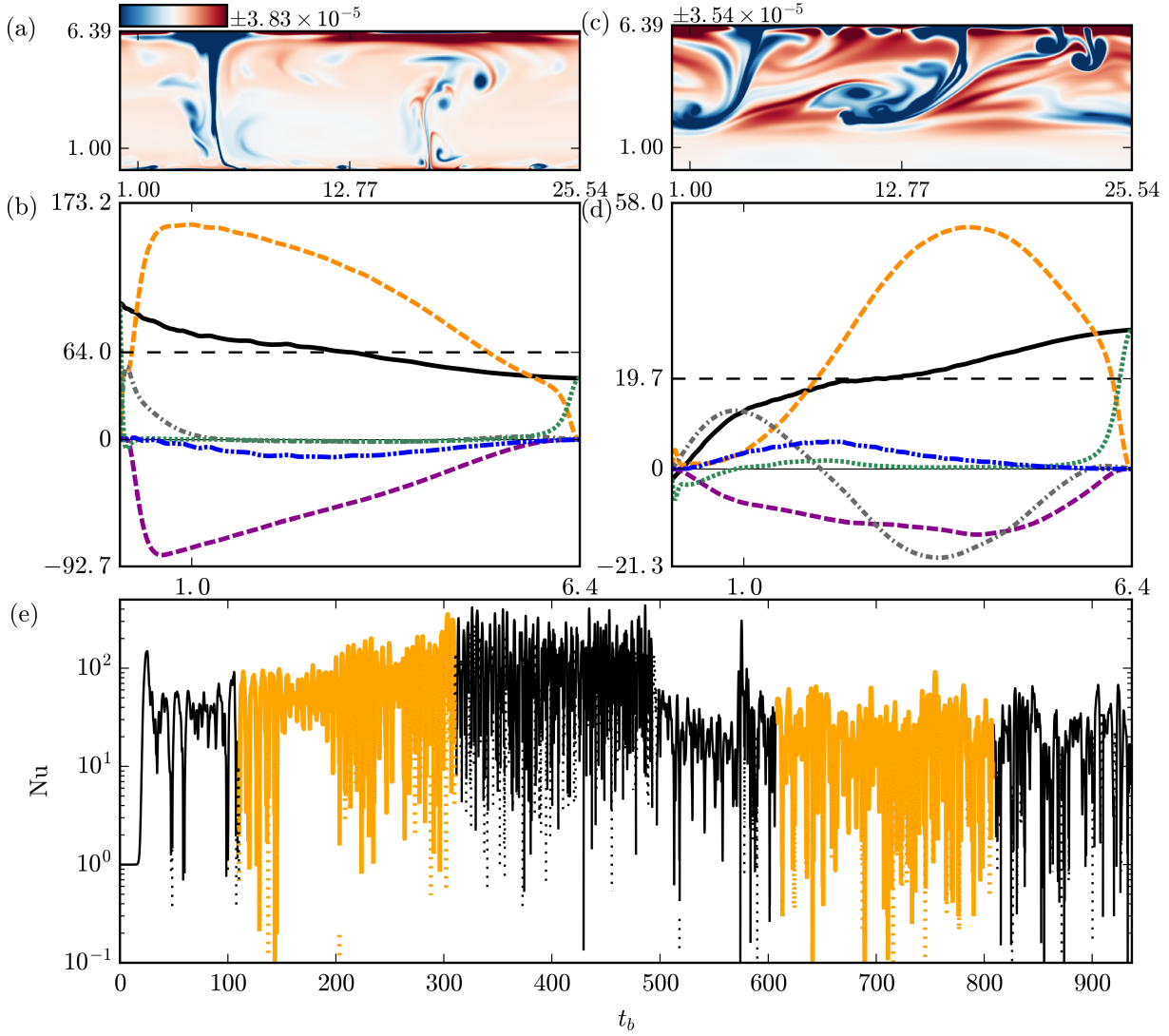


Figure 7.2: (a & c) Entropy anomaly snapshots in low-Mach number, fully compressible convection in a classic roll (a) and shearing (c) state. (b & d) The respective nondimensional fluxes in those systems. The dark black line shows the sum of the fluxes, and the yellow and purple dashed lines respectively show the enthalpy and kinetic energy fluxes. The conductive flux is shown as a dashed green line, and the potential energy flux is shown as a dash-dot-dot blue line. Interestingly, the viscous flux (dash-dot grey line) is never negligible. In the roll state, it is predominantly responsible for carrying the flux near the lower (stress-free) boundary. In the shearing state, it carries most of the flux in the lower part of the domain (and works against flux transport in the upper part of the domain). (e) A trace of the Nusselt number over time. The orange highlighted regions show the time windows over which averages were taken for the fluxes in the roll (left) and shearing (right) states, respectively. The overall magnitude of the flux in the shearing state, and thus the magnitude of Nu, is also very different.

7.3 Internally Heated, Fully Compressible Convection

Convective systems in nature (e.g., in stars) are generally not as simple as the purely boundary-driven convection generally examined in simulations. The next step up in complexity from boundary driven convection is **internally heated** convection, in which the convection is driven by deposition of energy in the bulk of the convective domain. Two instances of internally heated convection in nature are the Sun and the Earth's mantle. In the Sun, the increasing opacity within the solar convection zone (and subsequent divergence of radiative flux) leads to the gradual deposition of energy, as does radioactive decay in the Earth's mantle. Understanding internally heated convection is therefore crucial for characterizing geophysical and astrophysical processes. Inspired by the work of Goluskin & Spiegel (2012) and the concise review of Goluskin (2016), I had hoped to develop and study very simple internally heated, fully compressible systems. Just as polytropic atmospheres have linear temperature profiles and can be compared to Rayleigh-Bénard convection easily, our goal was to develop and study stratified atmospheres driven by a constant (or linear) internal heating term, which would in turn produce quadratic (or cubic) temperature profiles which could be compared to internally heated Boussinesq convection.

7.3.1 Preliminaries: convective stability and available flux

In Boussinesq convection, convective stability is entirely determined by the temperature gradient. There, negative temperature gradients drive convective motions, and positive temperature gradients are stable. When compressibility is taken into account, atmospheres can maintain stability even in the presence of a large, negative temperature gradient (Spiegel & Veronis, 1960). In such atmospheres, it is the gradient of **entropy** which determines stability. In an ideal gas, the specific entropy gradient is defined

$$\nabla S = c_V \nabla \ln T - R \nabla \ln \rho, \quad (7.12)$$

where S , T , and ρ are the specific entropy, temperature, and density; c_V is the specific heat at constant volume; and R is the specific gas constant defining pressure, $P = R\rho T$. Where stability

is concerned, the entropy gradient in compressible systems is a direct analog to the temperature gradient in Boussinesq systems. Regions with $\nabla S < 0$ are unstable to convection, and regions with $\nabla S > 0$ are stable.

Assuming that the convective system remains, to first order, in hydrostatic equilibrium, $\nabla P = \rho \mathbf{g}$, the temperature gradient which characterizes a perfectly adiabatic state is:

$$\nabla_{\text{ad}} = \mathbf{g}/c_P, \quad (7.13)$$

where \mathbf{g} is the gravity and c_P is the specific heat at constant pressure. The “adiabatic temperature gradient,” ∇_{ad} , can in general have a large magnitude, which makes the interpretation of the conductive (or radiative) flux in a system a bit harder to understand. The conductive flux is

$$\mathbf{F}_{\text{cond}} = -\kappa \nabla T, \quad (7.14)$$

where κ is the conductivity. If a system is driven by some quantity of flux, $\mathbf{F}_{\text{drive}}$, we define the “available flux” as

$$\mathbf{F}_{\text{avail}} \equiv \mathbf{F}_{\text{drive}} - \mathbf{F}_{\text{ad}}, \quad (7.15)$$

where the “adiabatic flux,” $\mathbf{F}_{\text{ad}} = -\kappa \nabla_{\text{ad}}$, is flux that can be conducted across an adiabatically stratified atmosphere. If $\mathbf{F}_{\text{avail}} \leq 0$, the system is stable to convection. If $\mathbf{F}_{\text{avail}} > 0$, the system is unstable to convection. Importantly, $\mathbf{F}_{\text{avail}}$ is the **only portion** of the flux that the convection is able to “tap” into. Any amount of $\mathbf{F}_{\text{drive}}$ that is conducted down the adiabatic gradient will not be carried by convection. Thus, $\mathbf{F}_{\text{avail}}$ is a direct analog in compressible systems to the **total** flux carried through a Boussinesq system.

Internally heated (or cooled) convection in which the domain has a convecting region and a stable region is characterized by a heating (or cooling) profile that changes the sign of $\mathbf{F}_{\text{avail}}$.

7.3.2 Disappearance of internal heating term from perturbation equations

Given a constant internal heating term, Q (in units of energy flux / length), the energy equation takes the form

$$\frac{DT}{Dt} + T(\gamma - 1)\nabla \cdot \mathbf{u} = \frac{1}{\rho c_V} (\nabla \cdot (\kappa \nabla T) + Q) + (\text{Viscous Heating}). \quad (7.16)$$

In a static, steady state, thermal equilibrium in the “background” atmosphere satisfies

$$-\nabla \cdot (\kappa \nabla T_0) = Q. \quad (7.17)$$

Assuming that this thermal equilibrium is always met by the background profile (and for simplicity, assuming constant and uniform κ), the energy equation is

$$\frac{DT}{Dt} + T(\gamma - 1)\nabla \cdot \mathbf{u} = \frac{1}{\rho c_V} \nabla \cdot (\kappa \nabla T_1) + (\text{Viscous Heating}). \quad (7.18)$$

In other words, the equation for the perturbations is precisely the same as it is for a case where internal heating is not present, and the internal heating disappears from the system. Internal heating therefore only enters the dynamics by modifying the background profile T_0 from a linear profile to something more complex. The differences in this temperature profile affect dynamics through, for example, the $\mathbf{u} \cdot \nabla T_0$ term in the temperature equation. But – importantly – **dynamics do not directly feel the source term.**

7.3.3 Two internally heated/cooled basic atmospheric models

For these atmospheres, I nondimensionalize the length scale on the **adiabatic** temperature gradient length scale, $\nabla_{\text{ad}} = -g/c_P = -1$, where g is the (uniform) gravity and c_P is the specific heat at constant pressure. The nondimensional timescale is the isothermal sound crossing time of that unit length at the top of the atmosphere. This choice of nondimensionalization makes it clear that these atmospheres are respectively quadratic and cubic perturbations away from a stable adiabatic profile.

7.3.3.1 A two-layer atmosphere

A two-layer, internally heated atmosphere can be simply constructed. These atmospheres have an unstable layer of depth L_C overlying a stable layer of depth L_R ; the total atmospheric depth is $L_z = L_R + L_C$. These atmospheres are constructed around a constant internal heating term,

$$Q = \kappa\epsilon, \quad (7.19)$$

where κ is the thermal conductivity, and this heating term is an $O(\epsilon)$ source term compared to a nondimensional adiabatic flux ($-\kappa\nabla_{\text{ad}} = \kappa$). We assume that the atmosphere satisfies thermal equilibrium,

$$-\kappa\nabla^2 T_0 = Q.$$

We integrate this equation such that the flux is perfectly adiabatic at $z = L_R$ (so $\partial_z T = \nabla_{\text{ad}} = -1$ there), and such that $T_0 = 1$ at the top of the atmosphere. Under these assumptions,

$$T_0 = 1 - (z - L_z) + \epsilon \left(\frac{1}{2}z^2 + L_R z + L_z \left[L_R - \frac{1}{2}L_z \right] \right), \quad (7.20)$$

is the thermally equilibrated profile. The $O(\epsilon)$ terms are the quadratic perturbation around the stable adiabatic profile.

7.3.3.2 A three-layer atmosphere

A three-layer, internally heated & cooled atmosphere can also be constructed. These atmospheres have a stable layer at the top of the atmosphere with depth L_{RT} , a convective layer with depth L_C , and a stable layer at the base of the atmosphere with depth L_{RB} ; the total atmospheric depth is $L_z = L_{RB} + L_C + L_{RT}$. These atmospheres are constructed around an internal heating/cooling profile with the shape

$$Q(z) = -\kappa\epsilon(z - L_{RB} - L_C/2), \quad (7.21)$$

where κ is the thermal conductivity, z is height, and this heating profile is once again an $O(\epsilon)$ source term compared to the adiabatic flux. This profile transitions from positive (heating) to

negative (cooling) halfway through the convection zone. The thermally equilibrated temperature profile which accompanies this heating term is a cubic perturbation from an adiabat,

$$T_0 = 1 - (z - L_z) + \epsilon(Az^3 + Bz^2 + Cz + D), \quad (7.22)$$

where $A = \frac{1}{6}$, $B = -\frac{1}{2}(L_{RB} + L_C/2)$, $C = \frac{1}{2}L_{RB}(L_{RB} + L_C)$, and $D = (-AL_z^3 + BL_z^2 + CL_z)$.

7.3.4 Density profile construction

For both atmospheres, the density profile is constructed numerically by solving a boundary value problem for hydrostatic equilibrium

$$\nabla P_0 = \rho_0 \mathbf{g}, \quad (7.23)$$

under the constraint that the nondimensional density is 1 at the top of the atmosphere.

7.3.5 Next steps

One difficulty of these atmospheres is that they have extremely long thermal relaxation timescales in the deep, stable zone. In order to study these atmospheres fully, it would either be necessary to develop a consistent accelerated evolution procedure for stratified convection (see section 7.4), or it would be necessary to run them down at great computational expense. Either way, the next steps would then be to compare e.g., modified Nusselt numbers in these atmospheres to those in Boussinesq internally heated systems, as laid out in Goluskin (2016).

7.4 Stratified Accelerated Evolution

A natural follow-up to the AE method presented in Ch. 4 is to explore AE in Polytropic, stratified atmospheres. The beginnings of an extension of AE to polytropes was explored. Preliminary results (see Fig. 7.3, experiments performed by Gabo Ortiz-Pena) showed promise in accelerating the atmospheres up to $\text{Ra} \approx 10^{8-9}$ (supercriticalities of $\gtrsim 10^7$).

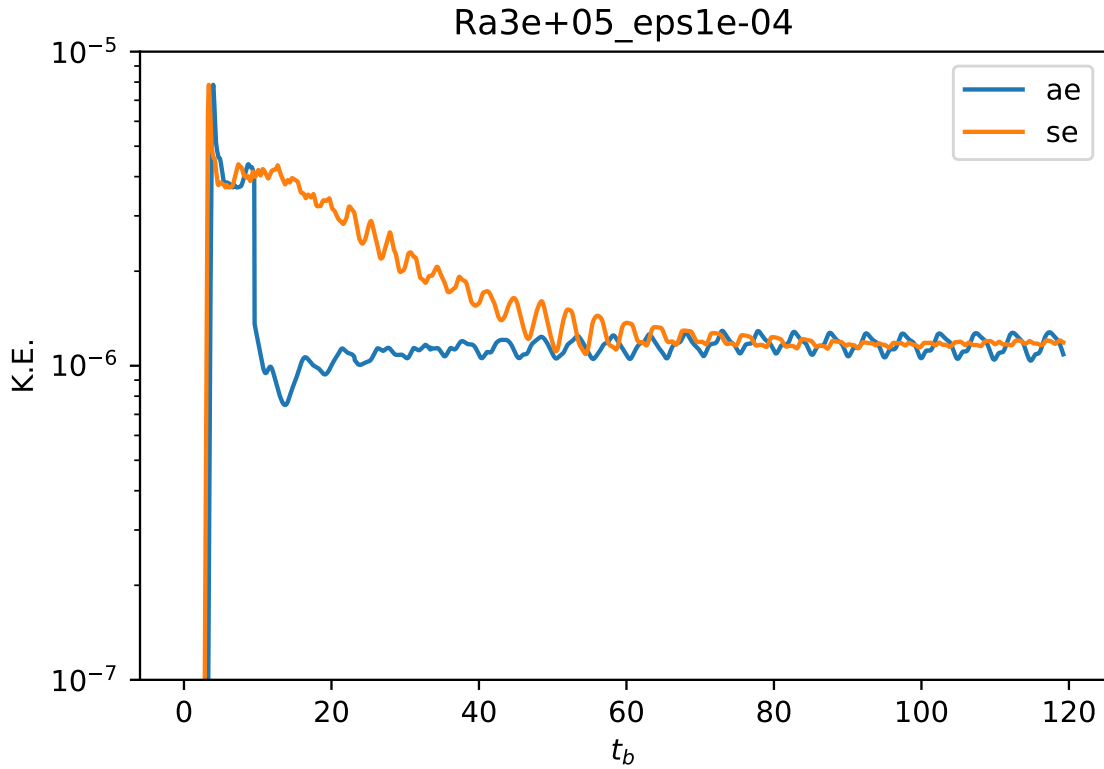


Figure 7.3: Kinetic energy trace of a stratified simulation ($\epsilon = 10^{-4}$, supercriticality $\sim 10^4$) comparing AE and SE kinetic energies. The AE procedure (described in section 7.4.1) seems to reach the proper mean value for the converged kinetic energy, but in this instance it put the system into an oscillatory state not achieved by the SE simulation.

7.4.1 Modifications to the method of Accelerated Evolution

For simplicity, we will restrict our study again to FT boundary conditions – that is, when the flux is fixed at the bottom of the atmosphere, and the temperature is fixed at the top boundary to T_{top} . We additionally restrict this study to the case in which the thermal conductivity, κ , is constant. As described in Sec. 7.3.1, we subtract off the adiabatic flux (\mathbf{F}_{ad}) from the input flux at the bottom boundary ($\mathbf{F}_{\text{drive}}$) to find the available flux for convection, $\mathbf{F}_{\text{avail}} = F\hat{z}$, a constant.

In stratified systems, convection carries energy not only through enthalpy fluxes, but also through fluxes of potential energy, kinetic energy, and viscous forces. All of these new fluxes are

driven by convection, and we therefore define the convective flux as in Ch. 2,

$$\mathbf{F}_{\text{conv}} \equiv \mathbf{F}_{\text{enth}} + \mathbf{F}_{\text{KE}} + \mathbf{F}_{\text{PE}} + \mathbf{F}_{\text{visc}}, \quad (7.24)$$

where $\mathbf{F}_{\text{enth}} \equiv \rho \mathbf{u} (c_V T + P/\rho)$ is the enthalpy flux, $\mathbf{F}_{\text{KE}} \equiv \rho |\mathbf{u}|^2 \mathbf{u}/2$ is the kinetic energy flux, $\mathbf{F}_{\text{PE}} \equiv \rho \mathbf{u} \phi$ (with $\phi \equiv -gz$) is the potential energy flux, and $\mathbf{F}_{\text{visc}} \equiv -\rho \nu \mathbf{u} \cdot \bar{\boldsymbol{\sigma}}$ is the viscous flux. This convective flux combined with the superadiabatic portion of the conductive flux, $\mathbf{F}_{\text{cond,s}} = -\kappa \nabla T - \mathbf{F}_{\text{ad}}$, will carry F_{avail} through the atmosphere in the evolved state.

As in Anders et al. (2018), we find that the fluxes carried through these systems at early times can exceed F_{avail} as the system leaks out its energy and approaches its relaxed states. As a result, we define the profile,

$$\xi(z, t) = \frac{F_{\text{avail}}}{F_{\text{conv}} + F_{\text{cond,s}}}, \quad (7.25)$$

which has a value of unity where the system is carrying the input flux, but whose value is generally less than one at early times while the system is converging. Here, ξ is a measure of the factor by which the flux through the system must be reduced in order for the system to reach its final, equilibrium state. In boundary-driven polytropic convection, where F_{avail} is a uniform, positive value throughout the whole domain, this definition of ξ is fairly robust. Extensions of the AE method which aim to study stable regions will have to come up with a clever adjustment to ξ , but that's beyond the scope of this discussion.

With this definition of ξ , we solve a mass-conserving boundary value problem for a modified thermal and hydrostatic equilibrium,

$$\partial_z M_1 = \rho_0 (e^{\ln \rho_1} - 1), \quad (7.26)$$

$$\kappa \partial_z^2 T_1 = \partial_z (\xi \langle F_{\text{conv}} \rangle), \quad (7.27)$$

$$\partial_z (T_1) + T_1 \partial_z (\ln \rho_0) + T_0 \partial_z (\ln \rho_1) = -T_1 \partial_z (\ln \rho_1) - \xi^{-\frac{2}{3}} \langle \mathbf{u} \cdot \nabla w \rangle. \quad (7.28)$$

with the boundary conditions $M_1 = 0$ at $z = [0, L_z]$, $\partial_z T_1 = 0$ at $z = 0$, and $T_1 = 0$ at $z = L_z$. Here, the exponent of $\xi^{2/3}$ in the hydrostatic equilibrium equation comes from the assumption that

the flux scales like the kinetic energy $F \sim \rho u^3$, so in scaling the flux by ξ , we must equivalently scale the velocities by roughly $\xi^{1/3}$. It's unclear if this is a good assumption.

7.4.2 Next steps

The first obvious next step is to actually see if this procedure works robustly (so far we've only checked it chi-by-eye). After that, a very important project would be to incorporating a procedure that successfully accounts for stable layers. It is probable that the knowledge gained in Ch. 5 will be essential in extending AE. This is to say: thermal relaxation happens in two parts (changes to the energy reservoir and stratification). AE should likely therefore have two parts (a change to the energy reservoir step based on current flux divergence, and a boundary value problem which solves for the proper stratification under those new energy constraints).

7.5 A Freefall Nondimensionalization of the Fully Compressible Equations

In our standard nondimensionalizations of the fully compressible equations, we nondimensionalize based on the sound speed rather than on the convective velocity (freefall) speed. In order to compare results with anelastic equations which were nondimensionalized on the freefall timescale, we presented a form of the fully compressible equations in Ch. 6 which were scaled so that one time unit was one freefall time unit. However, the version of the fully compressible equations presented in Ch. 6 is essentially nondimensionalized twice, which isn't ideal. Technically, it is first nondimensionalized on the sound speed and average atmospheric temperature (as in Ch. 2), and then it is again rescaled based off of the magnitude of thermodynamic perturbations and the freefall velocity. This works, but it's confusing. I have faith in the results of the **simulations** from that chapter, which were conducted using a numerical form of the compressible equations similar to the one presented in Ch. 2, and then rescaled in post-processing.

It would be ideal to have a set of fully compressible equations which are nondimensionalized on the freefall timescale. This would be useful both for future comparisons to anelastic simulations, but also for numerical stability at low Mach number (where thermodynamic perturbations are $O(\epsilon)$).

$O(1)$ would be better). The formulation of the equations that I will derive here aim to understand what the nondimensional fully compressible equations look like when the convective velocities and thermal perturbations are all $O(1)$, regardless of the Mach number.

7.5.1 Equation formulation derivation

We define the fully compressible equations in Anders & Brown (2017) as:

$$\partial_{\tilde{t}} \ln \tilde{\rho}_1 + \tilde{\mathbf{u}} \cdot \tilde{\nabla} \ln \tilde{\rho}_0 + \tilde{\nabla} \cdot \tilde{\mathbf{u}} = -\tilde{\mathbf{u}} \cdot \tilde{\nabla} \ln \tilde{\rho}_1 \quad (7.29)$$

$$\begin{aligned} \partial_{\tilde{t}} \tilde{\mathbf{u}} + R(\tilde{\nabla} \tilde{T}_1 + \tilde{T}_1 \tilde{\nabla} \ln \tilde{\rho}_0 + \tilde{T}_0 \tilde{\nabla} \ln \tilde{\rho}_1) - \tilde{\nu} \left(\tilde{\nabla}^2 \tilde{\mathbf{u}} + \frac{1}{3} \tilde{\nabla} (\tilde{\nabla} \cdot \tilde{\mathbf{u}}) + \tilde{\nabla} \ln \tilde{\rho}_0 \cdot \tilde{\tilde{\sigma}} \right) - \tilde{\nabla} \tilde{\nu} \cdot \tilde{\tilde{\sigma}} \\ = -\tilde{\mathbf{u}} \cdot \tilde{\nabla} \tilde{\mathbf{u}} - R \tilde{T}_1 \tilde{\nabla} \ln \tilde{\rho}_1 + \tilde{\nu} \tilde{\nabla} \ln \tilde{\rho}_1 \cdot \tilde{\tilde{\sigma}} \end{aligned} \quad (7.30)$$

$$\begin{aligned} \partial_{\tilde{t}} \tilde{T}_1 + \tilde{\mathbf{u}} \cdot \tilde{\nabla} \tilde{T}_0 + \tilde{T}_0 (\gamma - 1) \tilde{\nabla} \cdot \tilde{\mathbf{u}} - \frac{c_P}{c_V} \left(\tilde{\chi} \left\{ \tilde{\nabla}^2 \tilde{T}_1 + \tilde{\nabla} \ln \tilde{\rho}_0 \cdot \tilde{\nabla} \tilde{T}_1 + \tilde{\nabla} \ln \tilde{\rho}_1 \cdot \tilde{\nabla} \tilde{T}_0 \right\} + \tilde{\nabla} \tilde{\chi} \cdot \tilde{\nabla} \tilde{T}_1 \right) \\ = \frac{\tilde{\chi} c_P}{c_V} \tilde{\nabla} \ln \tilde{\rho}_1 \cdot \tilde{\nabla} \tilde{T}_1 - \tilde{\mathbf{u}} \cdot \tilde{\nabla} \tilde{T}_1 - \tilde{T}_1 (\gamma - 1) \tilde{\nabla} \cdot \tilde{\mathbf{u}} + \frac{\tilde{\nu}}{c_V} \tilde{\tilde{\sigma}} \cdot \tilde{\nabla} \cdot \tilde{\mathbf{u}}. \end{aligned} \quad (7.31)$$

Here, the tildes over the terms stand for “dimensionful” quantities (or quantities that I haven’t rescaled yet). Those are going to be dropped. Only two real assumptions have happened so far: I’ve assumed hydrostatic equilibrium of the background quantities in the momentum equation, and I’ve assumed thermal equilibrium of the background quantities in the energy equation. The rest of this nondimensionalization is predicated around the linearized equation of state,

$$\frac{\rho_1}{\rho_0} = \frac{P_1}{P_0} - \frac{T_1}{T_0},$$

and the assumption that for low Mach number flows, each of the quantities in this equation is essentially $O(\epsilon)$. We now nondimensionalize all quantities,

$$\begin{aligned} \tilde{T} &= \bar{T} T, \\ \tilde{\nabla} &= L^{-1} \nabla, \quad \partial_{\tilde{t}} = \tau^{-1} \partial_t, \\ \tilde{\nu} &= \nu \xi(z), \quad \tilde{\chi} = \chi \xi(z), \\ u_{\text{ff}} &= L/\tau, \end{aligned} \quad (7.32)$$

and note that $\ln \rho$ is already dimensionless in its nature. Here, $\xi(z)$ is the nondimensional shape of the diffusivity profiles. The nondimensional momentum equation is

$$\begin{aligned} & \frac{D\mathbf{u}}{Dt} + \frac{R\bar{T}}{u_{\text{ff}}^2} (\nabla T_1 + T_1 \nabla \ln \rho_0 + T_0 \nabla \ln \rho_1 + T_1 \nabla \ln \rho_1) \\ &= \frac{\nu\tau}{L^2} \left(\xi \left[\nabla^2 \mathbf{u} + \frac{1}{3} \nabla(\nabla \cdot \mathbf{u}) + \nabla \ln \rho_0 \cdot \bar{\boldsymbol{\sigma}} + \nabla \ln \rho_1 \cdot \bar{\boldsymbol{\sigma}} \right] + \nabla \xi \cdot \bar{\boldsymbol{\sigma}} \right) \end{aligned} \quad (7.33)$$

We now make the choice that the nondimensional scale of the temperature perturbations is $O(\epsilon)$ compared to the background temperature, $\bar{T} = \epsilon T_0$. Per Ch. 2, the isothermal Mach number of these flows is roughly $\text{Ma}_{\text{iso}} = \sqrt{\epsilon}$, so the choice that

$$u_{\text{ff}} = \sqrt{R\bar{T}} \sim \text{Ma}_{\text{iso}}$$

means that we're roughly nondimensionalizing on the freefall velocity of the flows. The continuity and momentum equation under this assumption are then

$$\begin{aligned} & \frac{D \ln \rho_1}{Dt} + (\mathbf{u} \cdot \nabla \ln \rho_0 + \nabla \cdot \mathbf{u}) = 0 \\ & \frac{D\mathbf{u}}{Dt} + (\nabla T_1 + T_1 \nabla \ln \rho_0 + T_0 \nabla \ln \rho_1 + T_1 \nabla \ln \rho_1) \\ &= \frac{1}{\text{Re}_{\text{ff}}} \left(\xi \left[\nabla^2 \mathbf{u} + \frac{1}{3} \nabla(\nabla \cdot \mathbf{u}) + \nabla \ln \rho_0 \cdot \bar{\boldsymbol{\sigma}} + \nabla \ln \rho_1 \cdot \bar{\boldsymbol{\sigma}} \right] + \nabla \xi \cdot \bar{\boldsymbol{\sigma}} \right) \end{aligned} \quad (7.34) \quad (7.35)$$

where the freefall Reynolds number is

$$\text{Re}_{\text{ff}} = \frac{u_{\text{ff}} L}{\nu} = \sqrt{\frac{\text{Ra}}{\text{Pr}}} \quad (\text{in the case of convection}).$$

The nondimensional temperature equation is

$$\begin{aligned} & \frac{DT_1}{Dt} + (\mathbf{u} \cdot \nabla T_0 + (T_0 + T_1)(\gamma - 1) \nabla \cdot \mathbf{u}) \\ &= \frac{\chi\tau c_P}{c_V L^2} \left(\xi \left[\nabla^2 T_1 + \nabla \ln \rho_0 \cdot \nabla T_1 + \nabla \ln \rho_1 \cdot \nabla T_0 + \nabla \ln \rho_1 \cdot \nabla T_1 \right] + \nabla \xi \cdot \nabla T_1 \right) + \frac{\nu}{c_V \bar{T}\tau} \xi \bar{\boldsymbol{\sigma}} \cdot \nabla \cdot \mathbf{u}. \end{aligned} \quad (7.36)$$

The viscous heating term is a bit tricky, but substituting $\bar{T} = u_{\text{ff}}^2/R^2$, we're left with

$$\begin{aligned} & \frac{DT_1}{Dt} + (\mathbf{u} \cdot \nabla T_0 + (T_0 + T_1)(\gamma - 1) \nabla \cdot \mathbf{u}) \\ &= \frac{c_P}{c_V \text{Pe}_{\text{ff}}} \left(\xi \left[\nabla^2 T_1 + \nabla \ln \rho_0 \cdot \nabla T_1 + \nabla \ln \rho_1 \cdot \nabla T_0 + \nabla \ln \rho_1 \cdot \nabla T_1 \right] + \nabla \xi \cdot \nabla T_1 \right) + \frac{R^2}{c_V \text{Re}_{\text{ff}}} \xi \bar{\boldsymbol{\sigma}} \cdot \nabla \cdot \mathbf{u}, \end{aligned} \quad (7.37)$$

where

$$P_{\text{eff}} = R_{\text{eff}} \Pr.$$

Note that it is **crucial** that you consistently nondimensionalize the background temperature profile so that both it—and gravity—are $O(\epsilon^{-1})$. Which is to say that, if you’re using a polytrope, rather than $T_0 = 1 + (L_z - z)$, you need to specify

$$T_0 = \epsilon^{-1} (1 + [L_z - z]),$$

and gravity will be $g = (1 + m)/\epsilon$, for m the polytropic index. Per the polytropic assumption, $\rho = T^m$ still holds, so $\ln \rho_0$ will be shifted by $-\ln(\epsilon)$.

One thing that’s nice about this nondimensionalization, in addition to having $O(1)$ flows for numerical stability, is that it’s clear to see where the linear wave terms come from. Any term that has a T_0 in it is large, or $O(\epsilon^{-1})$ compared to the other terms, so these are the stiff terms in the equations.

7.6 Convection with Kramer’s Opacity

All of the experiments presented in this work utilized a constant conductivity. The Sun, however, has a conductivity which varies by orders of magnitude over the course of its convection zone. In the optically thick, deep convection zone, the opacity in the Sun can be modeled as a Kramer’s Opacity (see e.g., Brandenburg, 2016), and the conductivity is a radiative conductively constructed with that opacity choice. Some recent simulation work by Käpylä et al. (2017) compared some convection which utilized polytropic-like stratifications with a constant conductivity to simulations with a Kramer’s-informed conductivity. They found some interesting things, including “Deardorff” layers, which are layers in the convection zone which are marginally stable but which have a positive convective flux. They claim that these are only seen with the realistic Kramer’s-like opacity. Internally, as a research group, we have observed extended Deardorff layers even in simpler polytropic atmospheres. In this project, we had hoped to discover what it is about a Kramer’s-like

opacity in their simulations that caused them to see such deep Deardorff layers. In the end, what we learned was that using a Kramer's opacity is difficult in DNS.

7.6.1 Single-layer, polytropic atmospheres

The radiative conductivity in a simulation with a Kramer's opacity (Käpylä et al., 2017) takes the form

$$\kappa(z) = \kappa_0 \left(\frac{\rho}{\rho_c} \right)^{-(1+a)} \left(\frac{T}{T_c} \right)^{(3-b)}.$$

The conductivity profile in the solar convection profile is fairly well described by such a formulation with $a = 1$ and $b = -7/2$. The thermal diffusivity is $\chi = \kappa/(\rho c_P)$. If a polytropic atmosphere is assumed ($\rho \propto T^m$), the polytropic index that achieves a constant Kramer's opacity (Jones, 1976) is

$$m_{kram} = \frac{3-b}{1+a}.$$

Note that if the adiabatic index is $\gamma = 5/3$, then the solar values for a and b produce $m_{kram} = 3.25 > m_{ad}$ (see Ch. 2), producing a stable stratification. However, a choice of $a = 1$ with values of $b = (0, 1]$ get the proper “flavor” of this opacity ($\rho^{-2}, T^{\text{nonzero integer}}$). Furthermore, this choice of exponents leads to

$$m_{kram} = 1.5 - b/2 = m_{ad} - b/2. \quad (7.38)$$

So b should behave like 2ϵ from Ch. 2, driving low or high Mach number flows accordingly. We had some success simulating these atmospheres (where we set up the initial conditions to have $m = m_{kram}$).

However, when we tried to reproduce some of the results of Käpylä et al. (2017), we ran into some roadblocks. The solar choices of $a = 1$ and $b = -7/2$ in the presence of a perfectly adiabatic atmosphere result in the conductivity dropping by orders of magnitude. This essentially drives convection which is $O(\text{large})$ and very high Mach number, and also requires impossibly large temperature gradients in the boundary layers to conduct the fluxes. Past authors used SGS tactics to get around this, but I didn't know how to choose a proper SGS model, nor did I trust that I

would be able to consistently interpret and compare simulations with SGS models to those without.

So – I dropped this project. However, it is still really unclear how nonlinear conductivities affect convective flows at a fundamental level, and this should be pursued in more detail.

7.6.2 A note on implementing a Kramer's Opacity in Dedalus

A fully nonlinear conductivity is not something that we often deal with in our Dedalus scripts. However, it's quite easy to implement a Kramer's-informed radiative conductivity (or any nonlinear conductivity) through the following procedure. If we have a radiative conductivity of the form,

$$\kappa(\ln \rho, T) = \kappa_0 \rho^{-(1+a)} T^{3-b} = \kappa_0 \left(e^{\ln \rho} \right)^{-(1+a)} T^{3-b}, \quad (7.39)$$

then we can Taylor expand around our thermodynamic variables ($T, \ln \rho$) into constant, linear, and nonlinear components,

$$\kappa(\ln \rho, T) = \kappa(\ln \rho_0, T_0) + \frac{\partial \kappa}{\partial T} \Big|_{\ln \rho_0, T_0} (T - T_0) + \frac{\partial \kappa}{\partial \ln \rho} \Big|_{\ln \rho_0, T_0} (\ln \rho - \ln \rho_0) + \kappa_{NL}. \quad (7.40)$$

To evaluate that, we need a couple of derivatives:

$$\begin{aligned} \frac{\partial \kappa}{\partial T} \Big|_{\rho_0, T_0} &= \kappa_0 (3-b) \rho_0^{-(1+a)} T_0^{2-b} = (3-b) \frac{\kappa(\ln \rho_0, T_0)}{T_0} \\ \frac{\partial \kappa}{\partial \ln \rho} \Big|_{\rho_0, T_0} &= \rho \frac{\partial \kappa}{\partial \rho} \Big|_{\rho_0, T_0} = -(1+a) \kappa_0 \rho_0^{-(1+a)} T_0^{3-b} = -(1+a) \kappa(\ln \rho_0, T_0), \end{aligned} \quad (7.41)$$

and after quick substitutions,

$$\kappa(\rho, T) = \kappa(\rho_0, T_0) \left(1 + (3-b) \frac{T_1}{T_0} - (1+a) \ln \rho_1 \right) + \kappa_{NL} \quad (7.42)$$

At this point, I will define the constant, linear, and nonlinear parts of κ ,

$$\begin{aligned} \kappa_C &\equiv \kappa(\rho_0, T_0) \\ \kappa_L &\equiv \kappa_C \left((3-b) \frac{T_1}{T_0} - (1+a) \ln \rho_1 \right) \\ \kappa_{NL} &\equiv \kappa - \kappa_C - \kappa_L. \end{aligned} \quad (7.43)$$

Note that the trick here is that we peel away the constant (trivial) and linear (easy) portions of the conductivity from the full, hard opacity. In general, at least at low Mach number, κ_{NL} is likely quite small.

The LHS of the energy equation has a term

$$\text{DivFcond} = \nabla \cdot (-\kappa \nabla T) = -(\kappa \nabla^2 T + \nabla \kappa \cdot \nabla T), \quad (7.44)$$

which can be simply broken up into linear (L) and nonlinear (NL) components,

$$\begin{aligned} \text{DivFcond_L} &= -(\kappa_L \nabla^2 T_0 + \kappa_C \nabla^2 T_1 + \nabla T_0 \cdot \nabla \kappa_L + \nabla T_1 \cdot \nabla \kappa_C) \\ \text{DivFcond_NL} &= -((\kappa - \kappa_L) \nabla^2 T_0 + (\kappa - \kappa_C) \nabla^2 T_1 + \nabla T_0 \cdot \nabla(\kappa - \kappa_L) + \nabla T_1 \cdot \nabla(\kappa - \kappa_C)), \end{aligned} \quad (7.45)$$

where the background profile has here been assumed to be in thermal equilibrium.

7.7 Turbulent Thermals

The next logical step in the study presented in Ch. 6 is a study of turbulent thermals. I have performed some initial simulations of anelastic, 3D thermals at $\text{Re} = 4 \cdot 10^3$, but the initial results from these simulations are rather perplexing. See Fig. 7.4.

While simulations of thermals are not computationally expensive in **time** (they are short), they are expensive in terms of **memory**. Even the laminar simulations presented in Ch. 6 took many coefficients to resolve, and were nearly at the limits of our computational abilities on a system like NASA Pleiades. Increasing the turbulence (the Reynolds number) by an order of magnitude is therefore quite difficult. In order to get around this problem, we changed the formulation of our diffusivities. Rather than holding the **dynamic** diffusivities constant (as we did in Ch. 6), we here held the diffusivities (in units of cm^2/s) constant. This means that the dynamic viscosities grow proportionally to density. Importantly, in compressible or anelastic domains, this means that the viscous heating term (in the equation for total entropy or for total energy) grows with density. This choice seems to eat away at the buoyant signature of our dense thermals by heating them as they fall, and this in turn reduces the thermal acceleration. This messes up our theory, because we assumed the buoyant signature was constant in time.

The theory of thermals that we derived in Ch. 6 revolved around the **momentum** and the **entropy** (which is density-weighted, unlike the specific entropy). The form of the diffusivities that

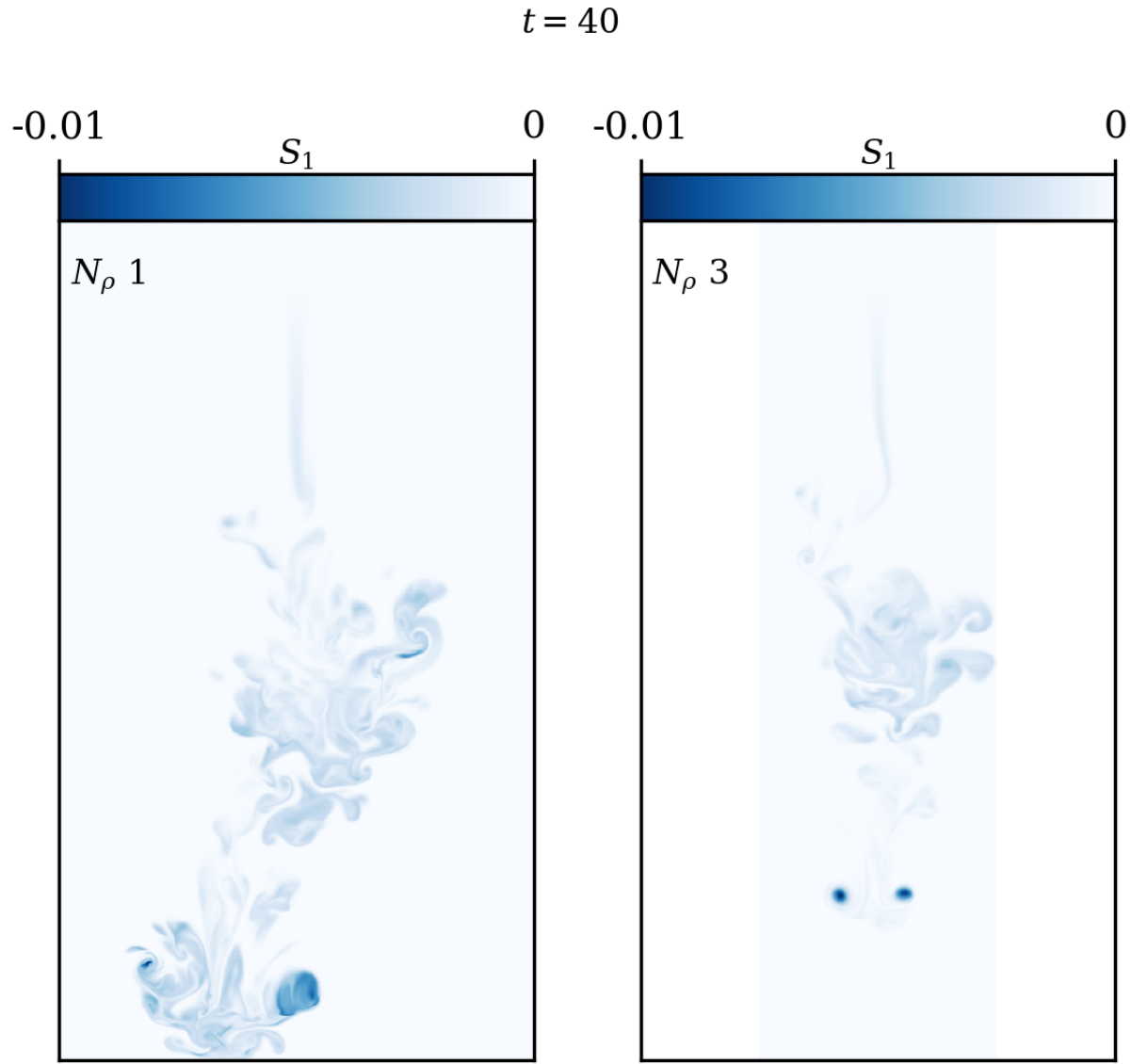


Figure 7.4: Horizontal slices through Cartesian domains containing evolved turbulent thermals. In both cases, the initial freefall Reynolds number of the thermals is $4 \cdot 10^3$. On the left is an evolved thermal in a 1-density-scale-height atmosphere. On the right is an evolved thermal in a 3-density-scale-height atmosphere. There are two observations that can be made from this figure that are strange. First, the vortex ring on the right looks quite laminar, whereas the one on the left looks quite turbulent. Second, unlike in the results of Ch. 6, the thermal in the highly stratified atmosphere is falling **slower** than the one on the right.

appear in the equations for those quantities are the **dynamic** diffusivities, which in these initial turbulent simulations grow with depth. Moreover, they grow more with depth in a highly stratified atmosphere than they do in an atmosphere which is not highly stratified. These initial results suggest that if one wants to study dynamics which are equally turbulent throughout the full depth of an atmosphere, the “proper” choice of diffusivities is to hold the dynamic diffusivities constant, meaning that the diffusivities shrink with depth like ρ .

Regardless, these initial struggles and the high computational expense of turbulent thermals have currently caused this project to stall out. Furthermore, from some conversations with Mark Rast, there is some reason to perhaps be concerned about simulating cylindrical structures in Cartesian domains (see e.g., Fig. 9 of Clyne et al., 2007), as the shape of the domain can lead to non-axisymmetric unrealistic perturbations. The striking similarity reported between 2D (cylindrical) and 3D (Cartesian) domains in Ch. 6 gives optimism that those calculations should be trusted, but it would likely be ideal to conduct future experiments in cylindrical domains if possible.

Bibliography

- Aerts, C., Christensen-Dalsgaard, J., & Kurtz, D. W. 2010, Asteroseismology (Springer Science)
- Ahlers, G., Grossmann, S., & Lohse, D. 2009, *Reviews of Modern Physics*, **81**, 503
- Akhmetov, D. G. 2009, Vortex rings (Berlin, Heidelberg: Springer Berlin Heidelberg), 1
- Anders, E. H. 2020, evanhanders/boussinesq-convection: Version of Code released with FT / TT paper (Anders+ 2020) submission.
- Anders, E. H., & Brown, B. P. 2017, *Physical Review Fluids*, **2**, 083501
- Anders, E. H., Brown, B. P., & Oishi, J. S. 2018, *Physical Review Fluids*, **3**, 083502
- Anders, E. H., Lecoanet, D., & Brown, B. P. 2019, *The Astrophysical Journal*, **884**, 65
- Anders, E. H., Lecoanet, D., & Brown, B. P. 2019a, Supplemental Materials for "Entropy Rain: Dilution and Compression of Thermals in Stratified Domains"
- Anders, E. H., Manduca, C. M., Brown, B. P., Oishi, J. S., & Vasil, G. M. 2019b, *The Astrophysical Journal*, **872**, 138
- . 2019c, Supplemental Materials: Predicting the Rossby number in convective experiments
- Anders, E. H., Vasil, G. M., Brown, B. P., & Korre, L. 2020, Supplemental Materials:
- Andrassy, R., Herwig, F., Woodward, P., & Ritter, C. 2020, *Monthly Notices of the Royal Astronomical Society*, **491**, 972
- Ascher, U. M., Ruuth, S. J., & Spiteri, R. J. 1997, *Applied Numerical Mathematics*, **25**, 151
- Augustson, K. C., Brown, B. P., Brun, A. S., Miesch, M. S., & Toomre, J. 2012, *The Astrophysical Journal*, **756**, 169
- Aurnou, J. M., Bertin, V., Grannan, A. M., Horn, S., & Vogt, T. 2018, *Journal of Fluid Mechanics*, **846**, 846
- Aurnou, J. M., & King, E. M. 2017, *Proceedings of the Royal Society of London Series A*, **473**, 20160731
- Avrett, E. H., & Loeser, R. 2008, *The Astrophysical Journal Supplemental Series*, **175**, 229

- Barker, A. J., Dempsey, A. M., & Lithwick, Y. 2014, *The Astrophysical Journal*, 791, 13
- Bedding, T. R., Butler, R. P., Kjeldsen, H., et al. 2001, *The Astrophysical Journal Letters*, 549, L105
- Bellinger, E. P. 2018, PhD thesis, Max Planck Institute for Solar System Research
- Bercovici, D. 2003, *Earth and Planetary Science Letters*, 205, 107
- Böhm-Vitense, E. 1958, *Zeitschrift fuer Astrophysik*, 46, 108
- Bordwell, B., Brown, B. P., & Oishi, J. S. 2018, *The Astrophysical Journal*, 854, 8
- Borrero, J. M., & Bellot Rubio, L. R. 2002, *Astronomy and Astrophysics*, 385, 1056
- Bouchy, F., & Carrier, F. 2001, *Astronomy and Astrophysics*, 374, L5
- Bouillaud, V., Lepot, S., Aumaître, S., & Gallet, B. 2019, *Journal of Fluid Mechanics*, 861, R5
- Braginsky, S. I., & Roberts, P. H. 1995, *Geophysical and Astrophysical Fluid Dynamics*, 79, 1
- Brandenburg, A. 2016, *The Astrophysical Journal*, 832, 6
- Brandenburg, A., Chan, K. L., Nordlund, Å., & Stein, R. F. 2005, *Astronomische Nachrichten*, 326, 681
- Brandenburg, A., & Dobler, W. 2010, Pencil: Finite-difference Code for Compressible Hydrodynamic Flows
- Brandenburg, A., & Hazlehurst, J. 2001, *Astronomy and Astrophysics*, 370, 1092
- Brandenburg, A., Jennings, R. L., Nordlund, Å., et al. 1996, *Journal of Fluid Mechanics*, 306, 325
- Brandenburg, A., & Subramanian, K. 2005, *Physics Reports*, 417, 1
- Brown, B. 2011, in *Journal of Physics Conference Series*, Vol. 271, GONG-SoHO 24: A New Era of Seismology of the Sun and Solar-Like Stars, 012064
- Brown, B. P., Browning, M. K., Brun, A. S., Miesch, M. S., & Toomre, J. 2008, *The Astrophysical Journal*, 689, 1354
- . 2010, *The Astrophysical Journal*, 711, 424
- Brown, B. P., Miesch, M. S., Browning, M. K., Brun, A. S., & Toomre, J. 2011, *The Astrophysical Journal*, 731, 69
- Brown, B. P., Vasil, G. M., & Zweibel, E. G. 2012, *The Astrophysical Journal*, 756, 109
- Brummell, N. H., Clune, T. L., & Toomre, J. 2002, *The Astrophysical Journal*, 570, 825
- Brummell, N. H., Hurlburt, N. E., & Toomre, J. 1996, *The Astrophysical Journal*, 473, 494
- . 1998, *The Astrophysical Journal*, 493, 955
- Brun, A. S., & Browning, M. K. 2017, *Living Reviews in Solar Physics*, 14, 4

- Brun, A. S., Strugarek, A., Varela, J., et al. 2017, *The Astrophysical Journal*, 836, 192
- Buldgen, G. 2019, arXiv e-prints, arXiv:1902.10399
- Burns, K., Vasil, G., Oishi, J., Lecoanet, D., & Brown, B. 2016, Dedalus: Flexible framework for spectrally solving differential equations, *Astrophysics Source Code Library*, [ascl:1603.015](#)
- Burns, K. J., Vasil, G. M., Oishi, J. S., Lecoanet, D., & Brown, B. P. 2019, arXiv e-prints, arXiv:1905.10388
- Busse, F. H. 1978, *Reports on Progress in Physics*, 41, 1929
- . 2002, *Physics of Fluids*, 14, 1301
- Calkins, M. A., Julien, K., & Marti, P. 2015, *Geophysical and Astrophysical Fluid Dynamics*, 109, 422
- Cattaneo, F., Brummell, N. H., Toomre, J., Malagoli, A., & Hurlburt, N. E. 1991, *The Astrophysical Journal*, 370, 282
- Cattaneo, F., Hurlburt, N. E., & Toomre, J. 1990, *Astrophys. J. Lett.*, 349, L63
- Chan, K. L., Sofia, S., & Wolff, C. L. 1982, *The Astrophysical Journal*, 263, 935
- Chandrasekhar, S. 1961, Hydrodynamic and hydromagnetic stability
- Charbonneau, P. 2010, *Living Reviews in Solar Physics*, 7, 3
- . 2014, *Annual Review of Astronomy and Astrophysics*, 52, 251
- Cheng, J. S., Stellmach, S., Ribeiro, A., et al. 2015, *Geophysical Journal International*, 201, 1
- Christensen, U. R. 2011, *Physics of the Earth and Planetary Interiors*, 187, 157
- Christensen-Dalsgaard, J. 2002, *Reviews of Modern Physics*, 74, 1073
- Christensen-Dalsgaard, J., Dappen, W., Ajukov, S. V., et al. 1996, *Science*, 272, 1286
- Cioni, S., Chaumat, S., & Sommeria, J. 2000, *Physical Review E*, 62, R4520
- Clarkson, O., Herwig, F., & Pignatari, M. 2018, *Monthly Notices of the Royal Astronomical Society*, 474, L37
- Clyne, J., Mininni, P., Norton, A., & Rast, M. 2007, *New Journal of Physics*, 9, 301
- Cossette, J.-F., & Rast, M. P. 2016, *The Astrophysical Journal Letters*, 829, L17
- Courant, R., Friedrichs, K., & Lewy, H. 1967, *IBM Journal of Research and Development*, 11, 215
- Couston, L. A., Lecoanet, D., Favier, B., & Le Bars, M. 2017, *Physical Review Fluids*, 2, 094804
- Couston, L.-A., Lecoanet, D., Favier, B., & Le Bars, M. 2019, arXiv e-prints, arXiv:1909.03244
- Currie, L. K., Barker, A. J., Lithwick, Y., & Browning, M. K. 2020, arXiv e-prints, arXiv:2002.02461
- Currie, L. K., & Browning, M. K. 2017, *The Astrophysical Journal Letters*, 845, L17

- Deardorff, J. W. 1970, *Journal of Fluid Mechanics*, **41**, 453
- Ecke, R. E., & Niemela, J. J. 2014, *Physical Review Letters*, **113**, 114301
- Featherstone, N. A., & Hindman, B. W. 2016a, *The Astrophysical Journal Letters*, **830**, L15
- . 2016b, *The Astrophysical Journal Letters*, **830**, L15
- Galsgaard, K. 2011, Stagger: MHD Method for Modeling Star Formation, *Astrophysics Source Code Library*, [ascl:1105.012](#)
- Gastine, T., Wicht, J., & Aubert, J. 2016, *Journal of Fluid Mechanics*, **808**, 690
- Gastine, T., Yadav, R. K., Morin, J., Reiners, A., & Wicht, J. 2014, *Monthly Notices of the Royal Astronomical Society*, **438**, L76
- Glatzmaier, G. A., & Gilman, P. A. 1982, *The Astrophysical Journal*, **256**, 316
- Goffrey, T., Pratt, J., Viallet, M., et al. 2017, *Astronomy and Astrophysics*, **600**, A7
- Goluskin, D. 2016, Internally Heated Convection and Rayleigh-Bénard Convection (Springer International Publishing)
- Goluskin, D., Johnston, H., Flierl, G. R., & Spiegel, E. A. 2014, *J. Fluid Mech.*, **759**, 360
- Goluskin, D., & Spiegel, E. A. 2012, *Physics Letters A*, **377**, 83
- Graham, E. 1975, *Journal of Fluid Mechanics*, **70**, 689
- Greer, B. J., Hindman, B. W., Featherstone, N. A., & Toomre, J. 2015, *Astrophys J. Lett.*, **803**, L17
- Greer, B. J., Hindman, B. W., & Toomre, J. 2016, *The Astrophysical Journal*, **824**, 4
- Grossmann, S., & Lohse, D. 2000, *J. Fluid Mech.*, **407**, 27
- Guerrero, G., Smolarkiewicz, P. K., Kosovichev, A. G., & Mansour, N. N. 2013, *The Astrophysical Journal*, **779**, 176
- Hanasoge, S. M., Duvall, T. L., & Sreenivasan, K. R. 2012, *Proceedings of the National Academy of Science*, **109**, 11928
- Hansen, C. J., Kawaler, S. D., & Trimble, V. 2004, Stellar interiors : physical principles, structure, and evolution (Springer Science)
- Hathaway, D. H., Teit, T., Norton, A. A., & Kitiashvili, I. 2015, *The Astrophysical Journal*, **811**, 105
- Held, L. E., & Latter, H. N. 2018, *Monthly Notices of the Royal Astronomical Society*, **480**, 4797
- Hotta, H. 2017, *The Astrophysical Journal*, **843**, 52
- Huber, D., Basu, S., Beck, P., et al. 2019, *Bulletin of the AAS*, **51**, 488
- Hurlburt, N. E., Toomre, J., & Massaguer, J. M. 1984, *The Astrophysical Journal*, **282**, 557

- . 1986, *The Astrophysical Journal*, 311, 563
- Johnston, H., & Doering, C. R. 2009, *Phys. Rev. Lett.*, 102, 064501
- Jones, C. A. 1976, *Monthly Notices of the Royal Astronomical Society*, 176, 145
- Jones, C. A., Mizerski, K., & Mouloud, K. 2019, compressible Convection Conference
- Jones, C. A., Moore, D. R., & Weiss, N. O. 1976, *J. Fluid Mech.*, 73, 353
- Jørgensen, A. C. S., & Weiss, A. 2019, *Monthly Notices of the Royal Astronomical Society*, 488, 3463
- Julien, K., Aurnou, J. M., Calkins, M. A., et al. 2016, *Journal of Fluid Mechanics*, 798, 50
- Julien, K., Knobloch, E., Rubio, A. M., & Vasil, G. M. 2012, *Phys. Rev. Lett.*, 109, 254503
- Julien, K., Knobloch, E., & Werne, J. 1998, *Theoretical and Computational Fluid Dynamics*, 11, 251
- Julien, K., Legg, S., McWilliams, J., & Werne, J. 1996, *Journal of Fluid Mechanics*, 322, 243
- Käpylä, P. J., Käpylä, M. J., & Brandenburg, A. 2014, *Astronomy and Astrophysics*, 570, A43
- Käpylä, P. J., Rheinhardt, M., Brandenburg, A., et al. 2017, *The Astrophysical Journal Letters*, 845, L23
- Käpylä, P. J., Viviani, M., Käpylä, M. J., Brandenburg, A., & Spada, F. 2019, *Geophysical and Astrophysical Fluid Dynamics*, 113, 149
- King, E. M., Stellmach, S., & Aurnou, J. M. 2012, *J. Fluid Mech.*, 691, 568
- King, E. M., Stellmach, S., & Buffett, B. 2013, *Journal of Fluid Mechanics*, 717, 449
- King, E. M., Stellmach, S., Noir, J., Hansen, U., & Aurnou, J. M. 2009, *Nature*, 457, 301
- Kjeldsen, H., Bedding, T. R., & Christensen-Dalsgaard, J. 2008, *The Astrophysical Journal Letters*, 683, L175
- Kjeldsen, H., & Frandsen, S. 1991, *Astronomy and Astrophysics, Supplement*, 87, 119
- Korre, L., Brummell, N., & Garaud, P. 2017, *Physical Review E*, 96, 033104
- Korre, L., Garaud, P., & Brummell, N. H. 2019, *Monthly Notices of the Royal Astronomical Society*, 484, 1220
- Koulakis, J. P., Pree, S., Thornton, A. L. F., & Putterman, S. 2018, *Physical Review E*, 98, 043103
- Lantz, S. R. 1992, PhD thesis, CORNELL UNIVERSITY.
- Lecoanet, D., Brown, B. P., Zweibel, E. G., et al. 2014, *The Astrophysical Journal*, 797, 94
- Lecoanet, D., & Jeevanjee, N. 2018, arXiv e-prints, arXiv:1804.09326
- Lecoanet, D., & Jeevanjee, N. 2019, *JAS*, <https://doi.org/10.1175/JAS-D-18-0320.1>

- Lecoanet, D., Vasil, G. M., Burns, K. J., Brown, B. P., & Oishi, J. S. 2019, *J. Comp. Phys.* **X**, 3, 100012
- Lecoanet, D., McCourt, M., Quataert, E., et al. 2016, *Monthly Notices of the Royal Astronomical Society*, **455**, 4274
- Lesur, G. 2015, Snoopy: General purpose spectral solver, Astrophysics Source Code Library, [ascl:1505.022](#)
- Malagoli, A., Cattaneo, F., & Brummell, N. H. 1990, *ApJL*, **361**, L33
- Malkus, W. V. R. 1954, *Proceedings of the Royal Society of London Series A*, **225**, 196
- Matilsky, L. I., Hindman, B. W., & Toomre, J. 2019, *The Astrophysical Journal*, **871**, 217
- McKim, B., Jeevanjee, N., & Lecoanet, D. 2019, arXiv e-prints, arXiv:1906.07224
- Mellado, J. P., Bretherton, C. S., Stevens, B., & Wyant, M. C. 2018, *Journal of Advances in Modeling Earth Systems*, **10**, 1421
- Miesch, M., Matthaeus, W., Brandenburg, A., et al. 2015, *Space Science Reviews*, **194**, 97
- Miesch, M. S. 2005, *Living Reviews in Solar Physics*, **2**, 1
- Mignone, A., Zanni, C., Tzeferacos, P., et al. 2012, *The Astrophysical Journal Supplemental Series*, **198**, 7
- Morton, B. R., Taylor, G., & Turner, J. S. 1956, *Proceedings of the Royal Society of London Series A*, **234**, 1
- Mosumgaard, J. R., Jørgensen, A. C. S., Weiss, A., Silva Aguirre, V., & Christensen-Dalsgaard, J. 2020, *Monthly Notices of the Royal Astronomical Society*, **491**, 1160
- Nordlund, A., Brandenburg, A., Jennings, R. L., et al. 1992, *The Astrophysical Journal*, **392**, 647
- Nordlund, Å., Stein, R. F., & Asplund, M. 2009, *Living Reviews in Solar Physics*, **6**, 2
- O'Mara, B., Miesch, M. S., Featherstone, N. A., & Augustson, K. C. 2016, *Advances in Space Research*, **58**, 1475
- Orszag, S. A. 1970, *Journal of Fluid Mechanics*, **41**, 363386
- Otero, J., Wittenberg, R. W., Worthing, R. A., & Doering, C. R. 2002, *J. Fluid Mech.*, **473**, 191
- Paxton, B., Bildsten, L., Dotter, A., et al. 2011, *The Astrophysical Journal Supplement*, **192**, 3
- Paxton, B., Cantiello, M., Arras, P., et al. 2013, *The Astrophysical Journal Supplemental Series*, **208**, 4
- Plumley, M., & Julien, K. 2019, *Earth and Space Science*, **6**, 1580
- Prandtl, L. 1925, *Zeitschrift Angewandte Mathematik und Mechanik*, **5**, 136
- Pratt, J., Baraffe, I., Goffrey, T., et al. 2017, *Astronomy & Astrophysics*, **604**, A125

- Rast, M. P. 1998, *Journal of Fluid Mechanics*, 369, 125
- Rast, M. P., & Toomre, J. 1993a, *The Astrophysical Journal*, 419, 224
- . 1993b, *The Astrophysical Journal*, 419, 240
- Rayleigh, L. 1916, *The London, Edinburgh, and Dublin Philosophical Magazine and Journal of Science*, 32, 529
- Rempel, M. 2014, *The Astrophysical Journal*, 789, 132
- Rempel, M., Schüssler, M., & Knölker, M. 2009, *The Astrophysical Journal*, 691, 640
- Romps, D. M., & Charn, A. B. 2015, *Journal of Atmospheric Sciences*, 72, 2890
- Santos, A. R. G., García, R. A., Mathur, S., et al. 2019, *The Astrophysical Journal Supplement Series*, 244, 21
- Santos, A. R. G., Campante, T. L., Chaplin, W. J., et al. 2018, *The Astrophysical Journal Supplemental Series*, 237, 17
- Schmitz, S., & Tilgner, A. 2009, *Physical Review E*, 80, 015305
- Schofield, M., Chaplin, W. J., Huber, D., et al. 2019, *The Astrophysical Journal Supplemental Series*, 241, 12
- Schubert, G., Turcotte, D. L., & Olson, P. 2001, *Mantle Convection in the Earth and Planets*
- Scorer, R. S. 1957, *Journal of Fluid Mechanics*, 2, 583
- Serenelli, A. M., Basu, S., Ferguson, J. W., & Asplund, M. 2009, *The Astrophysical Journal Letters*, 705, L123
- Shchukina, N. G., & Trujillo Bueno, J. 2019, *Astronomy and Astrophysics*, 628, A47
- Shishkina, O., Stevens, R. J. A. M., Grossmann, S., & Lohse, D. 2010, *New Journal of Physics*, 12, 075022
- Shivamoggi, B. K. 2010, *Physics Letters A*, 374, 4736
- Siggia, E. D. 1994, *Annual Review of Fluid Mechanics*, 26, 137
- Singh, H. P., Roxburgh, I. W., & Chan, K. L. 1995, *Astronomy and Astrophysics*, 295, 703
- Smagorinsky, J. 1963, *Monthly Weather Review*, 91, 99
- Soderlund, K. M., Sheyko, A., King, E. M., & Aurnou, J. M. 2015, *Progress in Earth and Planetary Science*, 2, 24
- Spiegel, E. A., & Veronis, G. 1960, *The Astrophysical Journal*, 131, 442
- Spitzer, L. 1962, *Physics of fully ionized gases* (Interscience Publishers)
- Sprague, M., Julien, K., Knobloch, E., & Werne, J. 2006, *Journal of Fluid Mechanics*, 551, 141

- Spruit, H. C. 1997, Memorie della Societa Astronomica Italiana, 68, 397
- Stein, R. F., & Nordlund, Å. 1998, *The Astrophysical Journal*, 499, 914
- Stein, R. F., & Nordlund, Å. 2012, *Astrophys J. Lett.*, 753, L13
- Stellmach, S., Lischper, M., Julien, K., et al. 2014, *Physical Review Letters*, 113, 254501
- Stevens, R. J. A. M., Lohse, D., & Verzicco, R. 2011, *Journal of Fluid Mechanics*, 688, 31
- Stevens, R. J. A. M., Verzicco, R., & Lohse, D. 2010, *Journal of Fluid Mechanics*, 643, 495
- Stix, M. 2003, *Solar Physics*, 212, 3
- Stone, J. M., Gardiner, T. A., Teuben, P., Hawley, J. F., & Simon, J. B. 2008, *The Astrophysical Journal Supplemental Series*, 178, 137
- Stone, J. M., Tomida, K., White, C., & Felker, K. G. 2019, Athena++: Radiation GR magneto-hydrodynamics code
- Strugarek, A., Beaudoin, P., Charbonneau, P., & Brun, A. S. 2018, *The Astrophysical Journal*, 863, 35
- Strugarek, A., Beaudoin, P., Charbonneau, P., Brun, A. S., & do Nascimento, J. D. 2017, *Science*, 357, 185
- Tarshish, N., Jeevanjee, N., & Lecoanet, D. 2018, *Journal of Atmospheric Sciences*, 75, 3233
- Thomsen, M. F., Roussos, E., Andriopoulou, M., et al. 2012, *Journal of Geophysical Research (Space Physics)*, 117, A09208
- Tobias, S. M., Brummell, N. H., Clune, T. L., & Toomre, J. 1998, *The Astrophysical Journal Letters*, 502, L177
- Toomre, J. 2019, in *EAS Publications Series*, Vol. 82, *EAS Publications Series*, 273
- Unno, W., Kato, S., & Makita, M. 1960, *Publications of the Astronomical Society of Japan*, 12, 192
- Van Kooten, S. J., & Cranmer, S. R. 2017, *The Astrophysical Journal*, 850, 64
- Vasil, G. M., Lecoanet, D., Brown, B. P., Wood, T. S., & Zweibel, E. G. 2013, *The Astrophysical Journal*, 773, 169
- Vasil, G. M., Lecoanet, D., Burns, K. J., Oishi, J. S., & Brown, B. P. 2019, *Journal of Computational Physics: X*, 3, 100013
- Verzicco, R., & Camussi, R. 1997, *Physics of Fluids*, 9, 1287
- Viallet, M., Baraffe, I., & Walder, R. 2011, *Astronomy & Astrophysics*, 531, A86
- . 2013, *Astronomy & Astrophysics*, 555, A81
- Viallet, M., Goffrey, T., Baraffe, I., et al. 2016, *Astronomy & Astrophysics*, 586, A153

- Vitense, E. 1953, Zeitschrift fuer Astrophysik, 32, 135
- Wall, J. V., & Jenkins, C. R. 2012, Practical Statistics for Astronomers
- Wang, D., & Ruuth, S. J. 2008, *Journal of Computational Mathematics*, 26, 838
- Weiss, A., Hillebrandt, W., Thomas, H. C., & Ritter, H. 2004, Cox and Giuli's Principles of Stellar Structure
- Wicht, J., Gastine, T., Barik, A., et al. 2017, MagIC: Fluid dynamics in a spherical shell simulator
- Wood, T. S., & Brummell, N. H. 2018, *The Astrophysical Journal*, 853, 97
- Yadav, R. K., Christensen, U. R., Wolk, S. J., & Poppenhaeger, K. 2016, *The Astrophysical Journal Letters*, 833, L28
- Yano, J. I. 2014, *Atmospheric Chemistry & Physics*, 14, 7019
- Yu, J., Huber, D., Bedding, T. R., et al. 2018, *The Astrophysical Journal Supplemental Series*, 236, 42
- Zhong, J.-Q., Stevens, R. J. A. M., Clercx, H. J. H., et al. 2009, *Physical Review Letters*, 102, 044502
- Zhu, X., Mathai, V., Stevens, R. J. A. M., Verzicco, R., & Lohse, D. 2018, *Physical Review Letters*, 120, 144502